Life after an academic death sentence *p. 408*

Ancient liaisons between bonobos and chimps *pp. 414 & 477*

Making climate science more policy-relevant *p. 421*

Science

$15
28 OCTOBER 2016
sciencemag.org

AAAS

LUNAR IMPACT

How this crater got its rings
pp. 438 & 441

CONTENTS

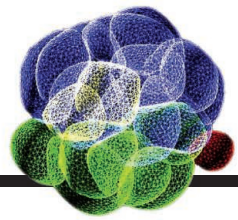

404 The power of embryos

28 OCTOBER 2016 • VOLUME 354 • ISSUE 6311

408

NEWS

IN BRIEF

IN DEPTH

FEATURES

INSIGHTS

PERSPECTIVES

POLICY FORUM

BOOKS *ET AL.*

LETTERS

425

Published by AAAS

CONTENTS

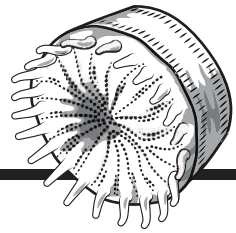

418 & 456
Sulfur's role in plankton communities

28 OCTOBER 2016 • VOLUME 354 • ISSUE 6311

RESEARCH

IN BRIEF

RESEARCH ARTICLES

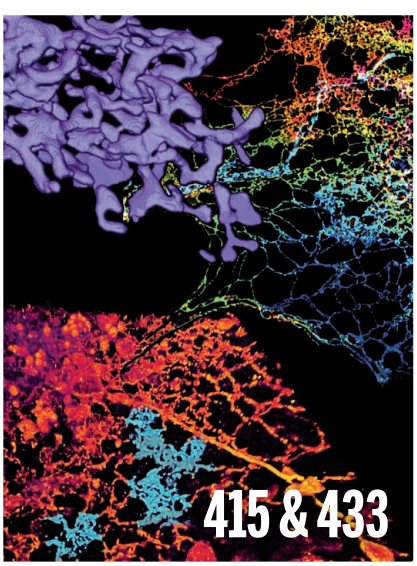

REPORTS

DEPARTMENTS

ON THE COVER

A view of the 930-kilometer Orientale impact basin on the Moon. A simulated digital terrain model is rendered 1 day after full moon. Overlain in color are gravitational anomalies measured by the Gravity Recovery and Interior Laboratory (GRAIL) spacecraft. Red indicates stronger-than-average gravity (blue, weaker), due to the topography and density of the underlying rocks. See pages 438 and 441. *Image: Ernest Wright, NASA/Goddard Space Flight Center Scientific Visualization Studio*

SCIENCE (ISSN 0036-8075) is published weekly on Friday, except the last week in December, by the American Association for the Advancement of Science, 1200 New York Avenue, NW, Washington, DC 20005. Periodicals mail postage (publication No. 484460) paid at Washington, DC, and additional mailing offices. Domestic individual membership and subscription (51 issues): $165 ($74 allocated to subscription). Domestic institutional subscription (51 issues): $1522; Foreign postage extra: Mexico, Caribbean (surface mail) $55; other countries (air assist delivery) $89. First class, airmail, student, and emeritus rates on request. Canadian rates with GST available upon request, GST #1254 88122. Publications Mail Agreement Number 1069624. **Printed in the U.S.A.**
Change of address: Allow 4 weeks, giving old and new addresses and 8-digit account number. **Postmaster:** Send change of address to AAAS, P.O. Box 96178, Washington, DC 20090–6178. **Single-copy sales:** $15.00 current issue, $20.00 back issue prepaid includes surface postage; bulk rates on request. *Science* is indexed in the *Reader's Guide to Periodical Literature* and in several specialized indexes.

Published by AAAS

Science
AAAS
1200 New York Avenue, NW, Washington, DC 20005
Clarendon House, Clarendon Road, Cambridge, UK CB2 8FH

SUBSCRIPTION SERVICES For change of address, missing issues, new orders and renewals, and payment questions: 866-434-AAAS (2227) or 202-326-6417, FAX 202-842-1065. Mailing addresses: AAAS, P.O. Box 96178, Washington, DC 20090-6178 or AAAS Member Services, 1200 New York Avenue, NW, Washington, DC 20005

INSTITUTIONAL SITE LICENSES 202-326-6730 **REPRINTS:** Author Inquiries 800-635-7181 **COMMERCIAL INQUIRIES** 803-359-4578 **PERMISSIONS** 202-326-6765, permissions@aaas.org **AAAS Member Services** 202-326-6417 or http://membercentral.aaas.org/discounts

Science serves as a forum for discussion of important issues related to the advancement of science by publishing material on which a consensus has been reached as well as including the presentation of minority of conflicting points of view. Accordingly, all articles published in *Science*—including editorials, news and comment, and book reviews—are signed and reflect the individual views of the authors and not official points of view adopted by AAAS or the institutions with which the authors are affiliated.

INFORMATION FOR AUTHORS See pages 624 and 625 of the 5 February 2016 issue or access www.sciencemag.org/authors/science-information-authors

Published by AAAS

EDITORIAL

Dealing with details in Marrakesh

Patricia Espinosa is the Executive Secretary of the United Nations Framework Convention on Climate Change

Over the next few weeks, two major events will take place—the 2015 Paris Agreement on climate change will enter into force on 4 November, and 3 days later, nearly 200 countries will convene in Marrakesh, Morocco, at the 22nd United Nations (UN) Conference of the Parties (COP22) to decide on how to rapidly implement the agreement. Indeed, the agreement's governing body will hold its first meeting during COP22. This swift action to commit and come up with climate action plans is a welcome departure for the international community, and it sends a clear message that success in tackling climate challenges requires more than just a historic political agreement.

The Paris Agreement was adopted in December 2015 at the COP21 meeting. For the first time, nations agreed on a single primary goal—to limit global warming to well below a 2°C rise (and as close to 1.5°C as possible), thereby preventing dangerous tipping points in the climate system. This means that global carbon emissions must be driven down drastically and balanced against carbon removal during the second half of this century.

"Achieving the aims of the Paris Agreement is not a given."

Paris was a milestone, yet the Marrakesh Summit is equally important given that governments must now deal with the details. This includes negotiating the rule book to the Paris Agreement, which is, in effect, a global blueprint for reporting and accounting for climate action under the agreement. Another detail is the need for a roadmap on how to mobilize $100 billion in pledged annual support, through 2020. This is critical for financing climate adaptation, strengthening capacity building, and assisting developing countries in taking greater climate action. Marrakesh will offer opportunities to fortify partnerships that accelerate transitions toward a low–carbon emissions future and promote the sustainable development goals that governments already have committed to meet.

Importantly, Marrakesh will see initiatives for implementing Nationally Determined Contributions—national climate plans—and integrating them into each country's development agenda alongside the UN Sustainable Development Goals (also adopted in 2015). The brilliance of the Paris Agreement is its decentralized approach. Success rests on national climate plans that will be updated every 5 years, and updates must demonstrate progress beyond previous plans. Thus, each plan's execution requires continued political leadership and momentum, as well as reinforced public understanding of the enormous social, health, and economic benefits that will accrue to citizens everywhere from strong, continually escalating climate action. The national plans therefore need to trigger more climate-friendly, coordinated laws, policies, and incentives. Favoring old growth and development models based on fossil fuels and high-carbon lifestyles must be abandoned as quickly as possible.

UN estimates show that achieving sustainable development worldwide will require $5 trillion to $7 trillion a year, a large slice of which must fund the essential transition to a low-carbon, resilient global economy. Governments and public- and private-sector institutions need to be willing to allocate tens of billions of dollars toward climate and sustainable investments. The shift is already under way in many nations, and money is also being allocated by multilateral development banks and by dedicated sources such as the UN Green Climate Fund. However, only the private sector has sufficient money, resources, and reach to support governments in the full implementation of national climate plans. The great breakthrough before and since COP21 is that businesses are increasingly convinced that their own profitable future is inextricably linked to low-carbon, sustainable development. Therefore, increasing the private sector's appetite to fund the transformation is essential.

Achieving the aims of the Paris Agreement is not a given. This is a multidecadal effort to turn around two centuries of world development that has been based on fossil fuels. COP22 is a crucial step onto a sustainable course for everyone, everywhere. We are embarking on the right path—let's accelerate action now.

–Patricia Espinosa

10.1126/science.aal2558

> "I remember their names. I remember what they looked like. I remember them in greater detail than patients I saw last week."
>
> **Michael Gottlieb**, who reported the first five AIDS patients in 1981, speaking at a Cold Spring Harbor Laboratory meeting in New York last week on the history and future of HIV/AIDS research. **http://scim.ag/AIDSmeeting**

IN BRIEF

Misconduct found in fetal study fight

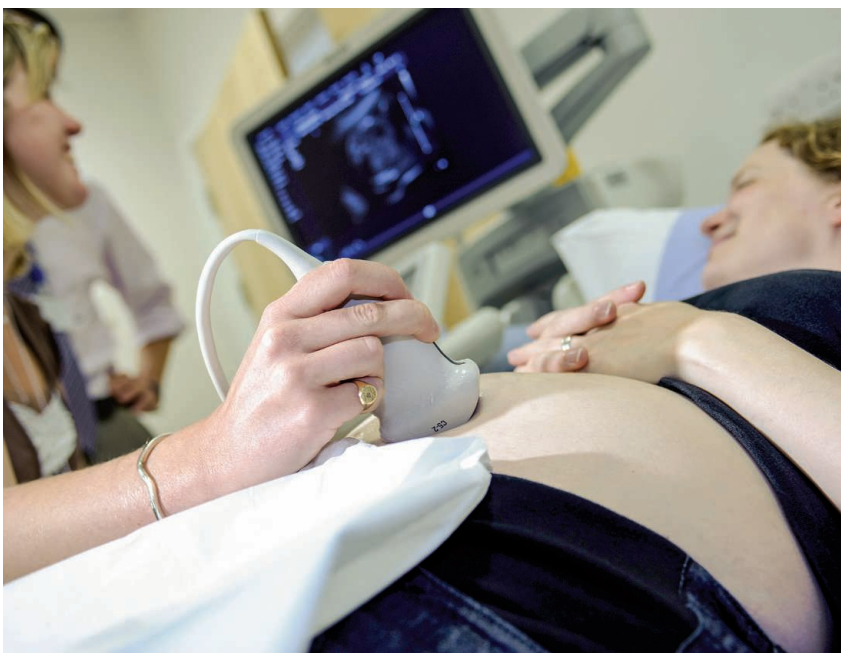

Research on fetal growth sparked a dispute among collaborators.

For the first time in its 68-year history, the World Health Organization (WHO) has concluded that researchers are guilty of research misconduct. The case, first reported by *Science* (9 September, p. 1081), involves two researchers from the University of Oxford in the United Kingdom, José Villar and Stephen Kennedy, who in 2006 were collaborators in a large fetal growth study coordinated by WHO. In March 2008, the two secured a $29 million grant from the Bill & Melinda Gates Foundation for a similar study, after which they withdrew from the WHO study group. Other group members charged that the duo had recycled their ideas for their competing grant proposal or even deliberately delayed the WHO study. Now, an independent review has found that "research ethics misconduct occurred," WHO announced on 20 October without further explanation. The agency, which is in the process of introducing a research misconduct policy, has referred the case to the U.K. General Medical Council. The University of Oxford says it is standing by its researchers, based on its own inquiries. **http://scim.ag/WHOfindsmisconduct**

AROUND THE WORLD

NCI delayed reporting deaths

BETHESDA, MARYLAND | Researchers at the National Cancer Institute (NCI) waited months longer than required to tell regulators about the deaths of two patients in a cancer study. The trial was testing a drug cocktail for lymphoma of the brain or spinal cord. Although tumors shrank in 15 of the 18 patients, two died in May and December 2015 from the same fungal infection. Francis Collins, director of the National Institutes of Health (NIH) in Bethesda, Maryland, said last week that after the second death suggested both were related to the treatment, the researchers and NCI should have told the U.S. Food and Drug Administration within days. Instead, they waited until last May. NIH will now review whether other treatment-related deaths in trials were properly reported. The incident follows safety problems at the NIH Clinical Center that have led to reforms.

Kuwait to scale back DNA law

KUWAIT CITY | Leaders of the Middle East nation say they will revise a controversial law mandating the collection of DNA samples from every citizen and visitor in the country. The 2015 law, a world first, was supposed to help authorities combat crime and terrorism. But critics in Kuwait and beyond have protested that the DNA collection plan was unconstitutional, compromised privacy, could be misused, and would not stop terrorist attacks. After Kuwaiti lawyers filed a lawsuit in September to block the plan and the country's emir raised objections, Kuwait's parliament said last week that only DNA samples from suspected criminals would be added to the collection. The European Society of Human Genetics called the move "a wise and responsible decision."

NSF requests salary cost-sharing

WASHINGTON, D.C. | The National Science Foundation (NSF) has decided that universities should pay 10% of the salaries of faculty members working temporarily at the agency. Until now, NSF has asked—but not required—institutions to pay 15% of

PHOTO: DAN DUNKLEY/SCIENCE SOURCE

what these so-called rotators are earning. But a majority of universities avoid paying anything after pleading poverty, and both Congress and NSF's Office of Inspector General, its in-house watchdog, have criticized the agency for being too lenient in its negotiations. Under a pilot project for 2017, NSF will also stop reimbursing new rotators for lost consulting income and will limit the number of reimbursable trips back to their university to supervise their labs to 12 annually. That last change may be a deal-breaker for some scientists thinking of joining the agency, and NSF officials say the new rules could be adjusted if they appear to be lowering the quality of the applicant pool. http://scim.ag/universitycostsharing

Major research institutes merge

SAN DIEGO, CALIFORNIA | One of the biggest nonprofit biomedical research outfits in the world is getting a new translational medicine research arm, aimed at speeding the conversion of basic research insights into novel medicines. Last week, officials at the Scripps Research Institute announced that it will merge with the California Institute for Biomedical Research (Calibr), which was launched in 2012 as a nonprofit drug development institute. Both Scripps and Calibr are headquartered in San Diego, California, and led by Scripps chemist Peter Schultz. Schultz says that proceeds from any commercial successes will be fed back into the institute's coffers to bolster future research. "We will generate significant revenues," he predicts. If true, that would be a boon for Scripps, which has operated in the red for years. http://scim.ag/researchmerger

MERS biosafety breach

SEOUL | A researcher from the Pasteur Institute Korea (IPK) brought samples taken during the country's outbreak of Middle East respiratory syndrome (MERS) on an intercontinental flight last year without the appropriate paperwork, hoping to get them studied at the Pasteur Institute (IP) in Paris. Both institutes have acknowledged the incident, which IP says was a breach in French biosafety protocol. But both say the trip never put anyone in danger, because the samples had undergone a standard treatment that would have killed any living virus. A review conducted with IPK's safety committee has shown that the samples were inactivated, and as a result, they were noninfectious and did not need any special approval from the airline to be taken onto the flight. IP President Christian Bréchot admitted that the import broke biosecurity rules, however, and that the samples were destroyed after arrival for that reason. http://scim.ag/unauthorizedMERS

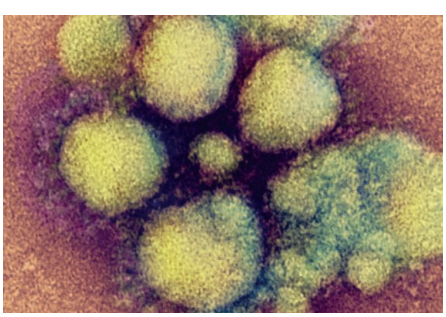

A researcher improperly transported Middle East respiratory syndrome virus samples.

PHOTOS: (TOP TO BOTTOM) SIRIPONG JITCHUM/ISTOCKPHOTO; AMI IMAGES/SCIENCE SOURCE

A faulty genetic switch suppresses limb development in snakes.

Tiny DNA tweaks made snakes legless

The ancestors of modern snakes began to lose their legs 150 million years ago. Now, two groups of scientists—using very different approaches—have pinpointed the genetic cause: Mutations in DNA located near a gene key to limb formation keep that gene from ever turning on. One team found DNA deletions in the switch that controls the activity of that gene in different snakes: Embryonic pythons—which have tiny leg bones inside their bodies—had three such deletions; other snakes with no leg bones at all have more genetic changes. The deletions likely make it difficult for the leg-associated genetic switch to turn on, the team reported in *Current Biology*. Meanwhile, a second team focused on the same genetic switch, substituting versions of the switch from humans, fish, and pythons into a mouse genome using the CRISPR-Cas9 gene-editing technique. With the python switch, the mice developed little nubs instead of legs, the team reported in *Cell*. http://scim.ag/leglesssnakes

NEWSMAKERS

Statistician nabs inaugural prize

The first ever International Prize in Statistics has been awarded to David Cox of the University of Oxford in the United Kingdom. The prize, which includes a cash award of $75,000, will be granted every other year for achievements using statistics to advance science, technology, and human welfare. In the 1970s, Cox developed a model to identify risk factors for mortality. It has bolstered research in areas from cystic fibrosis to effects of industrial air pollution. "Use of the Cox model in the physical, medical, life, earth, social, and other sciences, as well as engineering fields, has yielded more robust and detailed information that has helped researchers and policymakers address some of society's most pressing challenges," says Susan Ellenberg of the University of Pennsylvania, chair of the International Prize in Statistics Foundation.

Three Qs

Computational geneticist **Yaniv Erlich** of the New York Genome Center and Columbia University is known for attention-grabbing studies that harness big data. Erlich's latest project, DNA.land, aims to tap into the genetic data of up to 3 million people already tested by consumer genetics companies such as

23andMe—but unlike those companies, DNA.land would make consenting participants' information broadly available to researchers. Erlich chatted with *Science* about the year-old venture, which now has 32,000 participants. **http://scim.ag/ErlichQA**

Q: Is DNA.land enrollment on track?
A: It's phenomenal that we got so many people. Compared to other projects that try to crowdsource DNA or materials from people, I think we have achieved quite a lot.

Q: How many participants do you need for research?
A: It's already useful for research. We used [a pocket-sized sequencer] to see if we can identify people [using their known DNA profile] very rapidly. [Another] tool, called DNA Compass, was directly inspired by DNA.land's user community. You can upload your genome data to this website, then you can search for ... specific traits—let's say hair color or skin pigmentation.

Q: What's next for DNA.land?
A: We are working with a patient advocacy group, the National Breast Cancer Coalition [NBCC], to test a questionnaire about breast cancer recurrence. NBCC will amplify the presence of our tool to survivors of breast cancer, to people in a family with breast cancer who took one of these genetic tests.

FINDING

Parental training helps in autism

Training parents in how to communicate with their autistic preschoolers produces benefits that are evident 6 years later, researchers report in this week's issue of *The Lancet*. In the randomized, controlled trial, parents of one group of 2- to 4-year-olds were coached by therapists to improve their responsiveness to and interactions with their kids. The parents of the other group received no training. Six years later, the children were assessed using a scale that grades the severity of autistic symptoms. Compared with the control children, the children whose parents were trained by the therapists had on average significantly lower severity scores, driven down by improved social communication skills and fewer repetitive behaviors. The two groups did not differ significantly on measures of anxiety, problem behavior, and depression. "Our findings are encouraging, as they represent an improvement in the core symptoms of autism previously thought very resistant to change," says Jonathan Green, a child psychiatrist at the University of Manchester and Royal Manchester Children's Hospital in the United Kingdom, who led the study.

Cartilage that cushions the knee joint is a challenge to repair.

Tear your knee? Tap your nose

Researchers have found a promising source of cartilage to repair knee injuries ... right up patients' noses. Debilitating knee cartilage injuries are often treated by injecting or grafting healthy cells from a patient's own knee. But nose cartilage, known to easily form new tissue that holds up to mechanical stress, is less invasive to extract. In research published last week in *The Lancet*, a Swiss research team removed tiny chunks of nasal septum cartilage, grew the cells on a porous membrane, and transplanted them into the knees of 10 patients with damaged cartilage. The grafts took on key characteristics of knee cartilage, as measured by their concentrations of structural molecules like the protein collagen and sugar molecules called glycosaminoglycans. Preliminary evidence of improvements in participants' pain and daily function will need to be verified in a larger phase II study, now underway. **http://scim.ag/nosetoknee**

BY THE NUMBERS

$70 million

Amount donated by Tata Trusts to the University of California in San Diego (UCSD). UCSD will match the gift, which will help spur gene drive research that aims to engineer mosquitoes that can't spread malaria.

77%

Proportion of Grauer's gorillas lost in one generation, justifying the great ape's critically endangered status on the International Union for Conservation of Nature's Red List of Threatened Species (*PLOS ONE*).

79%

Accuracy of an artificial intelligence method developed by researchers in the United States and the United Kingdom at predicting judicial decisions of the European Court of Human Rights (*PeerJ Computer Science*).

PHOTO: MIKE DEVLIN/SCIENCE SOURCE

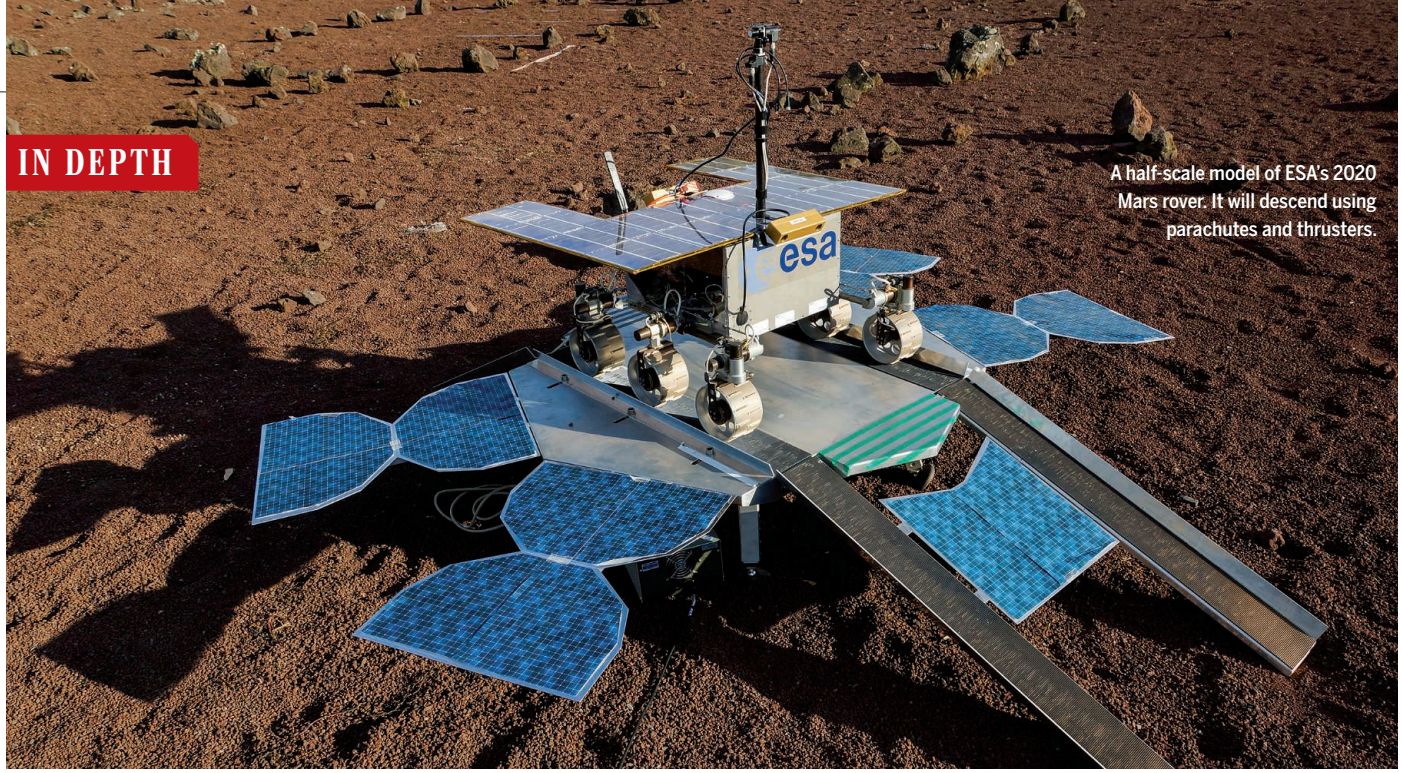

A half-scale model of ESA's 2020 Mars rover. It will descend using parachutes and thrusters.

IMAGE: ESA

PLANETARY SCIENCE

Mars lander crash adds to 2020 rover worries

European rover needs €300 million and uses parts like those on doomed Schiaparelli

By **Daniel Clery**

Engineers at the European Space Agency (ESA) are racing to figure out what went wrong with the Schiaparelli Mars lander. On 19 October, it seemed to drop out of the sky and crash to the surface less than a minute before its planned soft landing. A diagnosis is urgent, because many of the same pieces of technology will be used to get a much bigger ExoMars rover down to the surface in 2020.

More than engineering is at stake. If the ExoMars 2020 rover is to fly at all, ESA must persuade its 22 member states to cover a €300 million shortfall in the €1.5 billion cost of the 2016 and 2020 phases of ExoMars. On 1–2 December, at a meeting of government ministers, ESA officials will make their case that they are not throwing good money after bad. Following the Schiaparelli loss, securing funding for ExoMars 2020 "is really more important than ever, if Europe wants to be seen as part of exploring our solar system," says David Southwood of Imperial College London and ESA's director of science from 2001 to 2011.

At the ministerial meeting, ESA officials will emphasize the success of the Trace Gas Orbiter (TGO), the other part of the ExoMars 2016 mission. As Schiaparelli fell to its doom, the TGO entered a highly elongated 4.2-day orbit around Mars. Next month, it will begin to calibrate science instruments designed to sniff out methane and other trace gases in the atmosphere to pinpoint their origin—not just where they arise, but whether they emanate from geological or biological sources (*Science*, 11 March, p. 1122). In March 2017, TGO will begin dipping down into the martian atmosphere, generating friction that will slow and circularize its orbit so that it can begin science observations later in the year. "We have 100 kilograms of science instruments in orbit around Mars. Solving the mystery of methane is now in our future," David Parker, director of human spaceflight and robotic exploration at ESA headquarters in Paris, told reporters last week.

Compared with the expected science return of the TGO, the weather data that Schiaparelli would have collected with just a few days of battery power on the surface was an afterthought. But as students of ESA's comet-orbiting Rosetta mission learned, the fate of plucky landers resounds in the public consciousness. In November 2014, Rosetta dropped the Philae lander to the surface of a comet, where it survived a couple days. Even though its few pictures and measurements were far surpassed by those of its mother ship, it captured the public's fancy and was a public relations coup.

ESA engineers studying what happened to Schiaparelli are working with information from several sources: data the lander transmitted to the TGO during its descent and elements of the same signal that were picked up by ESA's Mars Express orbiter and a radio telescope on Earth. All sources agree that the signal abruptly stopped about 50 seconds before the expected landing. Early analysis suggested that something went awry after the lander shed its parachute and heat shield and fired its thrusters to slow the final descent. That transition seemed to begin too soon, and the thrusters only fired for a few seconds before cutting out.

On 20 October, the day after the landing, NASA's Mars Reconnaissance Orbiter (MRO) flew over the landing site and snapped images with its low-resolution camera. These showed a white dot, thought to be Schiaparelli's parachute, and 1 kilometer away a fuzzy dark patch, 15 by 40 meters in size. ESA says this dark smudge is probably soil disturbed by the impact of Schiaparelli or even the scar of an explosion, because the lander's propellant tanks would have been full on impact. ESA says the lander probably fell from a height of up to 4 kilometers (the parachute was meant to release it at 1.1 kilometers), and that it would have hit the ground at 300 kilometers per hour. The MRO is expected to take more pictures of the site this

week with its high-resolution camera.

The pressure is on Schiaparelli's engineers to find the problem because the ExoMars 2020 rover and its landing platform are already taking shape. Many components are being duplicated from Schiaparelli with little change and they need to be ready for integration into the spacecraft by next year, says Thierry Blancquaert, Schiaparelli's mission manager at the European Space Research and Technology Centre in Noordwijk, the Netherlands. The aeroshell that will protect the 2020 rover during descent is the same shape as Schiaparelli's, but instead will be built by Russia, which has been partnering with ESA on the ExoMars program since NASA pulled out in 2012. The parachute in 2020 will be the same type but will deploy in two phases—a small one followed by a big one—and the main chute will be much larger: 35 meters across compared with Schiaparelli's 12 meters.

The Russian-built thrusters that will ease the 2020 rover onto the surface will be different. But the radar Doppler altimeter—which senses the surface and allows the thrusters to bring the spacecraft down gently—as well as the guidance and navigation systems will be the same as Schiaparelli's, so their role in last week's descent will be under special scrutiny.

Earlier this year, the planned launch date for the rover was delayed from 2018 to 2020 because of problems mating the ESA-built rover with the Russian aeroshell. Many see this as a blessing in disguise. "The industrial and instrument teams were following aggressive schedules, but the delay is a bit of relief," says Andrew Coates of University College London, principal investigator of the rover's PanCam imaging system. "Now there's time to do something about it."

It remains to be seen whether government ministers will decide that the 2020 mission is a good bet. Enthusiasts like Southwood say ESA needs to follow the example of NASA which, despite a series of Mars mission failures in the 1990s, kept doggedly at it. "Space exploration is tough. As long as we believe in its societal worth, Europe needs to show the same resolve as our American cousins."

Even with seven successful landings under its belt, Mars still makes NASA engineers anxious, says Allen Chen, who heads the entry, descent, and landing team for NASA's Mars 2020 mission at the Jet Propulsion Laboratory in Pasadena, California. Mars's thin and unpredictable atmosphere means much can go wrong. Like ESA, NASA is also planning to drop a rover to the surface in 2020, as is China. "Every Mars landing attempt teaches us things," Chen says. "The only true failure is to stop trying." ■

PHOTO: CROZSTUDIOS/ALAMY STOCK PHOTO

BIOMEDICINE

Baby genome screening needs more time to gestate

Unenthused parents and missed diseases mar pilot efforts

By **Jocelyn Kaiser**

Genetics researchers have begun gingerly approaching an ethically fraught idea: As DNA sequencing gets ever cheaper, should every newborn baby, ill or seemingly healthy, have its genome analyzed? Would sequencing help spot rare diseases and guide future medical decisions? Or would it open a Pandora's box of needless costs and worries?

Two research projects exploring these questions are now delivering early results, and both are giving pause to newborn-sequencing advocates. One suggests that exome sequencing, which reads the protein-coding regions of a genome, is not comprehensive enough to replace standard newborn blood screening for rare diseases. And the other finds that parents are surprisingly uninterested in having their newborns sequenced.

Together, the findings suggest newborn sequencing "as available now is not the answer," says geneticist Jennifer Puck of the University of California in San Francisco, who co-leads one of the studies presented last week at the annual meeting of the American Society of Human Genetics (ASHG) in Vancouver, Canada.

The projects are among a quartet funded by the National Institutes of Health (NIH) to compare the risks and benefits of sequencing newborns' DNA with those of existing screening programs, which rely on biochemical analysis of newborn blood spots to test for dozens of metabolic diseases (*Science*, 13 September 2013, p. 1163). NBSeq, co-led by Puck, is sequencing exomes of deidentified samples from 1700 newborn blood spots archived after standard biochemical screening in California.

With 182 samples analyzed so far, the results are sobering: The DNA sequencing missed about 20% of confirmed disease cases that had been flagged by biochemical screening. All were very rare diseases, some of which may have been caused by mutations, perhaps in rearranged DNA or regions regulating gene activity, not detectable by exome sequencing. Whole genome sequencing might have found some of the culprit mutations, Puck says, but it's still too costly and challenging for routine use.

Exome sequencing does appear useful, however, in concert with the traditional screening. It can pin down the gene responsible for an abnormal biochemical result, yielding a definitive diagnosis. "In tricky cases it will help," Puck says. NBSeq is also finding that sequencing may help identify newborns with inherited immunodeficiency disorders. Only one of those diseases is detected by standard biochemical screening of a newborn's blood; others often only surface later, when the child develops recurrent infections.

Another NIH-funded newborn project aims to show whether sequencing a long list of genes could be useful for routine medical care. The BabySeq team, co-led by geneticist Robert Green at Brigham and Women's

Genome sequencing of babies may not quickly replace biochemical tests of blood from heel pricks.

Hospital in Boston, analyzes babies' DNA for mutations in roughly 7000 genes implicated in metabolic and other childhood diseases or adverse drug reactions. The effort, which began in May 2015, is hitting an unexpected snag: The parents of only 24 of 345 sick babies in neonatal intensive care, and 138 of 2062 healthy babies, have agreed to join BabySeq, Green reported at the ASHG meeting. That 7% response rate from both groups is much lower than expected based on a survey of hundreds of parents of newborns about 4 years ago, when nearly half declared they would be "very" or "extremely" interested.

Many parents were apparently put off by having to return to the hospital with their newborns to discuss the sequencing results. Others who met with a genetic counselor before being invited to join the study had concerns such as privacy, the prospect of worrisome or unclear results, and insurance discrimination. Although U.S. law prohibits health insurers from denying coverage based on genetic data, the children could be denied life, disability, or long-term care insurance. "A lot of that is literally 50 years in the future and they are concerned," Green says.

Green's study so far has delivered mixed evidence on whether the genetic data will be useful. Three of the newborns carried inherited mutations implicated in heart disease, but there were no signs of illness in the parents or child. Green's team will track whether the DNA results benefit the family, or lead to unnecessary anxiety and tests. Another baby had mutations linked to an enzyme deficiency that biochemical screening missed; although asymptomatic, the baby had enzyme levels that are slightly below normal and is being treated. A fifth infant carried a mutation in a gene linked to breast cancer. At first, Green's team did not plan to tell families about mutations linked to adult-onset diseases, but they got permission from the study's ethics boards to disclose the result. The mother, who had relatives with breast cancer, "was obviously concerned but grateful," Green says.

Because of the uncertainties and possible harms of routine newborn sequencing, ASHG's current position is that only babies with an undiagnosed illness should have their DNA read—and preferably only for genes likely to explain the disorder. But genomics policy expert Misha Angrist of Duke University in Durham, North Carolina, thinks the appeal of sequencing every newborn may grow. "These are still very early days," he says. "If more people do this and the discrimination and confidentiality risks do not materialize, then presumably more people will choose newborn sequencing." ■

PLANETARY SCIENCE

Hunt for Planet Nine heats up

Discovery of icy worlds in the distant solar system offer new clues in searches for hypothetical giant

By **Adam Mann**

New solar system objects used to be a distraction for Konstantin Batygin, a planetary scientist and theorist at the California Institute of Technology (Caltech) in Pasadena. Each discovery added another complication to his computer models of the solar system, which twirl planetoids around the sun. But now, Batygin is eager to find more of the objects himself, and missed opportunities pain him. In late September and early October, cloudy skies foiled a 6-night run at the Subaru Telescope atop Mauna Kea in Hawaii. All you can do, he says, is "just sit quietly and wait for things to get slightly better."

> ***"I'm probably 90% sure there's a planet out there."***
>
> **Scott Sheppard**, Carnegie Institution for Science

What drew Batygin into the hunt is the ultimate prize: a new planet, the first to be added to our solar system in more than a century. Colloquially called Planet Nine, this distant hypothetical world could have 10 times the mass of Earth and take 15,000 years to go around the sun. This past January, Batygin and Mike Brown, a Caltech astronomer, proposed that the giant could explain the peculiarly clustered orbits of six icy bodies beyond Neptune (*Science*, 22 January, p. 330). Now, several teams, including Batygin and Brown's, are racing to spot Planet Nine directly.

Studies presented last week at a meeting of the American Astronomical Society in Pasadena are giving them extra encouragement. Researchers have found another three transneptunian objects (TNOs) that, like the first six, may corroborate Planet Nine's existence and help narrow down its putative orbit. The influence of the unseen giant could also explain the strange orbits of two more objects, perpendicular to the plane of the solar system. And it might explain why the sun is tipped slightly on its axis, astronomers say.

The new evidence leaves astronomer Scott Sheppard of the Carnegie Institution for Science in Washington, D.C., "probably 90% sure there's a planet out there." But others say the clues are sparse and unconvincing. "I give it about a 1% chance of turning out to be real," says astronomer JJ Kavelaars, of the Dominion Astrophysical Observatory in Victoria, Canada.

The trail of Planet Nine began in 2003, when Brown spotted one of the most far-

Curious clusters

In January, astronomers announced evidence for Planet Nine, a new giant planet, based on the way it would shepherd six icy worlds into clustered orbits on the other side of the solar system. Three new objects add to the picture.

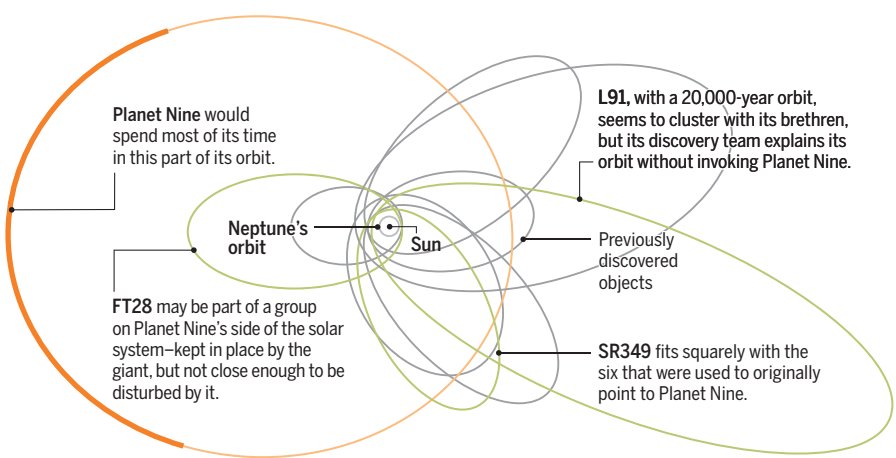

CREDITS: (DIAGRAM) G. GRULLÓN/*SCIENCE*; (DATA) SCOTT SHEPPARD/MICHELE BANNISTER

flung bodies in the solar system—an oddity known as Sedna whose orbit takes it out to more than 900 astronomical units (AU), the distance between Earth and sun. More important, Sedna doesn't come any closer than 76 AU—more than twice as far out as Neptune. That puts it beyond the gravitational influence of that last ice giant. Something else had to pull it into its strange elongated orbit: perhaps a passing star, or the gravitational tides of the Milky Way.

Or maybe a giant planet. When Brown and Batygin found five more TNOs curiously clustered in the sky, they realized with extensive modeling that a giant planet's gravity would have flung any objects away from its path, leaving the orbits of the remaining objects huddled on the opposite side of the solar system.

Now, additional objects may be adding to the pattern. At the conference, Sheppard and his colleague Chad Trujillo of the Gemini Observatory in Hilo, Hawaii, presented the first two new entrants: 2014 SR349 and 2013 FT28. "The big question is do they make the planet case better or worse," Sheppard says. "And they make it better."

The first, 2014 SR349, falls right in line with the earlier six objects. The second, 2013 FT28, is on the opposite side of the sky—well within the proposed orbit of Planet Nine, where computer modeling suggests it would be safe from gravitational kicks. L91—the third new TNO and one of the most distant objects in the solar system—looks as if it might fit in with the antialigned group, but astrophysicist Michele Bannister of Queen's University Belfast, who described the object at the meeting, cited modeling that suggests maybe it does not have anything to do with Planet Nine.

Kavelaars thinks Brown and Batygin's clustering is unlikely to be real. To spot these objects at all astronomers have to look away from the bright Milky Way. It may be that the odd ones occupy similar parts of the sky because that is the easiest place to look. He expects that as additional distant bodies are discovered, their orbits will start to look more random. Kavelaars's collaborator Cory Shankman of the University of Victoria has created models with the exact orbits of the six distant objects but found that a massive planet would not maintain the telltale clustering for long periods.

Not to be deterred, Planet Nine enthusiasts can now invoke two more lines of evidence. As they spin around the sun, the known planets, asteroids, and most TNOs stay in roughly the same plane, known as the ecliptic. But this year yielded some striking exceptions. One new object, known as 2016 NM56, has an orbit tilted so far out of the ecliptic that it essentially orbits backward. Another has a near-perpendicular orbit relative to the ecliptic. In a talk at the meeting, Batygin showed how Planet Nine might create these wonky trajectories. Through what's known as the Kozai mechanism, a massive object can induce a gravitational ratcheting effect that slowly changes the inclination of smaller worlds and "leads their orbits to flip upside-down," he says.

Batygin and Brown's proposed orbit for Planet Nine is itself rather slanted, poking out about 30° relative to the ecliptic. Their graduate student, Elizabeth Bailey, showed how the tilted orbit could potentially explain a curious feature of the sun: Rather than being pointed perpendicular to the ecliptic, its north pole is off by about 6°. Researchers have tried to explain the anomaly, discovered in the 19th century, by invoking interactions between the early sun's magnetic field and the disk of gas and dust that gave rise to the solar system. Bailey's simulations showed instead that, over the course of the solar system's history, the lopsided orbit of Planet Nine would have exerted a gravitational force on the sun that could have pushed it almost exactly 6° to one side. Astronomer Rodney Gomes of the National Observatory of Brazil in Rio de Janeiro and his collaborators independently came up with the same idea in July.

Few will believe in Planet Nine until it is seen directly. Planets spend the most time in the most distant part of their orbit, where they travel slowest. For Planet Nine, that would put it somewhere in the constellation Orion, which is just where astronomers are searching with the largest, widest angle telescopes they can find. Batygin, Brown, Sheppard, and Trujillo are all using the 8-meter Subaru Telescope, because its Hyper Suprime-Cam can cover large parts of the sky with each shot. After their recent run in late September, which covered 10% of the most distant part of Planet Nine's putative orbit, Batygin believes "there's a 10% chance it's in the bag."

Sheppard's team has also been awarded time on two telescopes in Chile, where Orion is also visible: the 4-meter Blanco Telescope and the 6.5-meter Magellan Telescopes. He says his team should scrutinize about a third of the outlying parts of Planet Nine's proposed orbit this year and feels there's a good chance they might see it by the end of 2017. Computational astrophysicist Peter Nugent of the University of California in Berkeley is taking a different tack: His graduate students will trawl through archival data from a survey begun in 2009 on the venerable 5.1-meter telescope on Mount Palomar in California to see whether it happened to spot the planet.

To the victors will go the glory of discovering a new planet. "We're trying to keep it friendly," Sheppard says, but adds that it's definitely a race. Early on, the different groups talked about sharing their intended search fields, so as to avoid duplicative efforts on the sky—but now "we each want to be the one to find it," Sheppard says. And should that happen, what then? "I'd basically retire at that point," he says, laughing. ■

Adam Mann is a freelance journalist based in Oakland, California.

Hide and seek

In order to spot Planet Nine, astronomers need to look away from the bright Milky Way using powerful, wide-field telescopes. Since 2007, one team has ruled out parts of the sky using three different telescopes (colored dots), and is now homing in on a likely part of Planet Nine's orbit.

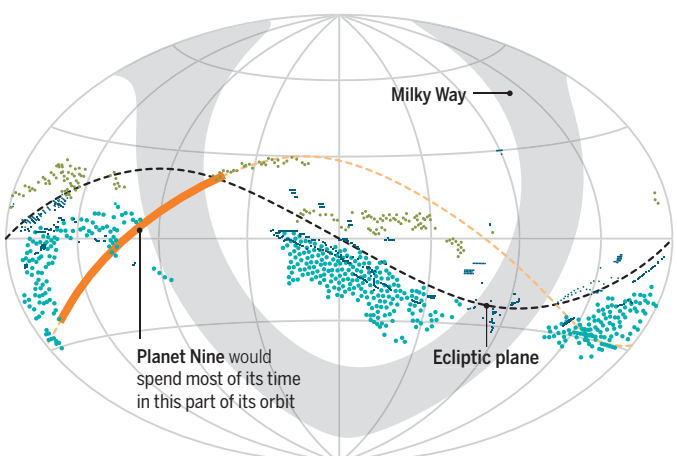

Blanco Telescope
Chile - 4 m
Although it has a smaller mirror, its Dark Energy Camera is one of the largest in astronomy.

Magellan Telescopes
Chile - 6.5 m
Although they have large mirrors, their cameras are small and relatively inefficient for searching.

Subaru Telescope
Hawaii - 8 m
It can search for Planet Nine even when it is well north of the ecliptic.

CREDITS: (DIAGRAM) G. GRULLÓN/*SCIENCE*; (DATA) SCOTT SHEPPARD

PHOTO: ZOONAR GMBH/ALAMY STOCK PHOTO

Storm clouds are too small for climate models to render directly, and so modelers must tune for them.

COMPUTER MODELING

Climate scientists open up their black boxes to scrutiny

Modelers becoming less hush-hush about tuning, the "secret sauce" that controls fine-scale processes

By **Paul Voosen**

It began with an unplanned leave of absence. But it has blossomed into a full-fledged transparency movement for climate science.

In 2010, Erich Roeckner, a longtime guru behind the global climate model at the Max Planck Institute for Meteorology (MPIM) in Hamburg, Germany, was unable to work. The timing was inopportune: Deadlines loomed for an international project that would compare the major climate models with one another, and MPIM's had a bug.

Roeckner's skill was handling details like the effects of rough terrain or the formation of clouds—processes too fine-grained for models to render within the imaginary boxes, tens of kilometers on a side, into which they divide the atmosphere and ocean. Instead, modelers "parameterize" such details, coming up with equations meant to approximate their effects. When the equations miss the mark and the model strays from the known climate, scientists like Roeckner bring it back into harmony by adjusting them. Other disciplines might call this calibration. In climate science, it's called tuning.

With Roeckner out of commission, a team of six people spent several months tuning the MPIM model to match the climate and eliminate the glitch. Their work, though laborious, was fairly routine. What was unusual was their decision, in 2012, to publish a detailed accounting of it. Roeckner's absence was random. But in hindsight, it was the butterfly flapping that has now led climate modelers to openly discuss and document tuning in ways that they had long avoided, fearing criticism by climate skeptics.

Next week, many of the world's 30 major modeling groups will convene for their main annual workshop at Princeton University; by early next year, these teams plan to freeze their code for a sixth round of the Coupled Model Intercomparison Project (CMIP), in which these models are run through a variety of scenarios. The output will ultimately help the next United Nations climate change panel make its predictions. By writing up their tuning strategies and making them publicly available for the first time, groups hope to learn how to make their predictions more reliable, says Bjorn Stevens, an MPIM director who has pushed for more transparency. And in a study that will be submitted by year's end, six U.S. modeling centers will disclose their tuning strategies—showing that many are quite different. "Most groups take pride in calibrating their models in different ways," says Gavin Schmidt, who's coordinating the study and directs NASA's Goddard Institute for Space Studies in New York City, another prominent modeling center.

At their core, climate models are about energy balance. They divide Earth up into boxes, and then, applying fundamental laws of physics, follow the sun's energy as it drives phenomena like winds and ocean currents. Their resolution has grown over the years, allowing current models to render Earth in boxes down to 25 kilometers a side. They take weeks of supercomputer time for a full run, simulating how the climate evolves over centuries.

When the models can't physically resolve certain processes, the parameters take over—though they are still informed by observations. For example, modelers tune for cloud formation based on temperature, atmospheric stability, humidity, and the presence of mountains. Parameters are also used to describe the spread of heat into the deep ocean, the reflectivity of Arctic sea ice, and the way that aerosols, small particles in the atmosphere, reflect or trap sunlight.

It's impossible to get parameters right on the first try. And so scientists adjust these equations to make sure certain constraints are met, like the total energy entering and leaving the planet, the path of the jet stream, or the formation of low marine clouds off the California coast. Modelers try to restrict their tuning to as few knobs as possible, but it's never as few as they'd like. It's an art and a science. "It's like reshaping an instrument to compensate for bad sound," Stevens says.

Indeed, whether climate scientists like to admit it or not, nearly every model has been calibrated precisely to the 20th century climate records—otherwise it would have ended up in the trash. "It's fair to say all models have tuned it," says Isaac Held, a scientist at the Geophysical Fluid Dynamics Laboratory, another prominent modeling center, in Princeton, New Jersey.

For years, climate scientists had been mum in public about their "secret sauce": What happened in the models stayed in the models. The taboo reflected fears that climate contrarians would use the practice of tuning to seed doubt about models—and, by extension, the reality of human-driven warming. "The community became defensive," Stevens says. "It was afraid of talking about things that they thought

could be unfairly used against them." Proprietary concerns also get in the way. For example, the United Kingdom's Met Office sells weather forecasts driven by its climate model. Disclosing too much about its code could encourage copycats and jeopardize its business.

But modelers have come to realize that disclosure could reveal that some tunings are more deft or realistic than others. It's also vital for scientists who use the models in specific ways. They want to know whether the model output they value—say, its predictions of Arctic sea ice decline—arises organically or is a consequence of tuning. Schmidt points out that these models guide regulations like the U.S. Clean Power Plan, and inform U.N. temperature projections and calculations of the social cost of carbon. "This isn't a technical detail that doesn't have consequence," he says. "It has consequence."

Recently, while preparing for the new model comparisons, MPIM modelers got another chance to demonstrate their commitment to transparency. They knew that the latest version of their model had bugs that meant too much energy was leaking into space. After a year spent plugging holes and fixing it, the modelers ran a test and discovered something disturbing: The model was now overheating. Its climate sensitivity—the amount the world will warm under an immediate doubling of carbon dioxide concentrations from preindustrial levels—had shot up from 3.5°C in the old version to 7°C, an implausibly high jump.

MPIM hadn't tuned for sensitivity before—it was a point of pride—but they had to get that number down. Thorsten Mauritsen, who helps lead their tuning work, says he tried tinkering with the parameter that controlled how fast fresh air mixes into clouds. Increasing it began to ratchet the sensitivity back down. "The model we produced with 7° was a damn good model," Mauritsen says. But it was not the team's best representation of the climate as they knew it.

Aside from being more open about episodes like this, many modelers say that they should stop judging themselves based on how well they tune their models to a single temperature record, past or predicted. The ability to faithfully generate other climate phenomena, like storm tracks or El Niño, is just as important. Daniel Williamson, a statistician at the University of Exeter in the United Kingdom, says that centers should submit multiple versions of their models for comparison, each representing a different tuning strategy. The current method obscures uncertainty and inhibits improvement, he says. "Once people start being open, we can do it better." ■

DATA CHECK

BEHIND THE NUMBERS

How a figure key to new HFC pact was born

By **Warren Cornwall**

When world leaders reached a deal last month in Kigali to curb the use of hydrofluorocarbons (HFCs)—planet-warming chemicals widely used in air conditioners and refrigerators—many boasted the move would prevent nearly 0.5°C in warming by 2100. That is a big number, given that the Paris climate agreement aims to keep total warming to less than 2°C. If the HFC number is correct, it will make it easier for nations to achieve the Paris goal.

But there's a bit more scientific uncertainty surrounding that half-degree claim than the politicians let on. The figure has its origins in a 2006 dinner held by five scientists in a village in the Swiss Alps. The U.S. and European researchers, who work for government and industry, were part of a group that advises policymakers on the Montreal Protocol, the 1987 pact that curbed the use of chemicals that harm the ozone layer. The researchers found that the protocol also helped reduce global warming, because some of the regulated chemicals were potent greenhouse gases. But they realized the pact had a warming downside too, says David Fahey, a physicist at the National Oceanic and Atmospheric Administration's Earth System Research Laboratory in Boulder, Colorado. That's because because some of the ozone-friendlier chemicals, such as HFCs, trap heat thousands of times more effectively than carbon dioxide. Soon, the researchers were trying to figure out what that meant for the planet.

Cooling down

New deal aims to reduce warming caused by hydrofluorocarbons.

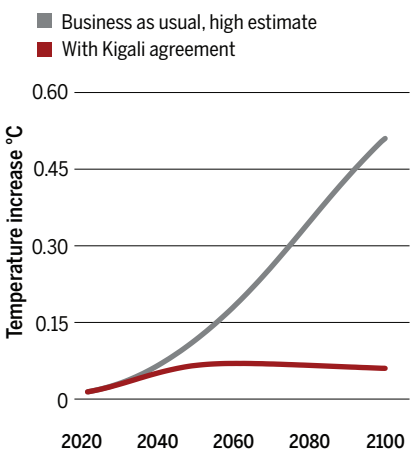

The half-degree estimate was first floated in a 2013 paper co-authored by one of the dinner guests, physicist Guus Velders of the National Institute for Public Health and the Environment in Bilthoven, the Netherlands. The study, published in *Atmospheric Chemistry and Physics*, forecast that rising HFC use in the developing world would push global temperatures up by 0.35°C to 0.5°C by 2100.

Those numbers caused a stir, because they were substantially higher than HFC warming forecasts made by other climate models, including those underpinning the massive reports of the Intergovernmental Panel on Climate Change (IPCC). Ultimately, however, they helped galvanize support for the Kigali agreement, which aims to cut HFC use by 80% to 85% by 2047. And advocates and negotiators tended to cite the higher, 0.5°C estimate in their public remarks.

That didn't sit well with Andrew Jones, co-director of Climate Interactive, a prominent climate analysis group. A day after nations announced the 15 October Kigali deal, Jones wrote a blog post hailing it as "excellent news for the climate." But he cautioned against counting on the full 0.5°C benefit. One reason, he wrote, is that he considers the 2013 paper to be an outlier, because it projects HFC warming that is roughly four times greater than that projected by a model cited by the IPCC. "I'm not really buying it," says Jones, who is in Asheville, North Carolina.

Velders says his team came up with higher warming estimates than the IPCC because their model accounts for trends that others don't, such as the faster-than expected adoption of HFCs driven by the Montreal Protocol, and an air-conditioning boom in the developing world. Still, he concedes that forecasting HFC use is difficult. If warming prompts greater demand for air conditioners in India, for instance, future HFC impacts could be even greater. His team was careful to clarify the uncertainty, he notes, by presenting a range of forecasts, with 0.5°C at the high end.

But although scientists routinely acknowledge such uncertainty, "that's not what politicians do," says Durwood Zaelke, president of the Institute for Governance & Sustainable Development in Washington, D.C., which backed aggressive HFC reductions.

Now, Velders is offering a single new number: 0.06°C. That is his new estimate of how much warming HFCs will cause by 2100 if the Kigali deal hits its targets. ■

CREDITS: (DIAGRAM) D. MALAKOFF/*SCIENCE*; (DATA) G. VELDER

Q&A

Mental health chief to stress neural circuits

Joshua Gordon will also prioritize computational pyschiatry and suicide prevention

PHOTO: COURTESY OF NIH

Joshua Gordon was a first year M.D.-Ph.D. student at the University of California in San Francisco bent on a career in cancer biology when he heard a talk describing how electrically stimulating cells in a key area of the brains of monkeys could alter the animals' perception of which direction dots were moving on a computer screen. The power of that manipulation—and the vast possibilities for probing the brain that it suggested—captivated Gordon. He switched his Ph.D. focus to neuroscience.

A quarter-century later, Gordon, 49, is director of the $1.55 billion National Institute of Mental Health (NIMH) in Bethesda, Maryland. He assumed the post last month after 19 years at Columbia University, where he completed a psychiatry residency and later joined the faculty. For much of that time, he explored neural circuits in mice with mutations relevant to schizophrenia, anxiety disorders, and depression. In recent years, Gordon also oversaw the research projects of Columbia's psychiatrists-in-training. And beginning in 2001, he maintained a private psychiatry practice 1 night a week, treating patients with depression and anxiety. Closing that practice to move to the NIMH was, he says, "very painful."

Just weeks into his new job, Gordon was challenged by two former colleagues in a pair of prominent op-eds. The clinical psychiatrists charged that under Gordon's predecessor, Thomas Insel, NIMH—the largest mental health research funder in the world—has swung too far toward basic neuroscience, neglecting research on the issues that touch patients every day. Gordon needs to change that, they asserted. *Science* sat down with Gordon last week to discuss his reaction and other matters. His responses have been edited for brevity and clarity. (A fuller version is online at http://scim.ag/GordonQA.)

By **Meredith Wadman**

Q: How has working in a lab informed your outlook as you take the reins at NIMH? And how has seeing patients done the same thing?
A: The lab has informed it in many ways, [including] the science that I know, which is around neural circuits and their relationship to psychiatric disease. I can pretty easily see the value of trying to understand how patterns of brain activity and the structure of the brain influence behavior. Perhaps the most profound influence from the clinical side is that virtually no patient I see fits into a neat category [from the *Diagnostic and Statistical Manual of Mental Disorders* (*DSM*).]

Q: What are your priorities for the institute as you come in?
A: One area that I consider a priority is neural circuits. Another is computational psychiatry. I think bringing more computational formalism to psychiatric research at all levels—basic, clinical, and perhaps even implementation research—will help us do our job better. Third, suicide is a huge clinical problem. It's a cross-diagnostic problem and it's one for which we have evidence bases for at least short-term treatment and prevention.

Q: How and why would you prioritize neural circuit work at NIMH?
A: Advances in technology have led to increasingly powerful tools that enable neuroscientists to measure and influence neural activity in specific neural circuits. Using these tools, we can, for instance, reduce depressionlike behavior in mouse models. It is tantalizing to imagine adapting these tools for use in humans. We don't yet know whether these techniques would be therapeutically useful. But unless we start laying the groundwork now, we won't be able to find out in the future. To some extent, the BRAIN [Brain Research through Advancing Innovative Neurotechnologies] Initiative is engaged in just this. But specific investments in NIMH areas of interest, such as developing approaches to identify and influence circuits related to mood and cognition in animal models that can bridge between mice and humans, will also be crucial.

Q: *The Washington Post* and *The New York Times* recently ran commentaries from clinical psychiatrists. One accused your predecessor of "strangling [NIMH's] clinical research budget." Another claimed that NIMH "has lost sight of its most fundamental mission: finding ways to ease the burden of mental illness for those affected by it today." It argued that since 2012, "a full 85 percent of non-AIDS–related grant funding has been channeled to basic scientific research," short-changing research on existing treatments and services. Will you change that balance?
A: I think that's an argument we have to pay attention to. [But] I don't think it's my duty to respond to these articles. Because I am trying to figure out the field as a whole, to listen to others in the field on all sides, and then make a decision about funding. In terms of the balance, I think my first priority is good science. Where there are opportunities in [clinical] psychiatry for short-term effects, we are going to try to take advantage of them. Absolutely. We'd be mad not to. We know so little about the brain, we have so few truly novel treatments in the pipeline that—I'm all ears. But I'm not hearing a lot of people say to me: "We have these short-term gains that we can make in this area and that area."

Q: The Research Domain Criteria (RDoc) project [started under Insel] aims to incorporate genetics, imaging, and other information to underpin a new psychiatric disease classification system. Is the implication that the *DSM*'s classification by symptoms should be dispensed with? Is it a 20th century artifact?
A: I'm not sure Tom [Insel] would agree with that last statement. But I certainly disagree. I think [the] *DSM* is incredibly useful. Doctors talk in terms of diagnoses. Maybe [the] RDoC is going to be very helpful and we are going to be able to say: "You have [this or that degree of] a deficit in the negative affect domain in fear expression." But it may also be useful to say: "And it is panic disorder," or, "It is [an] anxiety disorder." It may be mathematically that combining those two things [the RDoC assessment and the *DSM* assessment] gives you more information. And one of the reasons is that it tells you what the clinician sees. I am a strong supporter of the basic idea of breaking down behavior in parts and [the] RDoC is seemingly one way to do it. If we are going to make transformative progress for our patients, for individuals who are suffering, we need to get to the neurobiology. And so [the] *DSM* is, in my mind, not enough. ■

Magdalena Zernicka-Goetz and her son, Simon, who helped inspire some of her embryo research.

PUSHING THE LIMIT

By culturing human embryos for longer than ever, Magdalena Zernicka-Goetz is revealing their "powerful beauty"—and sparking debate

By **Gretchen Vogel**, *in Cambridge, U.K.*

In 2006, Magdalena Zernicka-Goetz was pregnant, unexpectedly, at age 42. A genetic test of the fetal portion of the placenta showed that roughly a third of the cells carried a serious abnormality: an extra copy of chromosome 2. The University of Cambridge professor's specialty, developmental biology, "was suddenly personal," she says.

Nature could hardly have come up with a more vivid irony. Zernicka-Goetz is not only a developmental biologist; she has spent more than a decade working in mice to pinpoint when and how cells in an early embryo start to differentiate. By the time of her pregnancy, her research had convinced her that individual cells are starting to go their separate ways when the embryo has just four cells—a stance that was and remains controversial. Her child's health depended in part on a question that had already captivated her as a scientist, she recalls: How much flexibility does the developing embryo retain? Or, as she puts it, "What is the minimum number of normal cells for the fetus to be normal?"

While still pregnant and uncertain about her baby's fate, Zernicka-Goetz started mouse work that led to a paper this March revealing new details about embryos' remarkable ability to cope with faulty cells. Her personal story, too, had a happy outcome, as newspaper pictures of her and her charming, healthy, 9-year-old son, Simon, made clear when the work was published. "Simon is my model for plasticity," Zernicka-Goetz tells audiences when she discusses that research.

Two months later, she caught the attention of other embryologists and the wider world with another demonstration of embryos' resilience. This time her lab showed—in concert with researchers in New York City—that human embryos created by in vitro fertilization (IVF) could be kept developing in the lab for nearly 2 weeks, well past the point at which they would normally implant in the wall of the uterus. That's almost twice as long as previously achieved, and it opens the way to studying a key phase of human development that had been inaccessible. Success was far from guaranteed—mentors had warned Zernicka-Goetz away from the difficult project—and took years of testing different culture conditions with mouse embryos. But it illustrated a hallmark of Zernicka-Goetz's work from the beginning, says Lilianna Solnica-Krezel, a developmental biologist at Washington University in St. Louis, Missouri: "the persistence with which she comes back to the same questions and same problems, using new technological advances … to find answers."

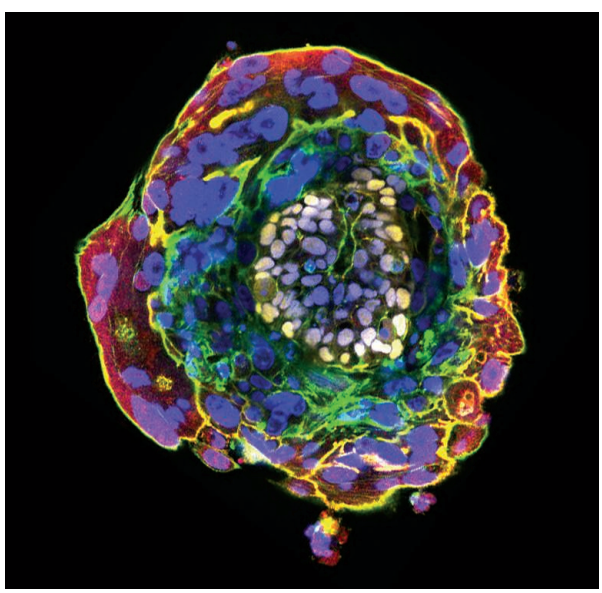

In this image of an 11-day-old human embryo tagged with fluorescent markers, gray cells are on a path to forming tissues of the body; others are beginning to form placenta and additional supporting cell types.

The feat has already sparked new ethical debates about limits to embryo research. In some places, laws prohibit any human embryo studies at all—several states in the United States explicitly forbid it, for example, and the National Institutes of Health isn't allowed to fund research in which such embryos are harmed or discarded. In most of the United States there are no legal restrictions on privately funded research, but widely accepted international guidelines dictate that human embryos should not be allowed to develop longer than 14 days in culture. (In the United Kingdom, that limit is mandated by law.)

The threshold was chosen in part because it's the point at which the embryo can no longer split to form twins. Until May, that "was a very hypothetical barrier, since we only knew how to keep [embryos] looking normal for 7 days at most," says Robin Lovell-Badge, a developmental geneticist at the Francis Crick Institute in London. The limit "has been a very useful thing to have because it has meant that scientists can conduct experiments with that nice clear boundary. And we're always happier knowing where the walls are."

But Zernicka-Goetz's culturing success, and that of the New York group her lab helped train, justifies taking another look at whether the wall is in the right place, Lovell-Badge says. Indeed, the Nuffield Council on Bioethics, a widely respected independent panel in the United Kingdom, is holding a workshop in December to explore whether the limit should be changed.

THE WOMAN WHOSE WORK has provoked this debate grew up behind the Iron Curtain in Warsaw, the only child of a dentist and a neuroscientist. (A number of cats that had

PHOTOS: M. N. SHAHBAZI *ET AL. NATURE CELL BIOLOGY* **18** (4 MAY 2016) © 2016 MACMILLAN PUBLISHERS LIMITED; (OPPOSITE PAGE) JOHN CAIRNS

been research subjects in her father's lab became pets, she says.) Long fascinated by human behavior, Zernicka-Goetz initially planned to study psychology at the University of Warsaw. But a lecture one Saturday morning by pioneering embryologist Andrzej Tarkowski, she says, "changed my life." Tarkowski was one of the first researchers to show that cells from two mouse embryos could be combined and develop into a normal pup. He "was sitting in front of the room, no slides, and he was just telling the story of how you manipulate embryos—and how he made chimeras. This was amazing. Magical," Zernicka-Goetz recalls. She was entranced by "the powerful beauty of our embryos."

A few years later, Tarkowski offered Zernicka-Goetz a position in his lab as a master's student. She took on a particularly challenging project: attempting to combine the embryos of two different rodent species to make a chimeric animal. For months she tried to fuse embryo cells from lab mice with those from wild voles. (Tarkowski had persuaded acquaintances who worked in the Białowieża Forest on the Belarusian border to collect and ship voles to his lab every 2 weeks.) She endured several months of vole bites, she says, but none of the embryos developed. Eventually she switched to studying rat embryos, which ultimately formed the basis of her Ph.D.

In 1990, she was one of a handful of Polish students who received a fellowship to study for a year at the University of Oxford. While in the United Kingdom, she met developmental biologist Martin Evans, whose University of Cambridge lab she joined a few years later as a postdoctoral fellow. When that appointment ended, both her family and Tarkowski urged her to return to Poland, in part to help build up the country's science after the fall of the Iron Curtain. She was torn, she says, "and in a way I left it to luck to decide." She applied for three fellowships to help set up her own lab here in Cambridge. If she had not received them, she would have returned home. She won all three, and has been here ever since.

Zernicka-Goetz soon demonstrated that she was unafraid to challenge long-held ideas. Her lab published a series of experiments that attempted to determine when mouse embryo cells first start to differ from one another. Unlike frog or fruit fly embryos, in which the animal's head and tail are already determined in the fertilized egg, early mammalian embryo cells are famously adaptable. In ground-breaking mouse experiments, Tarkowski and other embryologists had manipulated embryos in multiple ways—removing cells, dividing an embryo in two (to make twins), and even adding cells from a different embryo to make a chimera. In every case the embryo would adjust and go on to develop into a full-term mouse pup. It appeared that all the cells in the early mouse embryo have the same ability to form the tissues needed for healthy development. The consensus has been that cells in a mammalian embryo do not start to specialize until it has dozens of cells and begins to form a hollow ball called a blastocyst.

In spite of the flexibility Tarkowski and others had demonstrated, Zernicka-Goetz wasn't convinced that early embryonic cells are identical. By carefully tagging and tracing what happened to different cells, her team found evidence that even at the four-cell stage, the cells in mouse embryos are not all exactly alike. One cell, they concluded, is more likely to give rise to the placenta, one more likely to contribute to the fetus, and two seemed to inhabit a middle ground (*Science*, 6 May 2005, p. 782).

The idea was not popular. Zernicka-Goetz says that many colleagues think that her data contradicted the earlier picture of flexibility—a misunderstanding, in her view. If early cells already have slight differences, she says, that underscores their plasticity. "It is not that you work with material that is identical. No, the cells are different, but you can change them."

> ***"All of us want to know at the end of the day not how the mouse looks ... but how we develop."***
>
> **Magdalena Zernicka-Goetz**, University of Cambridge

In March, she and her colleagues added some new data to support their theory. Sequencing technology now allows scientists to read the RNA present in an individual cell, providing a snapshot of which genes are active, and when. Zernicka-Goetz and her colleagues found that, consistent with their earlier data, four-cell embryos tend to have one cell with particularly high levels of RNA from a gene called *SOX21*, which suppresses another gene that turns on genes for placental development. Two other cells have intermediate levels, and one—the likely progenitor of the placenta and other supporting tissues—has low levels, the team reported in *Cell*. In the same issue, an independent group showed a similar pattern in related genes.

Some embryologists remain unconvinced. Even if such early asymmetry exists, Lovell-Badge says, many still argue that "there's no evidence that it's important." But Juan-Carlos Izpisúa Belmonte, a developmental biologist at the Salk Institute in San Diego, California, says the work could have broad implications for how cells start down one developmental path or another. It suggests, he says, that well before any visible differences appear, gene expression patterns can foreshadow in which direction a cell is preparing to go. "I think this principle can potentially be applied to later cell fate decisions as well," he says. Understanding how cells "choose" a fate could be key to finding efficient ways of turning stem cells into a desired cell type, or reprogramming other cells into a new kind of tissue.

AS ZERNICKA-GOETZ was reminded in the most personal way, embryonic cells can develop pathological differences as well. In the days after receiving the worrying prenatal test result suggesting her baby had a serious chromosomal abnormality, she recalls, "the only thing I could do was go through the literature and look for examples" to help her understand what it could mean. The search was frustrating. "I could not find a good model that could explain what would happen to those [abnormal] cells. So we decided to find out." Her lab launched a series of experiments with mouse cells to determine what happens when some early cells carry too many or too few chromosomes.

Her personal story unfolded much faster than the research. Zernicka-Goetz says she never seriously considered an abortion, and a subsequent test of the amniotic fluid a month later came back normal, alleviating many of her concerns. And in the lab, her team eventually found that early mouse embryos can indeed weed out faulty cells, especially in the part of the embryo that ultimately develops into a baby. Even when half an embryo's cells carry chromosome mistakes, it can grow into a healthy pup, as the undamaged cells take over and fill in for the faulty ones.

The finding, Izpisúa Belmonte says, emphasizes the flexibility of early embryo cells, underscoring their ability to change course, if needed, to overcome environmental or genetic damage to other cells. The result is important not only for other parents who receive worrying early test results, Zernicka-Goetz notes, but potentially also for IVF clinics, where embryos that have cells that seem abnormal are often discarded.

FROM EARLY IN her graduate studies, Zernicka-Goetz was fascinated by the mysterious changes that an embryo undergoes when it no longer floats freely, but attaches to the wall of the uterus and invades it. Human

embryos implant about 9 days after fertilization; studying what happens afterward would require keeping an embryo alive in the lab for weeks instead of days. Her mentors at the time told her to forget about the project because her chance of success was so slim. In the 1970s, researchers had tried coaxing embryos to implant on a variety of tissues, including slices of uterine tissue and even lenses from cow eyes. None succeeded. "I am grateful" for the guidance to focus on other projects, she says, but the question stayed in the back of her mind.

Then, a few years ago, a talk about techniques for growing stem cells supported in a 3D gel instead of on a flat culture plate prompted her to try after all. The gamble paid off. In 2012, she and her colleagues described a method for keeping mouse embryos alive for more than 6 days—2 days past the usual time of implantation. One key ingredient was the culture medium: serum taken from human placentas—which she acquired with help from some of the doctors she saw during her pregnancy with Simon, she says. (The team has since replaced that ingredient with a more standardized recipe.)

The technique, which uses culture plates designed for high-quality imaging, offers researchers a chance to closely examine a crucial phase of mouse development, when the embryo forms the three distinct cell layers that will give rise to all the body's tissues. "It's incredibly useful," Lovell-Badge says. "You can do time-lapse studies" of the embryo as it undergoes a dramatic series of shape changes from a hollow ball of cells into an elongated cup. Seeing the process unfold has led to a new understanding of the forces that drive it, he notes. Earlier studies of embryonic stem cells had suggested that programmed cell death plays a key role in the shape-shifting. Zernicka-Goetz's work "clearly shows that that's not really happening," he says.

The decision to try the culture methods on human embryos was an easy one, Zernicka-Goetz says. "All of us want to know at the end of the day not how the mouse looks … but how we develop." The human experiments are fundamentally important, Lovell-Badge says. "We know next to nothing about human development between the last blastocyst [just before implantation] and about 4 weeks."

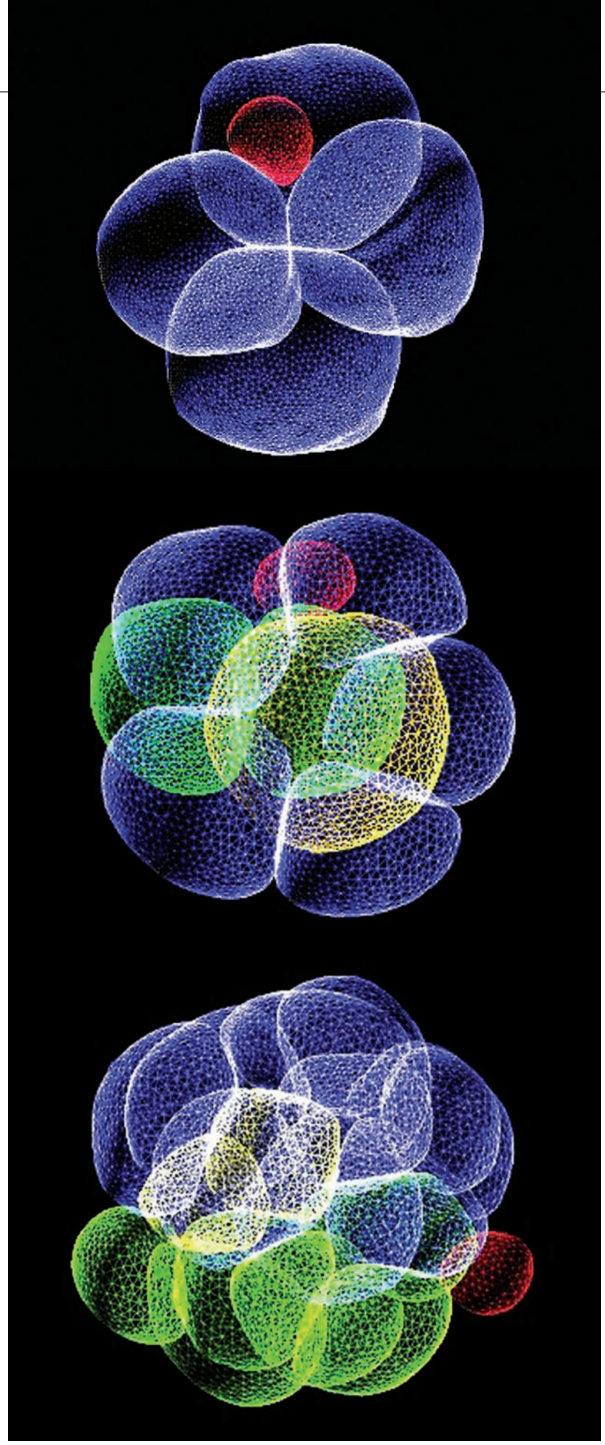

Zernicka-Goetz argues that cells of mouse embryos begin to differ very early. In these reconstructions of microscopy images of four-, eight-, and 16-cell embryos (top to bottom), yellow cells are more likely to become the fetus, green the placenta, and blue cells can scontribute to both. The red cell is a polar body, formed in the final stages of egg development.

The first time Zernicka-Goetz's lab tried the protocol, with two human embryos from an IVF clinic, one was still growing vigorously as it passed the previous record of 8 days. But beyond that point, the team did not know what a healthy human embryo should look like. "You see more and more cells, but we couldn't tell whether it had a structure," she says. "When you look at it, you are amazed by the beauty of it, but you don't know if it's normal."

It wasn't until day 11, she recalls, that her lab could say with confidence that the embryo "had self-organized and was growing the way you see in the books." By then, the 14-day limit was very close. They let it grow for one more day, she says, before terminating the experiment.

The results, described in May in papers in *Nature* and *Nature Cell Biology*, have highlighted significant differences between human and mouse embryo growth, says Ali Brivanlou, a developmental biologist at The Rockefeller University whose lab also successfully applied Zernicka-Goetz's culture technique to IVF human embryos. One of the most obvious: Whereas the mouse embryo rolls up into a tube at implantation, the human flattens out into a disk shape. Embryonic stem cells are derived from blastocysts, so a thorough understanding of the genes and cell interactions that control the next step in development is crucial for understanding how to coax those cells to become different types of mature tissue.

Indeed, the lack of knowledge about postimplantation development has hampered stem cell research, Brivanlou says. "We use assumptions from mouse cells and apply them to human ones. That's not a good idea. We will need to go back and correct all the literature that is based on developmental markers in the mouse."

For those interested in understanding the first steps of organ development, the third and fourth weeks of development are crucial. That is one reason Brivanlou is eager to revisit the 14-day limit. "I have been trying very hard to ignite that debate," he says.

Zernicka-Goetz says she, too, would like to see the 2-week limit extended. But she is willing to wait for a broad public consensus. "I do believe very strongly: It's not my decision or any individual scientist's decision" to push past the current limit. "It should be a decision taken with the general public, with their approval, and with their understanding of what benefits it brings."

In the meantime, she says, the first 2 weeks of embryonic development hold plenty of beauty and fascination. "We have a lot to do within the current limits," she says. "How many years did it take to work out the first 7 days? How many years will it take to work out the next 7 days?" ■

IMAGES: MARIA SKAMAGKI/ZERNICKA-GOETZ LAB

AFTER THE FALL

Some scientists debarred for research misconduct remain on the faculty. How that happens may surprise you

By **Jeffrey Mervis**

George Stancel was still shaking when he got back to his office. As the research integrity officer (RIO) for the University of Texas Health Science Center (UTHSC) in Houston, Stancel had just seized the computers of a tenure-track faculty member accused of plagiarism and fabrication on a grant application to the National Institutes of Health (NIH). "I closed the door and tried to depersonalize things. I asked myself, 'What's the penalty that fits this crime?'"

It wasn't the first time that Stancel, now UTHSC's executive vice president for academic and research affairs, had investigated alleged research misconduct, which covers plagiarism, fabrication, and falsification of data. But it never gets routine, he says, not when a guilty finding might mean the end of an academic career.

Stancel hadn't known what to expect when he walked into Dr. X's office. (*Science* has agreed not to use the researcher's name.) He had even asked the campus police to station an officer down the hall—"just in case." But Stancel's fear of a confrontation quickly dissipated. The accused "hung his head and immediately said, 'Yes, I did it.' He didn't go into a long-winded explanation, or say that he thought what he had done was OK."

After accepting the results of the university's investigation, the U.S. government in 2001 banned Dr. X from receiving any funds from NIH and its sister agencies within the U.S. Public Health Service (PHS) for 1 year. (Dr. X's debarment was technically a voluntary agreement between the government and the scientist, a mechanism used

ILLUSTRATION: DAVIDE BONAZZI/@SALZMANART

to avoid a lengthy and costly administrative appeals process.)

Dr. X isn't alone. On average, the federal Office of Research Integrity (ORI) annually receives more than 200 allegations of misconduct involving researchers funded by PHS agencies, which include the Centers for Disease Control and Prevention and the Food and Drug Administration. But it issues a finding of research misconduct in only a dozen cases a year. And in only six cases is the scientist debarred, the most serious sanction that ORI can impose. The comparable figures for the National Science Foundation (NSF), the only other federal agency with a sizable misconduct portfolio, are about 84 allegations a year, leading to 18 findings of research misconduct and 4.5 debarments.

The funding bans typically last 3 years. However, conventional wisdom holds that the rare punishment is a death sentence for an academic researcher. Unable to receive federal funding and stigmatized by their unacceptable behavior, many debarred scientists quietly leave their university, much to their employers' relief.

A debarment damages the university's reputation, administrators acknowledge, and some institutions respond to that insult by making the faculty member a pariah on campus. Such behavior can eventually lead to a nasty divorce and the departure of the faculty member.

"I felt humiliated," says one debarred scientist who moved to another university after his institution completed its investigation but before the government weighed in. "They took my students that I worked so hard to recruit and train and coach. They gave my competition in the field an advantage. They basically tore out my heart."

But some—including Dr. X—manage to resume productive academic research careers. An investigation by *Science*, based on the list of scientists debarred by either PHS or NSF, has identified at least two dozen such researchers. None of the scientists agreed to talk publicly about their experiences. But some gave permission for senior university administrators to discuss what happened. Those accounts provide a compelling glimpse into a world most scientists don't know even exists.

That climate of secrecy is sustained, in part, by how ORI and NSF handle disclosure. ORI publicly reveals the name of the researcher, details about the infraction, and the penalties for each case in which it has found research misconduct. But NSF is much less open about disclosing its findings, and its only public acknowledgement of a debarment is a cryptic notice on an obscure government website (see sidebar, p. 410).

But ORI and NSF do agree on one thing: Their primary mission is to determine whether a scientist has committed research misconduct and to protect the government's interests. But what happens to the individuals that have been found guilty—including those who are debarred—is someone else's concern.

In every case that *Science* examined, the university's response played out under a cone of silence. Only a few high-ranking administrators knew what the institution decided to do, and why. The secrecy is intended to protect both the individual's privacy and the institution's reputation. But it is a major impediment to understanding the process—including who undergoes rehabilitation and what penance they are required to perform—by which the disgraced researcher is welcomed back into the fold.

Some institutions essentially decide to preserve the status quo. That's especially true if university officials regard the offense as just an unfortunate misunderstanding or a bending of the rules. (For example, most administrators view plagiarism as a lesser offense than fabrication, although the federal government makes no such distinction.) But other institutions prescribe ethics training and monitoring that goes beyond what the federal government has already required, as well as financial penalties to emphasize the gravity of the offense.

> ***"I asked myself, 'What's the penalty that fits this crime?'"***
>
> **George Stancel**,
> University of Texas Health Science Center

Even scientists who believe their institutions and colleagues have treated them fairly say the rehabilitation experience is too painful to talk about publicly. "It's been a multiyear nightmare, and I've done it on my terms," says one faculty member who, after a 1-year debarment for plagiarism, is now at a different institution. "It's an important topic, and I wish you the best. But I just don't trust you to tell my story."

THE IDEA OF REHABILITATING faculty members arose relatively recently, because research misconduct was traditionally seen as exceedingly rare. ORI was created in 1992 after a few highly publicized cases caught the attention of Congress, and NSF's inspector general, which conducts misconduct investigations, has always maintained a low profile.

Notwithstanding the government's involvement in many cases, universities are the key players in ensuring ethical conduct of research by faculty and students and in responding to instances in which those community norms have been violated. "Federal findings aren't always the be-all, end-all to how we judge how serious something is," says Lauran Qualkenbush, the RIO for Northwestern University in Evanston, Illinois. In addition to reconciling inconsistent federal policies, she says, universities also deal with cases that don't involve federal funding.

Some people question the value of even trying to rehabilitate someone who has committed misconduct. Sociologist James DuBois encountered those doubts after he used a $500,000 grant from NIH to launch the first formal misconduct rehabilitation program. The 3-day course at Washington University School of Medicine in St. Louis in Missouri helps researchers explore why they messed up and learn what they can do to avoid repeating such mistakes.

Some two dozen institutions, including Qualkenbush's Northwestern, have referred people to the program. Only about one-third of the 39 participants to date have actually committed research misconduct, however. The majority are guilty of lesser offenses—DuBois calls them "sloppy research practices"—such as violating federal or institutional rules on the use of human subjects or the proper care of animals. And DuBois says he doesn't always know what his clients have done. "Some universities will send us all the investigative reports," he says, "while others will just say 'We want you to talk to [the scientist].' They view it as a confidential matter."

When Dubois discussed his fledgling program at a 2013 meeting marking ORI's 20th anniversary, "a lot of people in the room were skeptical," recalls James Tracy, vice chancellor for research at the University of Kansas (KU) in Lawrence. "They asked, 'Is it possible to rehabilitate someone who's really crossed the line?'"

DuBois admits that it's hard to judge the efficacy of his program, especially because recidivism of any sort would be highly unlikely in such a small sample. And there's very little else to go on in the scientific literature, notes sociologist Mark Davis, one of the few researchers who has tried to do follow-up studies of offenders.

White House budget officials rejected Davis's proposal in the early 2000s to interview the first 10-year cohort of ORI cases after concluding—correctly, as it turned out—that Davis wouldn't be able to get enough scientists to talk about their experiences. But his tiny sample of three (part of a pilot project that targeted nine offenders)

generated enough data to convince him that any attempt at rehabilitation must address the etiology of the errant behavior. "What was going on in their lives? What were the personal and job stressors that may have contributed to their actions?" asks Davis, now an emeritus professor at The Ohio State University in Columbus.

In particular, he thinks that someone pushed over the edge by the pressure-cooker atmosphere of modern academic science is probably a poor candidate for rehabilitation. "Telling a scientist at Harvard [University] or [the University of California in] Berkeley not to take on more than they can handle because the stress might cause them to commit misconduct isn't going to be very helpful if they are part of a culture where the rewards go to those who are busiest and who work the hardest," Davis says.

Likewise, he says, a foreign-born scientist raised in a society that prizes deference to one's superiors may find it very difficult to resist unrelenting pressure to deliver results. "What is the likelihood that a 3-day workshop will overturn 30 years of socialization?" Davis asks.

DR. X HAD JUST BEEN HIRED into a tenure-track position when he committed misconduct. But UTHSC's Stancel decided that the ensuing debarment shouldn't end his career. "In hindsight," Stancel says, "the fact that he was so forthcoming and embarrassed and clearly knew he had done something wrong probably was in the back of my mind when I decided what sanctions we would impose."

Stancel says UTHSC was ahead of the curve in the early 1980s in requiring all graduate students to take a course on research ethics. Two decades later, that ethics course became an important tool in the rehabilitation of Dr. X.

"I decided to have [him] sit in on one of the discussion sections after the lecture, which is always led by a faculty mentor," says Stancel, a longtime professor of pharmacology at UTHSC who had recently become dean of the graduate school. "I never told [the mentor] why. The students didn't know why he was there, either, but his boss knew."

> ***"It's really been a pleasure watching things work out. He has emerged as one of our most productive and respected researchers."***
>
> **James Newell**, Rowan University

The next semester Stancel chose Dr. X to be a section leader. In addition to doing all the student assignments, Dr. X was also required to write a paper—in English as well as his native language—about why plagiarism is unacceptable in science.

Dr. X received tenure several years after the funding ban had expired, and Stancel views him as "a real success story. He has received multiple NIH grants, he's publishing good papers, and recently he was elected to our faculty governance body. And now, when he sees me, he looks me in the eye and smiles. There's no hint of animosity."

Not every university decides that a debarred faculty member needs retraining. Some just let the researcher serve out the federally imposed punishment. That's what happened to Dr. Y, a tenured professor at the University of Central Florida (UCF) in Orlando. In 2011, NSF debarred Dr. Y for 2 years after finding he had plagiarized materials on a grant application and asked several federal agencies to fund the same research proposal. (Every application is supposed to be unique.)

"This person was doing good work and had a strong portfolio of publications and patents and funding," says Bahaa Saleh, dean of UCF's College of Optics and Photonics. The plagiarism, he says, was "just a failure to include the proper citations. … [It] came from not knowing that he is supposed to be very careful when using ideas that were previously published by someone else."

The multiple submissions were an outgrowth of that confusion, Saleh adds. "He should have simply told the agency, 'Here is what I'm hoping to do with this proposal, and here's where it differs from another proposal that you've funded.'" Dr. Y initially appealed NSF's punishment, Saleh says. "But in the end he accepted it, and he now understands the bounds."

For Saleh, plagiarism is less corrosive when it takes place in science than when it occurs in literature or, for that matter, in civic discourse by politicians. He puts it this way: "In science, the ideas are the essence, and the words are secondary, whereas in literature or politics, the words themselves are critical. People need to consider that distinction, whether NSF considers it or not."

Federally sanctioned faculty members should not be asked to bear an added burden, Saleh argues. "A person who violates the law and gets a penalty should not have additional punishment," he says. "A scarlet letter is a poor way of having a healthy society."

That approach shaped the university's decision not to require Dr. Y to undergo any additional training. Instead, Saleh says, "there were meetings to mark his progress. And Dr. Y was sufficiently resourceful to get funding from industry, not the federal government, for the duration of the debarment period."

Still, Saleh says that UCF wanted its response to the debarment "to conform to NSF's demands." So it decided to not renew Dr. Y's appointment to a prestigious chair while the debarment and other NSF sanc-

Name that offender? It depends

By **Jeffrey Mervis**

The U.S. government does not maintain a registry of research misconduct cases. And the two agencies that police scientific misconduct, the Office of Research Integrity (ORI) within the Department of Health and Human Services and the National Science Foundation (NSF), follow different practices.

ORI uses the *Federal Register* (the encyclopedic record of government actions published every workday) and its website to disclose cases in which researchers have been sanctioned. Once those penalties have expired, however, the information is removed from its listing of active cases. NSF's inspector general posts summaries of every completed case, but all identifying features, including the name, are redacted. Until a few years ago, NSF made an exception for those who were debarred. But their names are now also redacted in the summary document.

The General Services Administration, an agency responsible for managing federal properties, maintains a public website, called the System for Award Management, listing every person and company debarred by any government agency, including all scientists. The site is intended to prevent an agency from inadvertently giving a grant or contract to someone who is ineligible. But the listing provides no details of the case or the nature of the sanction, and the site is not easy to navigate. ■

tions were in place. "But that period has passed, and the person has been rehabilitated," Saleh says; Dr. Y once again holds a chaired faculty position. And Dr. Y is back in NSF's good graces, Saleh says, noting that in 2015 he received a grant from the agency.

AFTER NSF DEBARRED Dr. Z for 1 year in 2012 for plagiarism on two grant applications, administrators at Rowan University in Glassboro, New Jersey, combined elements of how Dr. X and Dr. Y were rehabilitated and then added their own twist.

"Once we concluded that we would be imposing internal sanctions, we realized that one of our challenges was not to overreact or underreact," says Rowan's provost, James Newell. "Some universities decide that the person is essentially dead to them, and that he or she should become somebody else's problem. And then there are universities that would prefer to bury it as best they can, and hope it just goes away. We wanted our response to show the event was significant and that engaging in such behavior would have real consequences."

As with Dr. Y, Rowan administrators wanted to impress on Dr. Z, a tenured professor, the importance of acting ethically. So Newell decided to put a dent in his wallet. The university delayed Dr. Z's scheduled promotion to full professor for several years, until 2015. That decision will cost him an estimated $60,000 over the lifetime of his employment at Rowan, Newell says, "and ought to be enough to get his attention." Dr. Z's department also weighed in, banning him from using its funds for travel or professional development.

In addition to those financial penalties, Dr. Z was appointed to serve on the university's academic integrity committee, which deals with ethical breaches by students and is supposed to promote responsible behavior. That might seem like putting a fox in charge of the henhouse, Newell admits. But it also meant that "every day for the next 2 years, the concept of academic integrity would be on his mind."

In line with Saleh at UCF, Newell viewed Dr. Z's misconduct as "a misdemeanor. ... This was a relatively minor plagiarism incident ... borrowing the assessment protocol from someone else's proposal. If he had given proper credit, we probably wouldn't be having this conversation." (Not surprisingly, NSF saw the case differently. Its report called Dr. Z's actions "a serious violation of the standards of scholarship" committed after a colleague "had explicitly told him not to use the text" from a document "copied from a successful proposal that had been submitted previously to NSF.")

NSF had already required Rowan to certify the integrity of any grant proposals and paper submissions from Dr. Z for 3 years after his debarment ended. Despite that additional monitoring, Dr. Z was able to keep his lab functioning with funding from nonfederal sources. And once the ban expired, he was allowed to reclaim a federal grant that had been transferred to a colleague.

"It's really been a pleasure watching things work out," Newell says. "I think he has really emerged as one of our most productive and respected researchers."

A university isn't just thinking of a scientist's well-being when it decides how to respond to a debarment. The overhead it receives along with each federal grant subsidizes the institution's costs of managing federally funded science projects, from paying the utility bills to following rules on the use of animals in research. As a result, university officials drawing up a rehabilitation plan also weigh the odds that a rehabilitated faculty member will be able to win government grants after the debarment has been lifted.

Federal officials say they do not tell members of the panels that review grant proposals about a debarment. But reviewers may already have heard it through the grapevine, says KU's Tracy, who once served on an NIH study section in which someone mentioned that a grant applicant had been debarred and was now eligible again. And he believes the information is relevant to a panel's deliberations.

"With so many people in science trying to do good work, and with the money being so limited, why would I want to give somebody the chance to start over when there are so many other people out there who haven't lied, cheated, or committed misconduct?" Tracy asks. The study section member "may have broken the rules," Tracy adds, "but everybody wanted to know it."

Rowan's Newell says that Dr. Z's prospects for winning federal grants were at best a secondary factor in deciding how the university would deal with his debarment. "That will never be the main issue," he asserts. "Having a rainmaker who is going to bring shame on the university is not in the best interests of the university."

Stancel says he follows the practice used by President Ronald Reagan in negotiating with the then–Soviet Union: Trust, but verify. "Your adviser will be watching you like a hawk," Stancel recalls telling one graduate student who was forced to retake the ethics course and write an essay after plagiarizing on her dissertation proposal.

"I've lost track of her over the years," he says about the student, who earned her degree. "But I think her adviser would have let me know if she had popped up" on the federal government's list of offenders. ■

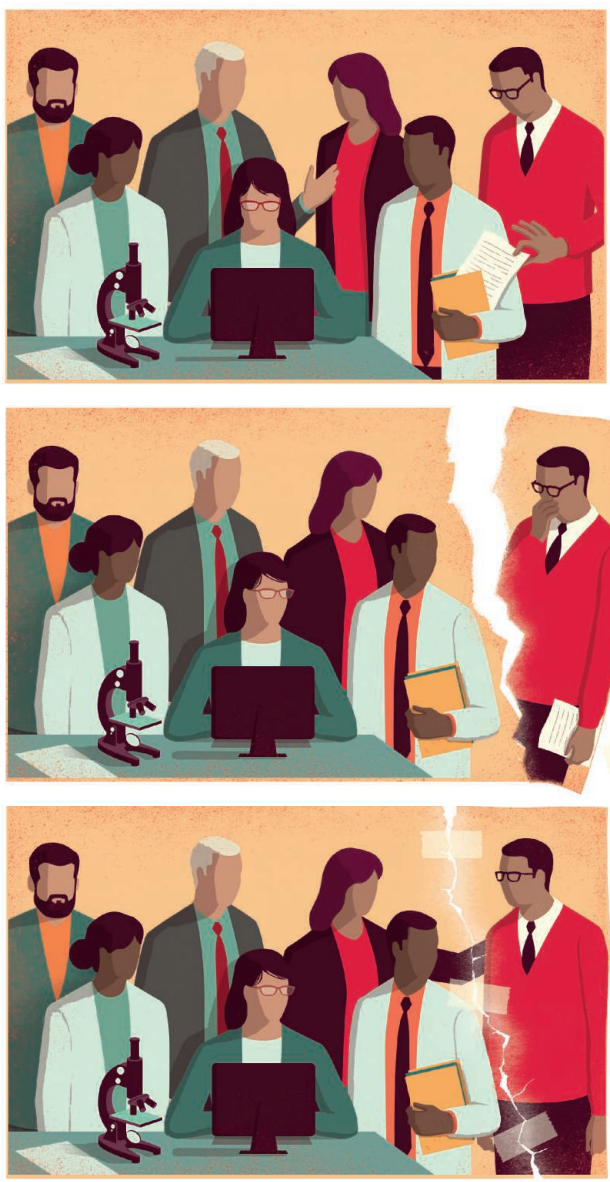

ILLUSTRATIONS: DAVIDE BONAZZI/@SALZMANART

PALEOECOLOGY

The fourth dimension of vegetation

100 years ago, Lennart von Post first used pollen analysis to reconstruct past ecosystems

By **H. John B. Birks,[1,2] Hilary H. Birks,[1] Brigitta Ammann[3]**

In July 1916, Swedish geologist Lennart von Post showed that by identifying and counting pollen preserved at different depths in Swedish peat bogs he could infer changes in forest composition through time (*1*–*3*). Following his pioneering work, pollen analysis quickly became established as a key tool for understanding past vegetation, climate, and ecosystems. Today, it is used widely to reconstruct past ecosystems and test hypotheses about drivers of ecosystem change.

VIDEO

See online video "Pollen, an indestructible clue" at http://scim.ag/vid-6311

Using pollen analysis, von Post explored the temporal changes in postglacial forest composition at many sites in southern Sweden. He then demonstrated the spatial patterns of change by mapping his pollen data at selected times. He formulated the concept of regional parallelism, according to which vegetation responses to climate change were parallel in different parts of the world. He also developed pollen analysis as a relative-dating technique for resolving postglacial sea-level changes.

In the 1930s to 1950s, pollen-analytical studies around the world were performed to establish vegetation history, estimate pollen-accumulation rates, elucidate the relationship of modern pollen spectra to vegetation, and map pollen data through time. Willard Libby's development of radiocarbon dating in the late 1940s freed pollen analysis from being a relative-dating technique (*4*) and allowed past ecosystem changes to be independently related to time. When Fægri and Iversen published the *Textbook of Modern Pollen Analysis* in 1950 (*5*), von Post wrote that "It can hardly be an exaggeration to characterize this book as the banner for a new era in pollen-analytical science. Now I shall leave the pollen statistics stage" [(*6*); translated from Swedish].

By 1966, pollen analysis had demonstrated the extent of impacts of prehistoric people on vegetation, characterized the vegetation and climate of interglacials and the interglacial cycle, and detected "no-analog" late-glacial and interglacial pollen assemblages not found today (*4*, *7*, *8*). Absolute pollen-accumulation rates (influx) and differential representation of taxa were studied in greater detail than was previously possible, and climate-driven shifts of major vegetational ecotones were characterized and dated.

During the past 50 years (*8*), dated pollen stratigraphies from all continents, including

[1]*Department of Biology, University of Bergen, Post Office Box 7803, N-5020 Bergen, Norway.* [2]*Environmental Change Research Centre, University College, London WC1E 6BT, UK.* [3]*Oeschger Centre for Climate Change Research and Institute of Plant Sciences, University of Bern, CH-3013 Bern, Switzerland. Email: john.birks@uib.no; hilary.birks@uib.no; brigitta.ammann@ips.unibe.ch*

Pollen spray from a Norway spruce. Analysis of pollen in sediments is widely used to elucidate past ecosystems.

highly dynamic records from Amazonia and Africa, have been produced. International open-access databases facilitate mapping of pollen values through time over large areas, thus revealing contrasting patterns and rates of spread of individual tree species. In parallel with computer technology, numerical techniques have been developed to summarize complex pollen data, test hypotheses, and provide quantitative reconstructions of past climate and vegetation. Global syntheses of past vegetation and climate inferred from pollen data have been used to validate climate-model simulations (*4*). Pollen-dispersal models and productivity estimates enable quantitative inferences of vegetation at different spatial scales, so that past landscapes can be reconstructed. These include "cultural landscapes" that provide insights into resources available to past human societies in Europe and, more recently, the Americas and parts of Asia and Africa. Pollen analysis has also been combined with other proxies to reconstruct lake development, aquatic ecosystem processes, and lake–catchment interactions.

Today, pollen analysis plays an ever-increasing role in ecology, Earth-system science, and biogeography by providing long-term overviews of population dynamics and ecosystem development. It is providing ecology and biogeography with the fourth dimension of detailed history: their paleoecology. For example, recent work at Gerzensee, Switzerland (see the figure), highlights the rapidity of vegetation and soil responses to major climate warming from glacial conditions into the late glacial that began ~14,665 years ago (*9*). The study compared stable oxygen isotope $\delta^{18}O$ data, which reflect temperature changes, with reconstructed vegetation responses and their rates. Pollen richness provides a measure of past biodiversity. Soil development, including atmospheric nitrogen fixation, can be inferred from the past flora. Thus, a uniquely detailed insight into ecosystem paleoecology and the operation of ecological processes in the past is revealed.

Another study assembled pollen values for 54 taxa at 500-year intervals in 859 detailed maps based on 828 sites in Europe (*10*). The maps reveal how temporally dynamic and spatially variable plant populations have been in the past 15,000 years, reflecting the traits of the taxa and their responses to climate changes and competition. The maps provide a firm historical background for interpreting geographical DNA patterns in extant tree populations such as beech, spruce, silver fir, and oak in Europe. Furthermore, they give an indication of possible responses of taxa to global warming.

Deevey has suggested that "when time is needed to see a result, there is no substitute for history" (*11*). Pollen analysis provides vegetation's fourth dimension of time that is increasingly essential in understanding many ecological and biogeographical patterns and processes. Future challenges in the field include deciphering ecological responses to past climate change and to human activities, identifying historical legacies in modern ecosystems, and interpreting novel ecosystems in the past, all of which will contribute to improving our understanding of the effects of future environmental change on the biosphere (*12*, *13*). It is therefore appropriate that the Royal Swedish Academy of Sciences is hosting a symposium in Stockholm to celebrate von Post's legacy (*14*). Von Post would have been amazed and delighted. ■

REFERENCES AND NOTES

1. L. von Post, *Geologiska Föreningen Stockholm Förh.* **38**, 384 (1916).
2. L. von Post, *Förh. ved 16 Skand. Naturforskermøte* **1916**, 433 (1918).
3. L. von Post, *Pollen et Spores* **9**, 375 (1967).
4. H. J. B. Birks, in *Natural Climate Variability and Global Warming: A Holocene Perspective*, R. W. Battarbee, H. A. Binney, Eds. (Wiley-Blackwell, Oxford, 2008), pp. 7–57.
5. K. Fægri, J. Iversen, *Textbook of Modern Pollen Analysis* (Munksgaard, Copenhagen, 1950).
6. L. von Post, *Geologiska Föreningen Stockholm Förh.* **72**, 363 (1950).
7. H. J. B. Birks, *Grana* **44**, 1 (2005).
8. J. C. Ritchie, *New Phytol.* **130**, 469 (1995).
9. B. Ammann *et al.*, *Palaeogeogr. Palaeoclimatol. Palaeoecol.* **391**, 40 (2013).
10. S. Brewer *et al.*, *J. Maps* 10.1080/17445647.2016.1197613 (2016).
11. E. S. Deevey, *BioScience* **19**, 40 (1969).
12. National Research Council, *The Geological Record of Ecological Dynamics: Understanding the Biotic Effects of Future Environmental Change* (National Academies, Washington, DC, 2005).
13. A. W. R. Seddon *et al.*, *J. Ecol.* **102**, 256 (2014).
14. "Centenary (1916–2016) of Pollen Analysis and the Legacy of Lennart von Post," 24–25 November 2016.

10.1126/science.aai8737

Understanding past vegetation changes

By combining different proxies, such as stable isotopes, with highly resolved pollen analysis, scientists can reconstruct the responses of vegetation and ecosystems to rapid climate change. The figure illustrates these ecosystem responses for the onset of the Early Bølling (~14,655 years ago) at Gerzensee, Switzerland (*9*).

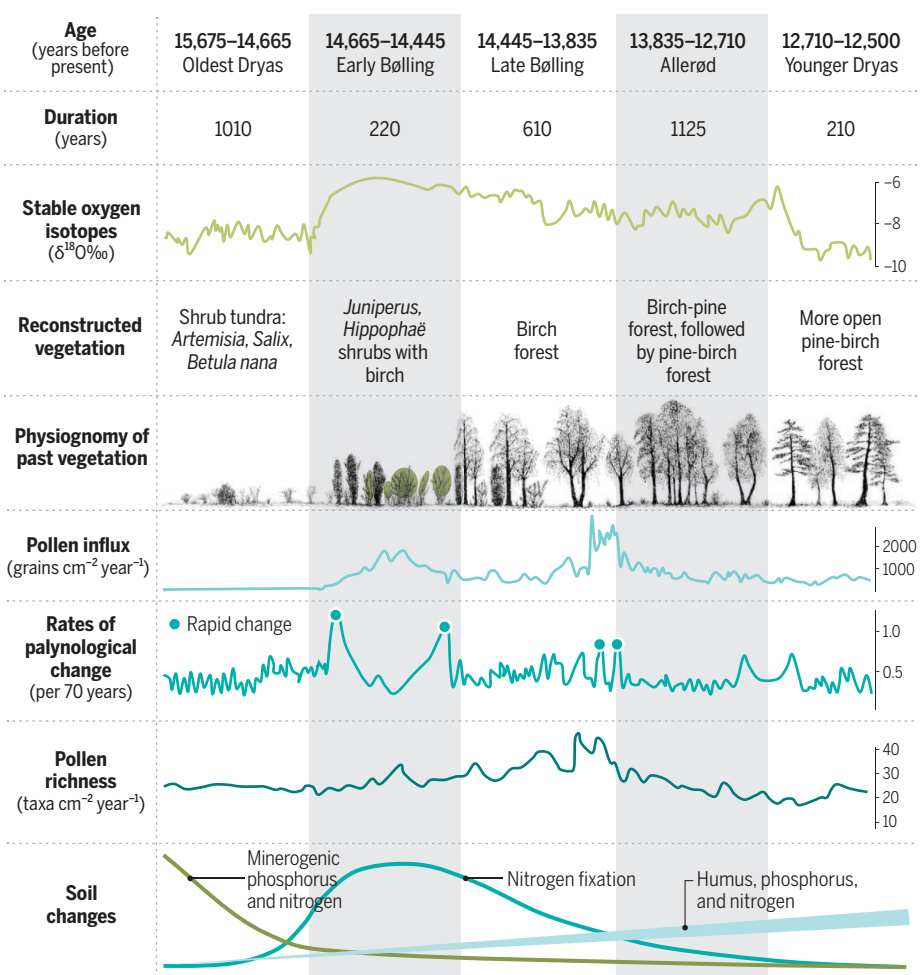

GRAPHIC: G. GRULLÓN/*SCIENCE*

Gene flow between bonobos (pictured) and chimpanzees occurred earlier than the equivalent gene flow between modern and archaic humans, and can still be detected in present-day genomes.

EVOLUTION

The road to speciation runs both ways

Chimpanzees and bonobos show signs of ancestral gene exchange, providing insight into the dynamics of speciation

By **A. Rus Hoelzel**

Some species, such as the giraffe or bottlenose dolphin, are immediately recognizable and might seem immutable. In fact, their evolutionary stories are often more complicated. Regional populations of giraffe with distinct pelage patterns have only recently been recognized as four different species (*1*), and the number of species represented by what we recognize as the bottlenose dolphin was historically as many as 20, refined down to one, then two, and the question is still being resolved (*2*). On page 477 of this issue, de Manuel *et al.* (*3*) describe the relationship between two other iconic species in unprecedented detail, comparing whole genomes from populations of bonobo (*Pan paniscus*) and chimpanzee (*Pan troglodytes*). They report evidence for gene flow between these species, contributing to our increasing appreciation for the complexities of the process of speciation.

Darwin (*4*) wrote about "strongly-marked varieties or doubtful species" when considering the boundary between what we would now consider conspecific populations (or subspecies) and sibling species. The bonobo, whose name may derive from a misspelling of the Zairian town name "Bolobo" on a crate label (*5*), was recognized as distinct from other chimpanzees in the early 20th century, and formally identified as a new species from detailed anatomical descriptions by Coolidge in 1933 (*6*). Although chimpanzees and bonobos will hybridize in captivity (*7*), molecular genetic data have clearly supported the species-level distinction, as reinforced by de Manuel *et al.* However, by contributing an additional 40 genome sequences, de Manuel *et al.* could compare the nuclear genomes (sequenced to a mean coverage of 25-fold) of 65 chimpanzees and 10 bonobos and thereby provide novel inference about their historical demography.

Consistent with earlier studies, de Manuel *et al.* find genetic distinction between four regional subspecies of chimpanzee in central Africa. They estimate a divergence time between chimpanzees and bonobos at 2.1 to 1.6 million years ago, and radiation among chimpanzee subspecies (each represented by 10 to 23 genomes) beginning around 600,000 years ago. Bonobos are found in the Democratic Republic of the Congo (formerly Zaire), and their distribution is bounded by the central chimpanzee (*P. t. troglodytes*) to the west, and by the eastern chimpanzee (*P. t. schweinfurthii*) to the north and east. The other two subspecies of chimpanzee are currently found north of the central chimpanzee range and further to the west (see the figure).

Using a method based on whole genomes and the distribution of gene divergence in a genealogy, de Manuel *et al.* track the historical demography of each population from the point at which bonobos diverged from chimpanzees around the start of the Pleistocene, 2.58 million years ago. Population sizes peaked at different times through this period for the different species and subspecies. De Manuel *et al.* report that during the period from ~550,000 to 100,000 years ago, there was gene flow from bonobo into the central subspecies population of chimpanzees, and into the ancestor of the eastern and central subspecies populations (see the figure). This was at a time when the bonobo population size was depressed and the eastern and central chimpanzee subspecies relatively abundant. Low levels of ongoing mixing and

The making of ancient hybrids

Distribution of chimpanzee and bonobo populations in equatorial Africa. Arrows show the proposed direction of historical gene flow. Date estimates shown as thousands of years ago (ka).

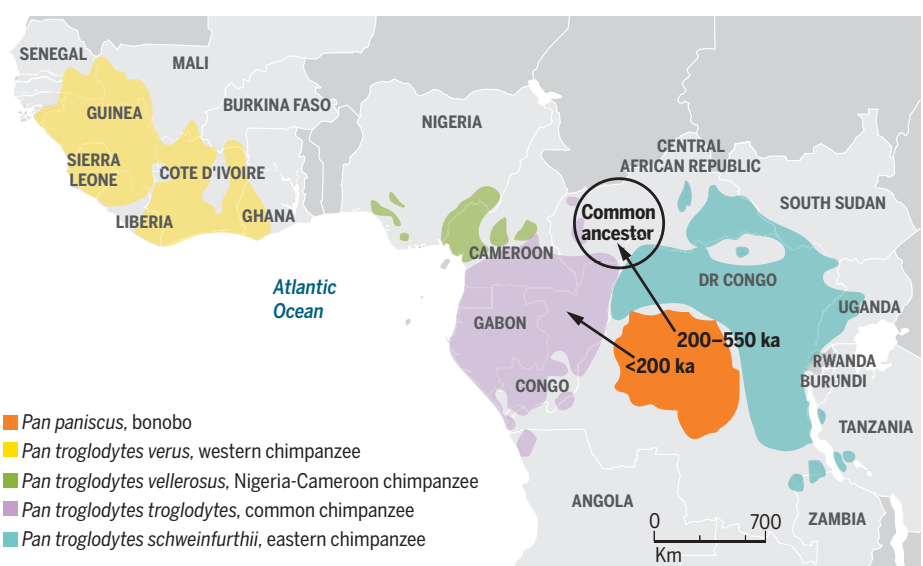

Department of Biosciences, Durham University, South Road, Durham DH1 3LE, UK. Email: a.r.hoelzel@durham.ac.uk

discreet periods of gene flow cannot easily be distinguished, but the data suggest two main phases of gene flow. Although some of the same signals identified by de Manuel *et al.* as gene flow had been previously dismissed as differential genetic drift among populations (*8*), the high-coverage genomes provide a more convincing case for gene flow.

While we can't be sure of the exact timing, or the extent to which environmental factors may have played a role (e.g., to facilitate overlapping distributions), this secondary contact was occurring during a period when the tropical African environment was changing through the Pleistocene epoch. For example, from ~900,000 to 600,000 years ago, the longer glacial periods were cool and humid, interspersed with relatively brief hot and dry interglacial periods. By ~200,000 years ago, the glacial periods had become cold and dry, and the interglacials hot and humid (*9*). Data from de Manuel *et al.* also indicate considerable gene flow among the regional subspecies over the last ~200,000 years. The apparent level of connectivity was comparatively low between bonobos and chimpanzees. Because comparisons could be made across the genome, it was possible to consider the frequency of interspecific heterozygotes by genomic region. Finding some chimpanzee chromosomes depleted of bonobo mixing suggested constitutive regions where bonobo alleles may be less fit, a result also suggested for hybrids between our species and archaic hominids (*10*).

De Manuel *et al.* show that this type of "reticulate" evolution, where there is divergence with continuing genetic exchange, is shared among the nonhominid great apes as well as among the hominids (*10*). However, it has also been reported for a diverse range of species of both plants and animals (*11*). There is evidence based on natural hybridization, but it will be the high-resolution genomic analyses like those presented by de Manuel *et al.* that will allow us to more fully understand the role of reticulation in evolutionary processes, and the impact of "unnatural" hybridization on natural populations when human activities affect the distribution and overlap of species. ■

REFERENCES

1. J. Fennessy *et al.*, *Curr. Biol.* **26**, 2543 (2016).
2. A. E. Moura *et al.*, *Syst. Biol.* **62**, 865 (2013).
3. M. de Manuel *et al.*, *Science* **354**, 477 (2016).
4. C. Darwin, *On the Origin of Species by Means of Natural Selection* (John Murray, 1859).
5. F. de Waal, F. Lanting, *Bonobo: The Forgotten Ape* (Univ. of California Press, 1997).
6. H. J. Coolidge, *Am. J. Phys. Anthropol.* **18**, 1 (1933).
7. H. Vervaecke, L. Van Elsacker, *Mammalia* **56**, 667 (1992).
8. C. Becquet, M. Przeworski, *Genome Res.* **17**, 1505 (2007).
9. L. M. Dupont *et al.*, *Geology* **29**, 195 (2001).
10. B. Vernot *et al.*, *Science* **352**, 235 (2016).
11. M. L. Arnold, *Divergence with Genetic Exchange* (Oxford Univ. Press, 2015).

10.1126/science.aaj2007

CELL BIOLOGY

A finer look at a fine cellular meshwork

The endoplasmic reticulum is imaged at super-resolution

By **Mark Terasaki**

Students learning about the eukaryotic cell are taught that mitochondria are the powerhouse of the cell, the nucleus is the information storehouse, and lysosomes are the garbage disposal. Summing up the role of the endoplasmic reticulum (ER) is more problematic, even for professional cell biologists. Classically, the ER is where membrane proteins, secreted proteins, and most lipids are synthesized. It is also the site of calcium regulation. More recent work shows that it is the site of antigen presentation by major histocompatibility complex class I molecules, and the location of the unfolded protein response, now thought to be central to several major diseases. A new frontier is its relationships with other organelles (*1*). On page 433 of this issue, Nixon-Abell *et al.* (*2*) describe how an armamentarium of super-resolution imaging techniques reveals new aspects of the ER's very heterogeneous morphology. Indeed, the "form follows function" adage may help to make sense of this organelle's functional issues.

"...the ER matrix exists in living cells..."

The ER is a single-membrane system distributed throughout the cell. Like the vascular and nervous systems, many ER functions are likely to be involved in coordinating processes. At the ultrastructural level, the ER is a complex system of interconnecting tubules and sheets. The discovery of "reticulons" and related proteins showed that gene products control the shape of the ER at this level of organization (*3*). ER membranes are now thought to be naturally flat, and these "hairpin" proteins convey curvature to ER membranes such as occurs in ER tubules and edges of ER sheets. Mutations in several of these proteins are directly associated with the human disease hereditary spastic paraplegia (*4*), though frustratingly, it is still not clear how.

Just as capillaries were discovered in the thin webbing of a frog's foot by Marcello Malpighi in the 17th century, the ER was discovered in 1945 by Keith Porter in a special situation where it is two-dimensional (2D). Fibroblasts (connective tissue cells) adhere to some substrates in vitro so strongly that the periphery of the cell spreads out in a thin layer. The periphery is thin enough (<1 μm) that Porter could see, by looking completely through this part of the cell with transmission electron microscopy, a "reticulum" that was present mostly in the "endoplasm" (nonmotile part of the cell) (*5*). The invention of the ultramicrotome in 1953 opened up detailed microscopic study of all cells of the body by producing 70-nm-thick sections that can be visualized at subnanometer resolution. The first serial section study demonstrated a complex system of ER tubules and sheets (think of pita bread) (*6*). Sheets are particularly well-established components of secretory cells. The work on fibroblasts was forgotten until years later, when improved optics and fluorescent probes such as dyes and, later, green fluorescent protein tags allowed the ER to be seen "whole" in the cell periphery. The discovery of the cytoskeletal (microtubule) interaction with the ER (*7*) and the visualization of protein traffic from the ER to the Golgi apparatus (*8*) were two of many highlights of this approach.

Nixon-Abell *et al.* subjected this classic cell preparation (10 different cell lines) to several super-resolution techniques. The resolution of conventional light microscopes is determined by diffraction, and is roughly half the wavelength of light (~0.5 μm). Super-resolution is accomplished by single-molecule techniques and by clever new methods of illumination. A live-cell technique, grazing incidence structured illumination microscopy (GI-SIM), provided substantial improvements in spatial and temporal resolution. ER tubules, which have a diameter of 50 to 100 nm, and three-way junctions of tubules were observed to oscillate ~70 nm with a period of ~250 ms. These movements were affected by inhibitors of energy metabolism, so they are not due to random molecular collisions. These observations of Nixon-Abell *et al.* are of interest for the ER, but also may be relevant to the long-standing question of whether the cytoplasm is like water (a dynamic gel) or has a kind of molecular association unique to living cells.

Department of Cell Biology, University of Connecticut Health Center, Farmington, CT 06030, USA. Email: terasaki@uchc.edu

When fluorescently labeled and observed by light microscopy, some of the peripheral ER has been thought to be structured as membrane sheets. However, the essentially 2D peripheral ER has always been difficult to capture by thin sectioning, so these "sheets" have never before been looked at by electron microscopy. The super-resolution methods used by Nixon-Abell *et al.* make it clear that these are, instead, a structure with many openings too small to be resolved previously. The authors observed that motions of the components of this dense network are similar to those seen in ER tubules and three-way junctions. They also found that the structure can rapidly form and dissipate at its edges. Macromolecular motion was stopped by chemical fixation and imaged by a high-density 3D fluorescent localization microscopy called lattice light sheet-point accumulation for imaging in nanoscale topography (LLS-PAINT), which combines novel light illumination with single-molecule imaging of fluorescent lipids. An image of a fine meshwork emerges, very consistent with the live-cell imaging.

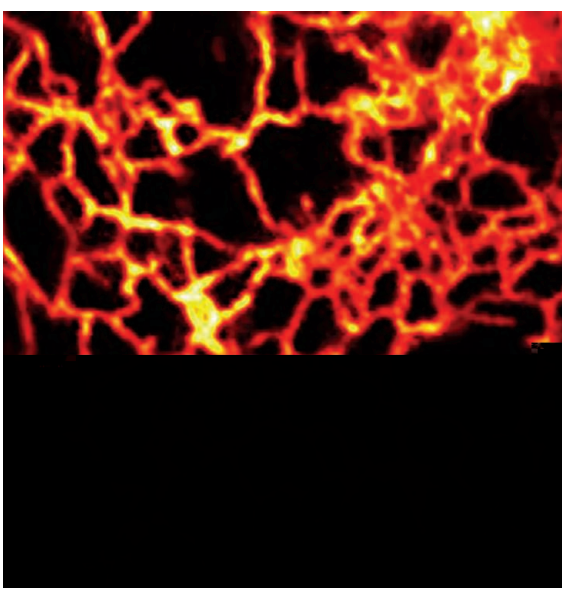

The ER, as visualized by structured illumination microscopy (SIM).

Focused ion beam–scanning electron microscopy (FIB-SEM) is a recently developed technique for producing very thin, 8-nm-thick serial section electron microscopic images. Although the peripheral ER was difficult to capture, Nixon-Abell *et al.* reconstructed an overlapping, dense tubular matrix (together with bona fide sheets) from a thicker part of the cell. This proposed "ER matrix" is reminiscent of a type of ER, sometimes called fenestrated sheets, which has been seen previously in various cell types (*9*). Nevertheless, Nixon-Abell *et al.* show that the ER matrix exists in living cells (i.e., is not an artifact of fixation), and document its dynamic properties.

A recent paper examines the involvement of membrane curvature in a loose tubular membrane network in a cell-free system (*10*). The membrane protein atlastin was required for the formation and maintenance of this network, whereas the ER tubule-forming proteins reticulons and lunapark had complementary roles. Nixon-Abell *et al.* also investigated the involvement of curvature-shaping proteins in ER morphology and observed atlastin in the ER matrix, with reticulons and cytoskeletal linking membrane protein (CLIMP) occasionally present in the ER matrix, but they did not report on lunapark. This raises the question of whether the ER matrix is a dense tubular network, a membrane sheet with densely packed holes, or something else. An additional issue is whether the ER matrix is confined by its components to be a 2D structure within the generally 3D ER.

The study of Nixon-Abell *et al.* reveals a dynamic type of densely packed ER (see the image). The authors offer several interesting speculations on its function, such as allowing for rapid changes in calcium regulation, lipid metabolism, or organelle interactions. For more ideas, it may be useful to focus on the nature of the unusual, very thin peripheral cytoplasm, because its particular cellular functions may be supported by this ER. There is no analog for the thin "peripheral cytoplasm" in some cell types, such as a liver hepatocyte. An important aspect of this work is that cells in culture are very amenable to experimental manipulation, so we can look forward to future testing of ideas using super-resolution techniques. The mystery of this ubiquitous changeable organelle endures. ■

REFERENCES

1. S. C. Lewis, L. F. Uchiyama, J. Nunnari, *Science* **353**, 5549 (2016).
2. J. Nixon-Abell *et al.*, *Science* **354**, aaf3928 (2016).
3. G. K. Voeltz, W. A. Prinz, Y. Shibata, J. M. Rist, T. A. Rapoport, *Cell* **124**, 573 (2006).
4. C. Blackstone, *Annu. Rev. Neurosci.* **35**, 25 (2012).
5. K. R. Porter, A. Claude, E. F. Fullam, *J. Exp. Med.* **81**, 233 (1945).
6. K. R. Porter, J. Blum, *Anat. Rec.* **117**, 685 (1953).
7. M. Terasaki, L. B. Chen, K. Fujiwara, *J. Cell Biol.* **103**, 1557 (1986).
8. J. F. Presley *et al.*, *Nature* **389**, 440 (1997).
9. M. Puhka, M. Joensuu, H. Vihinen, I. Belevich, E. Jokitalo, *Mol. Biol. Cell* **23**, 2424 (2012).
10. S. Wang, H. Tukachinsky, F. B. Romano, T. A. Rapoport, *eLife* 10.7554/eLife.e18605 (2016).

10.1126/science.aal0052

QUANTUM PHYSICS

Versatile cluster entangled light

Dark excitons are used to entangle strings of hundreds of photons for quantum information processing

By **Hans J. Briegel**

Performing a quantum computation may seem complicated, but it can be done with a specially prepared beam of light and good photodetectors. On page 434 of this issue, Schwartz *et al.* (*1*) report on a prototype device that uses semiconductor quantum dots that generate long strings of photons in an entangled cluster state of light. Cluster states (*2*) carry a specific sort of entanglement—that is, the way in which the properties of different photons are correlated. In two dimensions—when the entangling connections form a net or lattice—cluster states become a universal resource; they can be used for all kinds of quantum information processing and are like a fuel for quantum computers. The entanglement can be realized between the polarizations of individual photons—the directions in which their individual electric field vectors point. A quantum calculation (*3*) can be run by measuring the polarization of each photon, one by one, in a specific order and direction, almost as simple as moving the beads of an abacus.

Although this scheme is simple, actually producing large-scale cluster states of photons has been a formidable challenge. Previous experiments have demonstrated the feasibility of measurement-based quantum computation with single photons (*4*) and ions (*5*). Photonic implementations have mainly used parametric down-conversion to generate entangled pairs of photons from a laser beam focused on a nonlinear crystal. A toolbox of beam splitters, phase shifters, and photodetectors then enables photonic quantum information processing. The drawback of this approach is that the generation of entangled pairs and their combination to larger-scale cluster states work only probabilistically (it requires post-selection), which

Institute for Theoretical Physics, University of Innsbruck, 6020 Innsbruck, Austria. Email: hans.briegel@uibk.ac.at

PHOTO: C. OBARA, A. WEIGEL, AND J. LIPPINCOTT-SCHWARTZ

becomes inefficient for large photon numbers. Implementations that entangle the electronic states of ions are deterministic, but scaling them up to hundreds of ions is also challenging, and the experiments have so far focused on few-qubit proof-of-principle demonstrations.

Schwartz *et al.* have taken a major step toward large-scale implementations of photonic states using confined dark excitons (excited states of matter in semiconductor quantum dots) to produce a string of several hundred photons in a deterministic way. A dark exciton is an electron-hole pair with parallel spins in a semiconductor that exhibits a very long lifetime, as compared with that of its better-known sister, the bright exciton (with antiparallel spins). Dark excitons were recently put forward as a type of matter qubit (*6*). Exciting the confined dark exciton periodically with the help of timed laser pulses generates a photon deterministically and, notably, also entangles it with the photons that have already been emitted. The protocol follows an earlier theoretical proposal by Lindner and Rudolph (*7*), who considered the spin of an electron as the matter qubit. In their proposal, the electronic spin thereby acts as an entangler, so to speak—as the "needle" in a quantum knitting process. In every step, it creates a photon and at the same time entangles it with the existing string of photons, one by one, producing the fabric of cluster entangled photons (see the figure).

To demonstrate the quality of the entangling process, Schwartz *et al.* performed quantum process tomography, in effect a complete test of the function of the device for different input states. From the tomographic data, the fidelity of the process map was determined to be 81%, which is a measure for the reliability with which the device operates at each entangling step. An important property of the ideal cluster state, besides its high persistency of entanglement (*2*), is that any two chosen qubits from the cluster can be brought into a maximally entangled state, a so-called Einstein-Podolsky-Rosen (EPR) state, by performing single-qubit measurements on some other qubits of the cluster. The so-called localizable entanglement for any chosen pair of qubits is thus maximal. In practical terms, this means that, ideally, quantum information can be teleported from any qubit to any other qubit of the cluster, thus realizing, effectively, a quantum wire, which is necessary for universal quantum computation. In their experiment, Schwartz *et al.* found that the localizable entanglement exists over five sequential photons. The limited range of the entanglement arises from experimental imperfections—in particular, from the finite radiative lifetime of one of the exciton states (the so-called biexciton).

Although there is still room and need for experimental improvements, the good news is that even cluster states subject to noisy processes, with a finite range of localizable entanglement between two individual qubits, can still be universal (*8*). Measurement-based implementations for quantum computation and communication allow for rather high noise thresholds on the order of several percent (*9*), which might be reachable in the near future.

Future progress toward universal quantum computation will require the extension of the scheme to create two-dimensional cluster states, which can in principle be achieved by using two coupled quantum dots (*10*). In the knitting metaphor, two needles would be required. Another key challenge will be how to increase the overall light-harvesting efficiency, which is very limited in the current setup. Highly efficient photodetectors will be required to measure the higher multiphoton correlations of a given cluster state and verify the creation of a large-scale entangled state. They will also be essential to reliably process and readout the result of a measurement-based quantum computation.

A combination of these new techniques with existing quantum information technologies—for example, trapped atoms or ions in optical cavities (*11*) and superconducting photodetectors (*12*)—could open further avenues of research. Photonic cluster states generated by dark excitons might be used to entangle quantum memories of different types and at different places, realizing larger quantum networks. A direct application based on cluster states is blind quantum computation (*13*), which has recently been proposed as a secure quantum cloud-computing application. In any case, the experiment by Schwartz *et al.* has enlarged the set of promising quantum technologies that could eventually lead us to a "quantum Internet" and, indeed, to a bright future for quantum information processing. ■

"...ideally, quantum information can be teleported from any qubit to any other qubit of the cluster, thus realizing, effectively, a quantum wire..."

The quantum knitting machine

Periodic transitions between excited states—dark exciton (DE) and biexciton (BiE)—of a semiconductor quantum dot (square box) lead to the emission of a string of entangled photons (orange spheres).

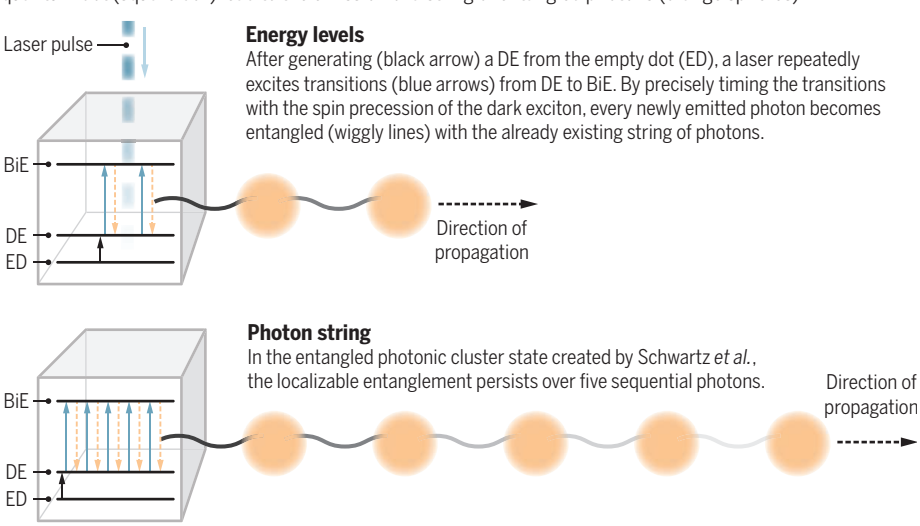

GRAPHIC: C. BICKEL/*SCIENCE*

REFERENCES AND NOTES

1. I. Schwartz *et al.*, *Science* **354**, 434 (2016).
2. H. J. Briegel, R. Raussendorf, *Phys. Rev. Lett.* **86**, 910 (2001).
3. R. Raussendorf, H. J. Briegel, *Phys. Rev. Lett.* **86**, 5188 (2001).
4. P. Walther *et al.*, *Nature* **434**, 169 (2005).
5. B. P. Lanyon *et al.*, *Phys. Rev. Lett.* **111**, 210501 (2013).
6. E. Poem *et al.*, *Nat. Phys.* **6**, 993 (2010).
7. N. H. Lindner, T. Rudolph, *Phys. Rev. Lett.* **103**, 113602 (2016).
8. R. Raussendorf *et al.*, *New J. Phys.* **9**, 199 (2007).
9. M. Zwerger *et al.*, *Appl. Phys. B* **122**, 50 (2016).
10. S. E. Economou *et al.*, *Phys. Rev. Lett.* **105**, 093601 (2010).
11. A. Reiserer *et al.*, *Nature* **508**, 237 (2014).
12. F. Marsili *et al.*, *Nat. Photon.* **7**, 210 (2013).
13. S. Barz *et al.*, *Science* **335**, 303 (2012).

ACKNOWLEDGMENTS

The author acknowledges support by the Austrian Science Fund (FWF) under grant SFB FoQuS F4012.

10.1126/science.aai8675

MARINE BIOLOGY

Putting the spotlight on organic sulfur

Diverse dissolved organic sulfur compounds play an active role in ocean biogeochemistry

By **Naomi M. Levine**

Marine microbes are the engines that drive global biogeochemical cycling in the oceans. They produce and cycle a dissolved organic matter (DOM) reservoir that is roughly as big as the atmospheric carbon dioxide pool (*1*). Interactions between DOM and marine microbes may also play a key role in the evolving climate through changes in remineralization rates (*2*). Historically, DOM has been thought of mainly in terms of its carbon, nitrogen, and phosphorus content. On page 456 of this issue, Ksionzek *et al.* (*3*) investigate the large pool of dissolved organic sulfur (DOS) compounds in the ocean and show that these compounds also play a key role in ocean biogeochemistry.

Because the sulfate (SO_4^{2-}) concentration in the oceans is high, scientists have traditionally assumed that sulfur never limits biological activity. As a result, the biogeochemistry of organosulfur compounds has received less attention than that of the primary limiting nutrients, nitrogen and phosphorus. However, recent work suggests that organosulfur compounds both in the water and the cell may play critical roles in microbial community dynamics (*4*, *5*) and in mediating the interactions between phytoplankton and heterotrophic bacteria (see the figure) (*6*). These compounds can also provide plasticity for microbes in nutrient limited regions by helping to reduce N and P requirements (*7*).

Ksionzek *et al.* now report that DOS accounts for 6700 to 18,600 Tg of sulfur in the ocean and that this pool turns over relatively slowly (less than 0.02% per year). The current knowledge of DOS derives from a small number of compounds that account for only ~25 Tg of sulfur and that turn over rapidly (within hours to days). By quantifying both the size and turnover rates of the DOS pool, the authors highlight an important class of molecules in the ocean and provide evidence for active biogeochemical cycling of DOS through selective remineralization.

Sulfate has an oxidation state of +6, whereas many organic molecules critical for life contain a reduced form of sulfur. For example, thiols, aromatic sulfur, and disulfides contain sulfur in the –2 oxidation state, and sulfonates contain sulfur in the +4 oxidation state. Some of the most ubiquitous heterotrophic bacterial groups in the oceans cannot reduce sulfate and thus depend on external sources of reduced sulfur—namely DOS—to fulfill their sulfur requirements (*8*, *9*). This exploitation of reduced forms of organic sulfur by marine heterotrophs is consistent with the findings of Ksionzek *et al.*

Using ultrahigh-resolution mass spectrometry, the authors identified 803 different molecular formulas for DOS compounds in Atlantic Ocean samples. About 10% of these compounds only occurred in the surface ocean. The authors also show that the chemical nature of DOS changes as one moves from the surface to the deep ocean: The average S:C ratio of the molecular formula decreases with depth, whereas the molecular size and degree of unsaturation increases with depth. This finding suggests that DOS is preferentially consumed by marine heterotrophs, resulting in both a decrease in the concentration of DOS concentration relative to DOM with depth (see the figure) and a change in the chemical nature of DOS.

Although Ksionzek *et al.* were able to identify the molecular formulas ($C_xH_yO_xN_xS_x$) of many DOS molecules, the identity and function of these organic sulfur compounds remain unknown. Of particular interest are those compounds that are present in the surface ocean but not at depth. Some insight into the potential importance of DOS cycling can be gained from a small number of organosulfur compounds that have been previously studied, in par-

Organosulfur mediators

Ksionzek *et al.* show that the DOS concentration decreases in depth relative to that of DOC. DOS concentration has been exaggerated in the water column to make the effect visible. These DOS compounds play key roles in ocean ecosystems.

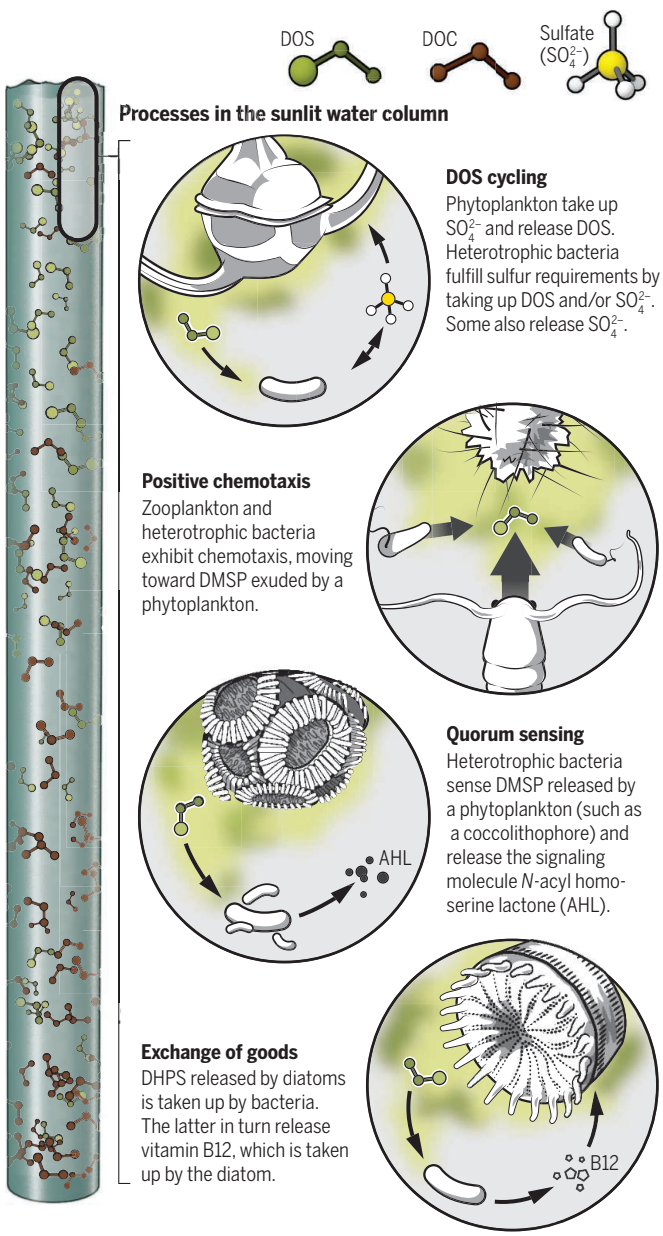

GRAPHIC: V. ALTOUNIAN/*SCIENCE*

Departments of Biological Sciences and Earth Sciences, University of Southern California, Los Angeles, CA 90089, USA. Email: n.levine@usc.edu

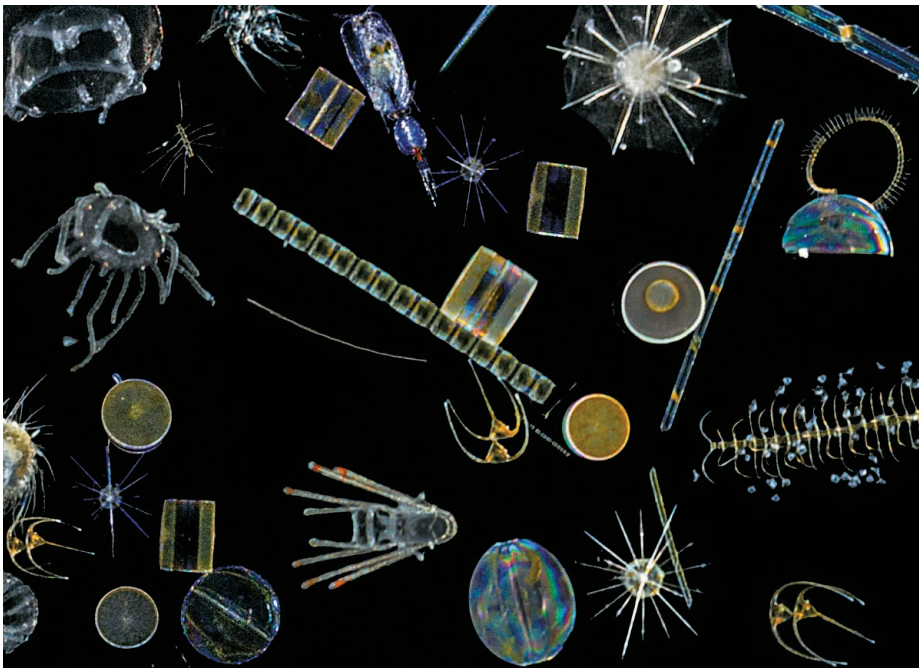

This plankton mix from the sunlit water column includes unicellular protists, multicellular organisms, and larvae.

PHOTO: CHRISTIAN SARDET FROM *PLANKTON: WONDERS OF THE DRIFTING WORLD*

ticular, dimethylsulfide (DMS) and its precursor dimethylsulfoniopropionate (DMSP). These compounds are rapidly cycled by the upper-ocean microbial food web and have low concentrations in the water column (in the nanomole range per liter, compared with micromole per liter for bulk DOS as found by Ksionzek *et al.*). DMSP is produced by many eukaryotic phytoplankton species and some cyanobacteria (*10*, *11*). Phytoplankton commit up to 10% of net photosynthesis (*12*, *13*) to this single compound, making DMSP a major intracellular metabolite for many phytoplankton groups (*6*, *14*). Interest in DMS and DMSP was initially sparked by their potential role in climate regulation (*15*), but DMSP may play an important role in several facets of ecosystem dynamics (see the figure).

In the ocean, where the vast majority of organisms are microscopic and the relative distances between them can be large, finding food can be difficult. To overcome this challenge, organisms use chemical signals to locate resources, a process known as chemotaxis. Bacteria also use chemical queues to regulate community behavior (quorum sensing); for example, they may increase the production of antibiotics once a population has reached a certain size. DMSP causes strong chemotactic behavior in heterotrophic bacteria and zooplankton (*4*) and induces the production of quorum-sensing molecules (*5*). Similarly, another organosulfur compound, dihydroxypropane-1-sulfonate (DHPS), is a key participant in an "exchange of goods" (vitamin B12 for organic carbon) between phototrophs and co-occurring heterotrophs (*6*).

We are only just beginning to understand the ecological relevance of a handful of the 81 labile (rapidly cycled) DOS compounds identified by Ksionzek *et al.* in the surface ocean. Some of these organic sulfur compounds may play a critical role in ecosystem dynamics. A necessary next step is to better characterize these DOS compounds (such as their sulfur oxidation state), their turnover rate, and local or regional variations in the composition of DOS. Further work is needed to understand the extent to which microbial dynamics are limited by the availability of reduced sulfur compounds and to elucidate the connection between the small, rapidly cycled, labile DOS pool and the large, non-labile DOS pool. ■

REFERENCES

1. D. A. Hansell, *Marine Science* **5**, 202 (2013).
2. M. A. Moran *et al.*, *Proc. Natl. Acad. Sci. U.S.A.* 10.1073/pnas.1514645113 (2016).
3. K. B. Ksionzek *et al.*, *Science* **354**, 456 (2016).
4. J. R. Seymour, R. Simó, T. Ahmed, R. Stocker, *Science* **329**, 342 (2010).
5. M. Johnson, M. C. K. Soule, E. B. Kujawinski, *ISME J.* **10**, 2304 (2016).
6. B. P. Durham *et al.*, *Proc. Natl. Acad. Sci. U.S.A.* **112**, 453 (2015).
7. B. A. Van Mooy *et al.*, *Nature* **458**, 69 (2009).
8. H. J. Tripp *et al.*, *Nature* **452**, 741 (2008).
9. C. L. Dupont *et al.*, *ISME J.* **6**, 1186 (2012).
10. M. D. Keller, W. K. Bellows, R. R. L. Guillard, in *Biogenic Sulfur in the Environment*, E. S. Saltzman, W. J. Cooper William, Eds. (ACS Symposium Series, American Chemical Society, 1989), pp. 167–182.
11. E. Bucciarelli *et al.*, *Limnol. Oceanogr.* **58**, 1667 (2013).
12. E. C. Howard, S. L. Sun, E. J. Biers, M. A. Moran, *Environ. Microbiol.* **10**, 2397 (2008).
13. N. M. Levine *et al.*, *Environ. Chem.* **13**, 302 (2016).
14. J. Stefels, M. Steinke, S. Turner, G. Malin, S. Belviso, *Biogeochemistry* **83**, 245 (2007).
15. R. J. Charlson, J. E. Lovelock, M. O. Andreae, S. G. Warren, *Nature* **326**, 655 (1987).

10.1126/science.aai8650

IMMUNE CELL METABOLISM

Warburg meets epigenetics

Glycolysis promotes T cell function by an epigenetic mechanism

By **Chirag H. Patel** *and* **Jonathan D. Powell**

We are all taught in biochemistry class that in the presence of oxygen, cells will use the tricarboxylic acid (TCA) cycle to efficiently generate adenosine 5′-triphosphate (ATP) via oxidative phosphorylation (OXPHOS). However, in 1924, the biochemist Otto Warburg observed that cancer cells do not follow this rule (*1, 2*). In fact, even in the presence of oxygen, cancer cells will depend on glycolysis (so-called aerobic glycolysis) to inefficiently generate ATP from glucose. More recently, there has been great interest in the observation that effector T cells will also use glycolysis to generate ATP in the presence of oxygen (*3, 4*). On page 481 of this issue, Peng *et al.* (*5*) make an important link between aerobic glycolysis and epigenetic regulation in T helper 1 (T_H1) cell differentiation.

"...there is an advantage to this metabolic reprogramming, both for rapidly proliferating tumor cells and immune cells."

It is becoming increasingly clear that metabolic reprogramming (i.e., up-regulating the glycolytic machinery) is a critical component of T cell activation (*6*). One key glycolytic protein is lactate dehydrogenase (LDHA). LDHA is involved in the conversion of pyruvate to lactate and, more importantly, in the oxidation of nicotinamide adenine dinucleotide (NADH) to regenerate NAD^+ and continuously drive glycolysis (*7*). However, pyruvate that is not converted to lactate is

Bloomberg-Kimmel Institute for Cancer Immunotherapy, Johns Hopkins School of Medicine, Immunology CRB I Rm 443, Baltimore, MD 21287, USA. Email: poweljo@jhmi.edu

converted to acetyl–coenzyme A (acetyl-CoA), allowing it to enter the TCA cycle.

Given the crucial role of LDHA in promoting glycolysis, Peng *et al.* genetically deleted this enzyme specifically in T cells [knockout (KO) T cells], and then activated those T cells and analyzed the consequences. KO T cells displayed less glycolytic activity and more oxygen consumption compared to wild-type cells. Glucose tracing experiments in KO T cells revealed a slowdown in glycolysis but an increase in labeled citrate via the TCA cycle, indicating an increase in OXPHOS.

Inhibiting glycolysis was shown to decrease T_H1 differentiation (*3, 4*). Likewise, Peng *et al.* demonstrate that LDHA deficiency also decreases T_H1 differentiation. Previously, Pearce and colleagues demonstrated that decreased glycolysis leads to a decrease in production of interferon-γ (IFN-γ) as a consequence of translational repression by glyceraldehyde-3-phosphate dehydrogenase (GAPDH) binding to the *3′*-untranslated region (*3′*UTR) of *Ifng* messenger RNA (mRNA) (*3*). By contrast, during glycolysis, GAPDH is enzymatically engaged, resulting in free *Ifng* mRNA for translation. Peng *et al.* assessed the role of LDHA-dependent glycolysis in regulating IFN-γ at the *3′*UTR of *Ifng* mRNA. Surprisingly, their data did not support a correlation between glycolytic activity and translational regulation of IFN-γ, thus prompting them to search for an alternative mechanism of regulation.

Subsequent RNA-sequencing (RNA-seq) analysis revealed decreased expression of *Ifng* mRNA in KO T cells. Previous studies have linked glucose metabolism to gene expression through acetylation of histones (*8*). By correlating gene expression and chromatin immunoprecipitation (CHIP)–seq analysis of acetylated histones between wild-type and KO T cells, Peng *et al.* determined that the differential expression of genes such as *Ifng* was indeed regulated by histone acetylation. Because KO T cells displayed more OXPHOS, less citrate was available for ATP–citrate lyase (ACL) to generate acetyl-CoA. This reduced the amount of acetyl-CoA available to fuel histone remodeling by histone acetyltransferases (HATs). Thus, the decrease in acetyl-CoA was exerting an effect on the epigenetic landscape of the T_H1 cell and thereby T cell function. The authors were able to rescue this defect in KO T cells by introducing exogenous acetate, thereby permitting histone remodeling of the *Ifng* locus and increasing *Ifng* mRNA transcription. Interestingly, KO T cells did not display a global reduction in gene expression. Therefore, one question that remains is how HATs selectively avoid certain loci with a diminished pool of acetyl-CoA available.

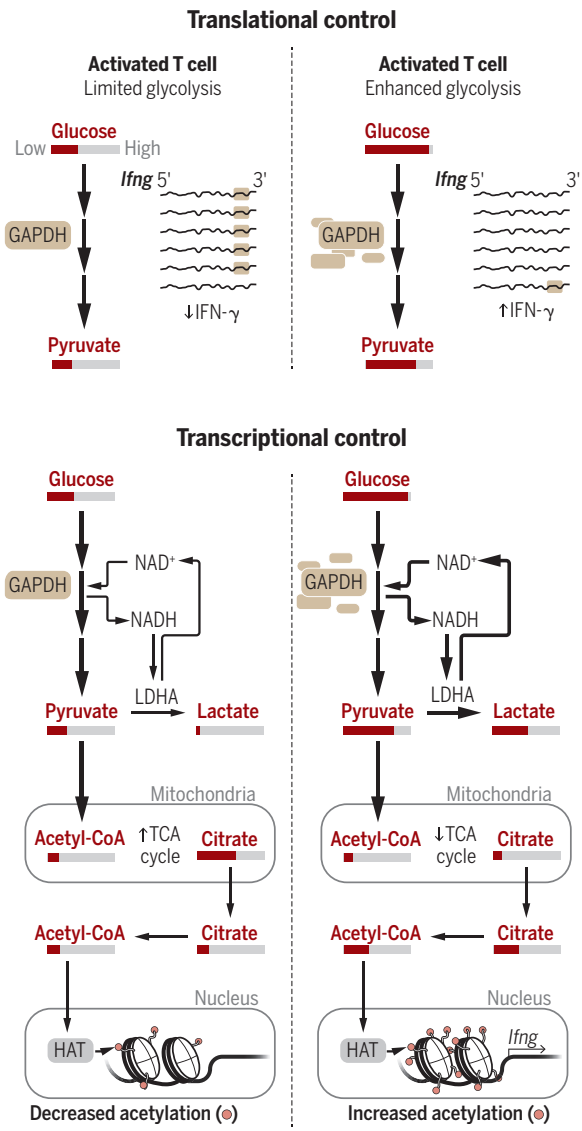

Dual control of T cell function. (Top) Translational control. Limited glycolysis (left) results in GAPDH binding to 3′UTR of *Ifng* mRNA, leading to translational control of IFN-γ, whereas enhanced glycolysis (right) increases GAPDH enzymatic activity, thereby releasing *Ifng* mRNA from translational control. (Bottom) Transcriptional control. Limited glycolysis (left) results in higher OXPHOS, limiting acetyl-CoA availability for histone acetylation via HAT at *Ifng* loci, whereas enhanced glycolysis (right) via LDHA leads to TCA-derived citrate conversion to acetyl-CoA, thereby enhancing histone acetylation to open *Ifng* loci for active transcription.

Thus, the mechanism by which glycolysis regulates T cell function as proposed by Peng *et al.* (via epigenetic regulation) sharply contrasts with the model set forth by Pearce and colleagues (via translational control) (see the figure). Interestingly, a recent report studying CD8 memory T cell function provides evidence that acetylation of GAPDH enhances its enzymatic activity, which could reduce its ability to regulate *Ifng* mRNA translation, thus linking acetylation to both models (*9*). Indeed, one might imagine that the glycolytic status in activated T cells may regulate T cell function at both the transcriptional and translational level. For example, in a glucose-sufficient environment, naïve T cells differentiating to T_H1 cells via glycolysis will generate an abundant amount of *Ifng* mRNA by modulating acetylation of histones, with this mRNA being robustly translated. However, if these T_H1 cells migrate to a glucose-deprived environment such as a tumor (*10*, *11*), the drop in glycolysis will lead to GAPDH sequestration of available *Ifng* mRNA as a translational control while preventing de novo transcription owing to lack of histone acetylation.

When Warburg initially made his observations, he thought that the use of glycolysis by cancer cells in the presence of oxygen represented defects in mitochondria (*2, 12*). We are now beginning to appreciate that there is an advantage to this metabolic reprogramming, both for rapidly proliferating tumor cells and immune cells (*1–6, 9–11*). The study by Peng *et al.* reveals an elegant connection between the ability of LDHA to promote glycolysis and epigenetically regulate critical genes for T cell function. Furthermore, these findings, along with previously published reports using other inhibitors of glycolysis, suggest that targeting LDHA to inhibit glycolysis might prove to be a potent means of regulating immune responses in both autoimmunity and transplantation (*13, 14*). ■

REFERENCES

1. O. Warburg, K. Posener, E. Negelein, *Biochem Z.* **152**, 319 (1924).
2. M. G. Vander Heiden *et al.*, *Science* **324**, 1029 (2009).
3. C. H. Chang *et al.*, *Cell* **153**, 1239 (2013).
4. A. N. Macintyre *et al.*, *Cell Metab.* **20**, 61 (2014).
5. M. Peng *et al.*, *Science* **354**, 481 (2016).
6. K. N. Pollizzi, J. D. Powell, *Nat. Rev. Immunol.* **14**, 435 (2014).
7. R. P. Donnelly, D. K. Finlay, *Mol. Immunol.* **68**, 513 (2015).
8. K. E. Wellen *et al.*, *Science* **324**, 1076 (2009).
9. M. L. Balmer *et al.*, *Immunity* **44**, 1312 (2016).
10. C. H. Chang *et al.*, *Cell* **162**, 1229 (2015).
11. P. C. Ho *et al.*, *Cell* **162**, 1217 (2015).
12. O. Warburg, *Science* **123**, 309 (1956).
13. Y. Yin *et al.*, *Sci. Transl. Med.* **7**, 274ra18 (2015).
14. C. F. Lee *et al.*, *Cell Rep.* **13**, 760 (2015).

10.1126/science.aak9776

POLICY FORUM

Smoke from a forest fire in the Sierra Nevada Mountains, California (16 June 2008).

CLIMATE POLICY

Making climate science more relevant

Better indicators for risk management are needed after Paris

By **Charles F. Kennel,[1,2] Stephen Briggs,[3,4] David G. Victor[5,6,7]**

For nearly three decades, the central goal in international climate policy had been to set the political agenda—to engage all countries on the need for action. So long as that was the goal, it was sufficient for policy-makers to focus on simple indicators of climate change, such as global average surface temperature. With the 2015 Paris Agreement, governments launched a process that can move beyond setting agendas to coordinating national policies to manage the climate. Next month in Marrakesh, diplomats will convene to flesh out the Agreement. They need to focus on the infrastructure of data and analysis that will be needed as the Agreement becomes operational. The scientific community can help by identifying better lagging indicators to describe what has changed as policy efforts progress, and leading indicators to focus policy on the right risks as the planet warms.

Instead of setting climate commitments centrally through a "top down" process, the genius of the Paris approach is to decentralize. Countries set, then extend, their own pledges. If the system works as planned, it will lead to deeper global cooperation that is flexible enough to accommodate the diversity in national interests and capabilities (*1*). Yet the flexibility of this approach is also its greatest risk in implementation. Managing this complex, highly decentralized process must engage all levels of government and the private sector. The scientific community should judge its relevance by whether it helps these decentralized actors and its processes craft and implement more effective policies.

PLANETARY VITAL SIGNS

The Paris Agreement continued the practice of setting goals according to global average surface temperature (*2*). Yet global temperature is not the most fundamental indicator of climate system change (*3*). A larger suite of indicators—what we called "planetary vital signs" (*4*)—could convey a more balanced picture (*5*). Earlier this year, policy-makers recognized the need for such information (*6*). Now, a concrete plan is needed to provide better vital signs. The first deadline is 2018 when the Paris Agreement will finish its first "stocktaking" of its progress.

The first steps to meeting that deadline are being taken. The Global Climate Observing System (GCOS), hosted by the World Meteorological Organization, defined 50 "essential climate variables" (ECVs) (*7*) that can organize acquisition of the observations needed to understand and model climate. This list is too long and complex, but GCOS is well suited to convening discussions about assembling ECVs into a few vital signs that can inform policy-makers and the public about climate change. Other groups are working on similar fronts, which is auspicious, but the scientific community needs to focus more on coordinating the many groups working in this area.

Making these vital signs useful for policy will require that scientists codevelop the indicators with policy-makers to align what we can measure technically (now and in the future) with what policy-makers actually need (*4*). If the scientific community is well organized by 2018, it will be poised to take advantage of a big political opportunity. The first Paris stocktaking will surely find that national pledges are far off track to meet the 2°C goal, which is likely to trigger a search for more realistic lagging indicators of progress.

BETTER RISK MANAGEMENT

Whereas better lagging indicators are essential, the real transformative potential lies with helping policy-makers address climate change as a risk-management problem.

King *et al.* (*8*) draw a useful distinction between two kinds of climate risk indicators. Direct risk refers to the probability of an ecological or societal impact of incremental change in climate, whereas systemic risk is the likelihood of major system compromise, natural or human. Direct risk is the easier of the two for scientists to estimate, in the realm of partial derivatives calculated against stable, orderly systems. It is calculated forward, starting from an ensemble of climate change forecasts, and is evaluated independently of the broader social system. Countries are doing these assessments (*9*), as are coastal zone managers, the insurance industry, and many others. Direct risk is familiar to anyone who has purchased fire insurance for their home or a policy-planner who has contemplated how to respond to a discrete, uncertain event.

Assessing systemic risk is more difficult yet more essential. It starts in a similar way—with an actuarial perspective that assesses the likelihood of impacts on valued assets—but aims to uncover how whole systems will respond. For example, there is growing interest in how climate changes will affect crop yields. In turn, yields affect incomes in

[1]*Scripps Institution of Oceanography, University of California San Diego, La Jolla, CA 92093, USA.* [2]*Centre for Science and Policy and Christ's College, University of Cambridge, Cambridge CB2 3BU, UK.* [3]*European Space Agency and European Centre for Space Applications and Telecommunications, Oxford-Harwell, Didcot, Oxford OX11 0FD, UK.* [4]*Chair, Steering Committee, Global Climate Observing System, World Meteorological Organization, 1211 Geneva, Switzerland.* [5]*School of Global Policy and Strategy, University of California San Diego, La Jolla, CA 92093, USA.* [6]*Brookings Institution, Washington, DC 20036, USA.* [7]*Global Agenda Council on Governance for Sustainability, World Economic Forum, 123 Cologny-Geneva, Switzerland. Email: david.victor@ucsd.edu*

farming communities and food supplies in local and global markets. But the questions of greatest import for policy-makers concern the whole system—in the face of rare extreme events—such as whether famine or economic recession will follow. Climate and remote-sensing experts can provide partial answers for some of the forces that drive famine; social scientists, less precisely, can generate indicators that synthesize those driving forces with the social conditions that are often the root cause of famine. Such analyses establish the plausibility of the risks decision-makers are prepared to act on. The more trustworthy the leading indicators are about impact, the better motivators of action they could be.

The Bayesian methodology for producing reliable systemic risk indicators has been understood for a long time. This approach relies on making best estimates—often through elicitation of the views of experts who may have insight into system behavior—and then adjusting estimates based on experience and other sources of new information. What's new—in contrast with existing integrated assessment models that dominate much of the climate science debate—is that useful Bayesian analysis for climate risks should start by asking decision-makers what matters to them along with their insights about social system response. Also new is the ability to inform this process with large data sets—including large numbers of climate model projections—that can inform climate risk analysis. The weaker link lies in the social sciences—in developing systematic ways to characterize how different types of societies respond to stresses of different types and magnitudes. When looking at flood or drought risks, for example, the natural science community is well geared to interrogate climate projections and complex watershed models that connect mountain snows, rainfall, and soil moisture to river and underground aquifer flows. Such methods arrive, with reproducible methods, at probabilistic estimates of the likelihood of floods and droughts of given magnitudes. But assessing the full systemic impacts requires knowing how humans and societies will respond.

Making this Bayesian approach to systemic risk useful will require that scientists and decision-makers codesign risk indicators—and update each other's prior assumptions about the best approaches. Such interactions will identify the data that can be brought to bear on the question of interest. Societies that are making big investments in climate impacts assessment—for example, California, which does regular evaluation of the state's exposure to climate risks (see the photo), such as wildfires and storm surge—are showing how science and policy communities can work in tandem. But such assessments remain the exception.

By itself, Bayesian logic will not be enough. Often the right questions about systemic risk are not apparent. To complement Bayesian analysis, "big data" analytics do not always start with questions, but can spot things to ask questions about. New techniques of empirical analysis and data mining are well suited to probing complex systems whose emergent properties—and risks—are often hard to fathom. For example, machine learning, which can recognize patterns in unstructured or unrelated data sets, could be used to diagnose hard-to-perceive ecological responses to slowly changing climate patterns.

A few societies—mainly in the world's richer countries—are poised to improve how they think about systemic risk. It is crucial that these insights spread to the rest of the world. Science along with policy support can help by showing how to apply these methods with replicable pilot projects. In Paris, the wealthier governments, which are most responsible for warming emissions, reaffirmed their commitment to financial help for less-developed countries to manage climate risks. Some of those funds should be earmarked for risk assessments to help the least-developed societies prepare. International science should work with local teams of scientists and decision-makers to pilot appropriate local examples. For example, the techniques being used in the California climate assessments could be demonstrated in reduced form within highly vulnerable, least-developed countries.

"...the real transformative potential lies with address[ing] climate...as a risk-management problem."

MAKING SCIENCE MORE RELEVANT

Full-blown efforts to manage climate risks will be extremely expensive. Even in the least-developed countries, the cost will likely far exceed new funds promised under the Paris Agreement. Leverage will be essential so that societies of all types build and embed effective risk management. Although local circumstances vary enormously and each society must work out its own details, a common set of indicators, well-established models, and case studies can help.

The good news is that governments, nongovernmental organizations and businesses are poised to do this if the scientific community can organize climate risk information in ways that align better with policy needs. Much of the needed data and many methods already exist. What is missing are demonstrations of how these data and methods can be used and improved for understanding systemic risks. In practice, it will be hard to work out the best examples within large intergovernmental processes in which formal decision-making requires consensus. Formal agreements on the best approaches to risk indicators are unlikely. Instead, volunteers are needed to show the way. The United States (*10*) and the European Union (*11*) are developing climate services that will provide more concrete assessments of risk and response. Such national efforts, along with local ones, should be designed with an eye to what they teach the rest of the world about what works. Similarly, commercial attention to climate risk management is rising quickly as data and analysis tools become available. Already, many firms are reporting their exposure to regulatory risks, as demanded by many shareholders and a growing number of stock exchanges. Science should help decision-makers understand their true exposure to risk and the full range of management options. The role of international policy processes should be to ensure that such experimentation with methods and approaches happens more globally.

The ultimate aim of scientific efforts on indicators should be more-robust decision support systems that can work at all levels of government, in firms, and in other social institutions. With the right tools and indicators, the practice of risk management can scale quickly through policy and commerce. For all its diplomatic difficulties, the hard work to turn the Paris process into a reality has just begun. There will be political squabbles and setbacks. Yet the task remains to build a more effective decentralized, yet global, system for risk management. ■

REFERENCES AND NOTES

1. R. O. Keohane, D. G. Victor, *Nat. Clim. Change* **6**, 570 (2016).
2. United Nations, "Adoption of the Paris Agreement" (UN, Paris, 2015).
3. D. G. Victor, C. F. Kennel, *Nature* **514**, 30 (2014).
4. S. Briggs, C. F. Kennel, D. G. Victor, *Nat. Clim. Change* **5**, 969 (2015).
5. C. Rapley, talk presented at *Global Climate Observation: The Road to the Future*, Amsterdam, 2 to 4 March 2016.
6. UN, "Matters relating to science and review: Research and systematic observation" (UN, Bonn, 2016).
7. World Meteorological Organization, "The Second Report on the Adequacy of the Global Observing System for Climate in Support of the UNFCCC" (WMO, Geneva, 2003).
8. D. King, D. Schrag, Z. Dadi, Q. Ye, A. Ghosh, *Climate Change: A Risk Assessment* (commissioned by the U.K. government, London, 2015); http://bit.ly/2dmYgi8.
9. J. M. Melillo, T. C. Richmond, G. W. Yohe, Eds., *Climate Change Impacts in the United States: The Third National Climate Assessment* (U.S. Global Change Research Program, Washington, DC, 2014).
10. A. C. Janetos, M. A. Kenney, *Front. Ecol. Environ.* **13**, 403 (2015).
11. R. B. Street, *Clim. Serv.* **1**, 2 (2016).

ACKNOWLEDGMENTS

We are indebted to P. Dasgupta, R. Douglas, S. O'Heiggerty, H. Price, C. Rapley, M. Rees, S. Sharpe, and E. Shuckburgh for useful discussions and two reviewers for detailed comments.

10.1126/science.aag3248

Previously an industrial eyesore, a 3.6-mile swath of the Cheonggyecheon River became a park in 2005.

PHOTO: DBIMAGES/ALAMY STOCK PHOTO

URBAN DEVELOPMENT

Striking the right chord

A wide-ranging treatise seeks to reshape cities with an eye toward equality and resilience

By **Scott D. Campbell**

Unsustainable, inefficient, often violent, and marked by stark inequalities of wealth and opportunity, cities are increasingly vulnerable to social and economic crises, natural disasters, climate change, and other challenges of the coming era. Yet in *The Well-Tempered City*, Jonathan Rose remains passionately optimistic about our potential to rebuild innovative, resilient, integrated urban communities and restore balance and harmony.

Rose writes neither as a scholar nor as an architect but rather as a keen urban observer and enlightened practitioner who fluidly crosses disciplinary boundaries: green building design and infrastructure, water ecology, community development, and public education, with detours into urban history, cognitive science, and the spirituality of happiness and community. He is a voracious collector of best practices and has a good ear for stories (a master synthesizer more than original theorist). The book is curiously both wide sweeping but also personal, reflecting the cumulative experiences, wisdom, and beliefs that Rose has amassed over his long career.

Rose organizes the book chapters around five qualities he ascribes to the "well-tempered" city: coherence, circularity, resilience, community, and compassion. These themes provide a broad structure, although the author strives to include so many ideas and case studies that the effect is both impressively wide-reaching and hurriedly underdocumented, with most examples serving as brief illustrations rather than fully developed evidence. (I would have welcomed more primary sources with scholarly citations.)

Readers with a nascent curiosity about urban history will enjoy the breezy opening chapters on urbanization, diverse models of city building, and contemporary sprawl. Environmentally minded readers will engage with the discussion of water, energy, and material flows in cities (and then should be encouraged to read more rigorous scholarly texts on urban metabolism, industrial ecology, and urban political ecology).

The strongest chapters are those in which Rose has the most direct and rich professional and community expertise: on green buildings and green urbanism (chapter 8) and also on natural infrastructure (chapter 7). Here, he narrates a grand tour of innovative, sustainable, often socially just projects. These stories provide encouragement that today's designers and planners are doing remarkable, inventive, and inspiring work.

Toward the end of the book, Rose more broadly explores happiness, spirituality, altruism, and compassion in the city. These are rather speculative but also the most thought-provoking chapters, in part because most scholarly writing on cities tends to steer clear of these so-called "soft" issues, safely adhering to cool analysis and structural critique.

There is a risk in having a scholar review such a book. We are professionally prone to find flaws in logic and documentation and skeptical of broad-sweeping generalizations and optimism. And we are wary of metaphors, knowing both their rhetorical-cognitive power but also their limitations.

At the core of this book is the metaphor of the well-tempered city, which resonates with our era's focus on sustainability, resilience, and restoring human-nature balance. It is an appealing metaphor, and Rose strives to also link personal attributes (mindfulness, compassion, harmony, and altruism) to cities. Can one make that leap of scale and scope?

Urbanists have learned that most metaphors fall short and can misguide urban planning; cities are not (just) gardens, or machines, or artworks, or marketplaces, or innovation laboratories, or zones of conflict resolution, or ecosystems. Cities are none of these, or rather, they are all of these (and more) in an irreducible, ever-changing assemblage. Urban complexity leads to a city's dynamic culture and economy but also to a persistent turmoil of uneven development, instability, and disharmony that can be managed and improved through design but never fully "resolved."

We can therefore imagine the well-tempered city, but building and maintaining it rarely can be realized. Alas, a city cannot be tuned like a pianoforte. Nevertheless, striving toward an aspirational but asymptotic goal might still be a useful target for an era that is often lacking a higher vision for its cities.

The Viennese social satirist Karl Kraus declared, "I demand from a city where I should live: asphalt, street cleaning, a front door key, heat, and piped hot water. Coziness I provide myself" (*1*). This is an enduring tension in the urban planning field: Should our municipalities just provide the basic infrastructural necessities, or must they also provide meaning and a comfortable (or even a spiritual) sense of place? Rose engagingly argues that the two are connected—that the health of the city's economic, social, and ecological networks is linked to promoting compassion, collective altruism, and a larger sense of purpose.

The Well-Tempered City
What Modern Science, Ancient Civilizations, and Human Nature Teach Us About the Future of Urban Life
Jonathan F. P. Rose
Harper Wave, 2016, 478 pp.

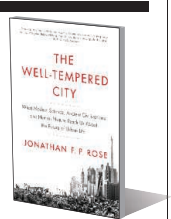

The reviewer is at the Taubman College of Architecture and Urban Planning, University of Michigan, Ann Arbor, MI 48109, USA. E-mail: sdcamp@umich.edu

REFERENCES

1. K. Kraus, *Pro domo et mundo, Ausgewählte Schriften* (*Bd. 4*) (A. Langen, 1912).

10.1126/science.aai8216

COSMOLOGY

Is anyone out there?

A witty romp through the cosmos explores the scientific search for intelligent alien life

By **Marcos Huerta**

For many people, there could be no greater scientific discovery than proof of the existence of life on another planet. This year alone, we have seen examples of how even the hint of alien civilization can capture the attention of the media and, by extension, the public. The so-far-inexplicable light curve of the star KIC 8462852 discovered by NASA's Kepler telescope has conjured speculation about "alien megastructures" orbiting the star. And for a few days in August, the press stirred over a "strong signal" from another star, HD 164595, that scientists thought could be of alien origin. (Subsequent observations and analysis quickly put a damper on initial reports.)

It is the quest for the discovery of alien life that Ben Miller explores in his new book *The Aliens are Coming!* In just over 300 pages, Miller provides a light-hearted but thorough exploration of the science behind alien life—what it might be like, where and how we might find it—and reflects on whether we could understand or recognize an alien at all.

Miller organizes the book into eight chapters but shifts from topic to topic with abandon. The opening chapter, "Extremophiles," starts with the entry of Voyager 1 into interstellar space, dives below the Pacific Ocean with the *Alvin* submarine, and ends with the Huygens probe entering the atmosphere of Saturn's largest moon, Titan. In between, Miller explains Darwinian evolution, managing to reference the television show *Twin Peaks*, the opening scenes of the movie *Contact*, and the "Get a Mac" advertising campaign of the late 2000s in the process.

The book continues in a similar vein—each chapter revolves around a theme but happily bounces off into sidebars and explanations. Some topics would have been enhanced with visuals. The third chapter, for example, has a single picture depicting the now defunct "Big Ear" radio telescope at the Ohio State University, which once (and only once) detected an incredibly strong narrowband radio signal from the constellation Sagittarius, but nothing to help the reader understand the science behind the detection of extrasolar planets.

As promised in the title, the book doesn't disappoint when it comes to aliens. The Drake equation (a simple way to estimate the number of intelligent civilizations in our galaxy that we may be able to receive signals from), the Search for Extraterrestrial Intelligence (SETI) Institute, and the Fermi paradox (the question of why an older alien civilization hasn't already colonized the galaxy) all receive excellent discussions. Despite the fact that we have so far failed to detect evidence of alien life, Miller is optimistic: "[I]f our galaxy contains 10,000 communicable civilizations among 200 billion stars, we'd need to search around ten million stars before we found anything. So far we have searched a paltry 10,000."

Mazlan Othman, a Malaysian astrophysicist, served as the director of the United Nations Office for Outer Space Affairs from 2010 to 2014.

PHOTO: TOMER APPELBAUM

The Aliens Are Coming!
The Extraordinary Science Behind Our Search for Life in the Universe
Ben Miller
The Experiment, 2016, 304 pp.

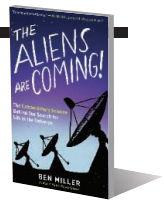

Miller is at his best when he tells a straightforward narrative about a particular discovery or presents an original interview. His conversation with Mazlan Othman—the official "ambassador for Earth" of the United Nations Office for Outer Space Affairs—is particularly amusing, for example. "I do my best to try and convince her that I am not a crazy person, that I know my stuff about science, and that, while I think the evidence for UFOs is feeble, I am very interested in the possibility that there is intelligent, communicable life on other planets," he writes. "And, in doing so, I am fairly sure that I come across as a crazy person."

The book's scope is not limited to alien civilizations. The origin of life on Earth is thoroughly discussed, in the context of what alien life could potentially be like and if it's even likely to exist. Is Earth particularly and luckily well suited to life? Is the universe itself predisposed to life? These are among the interesting questions Miller addresses.

The book suffers later on, as Miller struggles to pack too much and too varied information into the final chapters. I did not expect to find thermodynamic equations in a chapter entitled "Life," for example, but there they were. The appearance of these and other equations and the frequent use of field-specific jargon might frustrate some readers. Last, there are ample footnotes throughout the book, although no references—only a short (albeit good) "Further Reading" section at the end.

Despite the huge breadth of science—from cosmology to biogenesis—covered, *The Aliens are Coming!* is a concise work that will appeal to anyone who has ever wondered whether we are alone in the universe.

NOTES

The opinions expressed in this review are the author's own and do not reflect the views of the Department of Energy or the U.S. government.

10.1126/science.aah5387

The reviewer is at the Office of Science, U.S. Department of Energy, 1000 Independence Avenue SW, Washington, DC 20585, USA. E-mail: huerta.marcos@gmail.com

Edited by **Jennifer Sills**

Save the world's primates in peril

IN HIS IN DEPTH News story "Chimpanzee sanctuaries open door to more research" (29 July, p. 433), D. Grimm argues that partnerships between sanctuaries and research centers could see laboratory chimpanzees become extinct. This conclusion might be optimistic, given that new demands for precision medicine and neuroscience projects may lead to greater use of some species of primates in biomedical research. Worse yet, continued investment in research animals exacerbates the situation of wild primates in peril.

More than 70,000 monkeys are used in experiments every year in the United States (*1*). The federal government plans to invest over $434 million in the BRAIN Initiative alone in 2017 (*2*). However, very little funding is set aside for primate conservation. The continuing imbalance in interest and funding will see more wild primates becoming extinct, although accurate data are hard to find. The population of wild rhesus monkeys (*Macaca mulatta*)—the most common experimental primates in China—declined from 254,000 in 1998 to 77,000 in 2008 (*3*).

In addition, we are concerned that Grimm's story might deflect attention away from the plight of endangered wild chimpanzees. In the past 30 years, the Ebola virus has killed nearly one-third of the world's chimpanzees and gorillas (*4*). According to the International Union for Conservation of Nature, almost 50% of the world's 634 species of primates are in danger of extinction because of increasing human population, urbanization, tree felling, illegal capture, and climate change (*5*).

Most nonhuman primate species are found in developing countries that lack adequate capital, management, and technology to protect their wild primates. By contrast, many developed countries that lack indigenous primates tend to prioritize the value of primates for biomedical research rather than their conservation. Developed and developing countries should work together to address this issue. For example, to combat the decline of chimpanzees in Asia, where approximately 71% of species face extinction (*6*), the International Primatological Society should contact the decision-making departments in relevant Asian countries and establish an "Asian primatology alliance" to sustain wild primate populations. Such long-term international collaborations could redress the imbalance in capital and technology and save endangered primate species.

Bin Yang,[1,2] James R. Anderson,[3] Peng Zhang,[4] Baoguo Li[1,2]*

[1]College of Life Sciences, Northwest University, Xi'an, 710069, China. [2]Shaanxi Key Laboratory for Animal Conservation, Shaanxi Institute of Zoology, Shaanxi Academy of Sciences, Xi'an, 710032, China. [3]Department of Psychology, Kyoto University Graduate School of Letters, Kyoto, 606-8501, Japan. [4]Martin Hall, School of Sociology and Anthropology, Sun Yat-Sen University, Guangzhou, 510275, China.

*Corresponding author. Email: baoguoli@nwu.edu.cn

REFERENCES

1. E. W. Lankau, P. V. Turner, R. J. Mullan, G. G. Galland, *J. Am. Assoc. Lab. Anim. Sci.* **53**, 278 (2014).
2. White House Office of Science and Technology Policy, "Obama Administration proposes over $434 million in funding for the BRAIN Initiative" (2016).
3. Beijing Science and Technology News, "Primate rapidly disappearing: Gibbons will become history" (2009); http://blog.cdstm.cn/?uid-288984-action-viewspace-itemid-6370 [in Chinese].
4. S. J. Ryan, P. D. Walsh, *PLOS ONE* **6**, e29030 (2011).
5. A. H. Harcourt, S. A. Parks, *Biol. Conserv.* **109**, 137 (2003).
6. A. Shah, "Nature and animal conservation," *Global Issues* (2014); www.globalissues.org/article/177/nature-and-animal-conservation.

10.1126/science.aak9638

PHOTO: KALIAPPANVIJAYBABU/ISTOCKPHOTO.COM

The population of wild rhesus monkeys (*Macaca mulatta*), a species commonly used in research, is declining.

Adapting Chinese cities to climate change

ON 15 SEPTEMBER, Typhoon Meranti—the strongest recorded tropical cyclone to date in 2016 (*1*)—made landfall over the city of Xiamen, China. The winds and floods caused 10.2 billion RMB (1.6 billion USD) in direct economic losses (*2*). The havoc wreaked by Meranti makes clear that rapidly urbanizing coastal cities must prioritize adaptation to climate change.

The destruction and degradation of coastal ecosystems impair urban resilience to typhoon disasters, which will become more intense as the environment grows warmer (*3*). More than 90% of Xiamen's natural mangroves, and a large area of casuarina trees and mud flats, have been lost to coastal reclamation since the 1960s (*4*). As a result, the natural coastal ecosystem no longer provides the ecosystem service of an effective barrier to destructive winds and storm surges. This in turn has led to further loss: More than 0.65 million (about 90% of the total) street trees were uprooted during Meranti's landfall (*2*). The rapid urbanization has also led to increased impervious surfaces in built-up areas of Chinese cities (*5*), which has caused increased urban flooding and related economic losses.

Chinese cities excel at mobilizing people quickly [e.g., more than 47,000 people were evacuated shortly before Meranti's landfall (*2*)], and they have enhanced early-warning systems that are crucial to natural disaster preparedness. However, they have lagged behind cities in other countries in incorporating adaptations to climate change into city planning (*6*). As Meranti demonstrated, and the New Urban Agenda highlights, these changes are key to reducing urban vulnerability and building coastal resilience (*7*).

Urbanizing Chinese coastal cities should develop climate-smart marine and coastal spatial planning that is resilient to climate change and minimizes carbon emissions (*8*). In addition, China needs ecosystem-based marine functional zoning, which identifies the critical components and

processes of the marine ecosystem, to address conflicts between sea use and environment protection (*9*). Chinese urban decision-making and planning should be risk-informed, taking into account the risks of natural and man-made disasters, including both short-term and long-term effects of climate change, such as extreme weather and sea-level rise (*10*). The prevailing sector-by-sector planning system should be replaced by an integrated and unified system to ensure spatial consistencies. Chinese coastal cities should also invest in ecological restoration projects (*11*) and green infrastructure technology, such as the recent "sponge city" pilot program, which reduced impervious surface areas so that rainfall can be retained, stored, and reused to reduce severe urban flooding (*12*).

Qinhua Fang

Fujian Provincial Key Laboratory for Coastal Ecology and Environmental Studies, Coastal and Ocean Management Institute, Xiamen University, 361102, China. Email: qhfang@xmu.edu.cn

REFERENCES

1. B. Hensen, J. Masters," Taiwan, China brace for Cat 5 Meranti; TS Ian churns through open Atlantic," *Weather Underground* (2016); www.wunderground.com/blog/JeffMasters/taiwan-china-brace-for-cat-5-meranti-ts-ian-churns-through-open-atla.
2. "Xiamen Municipal Government's third conference: Typhoon Meranti causes Xiamen direct economic losses of 10.2 billion" (2016); www.taihainet.com/news/xmnews/szjj/2016-09-19/1789079.html [in Chinese].
3. P.J. Webster *et al.*, *Science* **309**, 1844 (2005).
4. Z. Ma *et al.*, *Science* **346**, 912 (2014).
5. Y. Chen *et al.*, *Environ. Res.* **139**, 3 (2015).
6. A. Aylett, Progress and Challenges in the Urban Governance of Climate Change: Results of a Global Survey (MIT, Cambridge, MA, 2014).
7. The New Urban Agenda (2016); http://habitat3.org/the-new-urban-agenda.
8. "World Bank: Climate-Smart Planning Platform" (2016); www.climatesmartplanning.org/.
9. Q. Fang *et al.*, *Coast. Manage.* **39**, 656 (2011).
10. E. Zio, N. Pedroni, "Overview of risk-informed decision-making processes" (FONSCI, 2012); www.foncsi.org/fr/publications/collections/cahiers-securite-industrielle/overview-of-risk-informed-decision-making-processes/CSI-RIDM.pdf.
11. M. McNutt, *Science* **349**, 905 (2015).
12. "Notice on pilot project of sponge city construction supported by the central government finance" (2014); http://jjs.mof.gov.cn/zhengwuxinxi/tongzhigonggao/201501/t20150115_1180280.html [in Chinese].

10.1126/science.aak9826

ONLINE BUZZ

Autonomous vehicles

IN THEIR REPORT "The social dilemma of autonomous vehicles" (24 June, p. 1573), J.-F. Bonnefon *et al*. found that, in theory, people support autonomous vehicles programmed to sacrifice passengers to save others, but they wouldn't want to drive or ride in one. Readers commented on the study design as well as possible next steps to make autonomous vehicles more practical. Excerpts from those comments are below. Read the full comments, and post your own, at http://science.sciencemag.org/content/352/6293/1573.e-letters.

A selection of your thoughts:

THE AUTHORS POSE a "social dilemma" for autonomous vehicles (AVs) with scenarios they describe as "unlikely" while relying on surveys (static self-reports) to make predictions about human preferences to these AV decisions. But we have known for decades that preferences self-reported by humans often misalign with human behavior... [S]elf-reported surveys [would be more effective for] these more likely ethical scenarios (see www.aaai.org/Symposia/Spring/sss16symposia.php#ss01): When four AVs approach an intersection with one AV "aware" that its human driver is impaired, should the AVs coordinate with each other to protect their human occupants? Should we as a society allow a robot pilot of a team to take control when the robot becomes "aware" of an impending suicide by the airliner's human copilot? Should a robot take command of a USS submarine prepared for rapid ascent to prevent the submarine from hitting a Japanese tour boat?

William F. Lawless

THE MAIN PROBLEM for the autonomous vehicles (AVs) that are created today is...that [they] are created for the existing environment, with pedestrians and humans operating vehicles.... [H]uman-driven vehicles and ships must not be used in the environment where the automatically driven vehicles and ships are used, and vice versa....

Vladimir Postnikov

10.1126/science.aal2546

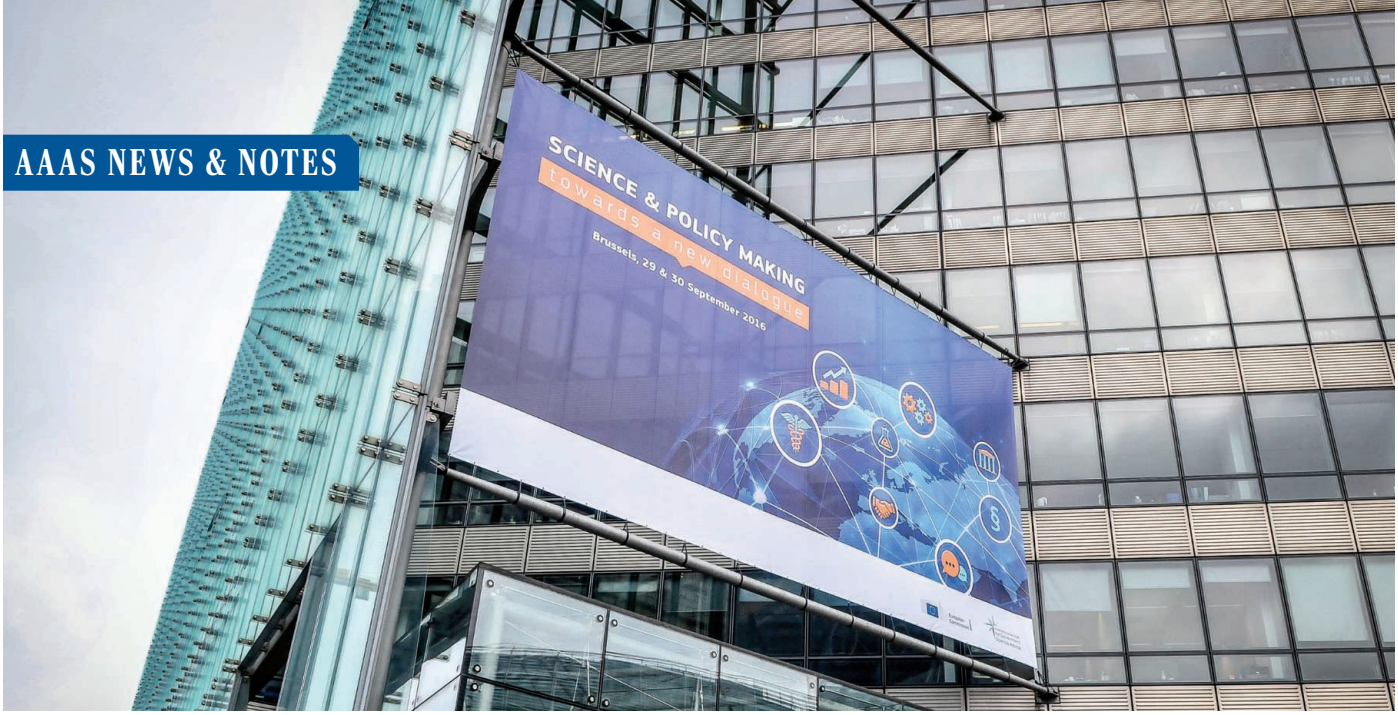

Conference navigates gap between science and government

International experts on both sides share best methods for achieving evidence-informed policy

By **Michaela Jarvis**

More than 600 professionals from the worlds of science and politics converged in Brussels late last month to mine internationally accumulated expertise on how best to connect scientific evidence with government decision-making. Infectious disease outbreaks, humanitarian crises, the use of genetically modified crops, climate change, and other pressing issues will all require the input of scientists, speakers said.

"We understand now that there is no societal issue in which social and natural sciences do not have an important role to play," Sir Peter Gluckman, chair of the International Network for Government Science Advice (INGSA), told the conference participants, who represented 72 different countries. In the opening session, Gluckman, who is the chief science adviser to the prime minister of New Zealand, defined the challenge of learning how best to "broker" the increasingly complicated evidence that science produces to meet the demands of government and society.

Allowing the exchange of best-practice principles among scientists who have provided science advice at the top levels of government around the world, the 29 to 30 September conference, organized by INGSA in partnership with the European Commission, also provided an intensive course applicable to all scientists and engineers who recognize a need to engage with decision-makers.

"The challenge of providing science advice that is relevant to public issues is the same for official science advisers or for any scientist performing his civic duty," said AAAS Chief Executive Officer Rush Holt, who attended the event. "Clarity in explaining the technical components of an issue is only a part of what the adviser must keep in mind."

Many of the speakers at the conference emphasized a need for researchers to immediately acknowledge that the scientific evidence they provide to government at any level—although more in demand than ever before—is just one of the ingredients that go into the messy process of policy-making. Holt, who is a physicist and served in the U.S. Congress for 16 years, said scientists providing advice to government sometimes fail to take into account the competing interests faced by elected officials serving their constituencies.

"Naive advisers think that they need only to teach the policy-maker what the facts are, and then good solutions and good policy will follow," said Holt, who is also the executive publisher of the *Science* family of journals. "Although science is the path to the most reliable knowledge, the public and government officials first must believe that and must trust the persons giving advice."

The adviser must put the advice within the context of the political and ethical considerations of the issue and must know

Heather Douglas (left), Pontifical Academy of Sciences Chancellor Marcel Sánchez Sorondo, University of Aberdeen Vice-Principal for External Affairs Dame Anne Glover.

PHOTOS: ©EUROPEAN COMMISSION 2016

AAAS Council reminder

The next meeting of the AAAS Council will take place during the 2017 AAAS Annual Meeting in Boston, Massachusetts, and will begin at 9:00 a.m. on 19 February 2017 at the Sheraton Boston Hotel.

Individuals or organizations wishing to present proposals or resolutions for possible consideration by the council should submit them in written form to AAAS Chief Executive Officer Rush Holt by 1 December 2016. This will allow time for them to be considered by the Committee on Council Affairs at its winter meeting.

Items should be consistent with AAAS's objectives and be appropriate for consideration by the council. Resolutions should be in the traditional format, beginning with "Whereas" statements and ending with "Therefore be it resolved."

Late proposals or resolutions delivered to the AAAS Chief Executive Officer in advance of the February 2017 open hearing of the Committee on Council Affairs will be considered, provided that they deal with urgent matters and are accompanied by a written explanation of why they were not submitted by the 1 December deadline. The Committee on Council Affairs will hold its open hearing at 2:30 p.m. on 18 February 2017 in the Sheraton Boston Hotel.

when exactly the advice is needed. For policy-makers, said political scientist Dame Helen Wallace, "very often it's not what you want to do, it's whether you can do it, whether you can implement it, whether it will be behaviorally acceptable, whether it will be ethically acceptable." Wallace is a member of Academia Europaea and a fellow of the British Academy.

Mark Ferguson, who is the chief scientific adviser to the Government of Ireland, said he asks the politicians he serves, "What is it that you are trying to achieve, and how can science help you?"

In addition to recognizing the multiple challenges facing politicians, scientists generally need a desire to work across disciplines, and especially to integrate the social sciences with the natural sciences in order to provide information that will affect important decisions. This is especially true at a time when whole sectors of society are rejecting experts and evidence in favor of political ideology, as is happening in the United States with regard to acknowledging climate change.

We need the social sciences "to understand why social change is not happening at the pace or in the direction we would like it to, despite all of the efforts that have been made to date," said Martin Porter, who serves the European Climate Foundation as the executive director for industrial innovation and European Union affairs. By integrating social science research "with the world of natural science, perspectives open up for more rapid change."

Social scientists at the conference recommended communicating with stakeholders to increase the applicability of scientific evidence in policy-making, as well as establishing a dialogue with citizens who are not stakeholders but who make up a representative sample of a population, both to sound them out on their views and to help inform them about the technical, social, and ethical aspects of a certain issue and the best corresponding scientific evidence. Such dialogue, said Heather Douglas, who is the Waterloo Chair in Science and Society at the University of Waterloo, can help both scientists and politicians to understand citizens' concerns.

"You need to know what people care about," said Douglas, "what risks they'll accept, which are not acceptable, and why."

Pushing public and stakeholder involvement a step further, conference experts recommended "citizen science" and "co-production" of scientific research, referring to it as a means of reaching out to citizens experiencing an overload of digitally delivered information—much of which is misleading—and reestablishing the public's trust in scientific evidence.

An excellent example of such participatory research is outlined in a report by the Pew Initiative on Food and Biotechnology, Douglas pointed out. An extremely contentious issue was the report's focus: the effect on monarch butterflies of a variety of corn bred to be insect resistant by genetically engineering it to produce a toxin derived from the *Bacillus thuringiensis* (Bt) bacteria, which in its natural form is used as a bio-pesticide by organic and conventional farmers. Scientists from academia, government, industry, and environmental groups worked together to plan the experiments for answering the question of whether the genetically modified corn posed a risk. Ultimately, virtually all of the participants accepted that any acute threat was negligible, especially compared to other threats such as conventional pesticides.

Panelists throughout the conference also emphasized transparency about how scientific results were derived and how the work was funded as crucial to policy-makers.

Mady Delvaux-Stehres, a member of the European Parliament who has often sought the advice of scientists, said, "Policy-makers know research is expensive, so they want to know who's financing it. Otherwise, they are suspicious."

Amid brand-new and time-tested ideas for fostering the connection between science and government, the longstanding AAAS Science & Technology Policy Fellowships won praise for their effectiveness during a presentation by UNESCO Assistant Director-General for the Natural Sciences Flavia Schlegel. The 43-year-old program, which places hundreds of scientists and engineers in U.S. government offices every year, is being viewed as a model for state and federal governments to consider.

After acknowledgment by many speakers of the many challenges of presenting increasingly complex scientific evidence to constrained policy-makers and a somewhat dismissive public, David Mair, head of the Geographic Coordination Unit of the Joint Research Centre of the European Commission, issued a battle cry.

"Evidence-informed policy is not axiomatic. It is not a requirement of any scientific or natural law. It is a value, and it needs to be fought for," he said. "I hope one of the positive things we take out of this conference is that there is a community of people prepared to fight."

David Mair participated in a panel discussion about the skills that experts and policy-makers need for effective dialogue.

PHOTO: ©EUROPEAN COMMISSION 2016

RESEARCH

Superresolution view of the peripheral endoplasmic reticulum

Nixon-Abell et al., *p. 433*

IN *SCIENCE* JOURNALS

Edited by **Stella Hurtley**

Direct nerve stimulation to improve tactile feedback for amputees

NEUROTECHNOLOGY

A touchy subject for neuroprostheses

Without tactile sensory input, amputees discern a firm handshake from a bone-crushing grip by visual cues and learned behavior. Next-generation prostheses aim to lend a more natural feel to artificial touch. Graczyk *et al*. looked at direct stimulation of the radial, ulnar, and median nerves by implanted electrodes in two amputees. By modulating the number of nerve fibers stimulated and the frequency of stimulation, sensory information could be transmitted so that the amputees could distinguish distinct levels of tactile intensity. —CC

Sci. Transl. Med. **8**, 362ra142 (2016).

QUANTUM PHYSICS

Weaving an entangled cluster

Entanglement is a powerful resource for quantum computation and information processing. One requirement is the ability to entangle multiple particles reliably. Schwartz *et al*. created an on-demand entangled cluster state of several photons by addressing a quantum dot with a sequence of laser pulses (see the Perspective by Briegel). They used an internal state of the quantum dot, a dark exciton, and its association with another internal state, a biexciton, to weave successive photons into an entangled cluster, generating entanglement between up to five photons. —ISO

Science, this issue p. 434; see also p. 416

METABOLISM

Keeping white fat from expanding

Excess body fat caused by adipogenesis—the expansion of white adipose tissue—poses serious health risks. Wong *et al*. found that mice exposed to glucocorticoids or fed a high-fat diet had decreased levels of the extracellular protein ADAMTS1 in white adipocytes, which was associated with increased adipogenesis. Increased caloric intake in human volunteers enhanced the expression of *ADAMTS1* in adipose tissue. Mice that overexpressed *Adamts1* had smaller white adipose deposits, suggesting that ADAMTS1 treatment could prevent diet- or glucocorticoid-induced obesity. —WW

White adipocytes expand as we fatten.

Sci. Signal. **9**, ra103 (2016).

CATALYSIS

Upgrading CO_2 with methane

The use of carbon dioxide as a reactant could help to mitigate its impact on climate, but it is difficult to activate as an oxidant. Buelens *et al*. combined methane in a high-temperature "super-dry" reforming process that generates reactive carbon monoxide. Both molecules were fed into a reactor containing a nickel methane-reforming catalyst, an iron oxide solid oxygen carrier, and calcium oxide as a CO_2 sorbent. The adsorbed CO_2 was treated with an inert gas purge that shifted the equilibrium, releasing mainly CO. This isothermal process avoids carbon buildup and can be used with biogas methane that contains substantial levels of CO_2. —PDS

Science, this issue p. 449

CLIMATE DATA

Models and data: A two-way street

Data are used to drive models of climate and other complex

CREDITS (FROM TOP): BENJAMIN CAMPILLO/SCIENCE SOURCE; MARK THIESSEN/NATIONAL GEOGRAPHIC; WONG *ET AL.*

systems, but is the relationship between data and models a one-way process? Massonnet *et al*. used climate models to assess the quality of the observations that such models use. Starting with a simple model and progressing to more complex ones, the authors show that models are better when they are assessed against the most recent, most advanced, and most independent observational references. These findings should help to evaluate the quality of observational data sets and provide guidance for more objective data set selection. —HJS

Science, this issue p. 452

NEURONAL MATURATION

Integration of adult-born brain cells

Physical exercise or exploration of a novel environment greatly influences the production, maturation, and connectivity of adult-born neurons. Alvarez *et al.* investigated how experience affects the incorporation of adult-born neurons into the hippocampal network. A brief period of sensory enrichment when new neurons were 9 to 10 days old led to neurons having larger dendrites and more functional spine synapses. A disynaptic preexisting feedback circuit promoted the growth and integration of the new cells. —PRS

Science, this issue p. 459

VASCULAR DISEASE

Wreaking havoc while (growth-)arrested

Cells enter a state of senescence in response to certain stresses. Studying mouse models, Childs *et al*. examined the role of senescent lipid-loaded macrophages (so-called "foam cells") in the pathogenesis of atherosclerosis. At early stages of atherosclerosis, senescent foam cells promoted the expression of inflammatory cytokines. At later stages, they promoted the expression of matrix metalloproteases implicated in the rupture of atherosclerotic plaque, which can lead to blood clots. Experimental removal of the senescent cells had beneficial effects at both stages of the disease. —PAK

Science, this issue p. 472

APE GENETICS

Of chimpanzees and bonobos

Modern non-African human genomes contain genomic remnants that suggest that there was interbreeding between ancient humans and archaic hominoid lineages. Now, de Manuel *et al*. show similar ancestral interbreeding between the ancestors of today's chimpanzees and bonobos (see the Perspective by Hoelzel). The study also provides population-specific genetic markers that may be valuable for conservation efforts. —LMZ

Science, this issue p. 477; see also p. 414

IMPACT CRATERS

On the origin of Orientale basin

Orientale basin is a major impact crater on the Moon, which is hard to see from Earth because it is right on the western edge of the lunar nearside. Relatively undisturbed by later events, Orientale serves as a prototype for understanding large impact craters throughout the solar system. Zuber *et al*. used the Gravity Recovery and Interior Laboratory (GRAIL) mission to map the gravitational field around the crater in great detail by flying the twin spacecraft as little as 2 km above the surface. Johnson *et al*. performed a sophisticated computer simulation of the impact and its subsequent evolution, designed to match the data from GRAIL. Together, these studies reveal how major impacts affect the lunar surface and will aid our understanding of other impacts on rocky planets and moons. —KTS

Science, this issue pp. 438 and 441

IN OTHER JOURNALS

Edited by **Sacha Vignieri** *and* **Jesse Smith**

COGNITION

Should I stay or should I go?

Much recent research on communication between dogs and humans has shown that dogs understand both our verbal and gestural commands, a fact well known to dog owners. Looking at working water rescue dogs, D'Aniello *et al*. asked which of these two types of commands has priority, especially if conflicting signals are given. Dogs responded better to gestural than to verbal commands, when given separately. Generally, priority was also given to gestures when conflicting commands were made, though females were better at responding to gestures, whereas males responded better to words. Interestingly, when asked both to "stay" and "come," dogs tended to choose to come, especially when the handler was walking away, suggesting that they sometimes chose the option that better coincided with their own choice. —SNV

Anim. Cogn. 10.1007/s10071-016-1010-5 (2016).

Dogs understand our gestures perhaps even better than our words.

PHOTO: TIERFOTOAGENTUR/ALAMY STOCK PHOTO

ANTIBIOTIC RESISTANCE

Quantifying the alarm from antibiotic resistance

Antibiotic resistance is a major global fear, but how fearful should we be? Multidrug resistance (MDR) is high among developing economies that are vulnerable to purveyors of substandard drugs and where over-the-counter sales are not controlled. Lim *et al.* collected mortality data on bacteremia from 10 public hospitals in northeast Thailand between 2004 and 2010. During this period, the incidence of bacteremia increased, and high case fatality rates were observed for MDR strains,

especially hospital-acquired *Acinetobacter* spp. Extrapolating to the whole of Thailand for 2010 indicates that among patients with hospital-acquired MDR bacterial infection, 43% of deaths represented excess mortality caused by MDR—which is high compared with similar estimates for the United States or Europe. —CA

eLife 10.7554/eLife.18082 (2016).

BIOETHICS

Personalized medicine by another name

A vision of the Human Genome Project was that molecular profiling would enable identification of the molecular underpinnings of disease on an individual basis; "personalized medicine" became a watchword. However, a rebranding has been occurring since roughly 2012 in which the concept has been transmogrified into "precision medicine." Juengst *et al.* describe conclusions from interviews and case studies conducted since 2011 with 143 supporters of personalized genomic medicine. The terminology change may minimize unrealistic expectations. However, a shift from "personal" could mean a reversal of the trend toward patient autonomy in decision-making. The need for population-level sequencing to identify groups with particular molecular profiles carries its own risks in terms of pressures to participate and the possibility of stigmatization. —BJ

Hastings Cent. Rep. **46**, 21 (2016).

CLIMATOLOGY

Atmospheric circulation in a warmer world

One of the most visible effects of climate change in recent decades has been the reduction of sea ice in the Arctic, which has raised the question of how weather at lower latitudes might be affected. This question has lately been asked often after a number of particularly cold winters in parts of the Northern Hemisphere. Meleshko *et al.* conducted a modeling study of how the polar and mid-latitude atmosphere might respond when a summer sea ice–free state is reached in the Arctic, as is projected for the next century. They find that although climate warming enhances northward heat transport, the resulting increase in polar surface air temperatures does not cause increased oscillation of atmospheric planetary waves, as has been proposed elsewhere. —HJS

Tellus A, 10.3402/tellusa.v68.32330 (2016).

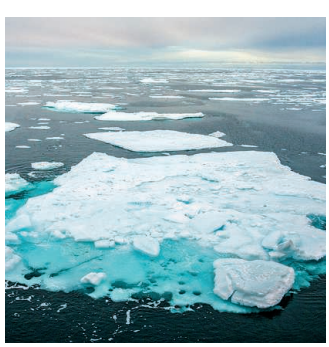

Arctic summer sea ice is expected to disappear by mid-century.

PHOTOS (FROM TOP): NASA & ESA; ROWAN ROMEYN/ALAMY STOCK PHOTO

The barred spiral galaxy NGC 1073

BARRED GALAXIES

Stellar bars knock holes in galaxy discs

About half of all spiral galaxies have a bar structure in their central region, but how these morphological features evolve over time remains uncertain. Kim *et al.* studied the distribution of infrared light in more than a hundred barred galaxies, using decomposition to separate the bar from other galaxy components. They quantify a deficit in surface brightness that appears around strong bars and investigate how it varies with other galaxy properties. They conclude that as the bar evolves, stars that were on near-circular disc orbits are perturbed onto the highly eccentric orbits that form the bar, causing the deficit. —KTS

Mon. Not. R. Astron. Soc. **462**, 3430 (2016)

SUPERCONDUCTIVITY

Controlling superconducting pairing

Interfacing superconductors with materials that have strong spin-orbit coupling can modify the superconductivity in unusual ways. Hart *et al.* sandwiched a HgTe quantum well between two superconducting leads, forming a junction. Normally, Cooper pairs—whose formation makes materials superconductive—consist of electrons of opposite momenta. Applying a magnetic field in the plane of the well, combined with an unusual electronic spin texture in HgTe, caused the Cooper pairs in the junction to acquire a nonzero total momentum. By comparing their data to theoretical models, the researchers were able to probe the nature of spin-orbit coupling in the system. —JS

Nat. Phys. 10.1038/NPHYS3877 (2016).

GERM CELL DEVELOPMENT

Primate germ cell origin

For species survival, reliable and efficient gamete production is crucial. In mammals, gametes arise from primordial germ cells (PGCs) that make their way to the developing gonads. Much is known about murine germ cell specification in the embryonic epiblast, but the mechanism in primates is less clear. Murine and primate embryos display different anatomical structures during development, so PGC origin may also vary. By examining cynomolgus monkeys (or crab-eating macaques, *Macaca fascicularis*), Sasaki *et al.* found that cynomolgus PGCs originate in the dorsal amnion, which itself provides signals to specify these cells. PGCs then migrate to the posterior yolk sac and eventually to the gonad. Preliminary analyses suggest that human germ cells may have a similar amniotic origin. —BAP

Dev. Cell. 10.1016/j.devcel.2016.09.007 (2016).

ALSO IN *SCIENCE* JOURNALS

Edited by **Stella Hurtley**

METABOLISM

Quantitation of metabolic pathway regulation

Although metabolic biochemical pathways are well understood, less is known about precisely how reaction rates or fluxes through the various enzymes are controlled. Hackett *et al*. developed a method to quantitate such regulatory influence in yeast. They monitored concentrations of metabolites, enzymes, and potential regulators by LC-MS/MS (liquid chromatography–tandem mass spectrometry) and isotope ratio measurements for 56 reactions, over 100 metabolites, and 370 metabolic enzymes in yeast in 25 different steady-state conditions. Bayesian analysis was used to examine the probability of regulatory interactions. Regulation of flux through the pathways was predominantly controlled by changes in the concentration of small-molecule metabolites rather than changes in enzyme abundance. The analysis also revealed previously unrecognized regulation between pathways. —LBR

Science, this issue p. 432

CELLULAR STRUCTURE

A dynamic view of the endoplasmic reticulum

The endoplasmic reticulum (ER) is a complex membranous structure that extends from the nuclear envelope to the cell periphery. It has important roles in many cellular processes, and numerous proteins are involved in maintaining its structure. Nixon-Abell *et al*. used super-resolution approaches to look at the ER at the periphery of the cell, where the ER contacts many other cellular organelles (see the Perspective by Terasaki). This peripheral ER has been thought to comprise tubules and sheets; however, the higher-resolution view revealed that most of the "sheets" consist of a dense clustering of tubules. This dynamic meshwork may allow the ER to change its conformation rapidly in response to cellular needs. —SMH and VV

Science, this issue p. 433; see also p. 415

CHEMICAL KINETICS

Combing through CO oxidation kinetics

Carbon monoxide reacts with OH radicals to produce CO_2. This process is central to combustion and atmospheric oxidation chemistry. The reaction sequence is widely assumed to involve the intermediacy of a HOCO adduct that has eluded direct monitoring under thermal conditions. Bjork *et al.* successfully observed the formation of the deuterated analog of this intermediate, DOCO, while simultaneously monitoring OD by using a multifrequency infrared comb. The results confirm the termolecular nature of the formation mechanism and its sensitivity to the ambient bath gas. —JSY

Science, this issue p. 444

CLIMATE CHANGE

A warming limit for the Mediterranean basin

Pollen cores from sediments provide rich detail on the history of vegetation and climate in the Mediterranean during the Holocene (the most recent ~10,000 years). Guiot and Cramer used this information as a baseline against which to compare predictions of future climate and vegetation under different climate-change scenarios. Vegetation and land-use systems observed in the Holocene records may persist under a 1.5°C warming above preindustrial temperature levels. A 2°C warming, however, is likely over the next century to produce ecosystems in the Mediterranean basin that have no analog in the past 10,000 years. —AMS

Science, this issue p. 462

OCEAN CHEMISTRY

Inventory of an essential marine element

Sulfur is necessary for marine primary production and has a large impact on climate processes. Because it is difficult to detect accurately, the amount of dissolved organic sulfur in the ocean is poorly defined. Ksionzek *et al*. measured dissolved organic sulfur in the Atlantic to estimate its distribution and infer its quantity in the world's oceans (see the Perspective by Levine). The findings suggest that dissolved organic sulfur exceeds all other forms of organic sulfur by a factor of 10. —HJS

Science, this issue p. 456; see also p. 418

GENE EXPRESSION

Plunging into a domain of silence

Female mammals have two X chromosomes. One must be silenced to "balance" gene dosage with male XY cells. The Xist long noncoding RNA coats the inactive X chromosome in female mammalian cells. Chen *et al*. show that the Xist RNA helps recruit the X chromosome to the internal rim of the cell nucleus, a region where gene expression is silenced. Xist is recruited to the domain through an interaction with the Lamin B receptor. This recruitment allows the Xist RNA to spread across the future inactive X chromosome, shutting down gene expression. —GR

Science, this issue p. 468

IMMUNOMETABOLISM

Metabolic support for T cell functions

For immunological T cells, responding to infections is energetically demanding. T cells rewire their metabolism so that they rely more heavily on aerobic glycolysis. This helps them to support important effector functions such as secreting the cytokine interferon γ (IFNγ). Peng *et al*. now provide insight into how aerobic glycolysis promotes T cell effector function. Activated T cells express the aerobic glycolysis–supporting enzyme lactate dehydrogenase A (LDHA), allowing these cells to maintain high amounts of acetyl–coenzyme A, which in turn promotes histone acetylation and transcription of cytokines such as IFNγ. Engineered mice whose T cells lacked LDHA were protected from IFNγ-dependent pathologies that often characterize autoinflammatory diseases. —KLM

Science, this issue p. 481

ECOLOGY

How palynology was born

Much of today's understanding of past ecosystems comes from studies of pollen in sediments, a field called palynology. In a Perspective, Birks *et al.* highlight the pioneering work of Lennart von Post, who published the first quantitative analysis of pollen. One hundred years ago, von Post showed that pollen from peat bogs in southern Sweden could be used to reconstruct postglacial vegetation changes. The work heralded a century of advances that has led to dated pollen stratigraphies from all continents. These data have, for example, helped to validate climate models. Palynology continues to play a crucial role by providing long-term overviews of ecosystems, elucidating the effects of climate and other environmental changes around the globe. —JFU

Science, this issue p. 412

RESEARCH ARTICLE

QUANTUM PHYSICS

Deterministic generation of a cluster state of entangled photons

I. Schwartz,[1]* D. Cogan,[1]* E. R. Schmidgall,[1,2] Y. Don,[1] L. Gantz,[1] O. Kenneth,[1] N. H. Lindner,[1] D. Gershoni[1]†

Photonic cluster states are a resource for quantum computation based solely on single-photon measurements. We use semiconductor quantum dots to deterministically generate long strings of polarization-entangled photons in a cluster state by periodic timed excitation of a precessing matter qubit. In each period, an entangled photon is added to the cluster state formed by the matter qubit and the previously emitted photons. In our prototype device, the qubit is the confined dark exciton, and it produces strings of hundreds of photons in which the entanglement persists over five sequential photons. The measured process map characterizing the device has a fidelity of 0.81 with that of an ideal device. Further feasible improvements of this device may reduce the resources needed for optical quantum information processing.

The concept of entanglement is a fundamental property of quantum mechanics (*1*) and an essential ingredient of proposals in the emerging technologies of quantum information processing (*2*, *3*), including quantum communication (*4*, *5*) and computation (*6*, *7*). In many cases, these applications require multipartite entanglement, encompassing a large number of quantum bits (qubits). Such entanglement is often very fragile and can be adversely affected, or even completely vanish, when one of the qubits interacts with its environment or is lost from the system. A special class of quantum states exhibits a persistence of their multipartite entanglement (*8*). The entanglement for this class of states is robust to adverse effects on a subset of the qubits. A prominent example of such a quantum state is a cluster state (*8*)—a string of mutually entangled qubits. Cluster states serve as an important resource for quantum computing, allowing its implementation solely via single-qubit measurements (*9*). A photonic implementation of cluster states enjoys many advantages, due to the noninteracting nature of photons that suppresses decoherence effects, as well as the precise single-qubit measurements provided by linear optics technology. Generating cluster states is, however, a formidable task. Previously, cluster states of finite size have been demonstrated in trapped ions (*10*, *11*) and in continuous-variable modes of squeezed light (*12*). In addition, photonic cluster states have been obtained using frequency down-conversion techniques (*13*–*16*). Despite these demonstrations, the quest for obtaining a scalable, deterministic source of cluster states is still under way. Here, we use quantum dots (QDs), "artificial atoms," which are on-demand sources of both single photons (*17*, *18*) and entangled photon pairs (*19*–*21*), to implement a scheme for deterministic generation of long strings of entangled photons in a cluster state (*22*). We demonstrate a prototype device that produces strings of a few hundred photons in which the entanglement persists over five sequential photons. Feasible improvements of the device provide a route for both determinism and scalability. Our implementation thereby forms a building block for future quantum information processing developments such as measurement-based quantum computation and quantum communication.

[1]Physics Department and Solid State Institute, Technion–Israel Institute of Technology, 32000 Haifa, Israel. [2]Department of Physics, University of Washington, Seattle, WA 98195, USA. *These authors contributed equally to this work. †Corresponding author. Email: dg@physics.technion.ac.il

Experimentally realizing a cluster state

Our implementation is based on a proposal of Lindner and Rudolph (*22*) in which repeated timed optical excitations of a confined electron in a single semiconductor QD result in the formation of a cluster state composed of the sequentially emitted single photons. The proposal uses the spin of the electron as a matter spin qubit, whose state is entangled with the polarization of the emitted photon (*19*, *23*–*26*) resulting from the optical excitation. This excitation can, in principle, be repeated indefinitely, whereas the precessing electron spin acts as an "entangler" and entangles the emitted photons to produce a one-dimensional (1D) cluster state.

We present a practical realization of this proposal, in which the QD-confined electron is replaced by a confined dark exciton (DE) (*27*–*29*). The DE is a semiconductor two-level system, effectively forming a matter spin qubit [see supplementary materials (SM) section 3 (*30*)]. The two ±2 DE spin projections on the QD symmetry axis $\hat{z}$ form a basis, $|\pm Z\rangle = |\pm 2\rangle$, for the DE space (Fig. 1, A and B). The DE energy eigenstates are $|\pm X\rangle = (|+Z\rangle \pm |-Z\rangle)/\sqrt{2}$, with an energy splitting $\Delta\varepsilon_2$ corresponding to a precession period of $T_{DE} = h/\Delta\varepsilon_2 \simeq 3$ nsec (*27*, *28*). In addition to the DE, our experiment uses two states of a biexciton (BiE)—a bound state of two excitons—whose total spin projections on $\hat{z}$ are either +3 or −3, with a precession period of $T_{BiE} = h/\Delta\varepsilon_3 \simeq 5$ nsec. We denote these states by $|\pm 3\rangle$. The experimental protocol relies on the optical transition rules $|+2\rangle \leftrightarrow |+3\rangle$ and $|-2\rangle \leftrightarrow |-3\rangle$ through right $|R\rangle$ and left $|L\rangle$ hand circularly polarized photons, respectively (*27*, *28*), in direct analogy with the original proposal (*22*). The energy-level diagram describing the DE, the BiE, and the optical transition rules is schematically summarized in Fig. 1C.

An ideal protocol for cluster-state generation

Before the protocol begins, the DE is deterministically initialized in its higher-energy spin eigenstate $|\psi_{DE}^{init}\rangle = |-X\rangle$ (*31*) by a short π-area picosecond pulse (*29*). A π-area pulse transfers the entire population from one quantum state to another.

The protocol, which begins immediately after the initialization, consists of repeated applications of a cycle. The cycle contains three elements: (i) a converting laser π-pulse, resonantly tuned to the DE-BiE optical transition. The pulse is rectilinearly horizontally $|H\rangle = (|R\rangle + |L\rangle)/\sqrt{2}$ polarized and coherently converts the DE population to a BiE population; (ii) subsequent radiative recombination of this BiE, resulting in a DE in the QD and emission of a photon; and (iii) timed free precession of the DE spin. This cycle can be applied multiple times to generate an entangled multiphoton cluster state. Figure 1D illustrates the above procedure and its equivalent circuit diagram. One full cycle of the protocol is indicated in the circuit diagram by a dashed rectangle.

The state generated by the above protocol is revealed by following the evolution of the system during the first three steps after the initialization. In step (i), the horizontally polarized π-area pulse "converts" the DE coherent state into a coherent BiE state: $|\psi_{BiE}\rangle = (|+3\rangle - |-3\rangle)/\sqrt{2}$. In step (ii), radiative recombination of this BiE results in an entangled state of the emitted photon polarization and the DE spin (*28*), $|\psi_{DE-1}\rangle = (|+Z\rangle|R_1\rangle - |-Z|L_1\rangle)/\sqrt{2}$, where $|R_1\rangle$ ($|L_1\rangle$) is the first photon right- (left-) hand circular polarization state. The excitation and subsequent photon emission are represented in Fig. 1D by a $\hat{C}_{NOT}$ gate between the DE and the emitted photon. In step (iii), the DE precesses for 3/4 of a precession period. The precession is represented in Fig. 1D by the single-qubit gate $\hat{G} = \exp(i\frac{3\pi}{4}\hat{\sigma}_x)$, where $\hat{\sigma}_x$ is the corresponding Pauli matrix. The sequential application of the $\hat{C}_{NOT}$ and $\hat{G}$ gates forms one full cycle in our protocol. In the beginning of the next cycle, the DE-photon state is given by

$$|\psi_{DE-1}\rangle = [(|+Z\rangle - i|-Z\rangle)|R_1\rangle - (|-Z\rangle - i|+Z\rangle)|L_1\rangle]/2 \quad (1)$$

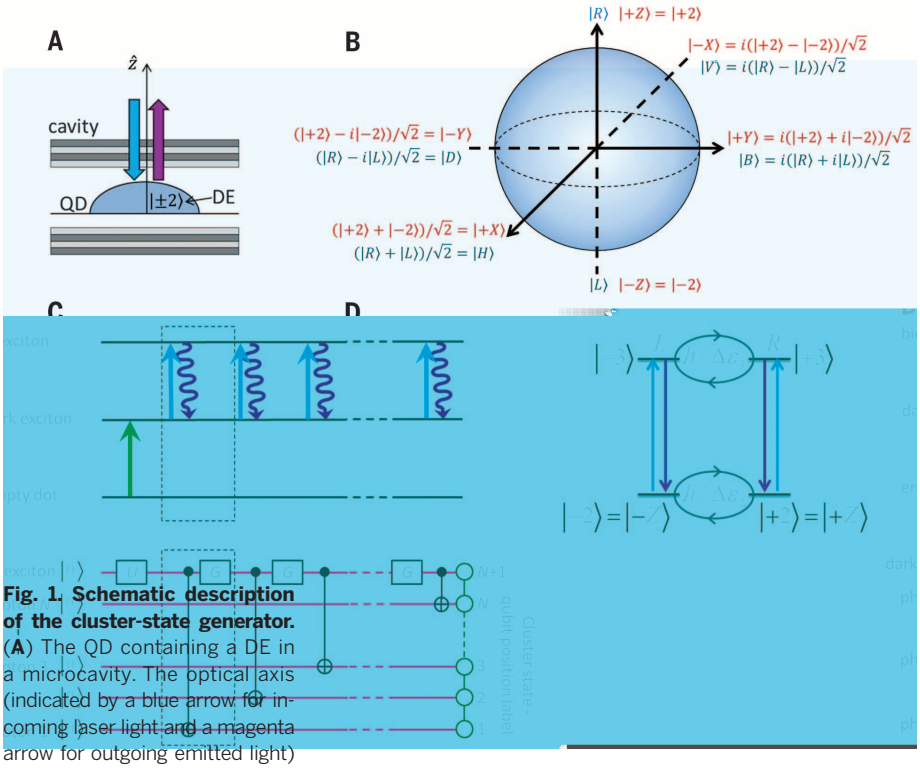

Fig. 1. Schematic description of the cluster-state generator. (**A**) The QD containing a DE in a microcavity. The optical axis (indicated by a blue arrow for incoming laser light and a magenta arrow for outgoing emitted light) is parallel to the QD symmetry axis. (**B**) Bloch sphere representation of the DE spin and photon polarization qubits. Red and blue define the bases for the DE and photon states, respectively. (**C**) The DE states ($|\pm 2\rangle = |\pm Z\rangle$), BiE states ($|\pm 3\rangle$), and optical transition rules between the states. Upward arrows represent resonant excitation. Downward arrows represent photon emission. The gray circular arrows represent precession of the DE and BiE states. (**D**) The sequence of transitions required to generate a cluster state. The green arrow represents the initialization pulse that generates a DE in spin eigenstate. Repeated timed excitations of the DE to the BiE (blue arrows) result in repeated emission of single photons (magenta arrows). Correct interpulse spacing results in an entangled cluster state. The lower panel is a circuit representation of the resulting 1D cluster state (*22*). Each horizontal line represents a qubit. The uppermost line represents the DE, and the lines below represent timed ordered emitted photons. $|0\rangle$ and $|1\rangle$ represent DE spin and photon polarization states. DE initialization is represented by the gate $\hat{U}$, and photons are initialized in the fiducial state $|0\rangle$. The timed DE precession is represented by the single-qubit gate $\hat{G}$, and excitation-emission is represented by a $\hat{C}_{NOT}$ gate (vertical line) between the DE and the emitted photon. The area enclosed in the dashed box represents one unitary cycle in the ideal protocol.

The above cycle is now repeated: reexcitation (*27*, *28*) to the BiE state, recombination of the second BiE, and timed precession associated with the $\hat{G}$ gate. This results in a second photon, whose polarization state is entangled with that of the first photon and the spin of the remaining DE, yielding the tripartite state

$$|\psi_{DE-2-1}\rangle = (|+Z\rangle[(|R_2\rangle - |L_2\rangle)|R_1\rangle + i(|R_2\rangle + |L_2\rangle)|L_1\rangle] + |-Z\rangle[-i(|R_2\rangle + |L_2\rangle)|R_1\rangle + (|R_2\rangle - |L_2\rangle)|L_1\rangle])/2\sqrt{2} \quad (2)$$

Repetition of the reexcitation-emission and subsequent precession cycle generates a 1D string of polarization-entangled photons in a cluster state, as shown in the equivalent circuit diagram of Fig. 1D. We have realized the above protocol in which the cycles were implemented with fidelity of 0.81 to the ideal cycle described above.

Considerations in practical realizations of the protocol using the dark exciton as entangler

The DE has many advantages as an entangler for sequential generation of entangled photons. It exhibits a long lifetime (~1000 nsec) and a long coherence time ($T_2^* \sim 100$ nsec) (*28*). In addition, the DE spin state can be deterministically written in a coherent state using one single short optical pulse (*28*, *29*) and can be reset (i.e., emptied from the QD) using fast all-optical means (*32*). Furthermore, the DE to BiE excitation resonance occurs at a higher energy than the BiE to DE main emission resonance (SM, section 3), thereby facilitating accurate background-free single-photon detection. In addition, the generated cluster state is unaffected by the coherence of the photons' wave packets (*22*).

Despite these advantages, several types of imperfections must be considered. The dominant imperfection originates from the finite BiE radiative lifetime, $t_{rad} \simeq 0.33$ nsec (*28*). Because the DE and BiE precess during the emission process, the purity of the polarization state of the photons is reduced (*22*). Another type of imperfection is the decoherence of the DE spin during its precession, resulting from the hyperfine interaction between the DE and nuclear spins in the semiconductor (*22*). Therefore, to ensure generation of a high-quality cluster state, three important parameters should be kept small: the ratio between the BiE radiative time t_{rad} and the DE and BiE precession times T_{DE} and T_{BiE}, and the ratio between the DE precession time and its decoherence time T_2^*. In our system, $t_{rad}/T_{DE} \sim t_{rad}/T_{BiE} \sim 0.1$ and $T_{DE}/T_2^* \sim 0.04$. Because all these parameters are much less than unity, the implemented protocol has high fidelity to the ideal one, as we now show.

Demonstrating an entangled cluster state

The demonstration that our device generates an entangled multiphoton cluster state is done in two complementary steps. First, we determine the nonunitary process map acting in each cycle of the protocol, which replaces the $\hat{C}_{NOT}$ and $\hat{G}$ unitary gates of Fig. 1D. The process map is a linear map from the initial DE qubit's space to the space of two qubits comprising the DE and the newly emitted photon. It fully characterizes the evolution of the system in each cycle of the protocol, thereby completely determining the multiphoton state after any given number of cycles. Then, we verify that the three-qubit state, consisting of the DE and two sequentially emitted photons, generated by applying two cycles of our protocol is a genuine three-qubit entangled state. We also quantify the degree of entanglement between each of the three pairs of qubits.

To measure the process map, we perform quantum process tomography. We first initialize the DE in four different states, $|\psi_{DE}^{init}\rangle = |+X\rangle$, $|-X\rangle$, $|-Y\rangle$, and $|+Z\rangle$. The states are defined in Fig. 1B. In reality, the initialization is in a partially mixed state (SM, section 4). For each DE initialization, we apply one cycle of the protocol and perform correlation measurements between the resulting emitted photon polarization and the DE spin. In these correlation measurements, we project the emitted photon on the polarization states $|H\rangle$, $|V\rangle$, $|D\rangle$, and $|R\rangle$, while making projective measurements of the DE's spin state. For the DE projective measurements, we apply either a right- or a left-hand circularly polarized π-area pulse at the end of the cycle. Due to the optical selection rules (Fig. 1C), this pulse deterministically excites either the $|+Z\rangle$ or the $|-Z\rangle$ DE to the BiE, respectively. Detection of an emitted photon after this excitation projects the DE spin on the states $|+Z\rangle$ or $|-Z\rangle$ at the time of the pulse. To project the DE onto the spin states $|-Y\rangle$ or $|+Y\rangle$ at the end of the cycle, we rotate the DE state by delaying the pulse a quarter of a precession

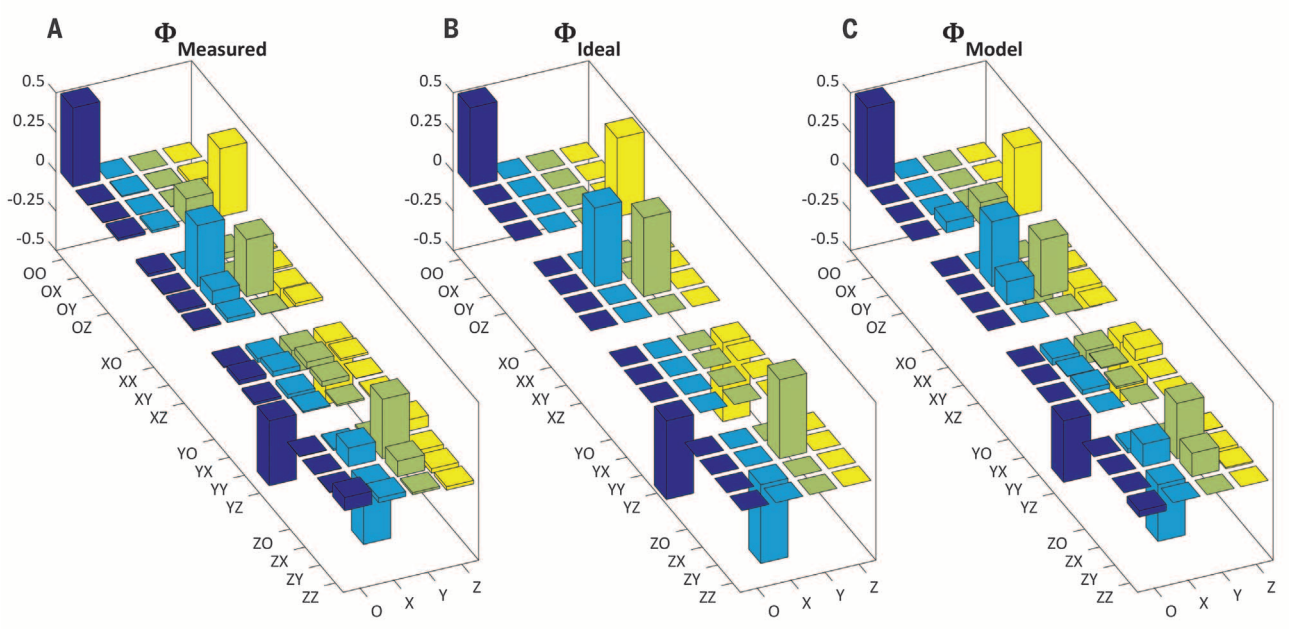

Fig. 2. The process map. The process map Φ, which describes the evolution of the system in each cycle of the protocol, is a completely positive and trace-preserving map from the DE one-qubit space to the two-qubit space composed of the DE and the emitted photon. The process map acts trivially on all other photons in the state. We use the convention $\Phi(\hat{\rho}^{(\mathrm{DE})}) = \sum_{\alpha\beta\gamma} \Phi^{\gamma}_{\alpha\beta} \rho^{(\mathrm{DE})}_{\gamma} \hat{\sigma}_{\alpha} \hat{\sigma}_{\beta}$, where $\hat{\rho}^{(\mathrm{DE})} = \sum_{\gamma} \rho^{(\mathrm{DE})}_{\gamma} \hat{\sigma}_{\gamma}$ is the density matrix that describes the DE state. The sums are taken over $\alpha, \beta, \gamma = 0, x, y, z$, where $\hat{\sigma}_0$ is the identity matrix and $\hat{\sigma}_{x,y,z}$ are the corresponding Pauli matrices. The 64 real parameters $\phi^{\gamma}_{\alpha\beta}$ thus fully specify ϕ. (**A**) The process map as measured by quantum process tomography. The values of $\Phi^{\gamma}_{\alpha\beta}$, are presented such that the rows correspond to the indices $\alpha\beta$ and the columns correspond to the index γ. (**B**) The unitary process map corresponding to the ideal protocol as in Fig. 1D. (**C**) The process map as calculated from a theoretical model with independently measured parameters (SM, section 5).

period. This method allows us to project the DE on the states $|\pm Z\rangle$ and $|\pm Y\rangle$ but not on the $|\pm X\rangle$ states. Therefore, by the above two-photon correlation measurements, we directly measure only 48 out of the required 64 process map matrix elements.

To complete the quantum process tomography, we use three-photon correlation measurements. For each of the four initializations of the DE, we apply two cycles of the protocol. We then perform full polarization state tomography between the resulted two emitted photons, while projecting the spin of the remaining DE on $|\pm Z\rangle$ and $|\mp Y\rangle$, as discussed above. The two- and three-photon correlations, which together uniquely determine all the 64 matrix elements of the process map, are fully described in sections 7 and 8 of the SM.

In Fig. 2A, we present the measured process map, and in Fig. 2B, we present the process map corresponding to the ideal protocol. The fidelity (see SM, section 10, for definition) between the measured and ideal process map is 0.81 ± 0.1. Figure 2C gives the process map obtained by modeling the evolution of the system using a master equation approach with independently measured system parameters (SM, section 5). The fidelity between the model and the measured process map is 0.92 ± 0.1. These fidelities indicate that our device is capable of deterministically generating photonic cluster states of high quality, thus providing a new resource for quantum information processing.

Using the measured process map, we can now describe the state $\hat{\rho}_{N+1}$, consisting of the DE and N photons, following successive applications of N protocol cycles. An important method to quantify the multipartite entanglement in $\hat{\rho}_{N+1}$ is to consider the maximal degree of entanglement between two chosen qubits once the rest of the qubits are measured. The resulting quantity is referred to as the localizable entanglement (LE) between the two chosen qubits (*33*). In an ideal cluster state, the localizable entanglement is maximal: Any two qubits can be projected into a maximally entangled state by measuring the rest of the qubits. For example, consider the three-qubit state described by Eq. 2. By projecting the DE on the $|+Z\rangle$ state, we obtain two photons in the maximally entangled state

$$|\psi_{2\text{-}1}\rangle = [(|R_2\rangle - |L_2\rangle)|R_1\rangle + i(|L_2\rangle + |R_2\rangle)|L_1\rangle]/2 = (|V_2\rangle R_1\rangle - |H_2\rangle|L_1\rangle)/\sqrt{2}i \quad (3)$$

To compute the LE between two qubits in the state $\hat{\rho}_{N+1}$, we obtain their reduced density matrix after the rest of the qubits have been measured in an optimized basis. The degree of entanglement between the two qubits is then evaluated by a standard measure: the negativity (*34*) $\mathcal{N}$ of their reduced density matrix. $\mathcal{N}$ is defined as the magnitude of the negative eigenvalue of the partially transposed density matrix. For $\mathcal{N} \geq 0$ the qubits are entangled, and $\mathcal{N} = \frac{1}{2}$ corresponds to maximally entangled qubits. Full definitions for the negativity and LE are given in the SM, section 6.

In Fig. 3, we plot using blue circles the LE in the state $\hat{\rho}_{N+1}$, obtained from the measured process map, as a function of the distance between two qubits in the string. As expected, the LE in the 1D state $\hat{\rho}_{N+1}$ decays exponentially with the distance between the chosen two qubits (*33*). The LE, which characterizes the robustness of the multipartite entanglement in the state produced by our device, is shown to persist up to five qubits.

Next, we used the measured correlations to directly obtain the LE between the different qubits. First, we consider the entanglement between the DE and the emitted photon after one application of the cycle. Using the first set of DE-photon correlation measurements, we obtain a lower bound of $\mathcal{N} \geq 0.20 \pm 0.04$ for the negativity of their density matrix. The obtained lower bound is marked as an orange data point in Fig. 3. Second, we consider the three-qubit state obtained after two applications of the protocol (comprising the DE and the two emitted photons). We measure the density matrix of the two emitted photons, while projecting the DE on the state $|+Z\rangle$. The negativity of this measured density matrix, $\mathcal{N} = 0.24 \pm 0.05$, is marked by the yellow data point in Fig. 3. The measured density matrix has fidelity of 0.73 ± 0.06, with the maximally

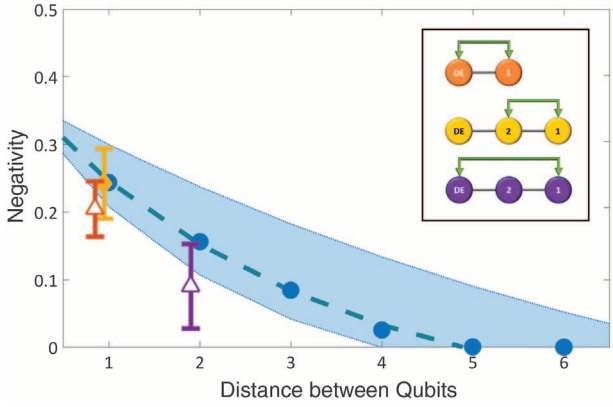

Fig. 3. The localizable entanglement in the generated state. The horizontal axis indicates the distance d between two qubits in the string (the qubits are ordered according to the labeling convention in Fig. 1D), and the vertical axis corresponds to the negativity of the reduced density matrix of the two qubits. The blue circles correspond to the LE between qubits m and $m + d$ ($\mathcal{N}^{LE}_{m,m+d}$) in the state $\hat{\rho}_{N+1}$ obtained using the measured process map (SM, section 6). Here, we use $m = 1$ and $d = N$, but other values for m and $d \le N + 1 - m$ yield similar results. The dashed lines represent the best fit to an exponential decay law, $\mathcal{N}^{LE}_{m=1,m+d} = \mathcal{N}_0 \exp[-(d-1)/\xi_{LE}]$ (SM, section 7). The blue shaded area represents mean ± 1 SD uncertainty in the measurements determining the process map. The yellow data point represents the directly measured LE between the two photons in a three-qubit string. The orange and purple data points describe a lower bound on the LE between the DE and the first emitted photon in a two- and a three-qubit string, respectively. The color-coded inset describes the configuration of qubits for each measured data point. To obtain the orange (purple) data points, we project the DE (second photon) on the state $|Z\rangle$ ($e^{i(0.1)\hat{\sigma}_z}|V\rangle$).

entangled state expected from the ideal case as given by Eq. 3. Note the good agreement between the LE obtained directly and the one obtained using the process map. Third, a lower bound on the LE between the DE and the first emitted photon, when the second emitted photon is projected on the optimized state $e^{i(0.1)\hat{\sigma}_z}|V\rangle$, is extracted from our three-photon correlations. The value of this lower bound, $\mathcal{N} \ge 0.09 \pm 0.06$, is marked in purple in Fig. 3. The full set of measurements leading to the above values of $\mathcal{N}$ is given in the SM, section 8.

Finally, we use the DE-photon-photon correlation measurements to directly verify that the three-qubit state generated by our device exhibits genuine three-qubit entanglement (*26*). Because we did not project the DE spin on the $|\pm X\rangle$ states, the density matrix of the three qubits cannot be fully reconstructed (*23*–*25*). However, our measurements are sufficient to obtain bounds for the fidelity between the three-qubit state $\hat{\rho}_3$ produced by our device and the three-qubit pure cluster state $|\psi\rangle$ of Eq. 2, expected from the ideal process map. The value $\mathcal{F} = \langle\psi|\hat{\rho}_3|\psi\rangle$ that we obtain is $0.54 \le \mathcal{F} \le 0.69$. The threshold for genuine three-qubit entanglement (*35*) is $\mathcal{F} > 1/2$. The experimentally measured lower bound on $\mathcal{F}$ is larger by more than 1 SD of the experimental uncertainty from this threshold. For full details on the calculation of $\mathcal{F}$, see the SM, section 9.

Both the quality of the state produced by our device and the correlation measurements can be improved. Our demonstration and analysis are based on high-repetition-rate (76 MHz) deterministic writing of the DE entangler and on time-tagged three-photon correlation measurements. Direct measurements of higher multiphoton correlations are very challenging in the current experimental setup, due to its limited light harvesting efficiency, where only about 1 in 700 photons are detected (SM, section 4). The limitation is mainly due to the low quantum efficiency of single-photon silicon avalanche photodetectors (<20%) and the low light collection efficiency from the planar microcavity (<20%). Both can, in principle, be considerably improved [see (*36*) and (*20*), respectively]. In addition, the current length scale of the LE is mainly limited by the radiative lifetime of the BiE. This lifetime can be considerably shortened by designing an optical cavity to increase the Purcell factor of the device (*20*) for this particular transition only.

Concluding remarks

We provide an experimental demonstration of a prototype device for generating on-demand 1D photonic cluster states (*22*). The device is based on a semiconductor QD and uses the spin of the DE as an entangler. Our prototype device can produce strings of a few hundred photons in which the localizable entanglement persists over five sequential photons. Further feasible optimizations of our device can enable faster and longer on-demand generation of higher-fidelity cluster states. Additionally, by using two nonidentical coupled QDs, it is possible to generate a 2D cluster state in a similar and scalable manner (*37*). A 2D cluster state carries a promise for robust implementation of measurement-based quantum computation (*38*). These may propel substantial technological advances, possibly bringing practical, widespread implementations of quantum information processing closer.

REFERENCES AND NOTES

1. A. Aspect, J. Dalibard, G. Roger, *Phys. Rev. Lett.* **49**, 1804–1807 (1982).
2. T. D. Ladd *et al.*, *Nature* **464**, 45–53 (2010).
3. H. J. Kimble, *Nature* **453**, 1023–1030 (2008).
4. M. Żukowski, A. Zeilinger, M. A. Horne, A. K. Ekert, *Phys. Rev. Lett.* **71**, 4287–4290 (1993).
5. H. J. Briegel, W. Dür, J. I. Cirac, P. Zoller, *Phys. Rev. Lett.* **81**, 5932–5935 (1998).
6. P. Shor, *Proceedings of the 35th Annual Symposium on the Foundations of Computer Science* (1994), pp. 124–134.
7. L. K. Grover, *Proceedings of the 28th Annual ACM Symposium on the Theory of Computing* (1996), p. 212.
8. H. J. Briegel, R. Raussendorf, *Phys. Rev. Lett.* **86**, 910–913 (2001).
9. R. Raussendorf, D. E. Browne, H. J. Briegel, *Phys. Rev. A* **68**, 022312 (2003).
10. O. Mandel *et al.*, *Nature* **425**, 937–940 (2003).
11. B. P. Lanyon *et al.*, *Phys. Rev. Lett.* **111**, 210501 (2013).
12. S. Yokoyama *et al.*, *Nat. Photonics* **7**, 982–986 (2013).
13. P. Walther *et al.*, *Nature* **434**, 169–176 (2005).
14. R. Prevedel *et al.*, *Nature* **445**, 65–69 (2007).
15. Y. Tokunaga, S. Kuwashiro, T. Yamamoto, M. Koashi, N. Imoto, *Phys. Rev. Lett.* **100**, 210501 (2008).
16. C.-Y. Lu *et al.*, *Nat. Phys.* **3**, 91–95 (2007).
17. E. Dekel, D. Gershoni, E. Ehrenfreund, J. M. Garcia, P. M. Petroff, *Phys. Rev. B* **61**, 11009–11020 (2000).
18. P. Michler *et al.*, *Science* **290**, 2282–2285 (2000).
19. N. Akopian *et al.*, *Phys. Rev. Lett.* **96**, 130501 (2006).
20. A. Dousse *et al.*, *Nature* **466**, 217–220 (2010).
21. M. Müller, S. Bounouar, K. D. Jons, M. Glassl, P. Michler, *Nat. Photonics* **8**, 224–228 (2014).
22. N. H. Lindner, T. Rudolph, *Phys. Rev. Lett.* **103**, 113602 (2009).
23. W. B. Gao, P. Fallahi, E. Togan, J. Miguel-Sanchez, A. Imamoglu, *Nature* **491**, 426–430 (2012).
24. K. De Greve *et al.*, *Nature* **491**, 421–425 (2012).
25. J. R. Schaibley *et al.*, *Phys. Rev. Lett.* **110**, 167401 (2013).
26. A. Reiserer, N. Kalb, G. Rempe, S. Ritter, *Nature* **508**, 237–240 (2014).
27. E. Poem *et al.*, *Nat. Phys.* **6**, 993–997 (2010).
28. I. Schwartz *et al.*, *Phys. Rev. X* **5**, 011009 (2015).
29. I. Schwartz *et al.*, *Phys. Rev. B* **92**, 201201 (2015).
30. Materials and methods are available as supplementary materials on *Science* Online.
31. Identical conclusions are obtained if the higher energy DE eigenstate is the $|+X\rangle$ state (*28*).
32. E. R. Schmidgall *et al.*, *Appl. Phys. Lett.* **106**, 193101 (2015).
33. M. Popp, F. Verstraete, M. A. Martín-Delgado, J. I. Cirac, *Phys. Rev. A* **71**, 042306 (2005).
34. A. Peres, *Phys. Rev. Lett.* **77**, 1413–1415 (1996).
35. G. Tóth, O. Gühne, *Phys. Rev. A* **72**, 022340 (2005).
36. F. Marsili *et al.*, *Nat. Photonics* **7**, 210–214 (2013).
37. S. E. Economou, N. Lindner, T. Rudolph, *Phys. Rev. Lett.* **105**, 093601 (2010).
38. R. Raussendorf, J. Harrington, *Phys. Rev. Lett.* **98**, 190504 (2007).

ACKNOWLEDGMENTS

We are grateful to P. Petroff for the sample growth and to T. Rudolph and J. Avron for useful discussions. The support of the Israeli Science Foundation (ISF), the Technion's RBNI, and the Israeli Nanotechnology Focal Technology Area on Nanophotonics for Detection is gratefully acknowledged. This project has received funding from the European Research Council (ERC) under the European Union's Horizon 2020 research and innovation program (grant agreement No 695188).The authors declare that they have no competing financial interests. The relevant data appear in this Research Article and in its supplementary materials.

SUPPLEMENTARY MATERIALS

www.sciencemag.org/content/354/6311/434/suppl/DC1
Materials and Methods
Figs. S1 to S9
Tables S1 and S2
References (*39*–*54*)

1 July 2016; accepted 30 August 2016
Published online 8 September 2016
10.1126/science.aah4758

REPORTS

IMPACT CRATERS

Gravity field of the Orientale basin from the Gravity Recovery and Interior Laboratory Mission

Maria T. Zuber,[1]* David E. Smith,[1] Gregory A. Neumann,[2] Sander Goossens,[3] Jeffrey C. Andrews-Hanna,[4,5] James W. Head,[6] Walter S. Kiefer,[7] Sami W. Asmar,[8] Alexander S. Konopliv,[8] Frank G. Lemoine,[2] Isamu Matsuyama,[9] H. Jay Melosh,[10] Patrick J. McGovern,[7] Francis Nimmo,[11] Roger J. Phillips,[5] Sean C. Solomon,[12,13] G. Jeffrey Taylor,[14] Michael M. Watkins,[8,15] Mark A. Wieczorek,[16] James G. Williams,[8] Johanna C. Jansen,[4] Brandon C. Johnson,[1,6] James T. Keane,[9] Erwan Mazarico,[2] Katarina Miljković,[1,17] Ryan S. Park,[8] Jason M. Soderblom,[1] Dah-Ning Yuan[8]

The Orientale basin is the youngest and best-preserved major impact structure on the Moon. We used the Gravity Recovery and Interior Laboratory (GRAIL) spacecraft to investigate the gravitational field of Orientale at 3- to 5-kilometer (km) horizontal resolution. A volume of at least (3.4 ± 0.2) × 10^6 km^3 of crustal material was removed and redistributed during basin formation. There is no preserved evidence of the transient crater that would reveal the basin's maximum volume, but its diameter may now be inferred to be between 320 and 460 km. The gravity field resolves distinctive structures of Orientale's three rings and suggests the presence of faults associated with the outer two that penetrate to the mantle. The crustal structure of Orientale provides constraints on the formation of multiring basins.

Basin-scale impacts disrupted early planetary crusts and imparted substantial kinetic energy that led to fracturing, melting, vaporization, seismic shaking, ejection, and redistribution of crustal and possibly mantle material. Impact basins preserve the record of these planet-altering events, and the study of these structures elucidates the partitioning of energy and its corresponding geological and environmental effects early in planetary history. Surface signatures of impact basins on solid planets have been extensively documented (*1*, *2*), but their subsurface structure has, to date, been poorly characterized. We present a high-resolution orbital gravity field model of the Orientale basin on the Moon as mapped by the Gravity Recovery and Interior Laboratory (GRAIL) mission (*3*).

Orientale, located on the southwestern limb of the lunar nearside, is the youngest (~3.8 billion years old) (*1*, *4*) large (~930-km diameter) impact basin on the Moon. As a consequence of its good state of preservation (*1*, *5*), with relatively few superposed large craters (*6*), it is often considered the standard example of a well-preserved, multiring basin in comparative studies of large impacts on terrestrial planetary bodies (*2*, *7*). Because of the basin's importance, the GRAIL Extended Mission (see the supplementary text) featured a low-altitude mapping campaign during the mission's Endgame phase (*8*), in which the dual spacecraft orbited the Moon at an average altitude of 6 km and acquired observations less than 2 km above the basin's eastern rings (figs. S1 and S2).

To produce the highest-resolution gravity map achievable from the data and to ensure that small-scale features resolved were robust, we developed two maps that used the same data but independent methodologies (*9*). The first is derived from a global spherical harmonic expansion of GRAIL's Ka-band (32 GHz) range-rate (KBRR) tracking data to degree and order 1200 (spatial block size = 4.5 km). The second is from a local model that implemented a short-arc analysis (*10*) of the tracking data and used a gravitational field model to degree and order 900 (*11*) as the a priori field. Local gravitational anomalies were estimated with respect to the spherical harmonic model at the center coordinates of a set of grid points. The final model has a mixed-grid resolution of 0.1° by 0.1° and 0.1667° by 0.1667°, corresponding to a maximum spatial resolution varying between 3 and 5 km. These independent analyses produced gravitational models of Orientale that are essentially indistinguishable (see fig. S4). The maps are shown in Fig. 1; they resolve the shallow subsurface structure of Orientale at a spatial resolution comparable to that of many geological structures at the surface, including simple and secondary craters.

The topography of the Orientale basin (*12*) from the Lunar Orbiter Laser Altimeter (*13*) and the free-air gravity anomaly field of the region are shown in Fig. 1, A and B. The maps show similar detail at small spatial scales because above degree and order 80 (spatial block size <68 km), more than 98% of the lunar gravity field is attributable to topography (*14*). The high correlation of topography and gravity at short horizontal scales is due to the large magnitude of the gravity anomalies arising from topography relative to the weaker anomalies attributable to density anomalies in the shallow subsurface (*14*).

Both topography and free-air gravity anomaly resolve Orientale's Inner Depression, as well as the Inner Rook ring, Outer Rook ring, and Cordillera ring (see Fig. 1). The rings, which were only partially resolved in pre-GRAIL gravitational models (*15*), formed in the process of cavity collapse during the modification stage of the impact event, within an hour of the initiation of basin formation (*16*). The mechanism for ring formation, however, has been controversial (*2*, *5*, *17*–*19*), in large part because of a lack of understanding of subsurface structure needed to provide constraints on impact basin formation models.

Variations in subsurface mass are best revealed in the Bouguer gravity anomaly field (Fig. 1C), a representation of the gravitational field after the attraction of surface topography has been removed. Determination of crustal structure requires careful consideration of likely crustal and mantle composition (supplementary text). For uniform-density crust and mantle [2550 and 3220 kg m^{-3}, respectively (*20*)], the Bouguer gravity anomaly can be used to map the crust-mantle boundary and thus crustal thickness (Fig. 1D and fig. S5). Although the assumption of uniform density is an approximation, its application to the regional crustal structure is supported by crustal density inferred from GRAIL (*20*), as well as from orbital remote sensing data (supplementary text and fig. S6). Some models for the crust invoke a mixed feldspathic layer that overlies a layer of pure anorthosite (*21*), but the density contrast between these rock types is small in comparison with that across the crust-mantle interface. In the mantle, there is likely a pronounced

[1]Department of Earth, Atmospheric and Planetary Sciences, Massachusetts Institute of Technology, Cambridge, MA 02139-4307, USA. [2]Solar System Exploration Division, NASA Goddard Space Flight Center, Greenbelt, MD 20771, USA. [3]Center for Research and Exploration in Space Science and Technology, University of Maryland, Baltimore County, Baltimore, MD 21250, USA. [4]Department of Geophysics and Center for Space Resources, Colorado School of Mines, Golden, CO 80401, USA. [5]Southwest Research Institute, Boulder, CO 80302, USA. [6]Department of Earth, Environmental and Planetary Sciences, Brown University, Providence, RI 02912, USA. [7]Lunar and Planetary Institute, Houston, TX 77058, USA. [8]Jet Propulsion Laboratory, Pasadena, CA 91109, USA. [9]Lunar and Planetary Laboratory, University of Arizona, Tucson, AZ 85721-0092, USA. [10]Department of Earth, Atmospheric, and Planetary Sciences, Purdue University, West Lafayette, IN 47907, USA. [11]Department of Earth and Planetary Sciences, University of California, Santa Cruz, Santa Cruz, CA 95064, USA. [12]Department of Terrestrial Magnetism, Carnegie Institution of Washington, Washington, DC 20015, USA. [13]Lamont-Doherty Earth Observatory, Columbia University, Palisades, NY 10964, USA. [14]Hawaii Institute of Geophysics and Planetology, University of Hawaii, Honolulu, HI 96822, USA. [15]Center for Space Research, University of Texas, Austin, TX 78712 USA. [16]Institut de Physique du Globe de Paris, Sorbonne Paris Cité, Université Paris Diderot, 75205 Paris Cedex 13, France. [17]Department of Applied Geology, Curtin University, Perth, Western Australia 6845, Australia.
*Corresponding author. Email: zuber@mit.edu

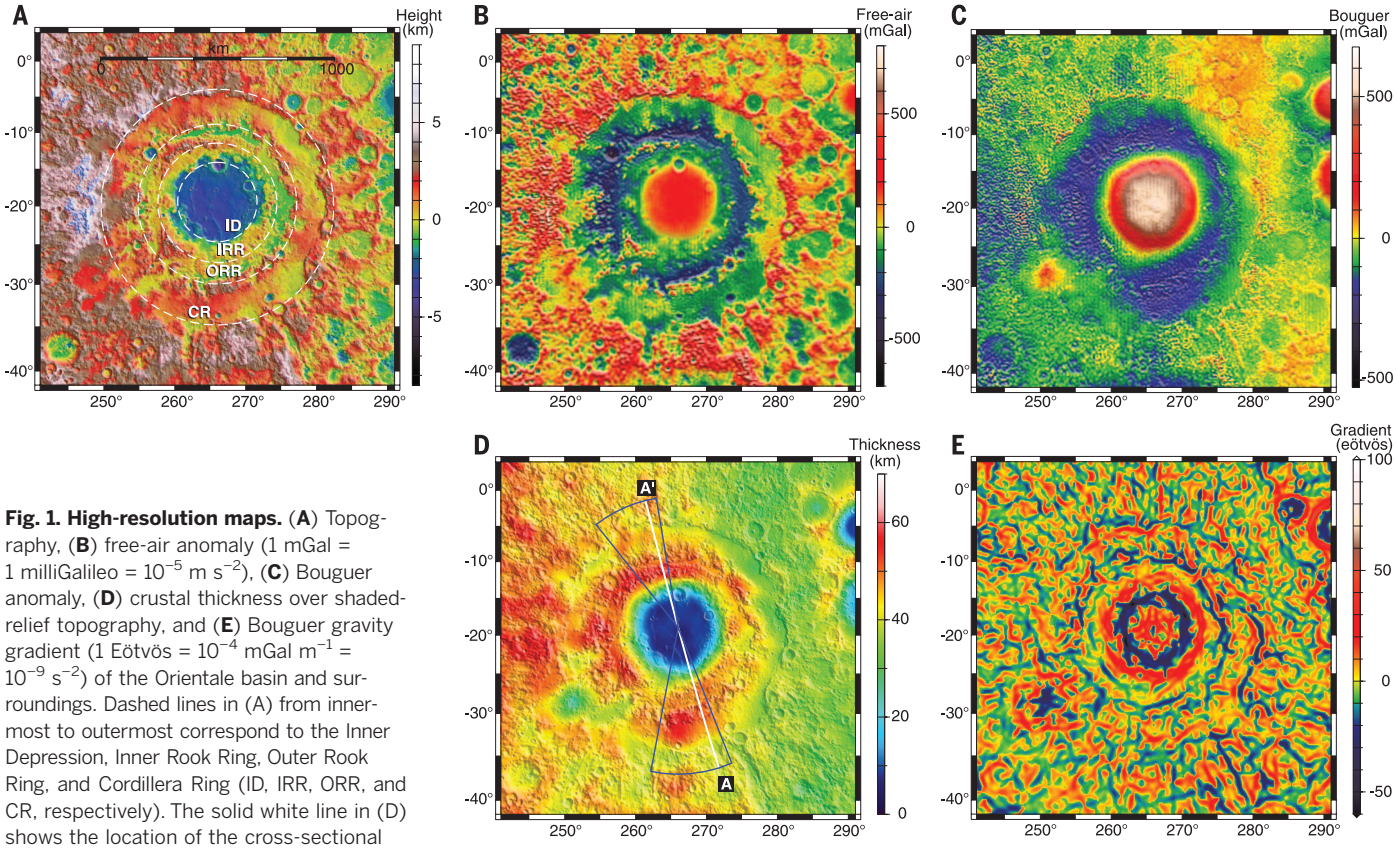

Fig. 1. High-resolution maps. (**A**) Topography, (**B**) free-air anomaly (1 mGal = 1 milliGalileo = 10^{-5} m s^{-2}), (**C**) Bouguer anomaly, (**D**) crustal thickness over shaded-relief topography, and (**E**) Bouguer gravity gradient (1 Eötvös = 10^{-4} mGal m^{-1} = 10^{-9} s^{-2}) of the Orientale basin and surroundings. Dashed lines in (A) from innermost to outermost correspond to the Inner Depression, Inner Rook Ring, Outer Rook Ring, and Cordillera Ring (ID, IRR, ORR, and CR, respectively). The solid white line in (D) shows the location of the cross-sectional profile A–A′ in Fig. 2A. Blue lines show the locations of the azimuthally averaged cross sections in Fig. 2B. Topography is updated from Lunar Orbiter Laser Altimeter (LOLA) (*12*) map LDEM_64, 0.015625° spatial resolution. To highlight short-wavelength structure, we have subtracted spherical harmonic degrees and orders less than 6 from the Bouguer gravity field. Calculation of crustal thickness and Bouguer gravity gradient is discussed in the supplementary materials (*9*).

seismic discontinuity at 500- to 600-km depth, about the scale of Orientale, marking a change in mantle composition and hence density (*22*); lateral variations in this depth will contribute to the Bouguer signal. However, the density contrast is provided by a change in mafic mineralogy and is small compared with the density change at the crust-mantle boundary. Furthermore, the signal is attenuated to the extent that only the broadest length scales of the crustal model might be affected.

A cross section of crustal structure along the profile in Fig. 1D is shown in Fig. 2. Crust-mantle boundary profiles take into account the effect on the crustal structure of a 10-km-thick sheet of density 2650 kg m^{-3} confined to the inner depression to represent solidified impact melt or crustal material formed by differentiation of Orientale's melt pool (*9*); in the end-member case, in which the sheet is instead identical in density to feldspathic crust, the minimum crustal thickness would be only 2 km less. Consequently, the presence of a high-density sheet does not have a substantial effect on the basin's crustal structure. Figure 1D indicates that the Orientale impact removed and redistributed a minimum of (3.4 ± 0.2) × 10^6 km^3 of material (*9*) from the lunar crust. Approximately one-third of the excavated material was deposited as ejecta in an annulus between the Cordillera ring and a radial distance from the basin center of one basin diameter (*23*), contributing to enhanced crustal thickness in this region (Fig. 1D). The high porosity (~18%) inferred in the Orientale ejecta blanket (*20*, *24*) is similar to the porosity observed in Apollo 14 samples of the Fra Mauro Formation, which consist of ejecta from the Imbrium basin (*25*).

The calculation of crustal thickness does not include the presence of the mare units that are generally less than 1 km thick and irregularly distributed within the Inner Depression and ponded irregularly inside the Outer Rook and Cordillera rings (*21*) (low-reflectance areas in fig. S7). The gravitational signal of the mare units is partially masked by the unknown characteristics of the impact melt sheet, and where these deposits are present, the underlying crustal thickness would be slightly greater than in the model.

Pre-GRAIL gravitational models have shown that the most distinct, well-preserved, large-scale gravitational signature associated with large lunar basins is a strong central positive free-air anomaly (*26*–*29*). These mass excesses, or mascons (*30*), are a consequence of the thinning of the crust beneath the basin combined with mantle rebound and subsequent isostatic uplift of the central basin that was mechanically coupled to surrounding crust (*31*, *32*). Figures 1 and 2 show that in Orientale, the diameter of crustal thinning corresponds closely to the diameter of the Inner Depression. We therefore identify the Inner Depression as an approximation to the basin excavation cavity—i.e., the region in which the crust was thinned from its pre-impact state (*21*).

Of interest in impact studies is the transient crater—the cavity formed at the culmination of excavation, before collapse and modification. The transient crater corresponds to the maximum displaced volume, and its diameter satisfies standard impact scaling laws (*33*, *34*), which allow many characteristics of an impact to be inferred from its size. Although there is general recognition that the transient crater should not be preserved, each of Orientale's basin rings has been variously interpreted as marking the diameter of the transient crater (*2*, *5*, *17*, *18*, *35*). GRAIL's improved spatial resolution and signal sensitivity show no evidence of the transient crater, indicating that any remnant is not preserved or at least not recognizable in the gravity field. However, the transient crater diameter may now be calculated with confidence from scaling laws (*36*). From the 530-km diameter of the annular maximum in crustal thickness (Fig. 1D), measured from an azimuthally averaged crustal

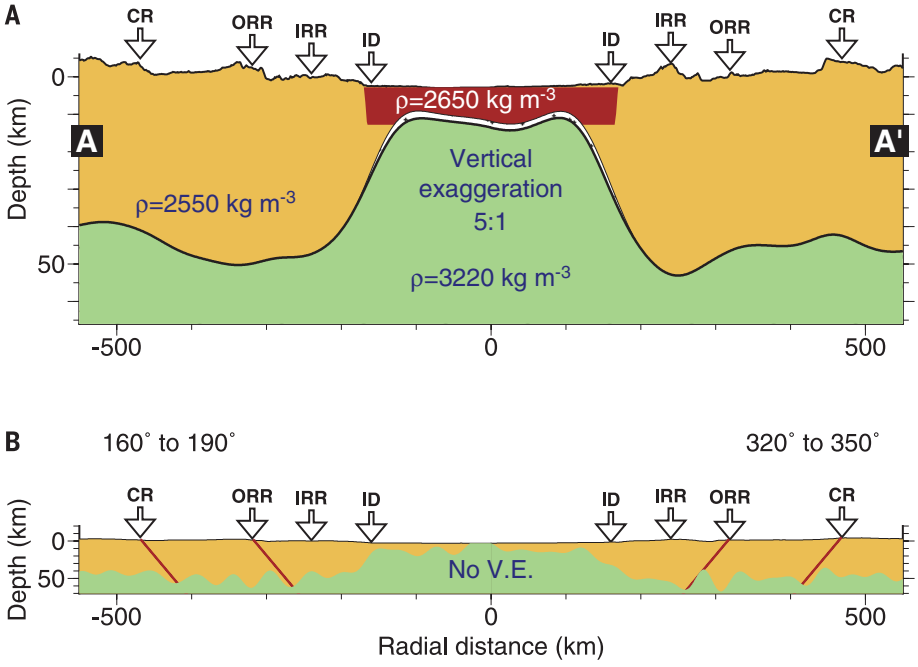

Fig. 2. Crustal cross section. (**A**) Subsurface structure of the Orientale basin along the profile shown in Fig. 1D, from southeast to northwest. Crust is shown as tan, melt sheet as red, and mantle as green. Arrows above the cross section denote, inward to outward, Orientale's ID, IRR, ORR, and CR. The heavy solid line indicates the base of the crust in the presence of a melt sheet that is 10 km thick, 350 km in diameter, and 2650 kg m^{-3} in density; the thin solid line indicates the base of the crust if the melt-sheet density is identical to that of the crust. Vertical exaggeration (V.E.) is 5:1. (**B**) As in (A), with no vertical exaggeration and filter for downward continuation (*9*) having higher resolution by a factor of 3; the profile is azimuthally averaged in sectors (azimuth measured clockwise from north; see Fig. 1D) to suppress noise. Red lines give the locations of proposed faults dipping inward at 50° dip angle from the nominal surface positions of the ORR and CR. Other variations in crust-mantle boundary depth suggest the presence of additional faults.

thickness profile (fig. S5), the transient crater diameter is between 320 and 460 km, placing it between the diameters of Orientale's Inner Depression and Inner Rook ring. The transient crater thus does not correspond to a specific ring; indeed, hydrocode modeling constrained by this crustal structure model (*16*) indicates that rings form subsequent to the transient crater, during the collapse phase.

The transition between the basin excavation cavity and the surrounding crust is well illustrated in Fig. 2. At the outer edges of the zone of mantle uplift, the crust-mantle boundary slopes outward and downward by at least 20° to 25°. The spatial correspondence of this plug of uplifted mantle with the Inner Depression is similar to the pattern seen in other multiring basins (*37*), but it is in contrast to peak-ring basins, where the zone of uplifted mantle is limited to the area within the peak ring.

The model also shows, beyond the basin depression, an annulus of thickened crust (Fig. 1D and fig. S8D), as well as radial structure in gravity gradients (Fig. 1E and fig. S8E) that locally correlates with observed ejecta structures (e.g., secondary crater chains) (*23*).

Aspects of Orientale's asymmetry in surface structure extend to the subsurface, as indicated in Figs. 1 and 2. For instance, the basin exhibits an east-west variation in regional crustal structure that predated formation of the basin.

There are also radial variations in crustal thickness, some of which are distinctly associated with Orientale's outer two basin rings. The simplest interpretation of the azimuthally averaged models is that they could correspond to displacements associated with normal faults that penetrate the crust. The crust-mantle boundary relief in Fig. 2B suggests that there could be multiple faults dipping inward from the Outer Rook and Cordillera rings. The crustal thickness model also suggests the presence of other crustal faults that lack a visible surface expression. Although these faults may be listric—i.e., the dip angle may decrease with depth—a dip of 50°, indicated by hydrocode simulations (*16*), is consistent with prominent changes in crust-mantle boundary depth. These simulations also support crustal faulting not associated with rings.

Insight into the distinctive nature of each ring can be gained from scrutiny of Figs. 1 and 2 and fig. S8. The Inner Depression has the most axisymmetric and the largest variation in crustal thickness; a change in the sign of the gravity gradient (*9*) marks the depression's edge. The topography of the Inner Rook ring is morphologically similar to that of peak rings in small basins (*16*). Individual peaks within the Inner Rook are associated with positive free-air and Bouguer anomalies embedded within an annulus of negative free-air and Bouguer anomalies. The Inner Rook also appears associated with a near–circumferentially continuous change in the sign of the gravity gradient (Fig. 1E) and a flattening in relief along the crust-mantle boundary.

The Outer Rook ring also displays well-developed topography consistent with the surface expression of a normal fault scarp (*38*). Ring topography has associated positive free-air anomalies embedded within the same annulus of negative free-air and Bouguer anomalies. The most negative Bouguer gravity in the region appears within the Outer Rook and may reflect a combination of thickening of the crust by ejecta and extensive fracturing in the crustal column. The Outer Rook displays a sign change in the gravity gradient and a mild shoaling of the crust-mantle boundary. The collective characteristics of the Outer Rook ring are consistent with local thinning of the crust by faulting.

The topography of the Cordillera ring deviates markedly from axisymmetry; it is less developed than the Inner and Outer Rook rings and has little expression in part of the basin's southwestern quadrant. This asymmetric structure may be a consequence of the northeast-to-southwest–directed oblique impact that formed the basin (*39*) or preexisting heterogeneity of crustal or lithospheric structure (*2*, *38*), with a clear west-to-east gradient of decreasing crustal thickness still preserved (Fig. 1D). The topography of this ring is also consistent with the surface expression of a normal fault scarp (*16*). The ring is characterized by positive free-air and Bouguer anomalies, a gradient in crustal thickness, and a circumferentially discontinuous sign change in the gravity gradient. The variation of relief along the crust-mantle boundary strongly suggests fault penetration to the lower crust and possibly upper mantle. The gravitational signature could alternatively reflect contributions from magmatic intrusions along the irregularly developed ring fault, but regional seismic reflection profiles of a portion of the terrestrial Chicxulub impact structure, 20 to 25% the size of Orientale, show ring faults that extend well into the lower crust (*40*).

Our observations, combined with the accompanying simulations (*16*), elucidate the planet-shaping thermal, tectonic, and geological consequences of Orientale and, by extension, other large impacts that dominated the early evolution of the Moon and other solid planets.

REFERENCES AND NOTES

1. D. E. Wilhelms, *The Geologic History of the Moon*. U.S. Geol. Survey Prof. Paper 1348 (U.S. Government Printing Office, Washington, DC, 1987).
2. P. D. Spudis, *The Geology of Multiring Impact Basins: The Moon and Other Planets* (Cambridge Univ. Press, Cambridge, England, 1993).
3. M. T. Zuber *et al.*, *Space Sci. Rev.* **178**, 3–24 (2013).
4. D. Stöffler *et al.*, *Rev. Mineral. Geochem.* **60**, 519–596 (2006).
5. J. W. Head, *Moon* **11**, 327–356 (1974).
6. C. I. Fassett *et al.*, *J. Geophys. Res.* **117**, E00H06 (2012).

7. K. A. Howard, D. E. Wilhelms, D. H. Scott, *Rev. Geophys. Space Phys.* **12**, 309–327 (1974).
8. T. H. Sweetser, M. S. Wallace, S. J. Hatch, R. B. Roncoli, Design of an Extended Mission for GRAIL, in *AIAA Astrodynamics Specialist Conference* (Minneapolis, MN, 2012) (2012), 18 pp.
9. Materials and methods are available as supplementary materials on *Science* Online.
10. D. D. Rowlands, R. D. Ray, D. S. Chinn, F. G. Lemoine, *J. Geod.* **76**, 307–316 (2002).
11. F. G. Lemoine *et al.*, *Geophys. Res. Lett.* **41**, 3382–3389 (2014).
12. D. E. Smith *et al.*, *Icarus* 10.1016/j.icarus.2016.06.006 (2016).
13. D. E. Smith *et al.*, *Space Sci. Rev.* **150**, 209–241 (2010).
14. M. T. Zuber *et al.*, *Science* **339**, 668–671 (2013).
15. Y. N. Kattoum, J. C. Andrews-Hanna, *Icarus* **226**, 694–707 (2013).
16. B. C. Johnson *et al.*, *Science* **354**, 441–444 (2016).
17. J. W. Head, in *Impact and Explosion Cratering*, D. J. Roddy, R. O. Pepin, R. B. Merrill, Eds. (Pergamon Press, New York, NY, 1977), pp. 563–573.
18. C. A. Hodges, D. E. Wilhelms, *Icarus* **34**, 294–323 (1978).
19. J. W. Head, *Geophys. Res. Lett.* **37**, L02203 (2010).
20. M. A. Wieczorek *et al.*, *Science* **339**, 671–675 (2013).
21. M. A. Wieczorek, R. J. Phillips, *Icarus* **139**, 246–259 (1999).
22. M. A. Wieczorek *et al.*, *Rev. Mineral. Geochem.* **60**, 221–364 (2006).
23. M. Xie, M.-H. Zhu, *Earth Planet. Sci. Lett.* **440**, 71–80 (2016).
24. J. Besserer *et al.*, *Geophys. Res. Lett.* **41**, 5771–5777 (2014).
25. W. S. Kiefer, R. J. Macke, D. T. Britt, A. J. Irving, G. J. Consolmagno, *Geophys. Res. Lett.* **39**, L07201 (2012).
26. M. T. Zuber, D. E. Smith, F. G. Lemoine, G. A. Neumann, *Science* **266**, 1839–1843 (1994).
27. G. A. Neumann, M. T. Zuber, D. E. Smith, F. G. Lemoine, *J. Geophys. Res.* **101**, 16841–16863 (1996).
28. A. S. Konopliv *et al.*, *Science* **281**, 1476–1480 (1998).
29. N. Namiki *et al.*, *Science* **323**, 900–905 (2009).
30. P. M. Muller, W. L. Sjogren, *Science* **161**, 680–684 (1968).
31. J. C. Andrews-Hanna, *Icarus* **222**, 159–168 (2013).
32. H. J. Melosh *et al.*, *Science* **340**, 1552–1555 (2013).
33. R. M. Schmidt, K. R. Housen, *Int. J. Impact Eng.* **5**, 543–560 (1987).
34. B. A. Ivanov, H. J. Melosh, E. Pierazzo, in *Large Meteorite Impacts and Planetary Evolution*, R. L. Gibson, W. U. Reimold, Eds. (Geological Society of America, Boulder, CO, 2010), pp. 29–49.
35. R. W. K. Potter, D. A. Kring, G. S. Collins, W. S. Kiefer, P. J. McGovern, *J. Geophys. Res.* **118**, 1–17 (2013).
36. R. W. K. Potter, D. Kring, G. S. Collins, W. S. Kiefer, P. J. McGovern, *Geophys. Res. Lett.* **39**, L18203 (2012).
37. G. A. Neumann *et al.*, *Sci. Adv.* **1**, e1500852 (2015).
38. A. Nahm, T. Öhman, D. Kring, *J. Geophys. Res.* **118**, 190–205 (2013).
39. J. F. McCauley, *Phys. Earth Planet. Inter.* **15**, 220–250 (1977).
40. S. P. S. Gulick *et al.*, *Rev. Geophys. Space Phys.* **51**, 31–52 (2013).

ACKNOWLEDGMENTS

The GRAIL mission is supported by NASA's Discovery Program and is performed under contract to the Massachusetts Institute of Technology and the Jet Propulsion Laboratory. Topography was obtained from the Lunar Orbiter Laser Altimeter on the Lunar Reconnaissance Mission, managed by NASA's Goddard Space Flight Center. The NASA Pleiades and Center for Climate Simulation supercomputers were used to compute the gravity solutions. All data used in this study are archived in the Geosciences Node of the NASA Planetary Data System at http://geo.pds.nasa.gov/missions/grail/default.htm.

SUPPLEMENTARY MATERIALS

www.sciencemag.org/content/354/6311/438/suppl/DC1
Materials and Methods
Supplementary Text
Figs. S1 to S8
References (*41*–*75*)

5 May 2016; accepted 16 September 2016
10.1126/science.aag0519

IMPACT CRATERS

Formation of the Orientale lunar multiring basin

Brandon C. Johnson,[1]*† David M. Blair,[2] Gareth S. Collins,[3] H. Jay Melosh,[4] Andrew M. Freed,[4] G. Jeffrey Taylor,[5] James W. Head,[6] Mark A. Wieczorek,[7] Jeffrey C. Andrews-Hanna,[8] Francis Nimmo,[9] James T. Keane,[10] Katarina Miljković,[1]‡ Jason M. Soderblom,[1] Maria T. Zuber[1]

Multiring basins, large impact craters characterized by multiple concentric topographic rings, dominate the stratigraphy, tectonics, and crustal structure of the Moon. Using a hydrocode, we simulated the formation of the Orientale multiring basin, producing a subsurface structure consistent with high-resolution gravity data from the Gravity Recovery and Interior Laboratory (GRAIL) spacecraft. The simulated impact produced a transient crater, ~390 kilometers in diameter, that was not maintained because of subsequent gravitational collapse. Our simulations indicate that the flow of warm weak material at depth was crucial to the formation of the basin's outer rings, which are large normal faults that formed at different times during the collapse stage. The key parameters controlling ring location and spacing are impactor diameter and lunar thermal gradients.

Orientale, the youngest and best-preserved lunar multiring basin, exhibits three concentric topographic rings and an Inner Depression (*1*). The Inner Depression is a central topographic low associated with the zone of excavated crust that extends to a radial distance R = 160 km from the basin center and is bounded by a scarp (*2*, *3*). The Outer Rook ($R \approx 330$ km) and Cordillera ($R \approx 430$ km) rings are topographically consistent with fault scarps (*3*, *4*). High-resolution gravity data from the Gravity Recovery and Interior Laboratory (GRAIL) spacecraft reveal that the Outer Rook and Cordillera rings are associated with offsets at the crust-mantle interface and localized zones of crustal thinning (*2*). The Inner Rook ($R \approx$ 230 km) is distinct, with a topographic signature similar to those of the peak rings of smaller basins (*3*, *5*) and is associated with a flattening of relief at the crust-mantle boundary (*2*).

To understand the processes that produced the subsurface structure inferred from gravity (*2*), we modeled the formation of Orientale using the two-dimensional version of iSALE, a multimaterial, multirheology, finite-difference shock physics code (*6*–*8*). Because iSALE is a continuum model, faults are manifest as localized regions of high strain rather than as discrete slip planes. Previous models of Orientale-scale impacts (*9*, *10*) showed subtle strain localization in the crust around the crater, hinting at ring fault formation during crater collapse, but were unable to resolve fault offsets (i.e., the amount of slip along the fault) and topographic expression. Below, we describe several model improvements that allowed us to directly resolve the formation of Orientale's rings and faults with kilometers of offset, in a manner not achievable with previous basin formation models (*9*–*13*). We include a dilatancy model (*14*), which describes how deformation increases the porosity of geological materials and contributes to shear localization (*15*). We use a damage model with an exponential dependence on strain (*15*), which results in more localized deformation in rocks that are already heavily fractured. For structures the size of Orientale, the curvature of the Moon's surface is important (*16*), so we model impacts into a spherical Moon-like target with a realistic central gravity field (*17*).

We assume a vertical impact of an asteroid made of dunite at a typical lunar impact velocity of 15 km/s (*18*). Our axisymmetric models have a spatial resolution of 1 km. We vary the impactor diameter, pre-impact crustal thickness, and thermal structure while attempting to match ring locations as well as the crustal thickness, which is derived from GRAIL gravity measurements and topography from the Lunar Orbiter Laser Altimeter (LOLA) on the Lunar Reconnaissance Orbiter (*19*, *20*). Because rock strength decreases as the melting temperature is approached (*7*), the assumed pre-impact thermal structure of the target body has the most

[1]Department of Earth, Atmospheric and Planetary Sciences, Massachusetts Institute of Technology, Cambridge, MA 02139, USA. [2]Massachusetts Institute of Technology Haystack Observatory, Route 40, Westford, MA 01886, USA. [3]Impacts and Astromaterials Research Centre, Department of Earth Science and Engineering, Imperial College London, London SW7 2AZ, UK. [4]Department of Earth, Atmospheric, and Planetary Sciences, Purdue University, West Lafayette, IN 47907, USA. [5]Hawai'i Institute of Geophysics and Planetology, University of Hawai'i, Honolulu, HI 96822, USA. [6]Department of Earth, Environmental and Planetary Sciences, Brown University, Providence, RI 02912, USA. [7]Institut de Physique du Globe de Paris, Sorbonne Paris Cité, Université Paris Diderot, Paris Cedex 13 75205, France. [8]Southwest Research Institute, Boulder, CO 80302, USA. [9]Department of Earth and Planetary Sciences, University of California, Santa Cruz, CA 95064, USA. [10]Department of Planetary Science, Lunar and Planetary Laboratory, University of Arizona, Tucson, AZ 85721, USA.
***Corresponding author. Email: brandon_johnson@brown.edu**
†Present address: Department of Earth, Environmental and Planetary Sciences, Brown University, Providence, RI 02912, USA.
‡Present address: Department of Applied Geology, Curtin University, Perth, WA 6102, Australia.

substantial effect on the formation of large impact basins (*9*–*12*, *16*, *21*). Our best-fitting model uses an impactor with a diameter of 64 km, a pre-impact crustal thickness of 52 km, and a linear thermal gradient of 14 K/km from a surface temperature of 300 K. The [illegible] transitions to an adiabat of [illegible] temperatures exceeding 1300 K [illegible] is consistent with the lunar therm[illegible]-4 billion years ago (*17*, *21*).

Our model provides insight into the extent and temporal progression of excavation and crustal disruption, including the timing and formation of Orientale's rings (Fig. 1). The impact first produces a bowl-shaped crater with

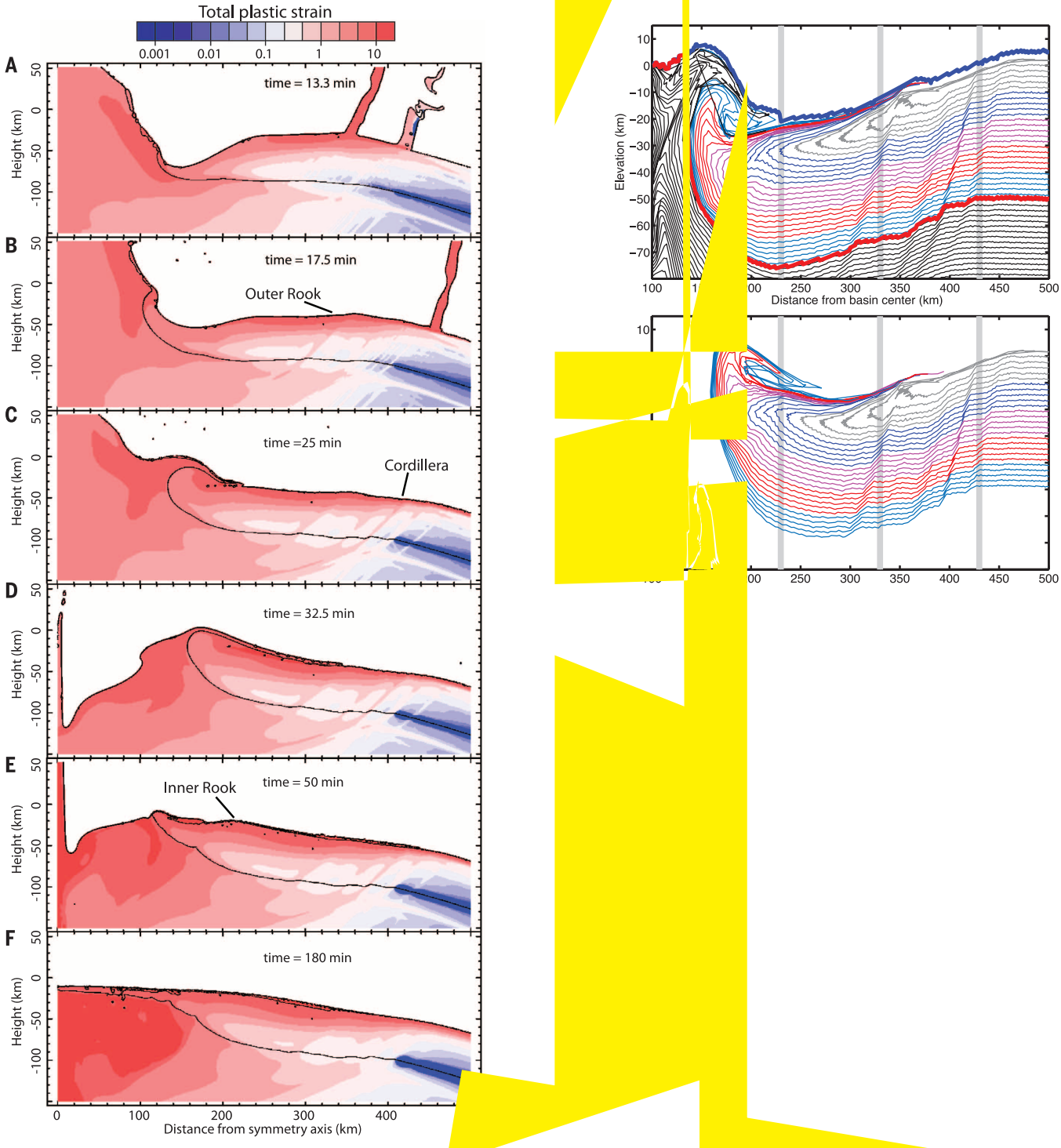

Fig. 1. Time series for the best-fitting model of Orientale crater collapse and ring formation. Material positions are colored according to their total plastic strain. The origin marks the point of impact. The thin black curves mark material interfaces (e.g., crust-mantle interface). Movie S1 is an animation of this figure.

a maximum depth of ~180 km; this cavity is unstable and experiences gravitational collapse. Although much of the deepest material collapses back into the crater, the maximum depth of excavation is ~55 km (i.e., into the mantle), where we define excavated material as any material on a ballistic trajectory and above the pre-impact surface at the time the crater has its maximum volume. Of the 5.7×10^6 km^3 of ejecta, 4.2×10^6 km^3 avoid collapsing into the crater and 1.2×10^6 km^3 are deposited between the basin rim and a distance of one basin diameter (R = 430 to 860 km). These values are consistent with constraints from GRAIL and LOLA (*2*).

The time when the crater reaches its maximal volume is also used to determine the width of the transient crater ($R \approx 195$ km), which extends to a radial distance between the present-day Inner Depression and the Inner Rook ring and precedes the formation of any of the observed rings. Older studies have attempted to relate the rim of the transient crater to Orientale's rings (*1*, *22*–*26*), but the relative difference in their time of formation suggests that there is no reason to expect a correlation, and indeed no present-day topographic features correspond to the transient crater (*2*). This implies that for large impact basins, the transient crater and impactor size must be deduced not from topography but rather from the gravity and crustal thickness signature, using empirical relations from numerical models (*21*).

As the bowl-shaped transient crater collapses, a central uplift forms, composed of mantle material (Fig. 1A). As the crater continues to collapse, the Outer Rook fault (Fig. 1B) forms and ejecta are emplaced well outside the location where the Cordillera ring eventually forms after further inward collapse (Fig. 1C and Fig. 2A). This aspect of the simulation is consistent with observations suggesting that the Cordillera formed subsequent to ejecta emplacement (*3*). Our model predicts that both normal faults cut through the crust, and their dip angle (i.e., angle with respect to the surface) gradually decreases in the mantle (Fig. 1C and Fig. 2A). As illustrated in Fig. 2A, each fault has an offset of a few kilometers and has an average dip angle of 50° to 55° within the crust. Although the fault offsets are still present at late times, as evidenced by the displacement along tracer lines (Fig. 2C), numerical diffusion smooths the localized total plastic strain associated with the faults (Fig. 1, C and F).

The Outer Rook and Cordillera rings appear to be the scarps of large normal faults [e.g., (*1*, *3*)]. Our models indicate that these faults are the result of inward flow of warm, weak mantle material during collapse of the transient crater. This flow of weaker underlying material (Fig. 1 and fig. S2) pulls the cooler crust along with it, ultimately causing extensional faulting with large offsets far from the transient crater rim. In the best-fitting model, the strongest crustal material prior to the impact has a yield strength of 147 MPa and the weakest mantle material has a yield strength of 63 MPa (fig. S1). The role of the weak underlying mantle material is consistent with the ring tectonic theory of multi-ring basin formation (*24*).

After rising as high as 140 km above the surface, the central uplift collapses and produces a topographic bulge of crustal material ~10 km in height at $R \approx 175$ km (Fig. 2B). The formation of this bulge drives the development of the Inner Rook ring (Fig. 1D and Fig. 2B). This outcome of the simulation is consistent with earlier suggestions that the formation of the Inner Rook ring is analogous to the formation of peak rings observed in smaller basins (*5*, *9*). A secondary phase of inward collapse modifies the topographic expression of the Inner Rook (Fig. 1, D and E, and Fig. 2, B and C), perhaps distinguishing it from peak rings of smaller craters (*27*). Although the topographic signature of the Inner Rook is inconsistent with a fault scarp (*3*), the Inner Rook is associated with a local flattening of relief at the crust-mantle boundary (*2*), which is reproduced in our simulations (Fig. 2C). Our modeling predicts that the Inner Rook is composed of unmelted, lightly shocked crustal material from 35- to 40-km depths that is pushed over previously emplaced ejecta (Fig. 2 and figs. S3 and S4). This is consistent with observations indicating a cluster of localities composed of nearly pure crystalline plagioclase around the Inner Rook (*28*) and suggests that the crust around Orientale is nearly pure crystalline plagioclase even at depths exceeding 35 km, consistent with lunar bulk composition estimates (*29*).

In the hours after the impact, relatively cool (~1000 K) crustal material flows inward toward the basin center and covers the denser impact melt pool, which is dominated by mantle material (Fig. 1F and fig. S4). Combined with the fact that deeply excavated material collapses into the crater (Fig. 1A), this explains how a basin-scale impact that penetrates to mantle depths could contain crustal material at the basin center, as implied by crustal thickness models (*2*, *20*). Our models indicate that a thin deposit of crustal impact melt (fig. S5) covers the interior surface of Orientale, consistent with the morphologic and spectral interpretation of the Maunder formation (*30*). More oblique impacts, characterized by shallower excavation depths, would produce thicker crustal impact melt units (*11*).

Three hours after initial impact, the center of the basin is ~7 km deeper than currently observed (fig. S6). A deep post-impact basin is integral to the process that produces positive gravity anomalies over most lunar basins (*11*, *31*). Over the next few hundred million years, the basin center rises to its present position in response to the post-impact stress state (*11*, *31*). Mechanical coupling of the lithosphere in the basin center with the lithosphere associated with the crustal collar (annulus of thickest crust after transient crater collapse) enables the initially subisostatic basin center to uplift, becoming superisostatic and producing the free-air gravity anomaly of ~250 mGal (1 mGal = 10^{-5} m s^{-2}) over the center of Orientale (*11*, *31*, *32*).

Although our models do not result in a scarp bounding the Inner Depression ($R \approx 160$ km), they suggest that this scarp formed after the Inner Rook. Any topographic feature formed interior of $R \approx 200$ km, including the transient crater rim, would be destroyed by collapse of the central uplift (Fig. 1). After crater collapse, the impact melt pool extends from the basin center out to the edge of the Inner Depression (fig. S7). The Inner Depression is clearly associated with the mantle uplift (*2*). Although we cannot rule out formation of the scarp bounding the Inner Depression within a few hours of the impact, our modeling supports the inference that the Inner Depression formed on a much longer time scale, tectonically as the basin adjusted in response to the post-impact stress state (*11*, *33*), aided by cooling and contraction of Orientale's massive melt pool (*34*, *35*).

In our models, some mantle material splashes out onto the crust as the central uplift collapses (Fig. 1, C to F, and fig. S4), but this may be attributable to the limitations of our axisymmetric model. The southwestern quadrant of Orientale exhibits at least four large normal faults instead of two seen in other regions (*3*). The initial crustal thickness varies over the broad area of the Orientale basin; coupled with

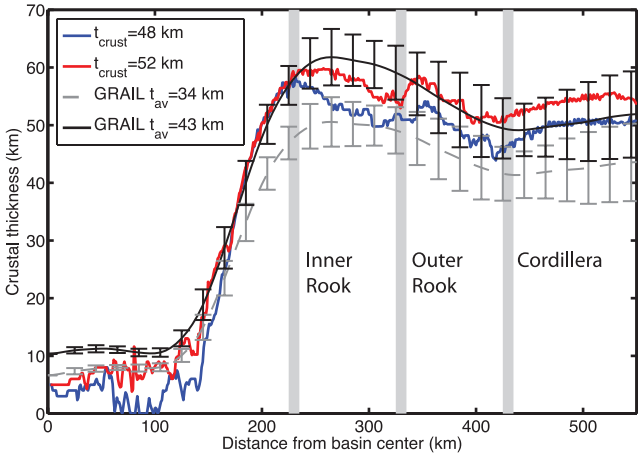

Fig. 3. Post-impact crustal thickness. The model thickness of the crust is plotted from the best-fitting model (red) and for a model with a pre-impact crustal thickness of 48 km (blue). Azimuthally averaged observed profiles of GRAIL-derived crustal thickness (*2*) are shown for comparison [global average crustal thickness t_{av} = 43 km (black) and t_{av} = 34 km (gray)]. Error bars are 1σ deviations from the mean.

the effects of an oblique impact, this may explain the marked difference between the development of rings in the eastern and western sectors of the basin.

In addition to forming rings in approximately the correct locations (Fig. 1 and fig. S8B), models with pre-impact crustal thicknesses that range from 48 to 52 km also reproduce the azimuthally averaged crustal thickness profile derived from GRAIL gravity and LOLA topography (Fig. 3). Our modeling shows that ring location and fault offsets are highly dependent on impactor size and the pre-impact thermal gradient (figs. S9 and S10). In our best-fitting model, the region where crust is thinned from the pre-impact value extends to $R_{thin} \approx 200$ km. The parameter R_{thin} also provides an estimate for the radius of the zone of ejecta provenance or excavation cavity (*36*). In our best-fitting model of Orientale, these two metrics agree to within 5%. We favor the model with pre-impact crustal thickness of 52 km because it produces a thicker cap of cool crustal material at the center of the basin (Fig. 3), consistent with gravity observations.

Inverse models of GRAIL gravity data suggest that the Outer Rook and Cordillera are associated with localized crustal thinning and offsets at the crust-mantle interface (*2*). The crustal structure also reveals offsets at the crust-mantle interface that do not correlate with rings and may indicate additional subsurface faults. The faults with small offsets forming on either side of the Cordillera in our simulations may be consistent with these additional faults (Fig. 2). The amount of crustal thinning and magnitude of crust-mantle relief, however, depend on the assumptions of these inverse models (*2*). Our models exhibit local minima in the crustal thickness (Fig. 3) and offsets at the crust-mantle interface (Fig. 2) associated with the Outer Rook and Cordillera. These results are consistent with normal faults with offsets of a few kilometers cutting through the crust-mantle interface. The simple geometry of a normal fault with a dip angle of 50° and offset of 4 km cutting through 50-km-thick crust will create a ~40-km-wide region where the crust is thinned by ~3 km. This idealized fault geometry is similar to the modeled Outer Rook ring (Fig. 3, red curve 300 to 340 km from basin center). When extension occurs close to a fault (within ~40 km), the zone of crustal thinning is broader (Figs. 2 and 3 and fig. S8B). Inverse models of the crust-mantle interface are limited in resolution to a wavelength approximately equal to the crustal thickness. Thus, the predicted broader zone of extension may explain in part why the signature of the Cordillera is more robust than that of the Outer Rook (*2*). Similar local minima in crustal thickness as observed by GRAIL may reveal ring faults in highly degraded or mare-filled basins.

REFERENCES AND NOTES

1. J. W. Head, *Moon* **11**, 327–356 (1974).
2. M. T. Zuber *et al.*, *Science* **354**, 438–441 (2016).
3. A. L. Nahm, T. Öhman, D. A. Kring, *J. Geophys. Res. Planets* **118**, 190–205 (2013).
4. Y. N. Kattoum, J. C. Andrews-Hanna, *Icarus* **226**, 694–707 (2013).
5. D. M. H. Baker *et al.*, *Icarus* **214**, 377–393 (2011).
6. A. A. Amsden, H. M. Ruppel, C. W. Hirt, *SALE: A Simplified ALE Computer Program for Fluid Flow at Speeds* (Los Alamos National Laboratories Report LA-8095, 1980).
7. G. S. Collins, H. J. Melosh, B. A. Ivanov, *Meteorit. Planet. Sci.* **39**, 217–231 (2004).
8. K. Wünnemann, G. S. Collins, H. J. Melosh, *Icarus* **180**, 514–527 (2006).
9. R. W. K. Potter, D. A. Kring, G. S. Collins, W. S. Kiefer, P. J. McGovern, *J. Geophys. Res. Planets* **118**, 963–979 (2013).
10. R. W. K. Potter, *Icarus* **261**, 91–99 (2015).
11. A. M. Freed *et al.*, *J. Geophys. Res. Planets* **119**, 2378–2397 (2014).
12. K. Miljković *et al.*, *Science* **342**, 724–726 (2013).
13. M.-H. Zhu, K. Wünnemann, R. W. K. Potter, *J. Geophys. Res. Planets* **120**, 2118–2134 (2015).
14. G. S. Collins, *J. Geophys. Res. Planets* **119**, 2600–2619 (2014).
15. L. G. J. Montési, *J. Geophys. Res.* **107** (B3), 2045 (2002).
16. B. A. Ivanov, H. J. Melosh, E. Pierazzo, *Geol. Soc. Spec. Pap.*, 29–49 (2010).
17. See supplementary materials on *Science* Online.
18. M. Le Feuvre, M. A. Wieczorek, *Icarus* **214**, 1–20 (2011).
19. D. E. Smith *et al.*, *Icarus* 10.1016/j.icarus.2016.06.006 (2016).
20. M. A. Wieczorek *et al.*, *Science* **339**, 671–675 (2013).
21. R. W. K. Potter, D. A. Kring, G. S. Collins, W. S. Kiefer, P. J. McGovern, *Geophys. Res. Lett.* **39**, L18203 (2012).
22. M. Laneuville, M. A. Wieczorek, D. Breuer, N. Tosi, *J. Geophys. Res. Planets* **118**, 1435–1452 (2013).
23. R. B. Baldwin, *Phys. Earth Planet. Inter.* **6**, 327–339 (1972).
24. H. J. Melosh, W. B. McKinnon, *Geophys. Res. Lett.* **5**, 985–988 (1978).
25. J. W. Head, *Geophys. Res. Lett.* **37**, L02203 (2010).
26. C. A. Hodges, D. E. Wilhelms, *Icarus* **34**, 294–323 (1978).
27. G. S. Collins, H. J. Melosh, J. V. Morgan, M. R. Warner, *Icarus* **157**, 24–33 (2002).
28. L. C. Cheek, K. L. Donaldson Hanna, C. M. Pieters, J. W. Head, J. L. Whitten, *J. Geophys. Res. Planets* **118**, 1805–1820 (2013).
29. G. J. Taylor, M. A. Wieczorek, *Philos. Trans. R. Soc. A* **372**, 20130242 (2014).
30. P. D. Spudis, D. J. P. Martin, G. Kramer, *J. Geophys. Res. Planets* **119**, 19–29 (2014).
31. H. J. Melosh *et al.*, *Science* **340**, 1552–1555 (2013).
32. M. T. Zuber *et al.*, *Science* **339**, 668–671 (2013).
33. P. K. Byrne *et al.*, *Earth Planet. Sci. Lett.* **427**, 183–190 (2015).
34. W. M. Vaughan, J. W. Head, L. Wilson, P. C. Hess, *Icarus* **223**, 749–765 (2013).
35. S. R. Bratt, S. C. Solomon, J. W. Head, *J. Geophys. Res.* **90**, 12415–12433 (1985).
36. M. A. Wieczorek, R. J. Phillips, *Icarus* **139**, 246–259 (1999).

ACKNOWLEDGMENTS

We thank two anonymous reviewers for their thoughtful reviews; the developers of iSALE (www.isale-code.de/redmine/projects/iSALE), including K. Wünnemann, D. Elbeshausen, and B. Ivanov; and all those involved with the development and operations of the GRAIL spacecraft and the collection and reduction of the GRAIL data. This work was funded by the GRAIL mission, which is supported by the NASA Discovery Program and is performed under contract to the Massachusetts Institute of Technology and the Jet Propulsion Laboratory, California Institute of Technology. G.S.C. was funded by UK Science and Technology Facilities Council grant ST/N000803/1. At present, iSALE is not publicly available. It is distributed on a case-by-case basis to academic users in the impact community, strictly for noncommercial use. Scientists interested in using or developing iSALE should see www.isale-code.de/redmine/projects/isale/wiki/Terms_of_use for a description of application requirements. Model output has been published at the Harvard Dataverse, doi:10.7910/DVN/BH9UXW.

SUPPLEMENTARY MATERIALS

www.sciencemag.org/content/354/6311/441/suppl/DC1
Materials and Methods
Figs. S1 to S10
Tables S1 and S2
Movie S1
References (*37*–*55*)

5 May 2016; accepted 8 September 2016
10.1126/science.aag0518

CHEMICAL KINETICS

Direct frequency comb measurement of OD + CO → DOCO kinetics

B. J. Bjork,[1]* T. Q. Bui,[1] O. H. Heckl,[1] P. B. Changala,[1] B. Spaun,[1] P. Heu,[2] D. Follman,[2] C. Deutsch,[3] G. D. Cole,[2,3] M. Aspelmeyer,[4] M. Okumura,[5] J. Ye[1]*

The kinetics of the hydroxyl radical (OH) + carbon monoxide (CO) reaction, which is fundamental to both atmospheric and combustion chemistry, are complex because of the formation of the hydrocarboxyl radical (HOCO) intermediate. Despite extensive studies of this reaction, HOCO has not been observed under thermal reaction conditions. Exploiting the sensitive, broadband, and high-resolution capabilities of time-resolved cavity-enhanced direct frequency comb spectroscopy, we observed deuteroxyl radical (OD) + CO reaction kinetics and detected stabilized *trans*-DOCO, the deuterated analog of *trans*-HOCO. By simultaneously measuring the time-dependent concentrations of the *trans*-DOCO and OD species, we observed unambiguous low-pressure termolecular dependence of the reaction rate coefficients for N_2 and CO bath gases. These results confirm the HOCO formation mechanism and quantify its yield.

The apparent simplicity of the gas-phase bimolecular reaction kinetics of free radicals often belies the complexity of the underlying dynamics. Reactions occur on multidimensional potential energy surfaces that can host multiple prereactive and bound intermediate complexes, as well as multiple transition states. As a result, effective bimolecular rate coefficients often exhibit complex temperature and pressure dependences. The importance of free radical reactions in processes such as combustion and air pollution chemistry has motivated efforts to determine these rate constants both experimentally and theoretically. Quantitative ab initio modeling of kinetics remains a major contemporary challenge (*1*), requiring accurate quantum chemical calculations of energies, frequencies, and anharmonicities; master equation

modeling; calculation of energy transfer dynamics; and, when necessary, calculation of tunneling and nonstatistical behavior. Experimental detection of the transient intermediates, which is the key to unraveling the dynamics, is frequently challenging.

The reaction of hydroxyl radical with CO

$$OH + CO \rightarrow H + CO_2,\ \Delta_r E_0 = -103.29\ kJ\ mol^{-1} \quad (1)$$

($\Delta_r E_0$, standard energy of the reaction at 0 K) has been extensively studied over the past four decades because of its central role in atmospheric and combustion chemistry (*2*); it has come to serve as a benchmark for state-of-the-art studies of the chemical kinetics of complex bimolecular reactions (*3*, *4*). In Earth's atmosphere, OH is critical as the primary daytime oxidant (*5*, *6*). CO, a byproduct of fossil fuel burning and hydrocarbon oxidation, acts through the reaction in Eq. 1 as an important global sink for OH radicals; this reaction is the dominant OH loss process in the free troposphere. In fossil fuel combustion, OH + CO is the final step that oxidizes CO to CO_2 and is responsible for a large amount of the heat released.

The rate of the reaction in Eq. 1 is pressure-dependent and exhibits an anomalous temperature dependence, which led Smith and Zellner (*7*) to propose that the reaction proceeds through a highly energized, strongly bound intermediate, HOCO, the hydrocarboxyl radical (Fig. 1A, inset). Formation of H + CO_2 products is an example of a chemically activated reaction. The course of the reaction is governed by the dynamics on the potential energy surface, shown schematically in Fig. 1A. The OH and CO pass through a prereactive weakly bound OH–CO complex to form a highly energized HOCO* (where the asterisk denotes vibrational excitation) in one of two isomers, *trans*-HOCO or the less stable *cis*-HOCO (*2*). In the low-pressure limit at room temperature, HOCO* primarily back-reacts to OH + CO, but there is a small probability of overcoming the low barrier (8.16 kJ mol^{-1}) and reacting to form H + CO_2. In the presence of buffer gas, energy transfer by collisions with third bodies M (termolecular process) can deactivate or further activate the HOCO*. Deactivation can lead to the formation of stable, thermalized HOCO products (reaction 1a in Fig. 1A, inset), which diminishes the formation of H + CO_2 (reaction 1b in Fig. 1A, inset). Approaching the high-pressure limit, HOCO formation becomes the dominant channel, and H + CO_2 product formation decreases. The overall reaction rate is characterized by an effective bimolecular rate constant $k_1([M],T) = k_{1a}([M],T) + k_{1b}([M],T)$, where T is temperature (*8*–*12*).

There have been numerous experimental studies of the temperature and pressure dependence of the overall rate coefficient $k_1([M],T)$; these all have measured OH loss in the presence of CO (*9*, *11*–*17*). In principle, master equation calculations with accurate potential energy surfaces within a statistical rate theory can compute $k_1([M],T)$, but a priori kinetics are rarely possible because the energy transfer dynamics are generally not known. A number of studies have thus fit the theoretical models to the observed overall rate constants, using a small number of parameters to describe collisional energy relaxation and activation (*9*, *11*, *15*, *16*, *18*, *19*). Although these previous studies have had success in describing $k_1([M],T)$, they do not capture the dynamics that would be revealed from the pressure-dependent branching between stabilization of HOCO and barrier crossing to form H + CO_2 products. Detection of the stabilized HOCO intermediate and measurement of its pressure-dependent yield would confirm the reaction mechanism and quantitatively test theoretical models. The spectroscopy of HOCO is well established, and recently HOCO has been observed in the OH + CO reaction generated in a discharge (*20*–*22*); however, measurements under thermal conditions are necessary to derive rate constants.

To directly and simultaneously measure the time-dependent concentrations of reactive radical intermediates such as HOCO and OH, we applied the recently developed technique of time-resolved direct frequency comb spectroscopy (TRFCS) (*23*). The massively parallel nature of frequency comb spectroscopy allows time-resolved, simultaneous detection of a number of key species, including intermediates and primary products, with high spectral and temporal resolution. The light source is a mid–infrared (IR) (wavelength $\lambda \approx 3$ to 5 μm) frequency comb, generated from an optical parametric oscillator (OPO) synchronously pumped with a high-repetition-rate (f_{rep} = 136 MHz) mode-locked femtosecond fiber laser (*24*). The OPO spectrum is composed of spectrally narrow comb teeth evenly spaced by f_{rep} and shifted by an offset frequency, f_0. By matching and locking the free spectral range of the enhancement cavity to $2 \times f_{rep}$, we keep the full comb spectrum resonant with the cavity during the data acquisition. The broadband transmitted light (~65 cm^{-1} bandwidth, ~7100 comb teeth) is spatially dispersed in two dimensions by a virtually imaged phased array etalon and a grating combination and is then imaged onto an InSb camera (fig. S1). Absorption spectra are constructed from these images as a function of time (with a resolution of ≥10 μs determined by the camera integration time), which are compared with known molecular line intensities to obtain absolute concentrations. The absorption detection sensitivity is greatly enhanced with our high-finesse ($F \approx 4100$) optical cavity that employs mid-IR mirrors with low-loss crystalline coatings. These mirrors, with a center wavelength of 3.72 μm and a spectral bandwidth of about 100 nm, have substantially lower optical losses and hence yield enhanced cavity contrast compared with traditional amorphous coatings [as covered in detail in (*25*)], enabling an improved sensitivity by a factor of 10 for the direct detection of *trans*-DOCO.

In this experiment, we studied the deuterium analog of Eq. 1, OD + CO → D + CO_2, exploiting the sensitivity and resolution of TRFCS to detect the reactant OD (in vibrational level, v = 0

[1]JILA, National Institute of Standards and Technology and University of Colorado, and Department of Physics, University of Colorado, Boulder, CO 80309, USA. [2]Crystalline Mirror Solutions, 114 East Haley Street, Suite G, Santa Barbara, CA 93101, USA. [3]Crystalline Mirror Solutions, Parkring 10, 1010 Vienna, Austria. [4]Vienna Center for Quantum Science and Technology, Faculty of Physics, University of Vienna, 1090 Vienna, Austria. [5]Arthur Amos Noyes Laboratory of Chemical Physics, Division of Chemistry and Chemical Engineering, California Institute of Technology, 1200 East California Boulevard, Pasadena, CA 91125, USA.
***Corresponding author. Email: bryce.bjork@colorado.edu (B.J.B.); ye@jila.colorado.edu (J.Y.)**

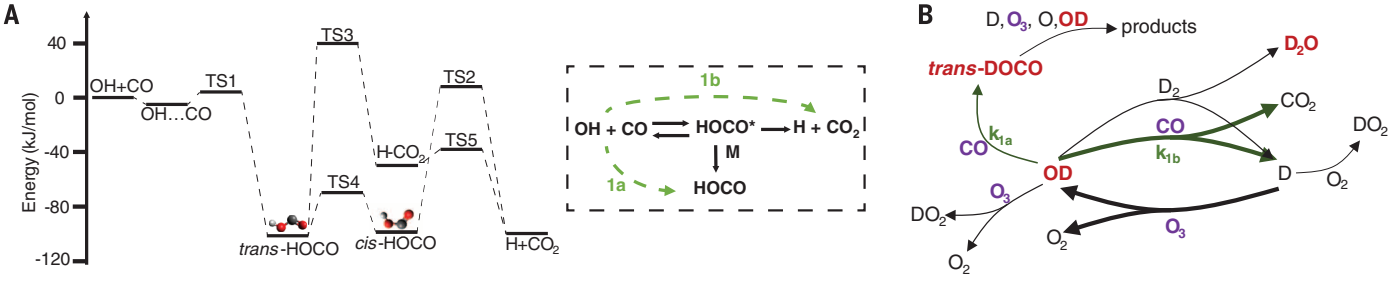

Fig. 1. Energetics of the OH + CO → H + CO_2 reaction. (**A**) Potential energy surface, with energies taken from Nguyen *et al*. (*2*). OH + CO → H + CO_2 proceeds through vibrationally excited HOCO*, which is either deactivated by bath gas M or reacts to form H + CO_2. The inset shows the simplified OH + CO reaction mechanism. TS, transition state. (**B**) Schematic showing the most important reactions in our system. Time-dependent concentrations of *trans*-DOCO, OD(v = 0), OD(v = 1), and D_2O (red) are measured by cavity-enhanced absorption spectroscopy; the concentrations of the precursors (purple) are set by flow controllers or meters. O_3 is measured by UV absorption.

and v = 1 states) and the product *trans*-DOCO by absorption spectroscopy in a pulsed-laser-photolysis flow cell experiment. We sought to measure the pressure-dependent effective bimolecular rate coefficients and the yield of *trans*-DOCO at total pressures of 27 to 75 torr (3.3 to 10 kPa). Such measurements would be especially sensitive to the competition between termolecular DOCO stabilization and the reaction to form D + CO_2. Detection of the deuterated species allowed us to avoid atmospheric water interference in our spectra. We further anticipated that the yield of stable DOCO would be higher, because deuteration substantially reduces the rate of tunneling to form D + CO_2 products while increasing the lifetime of DOCO* because of the higher density of states.

The OD + CO reaction was initiated in a slow-flow cell by photolyzing O_3 in a mixture of D_2, CO, and N_2 gases with 266-nm (32-mJ, 10-Hz) pulses from a frequency-quadrupled Nd:YAG laser, expanded to a profile of 44 mm × 7 mm and entering the cell perpendicular to the cavity axis. The initial concentration of O_3, $[O_3]_0$, was fixed at a starting concentration of 1×10^{15} molecules cm^{-3} and verified by direct ultraviolet (UV) absorption spectroscopy. The initial concentrations of CO, N_2, and D_2 were varied over the range 1 to 47 torr (0.13 to 6.3 kPa), whereas the O_3 concentration was restricted to 3 to 300 mTorr (4×10^{-4} to 4×10^{-2} kPa) to minimize secondary reactions. A complete description and tabulation of the experimental conditions is included in section 1 of the supplementary materials.

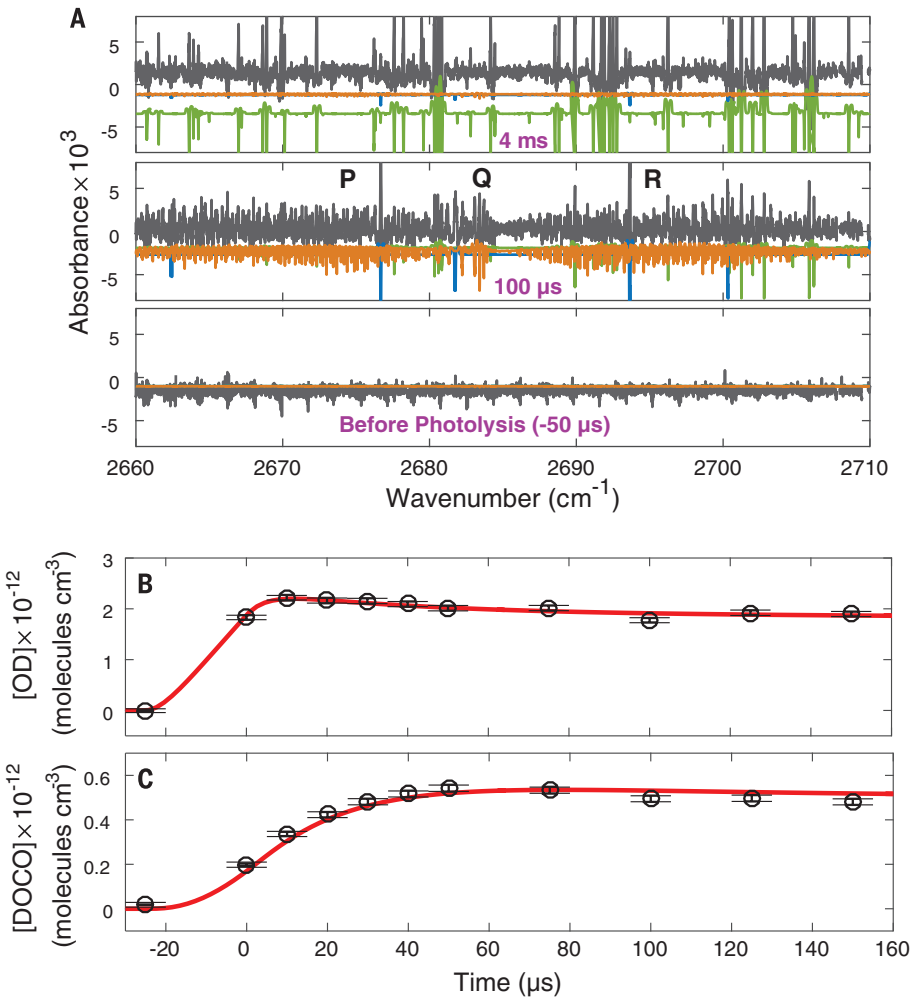

Fig. 2. Spectral acquisition and fitting. (**A**) Experimental spectra (black) were recorded with an integration time of 50 μs and offsets of −50 ("before photolysis"), 100, and 4000 μs from the photolysis pulse. These spectra were then fitted to the known line positions of OD (blue), D_2O (green), and *trans*-DOCO (orange) to determine their temporal concentration profiles. The P, Q, and R branches of *trans*-DOCO are indicated above the 100-μs experimental trace. (**B**) An analytical functional form for [OD](t) was obtained by fitting the data (black circles) to a sum of boxcar-averaged exponential functions (red line). At each time, the data point represents ~300 averaged spectra, and the error bars are from statistical uncertainties in the spectral fit. (**C**) The bimolecular *trans*-DOCO rise rate was obtained by fitting the data (black circles) to Eq. 3 (red line). The data in (B) and (C) were obtained at a 10-μs camera integration time and precursor concentrations of [CO] = 5.9×10^{17}, [N_2] = 8.9×10^{17}, [D_2] = 7.4×10^{16}, and [O_3] = 1×10^{15} molecules cm^{-3}.

Each photolysis pulse dissociated 15% of the ozone (supplementary materials, section 1) to form O_2 + $O(^1D)$ at nearly unity quantum yield (*26*). The resulting $O(^1D)$ either reacts with D_2 to form OD + D or is quenched by background gases to $O(^3P)$ within 1 μs. $O(^1D)$ + D_2 is known to be highly exothermic and produces vibrationally excited OD(v = 0 to 4) with an inverted population peaking at v = 2 and 3 (*27*). Vibrationally excited OD was rapidly quenched or formed D atoms by collisions with CO (*28*, *29*). Formation of vibrational Feshbach resonances of DOCO* from collisions of OD(v > 0) with CO may be possible, but the lifetimes are on the order of picoseconds, as previously observed for the HOCO* case (*30*–*33*). Therefore, only vibrationally and rotationally thermalized OD(v = 0) is expected to form DOCO by the mechanism described in the inset of Fig. 1A. OD and DOCO reach a steady state after 100 μs through the cycling reactions depicted in Fig. 1B: D atoms produced from OD + CO → D + CO_2 react with O_3 to regenerate the depleted OD.

Absorption spectra covering a ~65 cm^{-1} bandwidth were recorded at a sequence of delays from the time t = 0 photolysis pulse, using a camera integration time of either 10 or 50 μs, depending on the sensitivity to *trans*-DOCO signals. The broad bandwidth of the comb covers 6 OD, ~200 D_2O, and ~150 *trans*-DOCO transitions. These spectra were normalized to a spectrum acquired directly preceding the photolysis pulse and were fitted to determine time-dependent concentrations. With this approach, we captured the time-dependent kinetics of *trans*-DOCO, OD, and D_2O from OD + CO within a spectral window of 2660 to 2710 cm^{-1}. Representative snapshots at three different delay times are shown in Fig. 2A. The OD and *trans*-DOCO data were compared to simulated spectra, generated with PGopher (*34*) by using measured molecular constants (*35*–*37*) and known or computed intensities. The simulated spectra are fitted to these experimental data at each time delay to map out the full time trace of the three observed species (Fig. 2, B and C), with error bars derived directly from the fit residual. Section 2 of the supplementary materials includes details of the data analysis.

We determined the effective bimolecular rate coefficient for the *trans*-DOCO channel, $k_{1a}([M], T)$, from simultaneous measurements of time-dependent *trans*-DOCO and OD. In the low-pressure regime studied here, the DOCO formation rate obeys a termolecular rate law, whereas the effective bimolecular coefficient for the D + CO_2 channel remains close to the zero-pressure value, $k_{1b}([M] = 0)$. We measured the dependence of the effective bimolecular rate constant on the concentrations of all of the major species present in the experiment (N_2, CO, D_2, and O_3).

We analyzed the early-time (t < 200 μs) rise of *trans*-DOCO to decouple the measurement of k_{1a} from secondary loss channels at longer

times. The expected time dependence of the DOCO concentration is given by

$$\frac{d[\mathrm{DOCO}]}{dt} = k_{1a}[\mathrm{CO}][\mathrm{OD}](t) - k_{\mathrm{loss}}[\mathrm{X}][\mathrm{DOCO}](t) \quad (2)$$

k_{loss} describes a general DOCO decay through a reaction with species X, and [OD](t) refers to the time-dependent concentration of OD in the ground vibrational state. The solution to Eq. 2 is a convolution of the DOCO loss term with [OD](t), given by the integral in Eq. 3 (u is a dummy variable). [CO] is in large excess and remains constant throughout the reaction.

$$[\mathrm{DOCO}](t) = k_{1a}[\mathrm{CO}]\int_0^t e^{-(k_{\mathrm{loss}}[\mathrm{X}])(t-u)}[\mathrm{OD}](u)du \quad (3)$$

The effective bimolecular rate coefficient k_{1a} can be reduced into two terms dependent on N_2 and CO concentrations

$$k_{1a} = k_{1a}^{(\mathrm{CO})}[\mathrm{CO}] + k_{1a}^{(\mathrm{N_2})}[\mathrm{N_2}] \quad (4)$$

where $k_{1a}^{(\mathrm{CO})}$ and $k_{1a}^{(\mathrm{N_2})}$ are the termolecular rate coefficients with a third-body dependence on CO and N_2, respectively.

By simultaneously fitting [DOCO](t) and [OD](t) as a function of [CO] and [N_2], we uniquely determined all of the k_{1a} termolecular coefficients. Figure 2B shows an early-time segment of our data at 10-μs camera integration for both [*trans*-DOCO](t) and [OD](t). To fit the nonlinear time dependence of [OD](t), we used derived analytical functions composed of the sum of boxcar-averaged exponential rise and fall functions (supplementary materials, section 3). Equation 3 gives the functional form for fitting [*trans*-DOCO](t), which includes the integrated [OD](t) over the fitted time window of −25 to 160 μs. The fitted parameters are k_{1a} and a *trans*-DOCO loss rate, $r_{\mathrm{loss,exp}}$ ($\equiv k_{\mathrm{loss}}[\mathrm{X}]$).

For our first set of data, we varied the CO concentration. For each set of conditions, we acquired data at both 10- and 50-μs camera integration times. By plotting k_{1a} versus [CO] at 10 and 50 μs, we did not observe any systematic dependence on camera integration time. Moreover, we observed a clear linear dependence (with reduced chi-squared, $\chi^2_{\mathrm{red}} = 0.86$), indicating a strong termolecular dependence of k_{1a} on CO, or $k_{1a}{}^{(\mathrm{CO})}$ (Fig. 3A). The offset in the linear fit comes from the N_2 termolecular dependence of k_{1a}, or $k_{1a}^{(\mathrm{N_2})}$. We then varied N_2 concentration and observed a similar linear dependence of k_{1a} from Eq. 4. A 50-μs camera integration time was used for this second data set because of the lower *trans*-DOCO signals at higher N_2 concentrations. The results are shown in Fig. 3B. Because the offset terms from the linear fit to the CO data and the linear fit to the N_2 plot both correspond to $k_{1a}^{(\mathrm{N_2})}$, we performed a multidimensional linear regression to Eq. 4 to determine $k_{1a}^{(\mathrm{CO})}$, $k_{1a}^{(\mathrm{N_2})}$, and r_{loss} simultaneously. Because $r_{\mathrm{loss,exp}}$ describes *trans*-DOCO loss, it is expected to be invariant to [CO] and [N_2]. Therefore, $r_{\mathrm{loss,exp}}$ serves as a shared, fitted constant in the global fit across the CO and N_2 data sets. From the fits shown in red in Fig. 3, A and B, we obtained $k_{1a}^{(\mathrm{N_2})} = (9.1 \pm 3.6) \times 10^{-33}$ cm^6 molecules^{-2} s^{-1}, $k_{1a}^{(\mathrm{CO})} = (2.0 \pm 0.8) \times 10^{-32}$ cm^6 molecules^{-2} s^{-1}, and $r_{\mathrm{loss,exp}} = (4.0 \pm 0.4) \times 10^4$ s^{-1}. The statistical and systematic errors in these parameters are given in table S4.

To verify the reaction kinetics, we constructed a rate equation model of the OD + CO chemistry, which included the decay channels from secondary chemistry, to fit the *trans*-DOCO and OD time traces up to 1 ms (supplementary materials, section 4). We fit one overall scaling factor for both OD and *trans*-DOCO, which accounts for uncertainties in (i) the optical path length and (ii) photolysis yield and subsequent OD* quenching reactions that establish the initial steady-state concentration of OD. We also fit an additional *trans*-DOCO loss, $r_{\mathrm{loss,model}}$, to correctly capture the *trans*-DOCO concentration at t > 100 μs.

The *trans*-DOCO + O_3 → OD + CO_2 + O_2 rate coefficient (*9*) ($k_{\mathrm{O_3+DOCO}} \approx 4 \times 10^{-11}$ cm^3 molecules^{-1} s^{-1}) and the OD + CO termolecular rate coefficients from our experimentally measured values were fixed in the model. Representative fits for two different conditions based on the same rate equation model are shown in Fig. 4, A and B. We found good fits ($\chi^2_{\mathrm{red}} = 0.71$) with a single, consistent set of parameters over a wide range of CO, N_2, and O_3 concentrations, giving $r_{\mathrm{loss,model}} = (4.7 \pm 0.7) \times 10^3$ s^{-1} for all conditions (fig. S13A). The sum of loss contributions from $k_{\mathrm{O_3+DOCO}}[\mathrm{O_3}]$ and an additional loss from $r_{\mathrm{loss,model}}$ gives a total loss of ~4.5×10^4 s^{-1}, consistent with our measured $r_{\mathrm{loss,exp}}$. One possibility for $r_{\mathrm{loss,model}}$ is a second product branching channel of *trans*-DOCO + O_3 to produce DO_2 + CO_2 + O. The slight discrepancy of the *trans*-DOCO data with the rate equation model in Fig. 4B is possibly due to the inadequately constrained loss processes at long delay times.

Sources of systematic uncertainty have been carefully evaluated. First, we considered the impact of vibrationally hot OD at early times. We constrained the population of vibrationally excited OD in our system by directly observing several hot band transitions from OD(v = 1) (fig. S7). We observed that CO is an efficient quencher of OD vibration, with a measured OD(v = 1) lifetime (fig. S8) that is consistent with the OD(v = 1) + CO quenching rate reported by Brunning *et al.* (*17*) and Kohno *et al.* (*29*). These measurements reveal that the lifetime is well below the minimum integration time of 10 μs and that [OD(v = 1)] is less than 10% of [OD(v = 0)] in this time window. Given that OD(v = 1) is expected to produce stabilized *trans*-DOCO less efficiently than OD(v = 0), the systematic effect caused by the vibrationally hot OD is estimated to be <10%, which has been included in our total error budget (table S4).

Another systematic uncertainty arises from the finite camera integration time, which is large relative to (50 μs) or comparable to (10 μs) the early *trans*-DOCO rise time. The recovered k_{1a} values from the two integration times are consistent with each other to within 21%, which we have included as a systematic uncertainty in our measurement (fig. S6).

A third source of systematic uncertainty comes from any factors that would cause deviations from Eq. 2; therefore, we investigated the dependence of k_{1a} on D_2 and O_3 concentrations. Additional experiments were conducted in the same manner as the CO and N_2 experiments, but varying [O_3] (1×10^{14} to 4×10^{15} molecules cm^{-3}) and [D_2] (7×10^{16} to 1×10^{18} molecules cm^{-3}). Under our experimental conditions and using a 50-μs camera integration window, we observed a weak dependence of k_{1a} on [O_3]

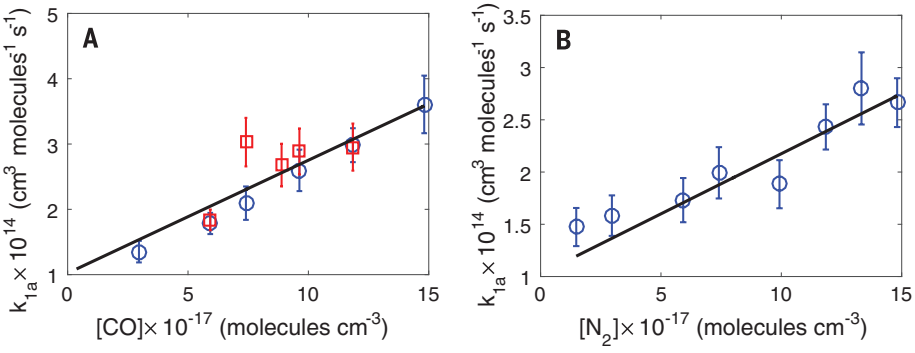

Fig. 3. Determination of the termolecular *trans*-DOCO formation rate. The bimolecular *trans*-DOCO formation rate coefficient, k_{1a}, is plotted as a function of [CO] and [N_2] to determine the termolecular rate coefficients $k_{1a}^{(\mathrm{CO})}$ and $k_{1a}^{(\mathrm{N_2})}$. Each point represents one of 26 experimental conditions tabulated in table S1. In both panels, the error bars represent uncertainties from fits to Eqs. 2 to 4 and the measured densities of the gases. (**A**) k_{1a} is plotted as a function of [CO] while [N_2] = 8.9×10^{17} molecules cm^{-3} is held constant. (**B**) k_{1a} is plotted as a function of [N_2] while [CO] = 5.6×10^{17} molecules cm^{-3} is held constant. In both plots, D_2 and O_3 concentrations are fixed at 7.4×10^{16} and 1×10^{15} molecules cm^{-3}, respectively. Blue and red data points indicate 50- and 10-μs camera integration times, respectively. The data in (A) and (B) are simultaneously fitted to Eq. 4. The black lines in (A) and (B) are obtained from weighted linear fits ($\chi^2_{\mathrm{red}} = 0.86$). The y offsets in the data arise from the nonzero concentrations of N_2 and CO in (A) and (B), respectively.

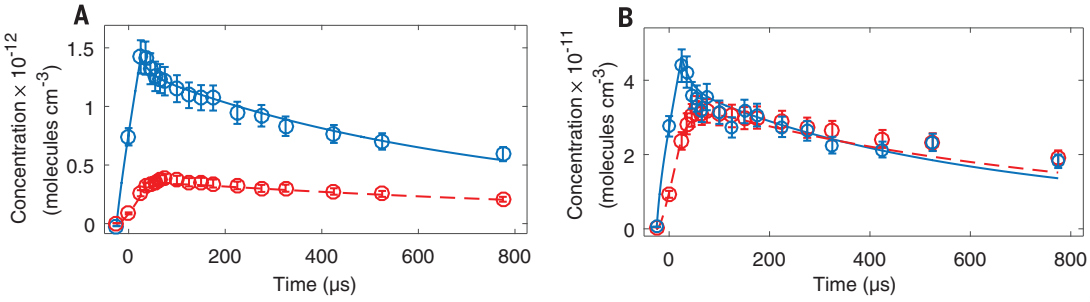

Fig. 4. Rate equation model fitting. The OD (blue circles) and *trans*-DOCO (red circles) traces are weighted fits to the model (solid and dashed lines for OD and *trans*-DOCO, respectively) described in the supplementary materials. The integration time was 50 μs. The error bars are from uncertainties in the spectral fit, in the same manner as for Fig. 2B. The input k_{1a} values for both CO and N_2 were from the early-time *trans*-DOCO rise analysis and were fixed in the fit. The floated parameters included a single scaling factor for the OD and *trans*-DOCO intensities and an extra DOCO loss channel. (**A**) [CO] = 5.9×10^{17} molecules cm^{-3}. (**B**) [CO] = 1.2×10^{18} molecules cm^{-3}. For both data sets, [N_2] = 8.9×10^{17}, [D_2] = 7.4×10^{16}, and [O_3] = 1×10^{15} molecules cm^{-3} were fixed.

(fig. S11) and no statistically significant variation with [D_2] (fig. S10). The O_3 dependence was measured at a CO concentration of 1.5×10^{17} molecules cm^{-3}. From analysis of the early-time *trans*-DOCO rise as a function of [O_3] and [D_2], we determined that O_3 and D_2 contribute an additional 11 and 8% statistical uncertainty, respectively, to our total budget (table S4).

We found that CO is ~100% more effective as a collision partner than N_2 in promoting the termolecular association of *trans*-DOCO. This result was missed in previous studies, which minimized the CO concentration ($<4 \times 10^{16}$ molecules cm^{-3}) to avoid biasing a pseudo–first order kinetics measurement (*12*, *38*). One might naïvely expect CO to be similar to N_2 as a third body; the significant difference observed here could be due to (i) near-resonant energy transfer between CO and the CO mode in DOCO, (ii) a stronger interaction potential between CO and DOCO*, or (iii) an influence of more efficient CO on OD(v) quenching for which we have not correctly accounted.

In the low-pressure regime, our measurements of the association rate coefficient, k_{1a}, can be compared to the pressure dependence of the overall rate of OD + CO, k_1, measured in previous experiments in N_2. Most of the pressure dependence of k_1 comes from k_{1a}, because k_{1b} is expected to change only slightly in this range. The termolecular (linear) components of the reported k_1 values from earlier studies by Paraskevopoulos *et al.* (*14*) and Golden *et al.* (*11*) fall within 1σ of our measured $k_{1a}^{(N_2)}$, which may suggest a k_{1a} contribution to the previously reported k_1. Apparent curvature in the pressure dependence observed elsewhere suggests that k_{1a} may already be in the fall-off regime. To estimate the *trans*-DOCO branching yield {percent yield ≈ $k_{1a}/[k_{1a} + k_1(\text{total pressure } p = 0 \text{ torr})]$}, we took the average value of k_1 from Paraskevopoulos *et al.* (*14*), Golden *et al.* (*11*), and Westenberg *et al.* (*39*). Even at low total pressures (75 torr of N_2), our results show that OD + CO produces a *trans*-DOCO yield of nearly 28 ± 11%.

Optical frequency comb spectroscopy allows broadband, time-resolved absorption detection of radicals with exceptional sensitivity and high spectral resolution. Our results demonstrate the capabilities of time-resolved cavity-enhanced direct frequency comb spectroscopy to elucidate chemical mechanisms through the quantitative detection of intermediates and primary products in real time. Our quantification of the termolecular dependence reveals additional factors that affect the product branching of the OH + CO reaction, which must be included in future atmospheric and combustion model predictions. For example, sensitivity analyses by Boxe *et al.* (*40*) have shown that, depending on the branching ratio, HOCO could contribute 25 to 70% of the total CO_2 concentration in the Martian atmosphere. Our experiment can be readily extended to detect other primary products (DO_2 or CO_2), as well as to study the OH/HOCO system. Furthermore, dynamics and nonthermal processes such as chemical activation, energy transfer, and rovibrational state-specific kinetics can be studied. With the bandwidth of optical frequency comb sources spanning an octave or more, the potential of this approach has not yet been fully realized. The technologies of frequency comb sources, detection methods, and mirror coatings are developing rapidly and will allow for more expansive applications of this multiplexed technique to many other important chemistry problems.

REFERENCES AND NOTES

1. A. W. Jasper *et al.*, *Science* **346**, 1212–1215 (2014).
2. T. L. Nguyen, B. C. Xue, R. E. Weston Jr., J. R. Barker, J. F. Stanton, *J. Phys. Chem. Lett.* **3**, 1549–1553 (2012).
3. J. S. Francisco, J. T. Muckerman, H. G. Yu, *Acc. Chem. Res.* **43**, 1519–1526 (2010).
4. C. J. Johnson, R. Otto, R. E. Continetti, *Phys. Chem. Chem. Phys.* **16**, 19091–19105 (2014).
5. J. Lelieveld *et al.*, *Nature* **452**, 737–740 (2008).
6. R. L. Mauldin 3rd *et al.*, *Nature* **488**, 193–196 (2012).
7. I. W. M. Smith, R. Zellner, *J. Chem. Soc., Faraday Trans. II* **69**, 1617–1627 (1973).
8. J. Troe, *J. Chem. Phys.* **75**, 226–237 (1981).
9. D. Fulle, H. F. Hamann, H. Hippler, J. Troe, *J. Chem. Phys.* **105**, 983–1000 (1996).
10. C. W. Larson, P. H. Stewart, D. M. Golden, *Int. J. Chem. Kinet.* **20**, 27–40 (1988).
11. D. M. Golden *et al.*, *J. Phys. Chem. A* **102**, 8598–8606 (1998).
12. D. C. McCabe, T. Gierczak, R. K. Talukdar, A. R. Ravishankara, *Geophys. Res. Lett.* **28**, 3135–3138 (2001).
13. G. Paraskevopoulos, R. S. Irwin, *J. Chem. Phys.* **80**, 259–266 (1984).
14. G. Paraskevopoulos, R. S. Irwin, *Chem. Phys. Lett.* **93**, 138–143 (1982).
15. M. J. Frost, P. Sharkey, I. W. M. Smith, *Faraday Discuss.* **91**, 305–317 (1991).
16. M. J. Frost, P. Sharkey, I. W. M. Smith, *J. Phys. Chem.* **97**, 12254–12259 (1993).
17. J. Brunning, D. W. Derbyshire, I. W. M. Smith, M. D. Williams, *J. Chem. Soc., Faraday Trans. II* **84**, 105–119 (1988).
18. R. E. Weston Jr., T. L. Nguyen, J. F. Stanton, J. R. Barker, *J. Phys. Chem. A* **117**, 821–835 (2013).
19. W. C. Chen, R. A. Marcus, *J. Chem. Phys.* **123**, 094307 (2005).
20. C. H. Chang, G. T. Buckingham, D. J. Nesbitt, *J. Phys. Chem. A* **117**, 13255–13264 (2013).
21. T. Oyama, W. Funato, Y. Sumiyoshi, Y. Endo, *J. Chem. Phys.* **134**, 174303 (2011).
22. M. C. McCarthy *et al.*, *J. Chem. Phys.* **144**, 124304 (2016).
23. A. J. Fleisher *et al.*, *J. Phys. Chem. Lett.* **5**, 2241–2246 (2014).
24. F. Adler *et al.*, *Opt. Lett.* **34**, 1330–1332 (2009).
25. G. D. Cole *et al.*, *Optica* **3**, 647–656 (2016).
26. J. C. Brock, R. T. Watson, *Chem. Phys. Lett.* **71**, 371–375 (1980).
27. J. E. Butler, R. G. Macdonald, D. J. Donaldson, J. J. Sloan, *Chem. Phys. Lett.* **95**, 183–188 (1983).
28. M. Brouard, D. W. Hughes, K. S. Kalogerakis, J. P. Simons, *J. Chem. Phys.* **112**, 4557–4571 (2000).
29. N. Kohno, M. Izumi, H. Kohguchi, K. Yamasaki, *J. Phys. Chem. A* **115**, 4867–4873 (2011).
30. N. F. Scherer, L. R. Khundkar, R. B. Bernstein, A. H. Zewail, *J. Chem. Phys.* **87**, 1451–1453 (1987).
31. S. I. Ionov, G. A. Brucker, C. Jaques, L. Valachovic, C. Wittig, *J. Chem. Phys.* **99**, 6553–6561 (1993).
32. D. C. Clary, G. C. Schatz, *J. Chem. Phys.* **99**, 4578–4589 (1993).
33. M. I. Hernández, D. C. Clary, *J. Chem. Phys.* **101**, 2779–2784 (1994).
34. C. Western, *J. Quant. Spectro. Rad. Transfer* 10.1016/j.jqsrt.2016.04.010 (2016).
35. J. T. Petty, C. B. Moore, *J. Chem. Phys.* **99**, 47–55 (1993).
36. M. C. Abrams, S. P. Davis, M. L. P. Rao, R. Engleman, *J. Mol. Spectrosc.* **165**, 57–74 (1994).
37. R. A. Toth, *J. Mol. Spectrosc.* **195**, 98–122 (1999).
38. Y. Liu, S. P. Sander, *J. Phys. Chem. A* **119**, 10060–10066 (2015).
39. A. A. Westenberg, W. E. Wilson, *J. Chem. Phys.* **45**, 338–342 (1966).
40. C. S. Boxe *et al.*, *Icarus* **242**, 97–104 (2014).

ACKNOWLEDGMENTS

Additional data supporting the conclusions are available in supplementary materials. We thank K. Sung of the NASA Jet Propulsion Laboratory (JPL) for providing a list of D_2O mid-IR line positions and intensities measured by R. A. Toth of JPL. We acknowledge financial support from the Air Force Office of Scientific Research, the Defense Advanced Research Projects Agency (DARPA) Spectral Combs from UV to THz (SCOUT) program, the National Institute of Standards and Technology, NSF, and DARPA (grants FAA-9550-14-C-0030 and W31P4Q-16-C-0001). M.O. is supported by NSF grant CHE-1413712. T.Q.B. and B.S. are supported by the National Research Council Research Associate Fellowship, P.B.C. is supported by the NSF Graduate Research Fellowship Program, and O.H.H. is partially supported through a Humboldt Fellowship. P.H., D.F., and C.D. are employees of a startup company (Crystalline Mirror Solutions), cofounded by G.D.C. and M.A., and coinventors on a submitted patent focusing on the crystalline mirror technology applied in this Report.

SUPPLEMENTARY MATERIALS

www.sciencemag.org/content/354/6311/444/suppl/DC1
Materials and Methods
Figs. S1 to S13
Tables S1 to S4
References (*41*–*62*)

20 May 2016; resubmitted 24 August 2016
Accepted 28 September 2016
10.1126/science.aag1862

CATALYSIS

Super-dry reforming of methane intensifies CO_2 utilization via Le Chatelier's principle

Lukas C. Buelens,[1] Vladimir V. Galvita,[1]* Hilde Poelman,[1] Christophe Detavernier,[2] Guy B. Marin[1]*

Efficient CO_2 transformation from a waste product to a carbon source for chemicals and fuels will require reaction conditions that effect its reduction. We developed a "super-dry" CH_4 reforming reaction for enhanced CO production from CH_4 and CO_2. We used $Ni/MgAl_2O_4$ as a CH_4-reforming catalyst, $Fe_2O_3/MgAl_2O_4$ as a solid oxygen carrier, and CaO/Al_2O_3 as a CO_2 sorbent. The isothermal coupling of these three different processes resulted in higher CO production as compared with that of conventional dry reforming, by avoiding back reactions with water. The reduction of iron oxide was intensified through CH_4 conversion to syngas over Ni and CO_2 extraction and storage as $CaCO_3$. CO_2 is then used for iron reoxidation and CO production, exploiting equilibrium shifts effected with inert gas sweeping (Le Chatelier's principle). Super-dry reforming uses up to three CO_2 molecules per CH_4 and offers a high CO space-time yield of 7.5 millimole CO per second per kilogram of iron at 1023 kelvin.

One strategy for mitigating CO_2 emissions is to use it to produce value-added chemicals or fuels (*1*–*4*). Its conversion can provide an efficient means of storing renewable energy (*5*) because the produced chemicals and fuels have a high energy density (*3*). Biological processes can reduce CO_2 (*6*)—for example, conversion into carbohydrates via photosynthesis—but are relatively slow. Three main approaches have been used to overcome the endothermicity of CO_2 in an industrial setting: (i) Electrochemical reduction makes use of a (photo)electric current (*7*, *8*). (ii) Thermal reduction splits CO_2 into CO and O_2, typically above 1400 K. Despite the advances made in high-temperature solar heat accumulation and the development of promising thermochemical redox cycles (*9*–*12*), its commercial application still faces several major challenges (*12*). (iii) Chemical reduction of CO_2 involves the rearrangement of chemical bonds in a reducing agent such as methane (CH_4) (*13*–*15*) or H_2. Compared with electrochemical, thermal, and biological processes, dry reforming of CH_4 (DRM) (Eq. 1), a chemical reduction process that produces CO and H_2 ("syngas"), has actually been developed on a commercial scale for steel industry (*16*).

$$CH_{4\,(g)} + CO_{2\,(g)} \rightarrow 2CO_{(g)} + 2H_{2\,(g)} \quad \Delta H°_{298K} = 247\ kJ\ mol^{-1}_{CH_4} \qquad (1)$$

However, because DRM proceeds in conditions in which water is generated, the water-gas shift (WGS) reaction (Eq. 2) can lead to unwanted back-reaction to CO_2.

$$CO_{(g)} + H_2O_{(g)} \rightleftharpoons CO_{2\,(g)} + H_{2\,(g)} \quad \Delta H°_{298K} = -41\ kJ\ mol^{-1}_{CO} \qquad (2)$$

We propose an approach for CO_2 transformation through chemical reduction that leads to

[1]Laboratory for Chemical Technology, Ghent University, Technologiepark 914, B-9052 Ghent, Belgium. [2]Department of Solid State Sciences, Ghent University, Krijgslaan 281, S1, B-9000 Ghent, Belgium.
*Corresponding author. Email: vladimir.galvita@ugent.be (V.V.G.); guy.marin@ugent.be (G.B.M.)

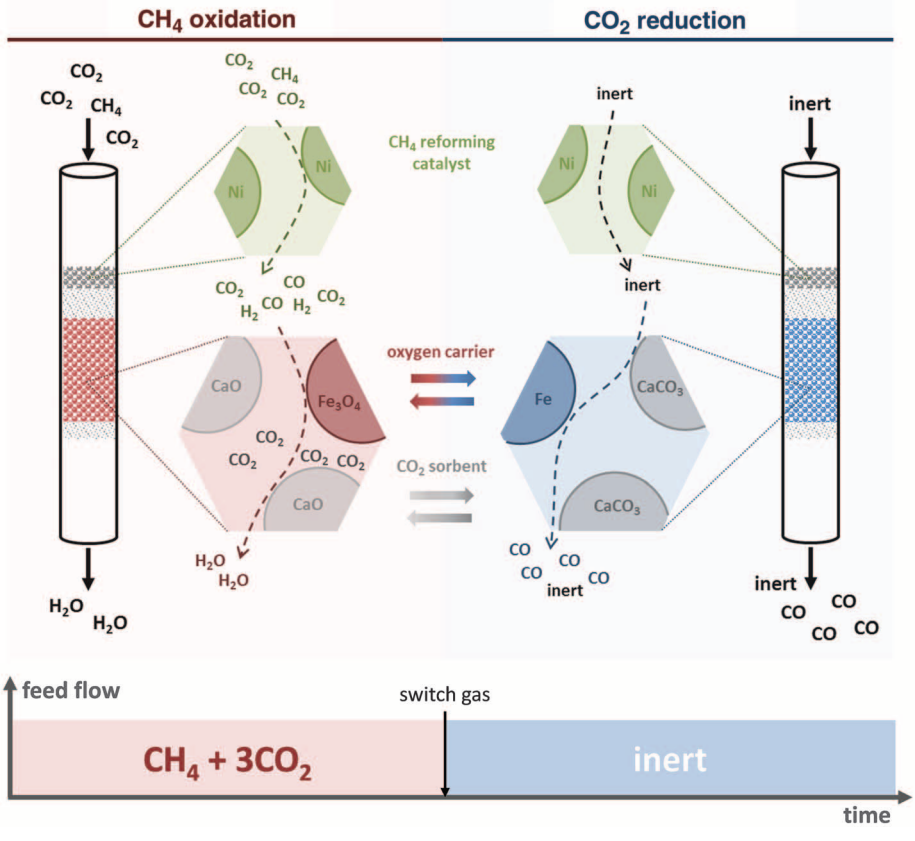

Fig. 1. Schematic representation of the proposed process. Super-dry reforming of CH_4-enhanced CO production from CH_4 and CO_2. In the CH_4 oxidation step, Ni catalyzes the CO_2-reforming of CH_4 into syngas, Fe_3O_4 is reduced by syngas with formation of CO_2 and H_2O, and carbonation of CaO yields in situ CO_2 removal. Overall, CH_4 is oxidized into CO_2 and H_2O, Fe_3O_4 has been reduced to Fe, and $CaCO_3$ has been formed from CaO and CO_2. The CO_2-reduction step consists of $CaCO_3$ decomposition into CaO and CO_2 and Fe oxidation to Fe_3O_4 through the reduction of CO_2 into CO.

intensified CO production. Super-dry reforming of CH_4 uses earth-abundant materials 90CaO/Al_2O_3 as a CO_2 sorbent, 50Fe_2O_3/$MgAl_2O_4$ as a solid oxygen carrier (*17*), 10NiO/$MgAl_2O_4$ as a CH_4 reforming catalyst (*18*), a ratio of CO_2 to CH_4 that approaches 3:1, and two flow processes (Fig. 1). Although the reaction proceeds at high temperatures (1023 K), carbon deposition is avoided.

The application of CaO as a CO_2 sorbent has received much attention for several applications, among which are sorption-enhanced steam reforming for H_2 production (*19*) and combined chemical looping (*5*). All of these processes, however, require a temperature swing to regenerate the CO_2 sorbent. In this work, we applied CaO as a CO_2 sorbent in an isothermal fashion. Besides improving the total oxidation of CO by Fe_3O_4 following Le Chatelier's principle, the removal of CO_2 by CaO during CH_4 oxidation has several other benefits. First, in situ CO_2 removal allows the use of reducing gas feedstocks that are ranked lower in the value chain than natural gas—for example, biogas containing up to 40% CO_2—that are cheaper than natural gas. The effect of in situ CO_2 removal is best assessed by defining the ratio between reducing and oxidizing gases, also called the reduction capacity (R_c) of the gas mixture (Eq. 3)

$$R_c = \frac{p_{CO} + p_{H_2}}{p_{CO_2} + p_{H_2O}} \quad (3)$$

The most stable oxidation state of Fe tends to decrease with increasing reduction capacity. Another benefit lies in the combination of $CaCO_3$ formation, an exothermic process, with CH_4-reforming and iron oxide reduction reactions, which are mostly endothermic processes (table S1) (*20*). Moreover, upon isothermal decomposition of $CaCO_3$, CO_2 is released during the CO_2 reduction step and converted in situ into CO over the adjacent solid oxygen carrier. By switching the feed to an inert sweep gas in the CO_2 reduction step, the remaining H_2O formed during CH_4 oxidation is purged, and the formation of an equilibrium mixture of CO_2, CO, H_2O, and H_2 is circumvented. Thus, the proposed process avoids loss in CO yield caused by the WGS reaction and is "super-dry." Instead, a mixture of mainly CO along with CO_2 is formed, resulting in a more efficient utilization of CH_4 for CO_2 conversion. This method for intensified CO_2 utilization is termed "super-dry reforming of CH_4." The global reaction of this two-step process is shown in Eq. 4, in which CO and H_2O are inherently separated because of the two-step process configuration

$$CH_{4\,(g)} + 3CO_{2\,(g)} \rightarrow 4CO_{(g)} + 2H_2O_{(g)}$$
$$\Delta H^\circ_{298K} = 330\ \text{kJ mol}^{-1}_{CH_4} \quad (4)$$

Despite the apparently higher endothermicity of the super-dry reforming process as compared with that of conventional DRM (Eq. 1), the required heat input per mole CO_2 converted is much lower (110 kJ $mol^{-1}_{CO_2}$ compared with 247 kJ $mol^{-1}_{CO_2}$). Last, given the availability of a renewable source of H_2, applications are possible in which CO and H_2 can be combined in different ratios for the formation of chemicals or fuels (*2*, *21*, *22*). Indeed, an efficient and separate production of high-purity CO and H_2 would further establish the role of syngas as a versatile and flexible platform mixture.

The role of calcium oxide for the reducibility of iron oxide was studied through time-resolved in situ x-ray diffraction (XRD). CaO promoted by Al_2O_3 was used as the CO_2 sorbent because of its stability during cycles of carbonation and regeneration. The role of Al_2O_3 is to cover the active CaO phase and improve its resistance to sintering. An example of this property is given in Fig. 2A, which shows the enrichment of Al_2O_3 on the surface of CaO particles. The oxygen carrier material consists of active Fe_2O_3 particles, dispersed in a matrix of $MgAl_2O_4$ particles (Fig. 2B).

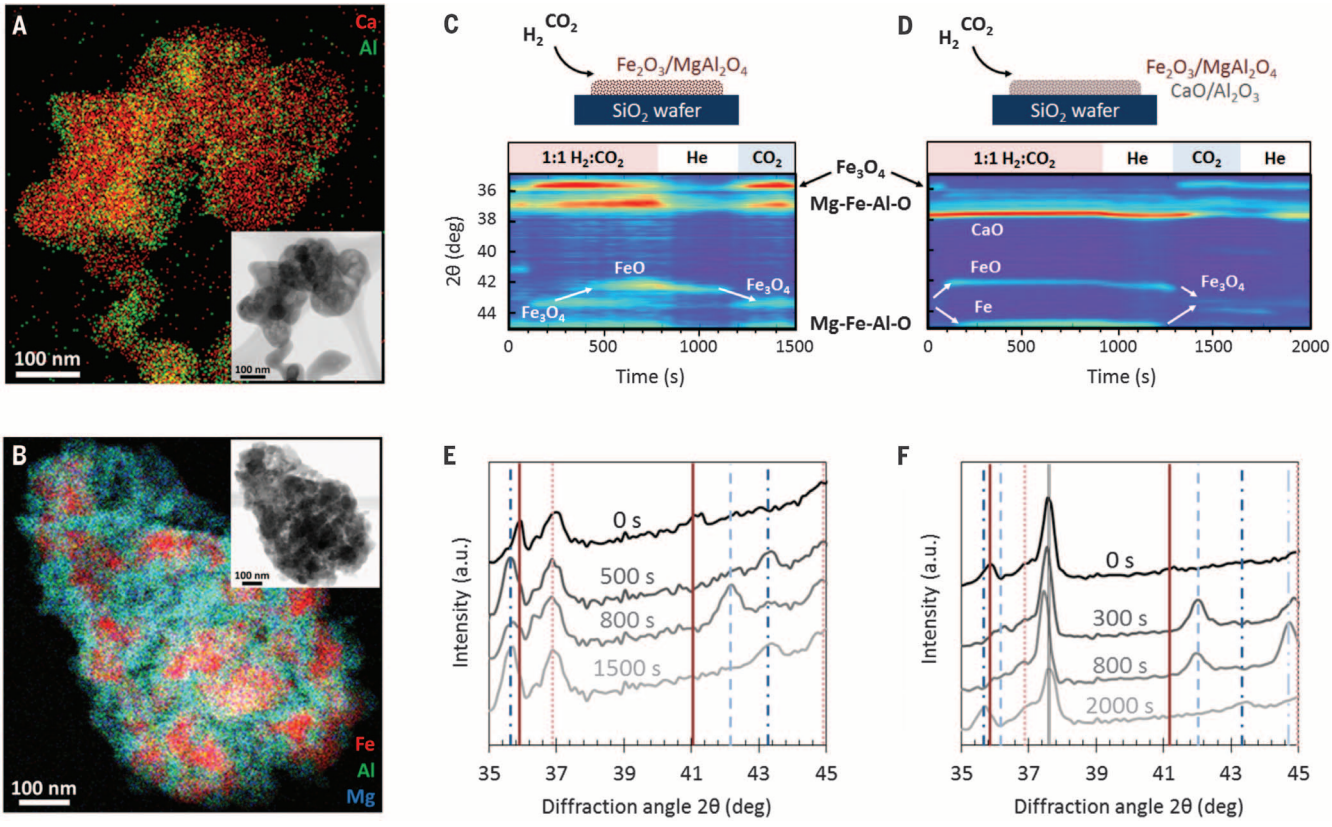

Fig. 2. Characterization studies. (**A** and **B**) Energy-dispersive x-ray elemental map of fresh (A) 90CaO/Al_2O_3 and (B) 50Fe_2O_3/$MgAl_2O_4$. (Inset) Corresponding bright-field scanning transmission electron microscopy (BF-STEM) image. (**C** and **D**) 2D in situ XRD map representing experiments with (C) 50Fe_2O_3/$MgAl_2O_4$ and (D) 50Fe_2O_3/$MgAl_2O_4$ + 90CaO/Al_2O_3 [1:2 weight % (wt %)] at pressure (p) = 1.013 bar, temperature (T) = 1023 K, and feed flow rate (F_0) = 1.8 Nml s^{-1} (5% H_2 and 5% CO_2 in N_2; 100% He; 100% CO_2). White arrows indicate the reduction of Fe_3O_4 to FeO/Fe and subsequent reoxidation to Fe_3O_4. (**E** and **F**) In situ XRD cross sections for (E) 50Fe_2O_3/$MgAl_2O_4$ at 0, 500, 800, and 1500 s and (F) 50Fe_2O_3/$MgAl_2O_4$ + 90CaO/Al_2O_3 at 0, 300, 800, and 2000 s. Brown line, Fe_2O_3 (35.9°); dotted pink line, Mg-Fe-Al-O (37°); dot-dashed dark blue line, Fe_3O_4 (35.6°); dashed light blue line, FeO (42.2°); dot-dot-dashed gray line, Fe (44.6°); and black double line, CaO (37.6°).

This structure provides high thermal stability (fig. S15) (*20*) and hence allows the maintaining of high redox activity of the oxygen carrier. A two-dimensional (2D) representation of XRD spectra is shown in Fig. 2C, taken while treating $Fe_2O_3/MgAl_2O_4$ with an equimolar feed of H_2 and CO_2 at 1023 K. In Fig. 2E, a selection of single XRD patterns corresponding with cross sections of the 2D map in Fig. 2C are presented.

To study the influence of CaO as CO_2 sorbent, a similar experiment was performed, in which CaO/Al_2O_3 was added to $Fe_2O_3/MgAl_2O_4$ in a physical mixture with a weight ratio of 2:1. The in situ XRD results are presented in Fig. 2, D and F. In this case, applying an equimolar feed of H_2 and CO_2 at 1023 K allowed the reduction to reach equilibrium between FeO and Fe. These findings are in good agreement with thermodynamic calculations (fig. S7) (*20*). Indeed, the latter indicate that the applied conditions lie near the equilibrium line of Fe_3O_4 and FeO where no CO_2 is removed. On the basis of thermodynamic equilibrium between CaO and $CaCO_3$ (fig. S5) (*20*) and Eq. 4, the expected effect of the CO_2 sorbent is to reduce the partial pressure of CO_2 and thereby increase the reduction capacity R_c. Hence, the extent of reduction has increased drastically (fig. S7, equilibrium line FeO/Fe) (*20*). Thus, the addition of CaO improves the reduction of iron oxide when applying a mixture of reducing and oxidizing gases such as biogas.

On the basis of thermodynamic calculations (figs. S3 and S4) (*20*) and experimental results (fig. S8) (*20*), working conditions were selected to obtain a high CH_4 conversion (> 99%) while avoiding formation of carbon deposits. These conditions efficiently use CH_4 as reducing agent, resulting in a lower oxidation state of Fe in the oxygen carrier after the CH_4 oxidation step and a higher yield of CO in the CO_2 reduction step. Shown in Fig. 3A are the results obtained under isothermal operation at 1023 K of the process scheme as given in Fig. 1. At breakthrough of CO_2, after 20 s of CH_4 oxidation, the feed was changed to He as sweep gas to initiate the CO_2 reduction. As $CaCO_3$ decomposed, CO_2 was released and immediately converted into CO over FeO and/or Fe, which is thereby oxidized to Fe_3O_4.

The experiment shown in Fig. 3A resulted in an integrated yield of 2.9 $mol_{CO}\ mol_{CH_4}^{-1}$ (table S4) (*20*), which proved to be stable over 25 cycles. In comparison with the theoretical CO yield of 2 $mol_{CO}\ mol_{CH_4}^{-1}$ corresponding with the conventional DRM (Eq. 1), a 45% higher CO yield is obtained. However, when feeding extra CO_2 subsequent to the super-dry reforming process, an additional amount of CO was formed. This additional CO indicates that FeO and/or Fe was not completely reoxidized into Fe_3O_4 upon CO_2 release by decomposition of $CaCO_3$ and brought the maximum CO yield to 3.9 $mol_{CO}\ mol_{CH_4}^{-1}$. This yield corresponds well with the global reaction stoichiometry for super-dry reforming of CH_4 (Eq. 4). The actual CO yield could be further improved by increasing the amount of CO_2 fed to the reactor in the first step—for example, to 3.1 $mol_{CO}\ mol_{CH_4}^{-1}$ when feeding CH_4:CO_2 in 1:4 molar ratio (fig. S18 and table S4) (*20*), albeit at the cost of a lower overall CO_2 conversion (62 versus 73%) and a reduced purity of the CO product stream. Alternatively, an improved CO yield could be achieved by changing the reactor configuration from alternating cocurrent feed to alternating countercurrent feed operation (*23*).

Presented in Fig. 3B is a dynamic simulation of the space-time yield of CO and CO_2 when considering a multireactor configuration (fig. S2 and eq. S7) (*20*), starting from the single-reactor experiment (Fig. 3A). Similar configurations are successfully applied on an industrial scale, for instance in pressure swing adsorption units for H_2 production and recovery. The results indicate that using this configuration, a space-time yield of 7.5 $mmol_{CO}\ s^{-1}\ kg_{Fe}^{-1}$ could be achieved in cyclic steady state, forming a product stream composed of 85% CO and 15% CO_2. Besides CO,

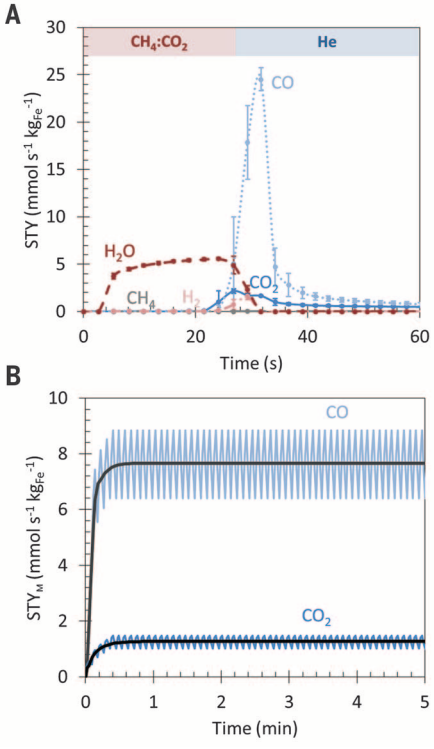

Fig. 3. Reaction studies. (**A**) Space-time yield during a cyclic experiment performed in a single-reactor configuration by using $10NiO/MgAl_2O_4$ + $50Fe_2O_3/MgAl_2O_4$ + $90CaO/Al_2O_3$ (1:3:6 wt %) at T = 1023 K, p = 1.3 bar, and $F_0 = 1.35\ 10^{-6}$ mol s^{-1} (CH_4:CO_2 in 1:3 molar ratio; He as sweep gas). Dot-dot-dashed dark gray line, CH_4; dotted light blue line, CO; dot-dashed pink line, H_2; dark blue line, CO_2; and dashed brown line, H_2O. Error bars indicate the 95% confidence interval based on five repeat experiments. (**B**) Dynamic simulation of the space-time yield when applying the conditions and results of the single-reactor experiment shown in (A) to an eight-reactor configuration for super-dry reforming of CH_4 (fig. S2). Light blue line, CO; dark blue line, CO_2. Thick curves in (B) are guides to the eye, representative for the time-averaged space-time yield. Space-time yield for single reactor and for multitubular reactor configuration are calculated with eqs. S5 and S7.

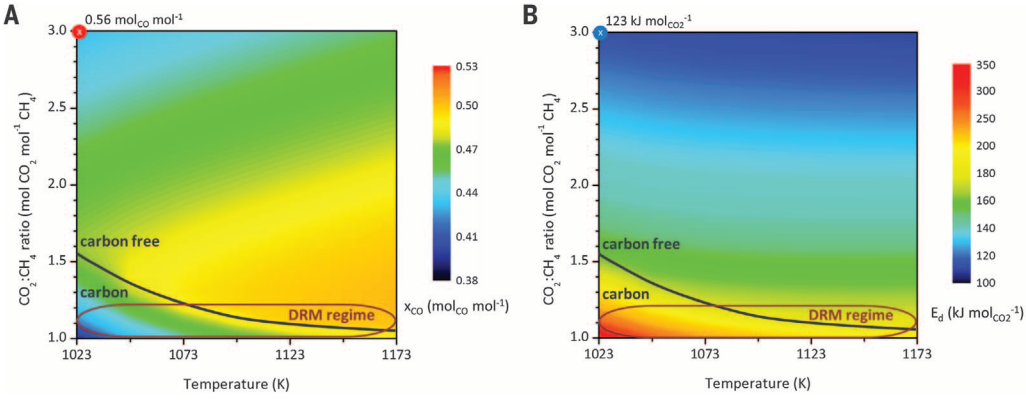

Fig. 4. Thermodynamics studies. (**A**) CH_4 dry reforming equilibrium molar fraction of CO as a function of CO_2:CH_4 feed ratio and temperature (p = 1.013 bar). (**B**) Equilibrium exergy destruction (kilojoules per mole CO_2 converted) as a function of CO_2:CH_4 feed ratio and temperature (p = 1.013 bar). The region under the black curve represents the conditions under which carbon formation is thermodynamically favorable, and the oval shows the region of interest for conventional dry reforming of CH_4 (DRM regime). The solid-circled "X" indicates the conditions and value that apply to super-dry reforming.

water vapor was produced in high purity in the case of full CH_4 conversion. Because a sweep gas was used, the CO in the product stream was diluted, and a molar fraction of 0.56 rather than 0.85 was obtained. However, this is still 30% higher than the equilibrium molar fraction of CO in conventional dry reforming at the same conditions (Fig. 4A). Moreover, our goal was not to optimize the flow of sweep gas, but rather to highlight the possibilities based on a combination of known processes. Hence, it may be possible to further increase the yield and purity of CO by fine-tuning process variables, reactor configuration, or materials. This flexibility is not evident at all for the conventional DRM process, which is limited in yield by the WGS reaction (Eq. 2).

Exergy calculations (which account for irreversible losses) were performed to estimate the energetics of the proposed process (Fig. 4B and fig. S23B) (*20*). Along with the advantage of improved product purity, super-dry reforming of CH_4 also resulted in a very low exergy destruction per mole CO_2 converted (Fig. 4B). Indeed, the exergy destruction for CO_2 conversion is up to 25 to 50% lower as compared with that of conventional DRM. The latter typically requires operating temperatures of 1073 to 1273 K in order to reach high-equilibrium conversion of CH_4 and CO_2 while minimizing the thermodynamic driving force for carbon formation (*13*). Compared with these requirements, super-dry reforming shows both practical and economic benefits. For one, the requirement of a noble metal catalyst in order to mitigate excessive carbon formation (*13*) becomes obsolete because conditions of super-dry reforming are thermodynamically unfavorable for carbon deposition. Hence, the application of cheaper Ni-based catalysts is perfectly feasible, even at temperatures as low as 1023 K.

The product streams of super-dry reforming have a higher purity than those of conventional CH_4 reformers, which should reduce separation costs. Moreover, by applying Le Chatelier's principle to lift CO_2 utilization efficiency, each molecule of CH_4 theoretically allows the conversion of three molecules of CO_2, making super-dry reforming of CH_4 an intensified process for isothermal CO_2 utilization. The presence of a CO_2 acceptor, in this case CaO, allows for the application of renewable feedstocks such as biogas as a reducing agent for iron oxide reduction.

REFERENCES AND NOTES

1. L. Li, N. Zhao, W. Wei, Y. Sun, *Fuel* **108**, 112–130 (2013).
2. C. Song, *Catal. Today* **115**, 2–32 (2006).
3. M. Aresta, A. Dibenedetto, A. Angelini, *J. CO_2 Util.* **34**, 65–73 (2013).
4. M. E. Boot-Handford *et al.*, *Energ. Environ. Sci.* **7**, 130–189 (2014).
5. V. V. Galvita, H. Poelman, G. B. Marin, *J. Power Sources* **286**, 362–370 (2015).
6. J. C. Liao, L. Mi, S. Pontrelli, S. Luo, *Nat. Rev. Microbiol.* **14**, 288–304 (2016).
7. S. Lin *et al.*, *Science* **349**, 1208–1213 (2015).
8. M. Schreier *et al.*, *Nat. Commun.* 10.1038/ncomms8326 (2015).
9. J. R. Scheffe, J. Li, A. W. Weimer, *Int. J. Hydrogen Energy* **35**, 3333–3340 (2010).
10. J. R. Scheffe, A. Steinfeld, *Mater. Today* **17**, 341–348 (2014).
11. C. L. Muhich *et al.*, *Science* **341**, 540–542 (2013).
12. T. Kodama, N. Gokon, *Chem. Rev.* **107**, 4048–4077 (2007).
13. D. Pakhare, J. Spivey, *Chem. Soc. Rev.* **43**, 7813–7837 (2014).
14. J. Hu *et al.*, *J. CO_2 Util.* **16**, 8–16 (2016).
15. V. V. Galvita, H. Poelman, C. Detavernier, G. B. Marin, *Appl. Catal. B* **164**, 184–191 (2015).
16. O. Muraza, A. Galadima, *Int. J. Energy Res.* **39**, 1196–1216 (2015).
17. N. V. R. A. Dharanipragada *et al.*, *J. Mater. Chem. A* **3**, 16251–16262 (2015).
18. S. A. Theofanidis, V. V. Galvita, H. Poelman, G. B. Marin, *ACS Catal.* **5**, 3028–3039 (2015).
19. D. P. Harrison, *Ind. Eng. Chem. Res.* **47**, 6486–6501 (2008).
20. Materials and methods are available as supplementary materials on *Science* Online.
21. F. Jiao *et al.*, *Science* **351**, 1065–1068 (2016).
22. H. M. Torres Galvis *et al.*, *Science* **335**, 835–838 (2012).
23. P. Heidebrecht, K. Sundmacher, *Chem. Eng. Sci.* **64**, 5057–5065 (2009).

ACKNOWLEDGMENTS

This work was supported by the Long Term Structural Methusalem Funding of the Flemish Government, the Interuniversity Attraction Poles Programme, IAP7/5, Belgian State–Belgian Science Policy, and the Fund for Scientific Research Flanders (FWO; project G004613N). L.C.B. acknowledges financial support from the Institute for the Promotion of Innovation through Science and Technology in Flanders (IWT Vlaanderen). Additionally, he thanks his colleagues A. Dharanipragada and S. Theofanidis for supplying the oxygen carrier material and CH_4 reforming catalyst. We thank V. Bliznuk (Department of Materials Science and Engineering of Ghent University) for his technical support concerning STEM analysis, G. Rampelberg for help with in situ XRD (Department of Solid State Sciences, Ghent University), and O. Janssens (Department of Solid State Sciences, Ghent University) for performing ex situ XRD and SEM measurements. All data are presented in the main text and supplementary materials.

SUPPLEMENTARY MATERIALS

www.sciencemag.org/content/354/6311/449/suppl/DC1
Materials and Methods
Supplementary Text
Figs. S1 to S23
Tables S1 to S4
References (*24–39*)

4 August 2016; accepted 26 September 2016
10.1126/science.aah7161

CLIMATE DATA

Using climate models to estimate the quality of global observational data sets

François Massonnet,[1,2]* Omar Bellprat,[1] Virginie Guemas,[1,3] Francisco J. Doblas-Reyes[1,4]

Observational estimates of the climate system are essential to monitoring and understanding ongoing climate change and to assessing the quality of climate models used to produce near- and long-term climate information. This study poses the dual and unconventional question: Can climate models be used to assess the quality of observational references? We show that this question not only rests on solid theoretical grounds but also offers insightful applications in practice. By comparing four observational products of sea surface temperature with a large multimodel climate forecast ensemble, we find compelling evidence that models systematically score better against the most recent, advanced, but also most independent product. These results call for generalized procedures of model-observation comparison and provide guidance for a more objective observational data set selection.

There is now overwhelming evidence that Earth's climate has changed at an unusually rapid pace during the last century, that these changes bear a clear human signature, and that they will be enhanced if anthropogenic emissions continue unabated (*1*). The development of large-scale observational networks has been a major advance to reaching such levels of evidence. Observations of essential climate variables [e.g., sea surface temperature (SST), sea ice extent (*2*)] are indeed central for the study of climate variability (*1*), for detection and attribution of human-induced climate change (*1*, *3*), and for constraining long-term projections (*1*, *4*). Major international and coordinated observing programs are currently underway to continue these efforts (*5*). However, with the emergence of multiple observational references (ORs), sometimes divergent, a natural question arises: What is the underlying quality of these products? A direct answer to this question is not easily achieved because there is by definition no universal knowledge of the true state of our climate (*6*).

Here we present a framework for the evaluation of ORs addressing this gap. The approach relies on the use of climate models taken as references, and not as subjects of assessment as

[1]Earth Sciences Department, Barcelona Supercomputing Center–Centro Nacional de Supercomputación (BSC-CNS), Barcelona, Spain. [2]Georges Lemaître Centre for Earth and Climate Research (TECLIM), Earth and Life Institute (ELI), Université catholique de Louvain, Louvain-la-Neuve, Belgium. [3]Centre National de Recherches Météorologiques (CNRM), Toulouse, France. [4]ICREA, Pg. Lluís Companys 23, 08010 Barcelona, Spain.
*Corresponding author. Email: francois.massonnet@bsc.es

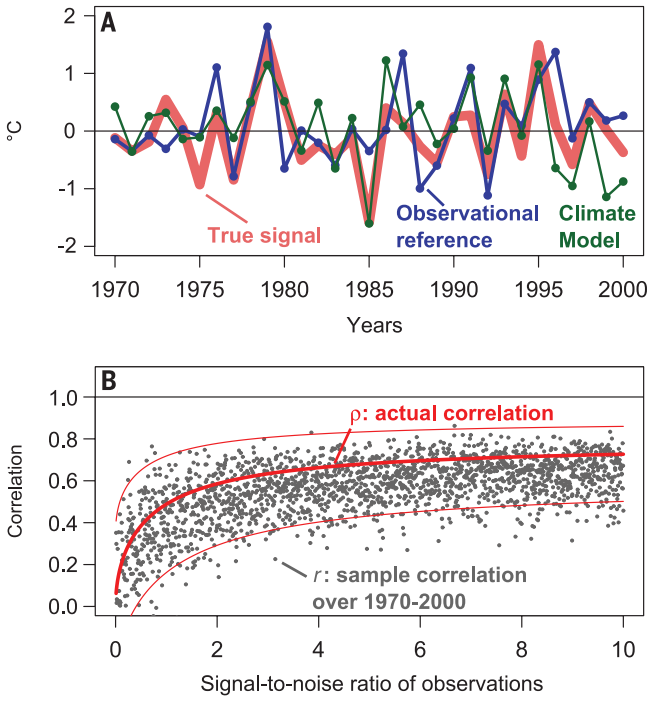

Fig. 1. A simple statistical toy model (Eq. 1) for understanding the dependence of correlation on observational error. (**A**) A true but unknown signal ϵ (light red) mimicking, for example, annual mean SST anomalies over some region is generated over 1970 to 2000 as a white-noise process with SD σ_ϵ = 0.8°C. An observationally based reference (blue) systematically underestimating the true variability (α_{OR} = 0.8) is then sampled according to Eq. 1 with SD σ_{OR} = 0.6°C. Finally, a climate model estimate (green) is shown with multiplicative bias α_{CM} = 0.7 and with its own and irreducible errors having SDs $\sigma_{CM,p}$ = 0.2°C and $\sigma_{CM,i}$ = 0.4°C, respectively. (**B**) Dependence of the linear correlation coefficient on the signal-to-noise ratio of observations $\gamma_{OR} = \sigma_\epsilon^2/\sigma_{OR}^2$. The red lines show the analytical, predicted dependence (Eq. 2) and the 95% confidence interval using Fisher's *z* transform (*32*). Gray dots are sample correlations between generated observation and model data for different levels of observational error, keeping the true signal unchanged [as in (A)] but each time generating a new model realization (with fixed error statistics α_{CM} = 0.7, $\sigma_{CM,p}$ = 0.2°C and $\sigma_{CM,i}$ = 0.4°C) and an observation (α_{OR} = 0.8) while varying the SE so that a desired signal-to-noise ratio is achieved.

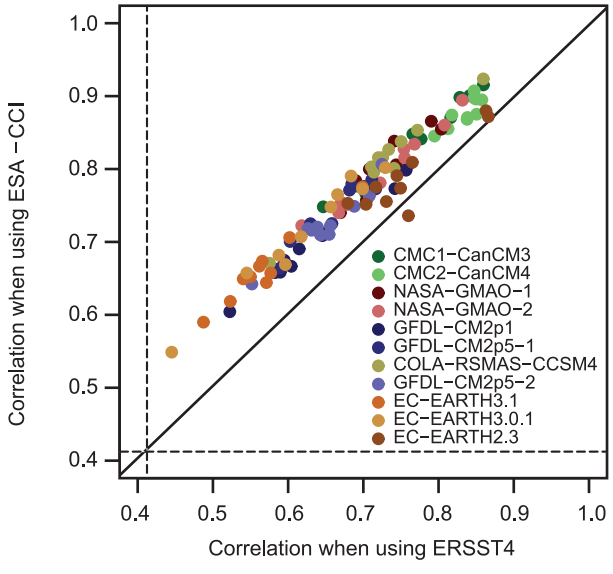

Fig. 2. Systematic dependence of correlation on verification product. Each dot highlights the relationship between the correlation of one August SST forecast verified against the ESA-CCI product (*y* axis; product based on satellite information only) and the correlation of the same forecast verified against the ERSST4 product (*x* axis; product based on in situ information only). Reference period is 1993 to 2009. There are 110 forecasts in total (11 models, 10 members each). The solid line is the 1:1 line and delimits regions where ESA-CCI or ERSST4 scores better. The dashed lines are the threshold above which correlations are significant at the 0.05 level (the 1-year autocorrelations of the time series considered are weak and not significant).

has been widely done in the past (*7*, *8*). The rationale behind this approach relies on the so-called "truth-plus-noise" paradigm (*9*–*14*), which assumes that observations and models are both noisy versions of the true (but unknown) state of the climate system. In that view, observations and models play symmetrical roles so that it is possible to use one to estimate how close the other is from the true state, and vice versa. In line with this paradigm, we claim that climate models can be appropriate tools for estimating the quality of ORs. We accumulate the necessary evidence in three steps. First, we rely on elementary logic and take advantage of the symmetry of common metrics of model performance. Then, we show with a simple statistical toy model how observational error can degrade model performance (symmetrically to model error), turning this into an opportunity to reverse the process of model evaluation into one of OR evaluation. Finally, we apply the proposed procedure to a realistic test case involving simulations conducted with large-scale general circulation models and a set of ORs.

"Quality" is here measured in terms of a primary metric of performance widely used in the climate community: the (Pearson) linear correlation between two variables (*15*). Because this metric of performance is mathematically symmetric, the process of evaluation is also inherently symmetric. Provided that this metric of performance is appropriate to characterizing the quality of climate models or forecast systems (*16*–*18*), it also becomes a way to measure the quality of ORs. The same argument holds for other metrics, provided that they respect the underlying hypothesis of symmetry.

To frame this idea in a more concrete context, consider the following simple, yet generic enough, toy model (*19*) consisting of an observational reference (X_{OR}) and model-based (X_{CM}) estimate of some true, but unknown, climate variable ϵ:

$$\begin{cases} X_{OR} = \alpha_{OR}\epsilon + \eta_{OR} \\ X_{CM} = \alpha_{CM}\epsilon + \eta_{CM,p} + \eta_{CM,i} \end{cases} \quad (1)$$

The observational reference X_{OR} is related to the true signal by a multiplicative bias factor $\alpha_{OR} > 0$, that accounts, e.g., for the systematic errors in retrieval from the raw measurement to the final product. The OR estimate is further polluted by a random error η_{OR} that reflects instrumental and sampling errors. Another estimate X_{CM} of the true variations can be obtained through a climate model (see Fig. 1A for an example). Like the OR, the climate model does not necessarily capture the correct amplitude of the variability (hence a multiplicative bias term $\alpha_{CM} > 0$ to model, e.g., the possible incorrect response to external forcings) and is subject to random error $\eta_{CM,p}$ (because of, e.g., unresolved or misrepresented processes including forcings) and random error $\eta_{CM,i}$ due to the inherent chaotic nature of climate dynamics and its intrinsic unpredictability (*20*). All error terms are assumed to follow Gaussian distributions with zero means and known standard deviations. Focusing on the evaluation of anomalies is motivated by the fact that constant offsets between ORs and climate model time series are usually removed by classical linear bias correction techniques. In that sense, we focus on the ability of ORs and climate models to reproduce variability rather than mean states. Finally, all error terms are assumed to be uncorrelated with each other. Under these ideal

conditions, the actual correlation between X_{OR} and X_{CM} follows the expression

$$\rho = \frac{1}{\sqrt{\left(1+\frac{1}{\alpha_{OR}^2\gamma_{OR}}\right)\cdot\left(1+\frac{1}{\alpha_{CM}^2\gamma_{CM}}\right)}} \quad (2)$$

where γ_{OR} and γ_{CM} denote the signal-to-noise ratios of the observation and the model, respectively (see the supplementary text for the demonstration of the relationship and Fig. 1B caption for the definition of signal-to-noise ratios). The relationship, displayed graphically in Fig. 1B for a given model error level, highlights that observational and model error play exchangeable roles in the definition of correlation: Correlation will decrease whenever either observational or model error increases. Despite its simplicity, the toy model illustrates two essential points: (i) Models and ORs are two sides of the same coin and make the process of evaluation intimately intertwined; and (ii) model error is not the only cause of poor model performance: Observational error also contributes to poor correlations. We now investigate this aspect in a more realistic case.

We compiled data from 11 state-of-the-art climate models for which 10-member-ensemble May to August (4-month-long) retrospective predictions of average SST in the Niño3.4 box (120°W to 170°W, 5°S to 5°N) were available between 1993 and 2009 (see supplementary materials for the choice of the period and a thorough description of this ensemble). Unlike the toy model presented above, forecast errors are not independent from each other (fig. S2). Besides, we computed monthly-mean SSTs in the Niño3.4 box for four ORs at various resolutions and based on various methods of retrieval (see supplementary materials for a complete description): ESA-CCI (~0.05° resolution, satellite data only), ERA-Interim (~0.7°, an atmospheric reanalysis also providing SST information), HadISST (1°, based on in situ data but interpolated with satellite data), and ERSST4 (2°, in situ data only). We find that the choice of OR used to verify the forecasts has a systematic and nonnegligible influence on the correlation between the forecast and the OR (Fig. 2). All August forecasts but one score better when assessed against the ESA-CCI product instead of ERSST4, and differences in correlation are commensurate with changes between model versions. For the example given in Fig. 2, the average change in Niño3.4 SST correlation when using ESA-CCI instead of ERSST4 is +0.07 (minimum = −0.02; maximum = 0.11). As a comparison, the mean change in correlations between EC-Earth 3.0 and EC-Earth 3.1 (two model versions) is 0.05 when assessed against ESA-CCI.

To obtain a broader picture, we recorded for each OR the number of forecasts amongst the 440 available (11 models, 10 members each, 4 months of forecasts) that reached the highest correlation with that particular OR (Fig. 3). The results show that forecasts, as a group, tend to favor one particular OR (ESA-CCI), which also happens to be the most recent, at the highest resolution and resorting to the most advanced technology for SST retrieval (*21*). In addition, none of the forecast systems uses the ESA-CCI SST OR for initialization, postprocessing, or validation, which excludes the possibility of reaching high correlation only by construction (*22*). At the other end of the diagram lies ERSST4, the OR that is arguably least adapted for this exercise of SST comparison in the middle of the Pacific Ocean, where sampling is poorer than in other regions of the Pacific (*23*). It is also worth noting that ORs that are a priori not relevant for SST evaluation (ERA-Interim, an atmospheric reanalysis) can score high for the wrong reasons. Five of the 11 models considered are initialized with the same SST fields as those used in ERA-Interim, making the evaluation dependent through a methodological artefact. This OR was deliberately included in our analysis to show that high correlations are a necessary, but not sufficient, indicator of high observational quality.

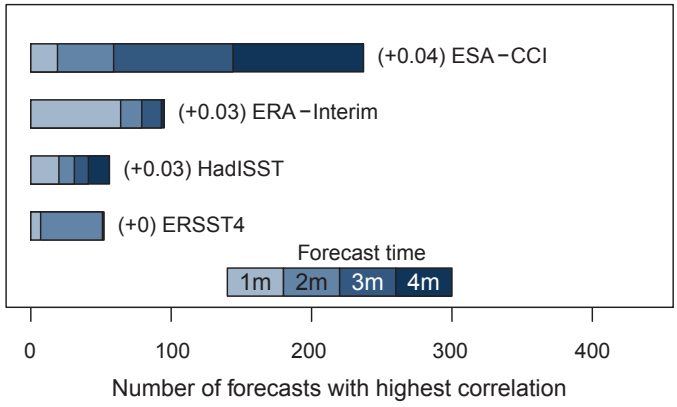

Fig. 3. Impact of the choice of OR on the assessment of forecast quality. A total of 440 seasonal retrospective forecasts of SST in the Niño3.4 box (11 models, 10 members each integrated for 4 months starting from 1 May) are correlated with four ORs of SST for verification over 1993 to 2009. For each OR, we record the number of times that this OR yields the highest correlation. Numbers in parentheses before each OR indicate the average increase in correlation when using that OR instead of ERSST4. Corresponding figures for an alternative metric (RMSE) and an alternative test case (sea ice) can be found in the supplementary materials.

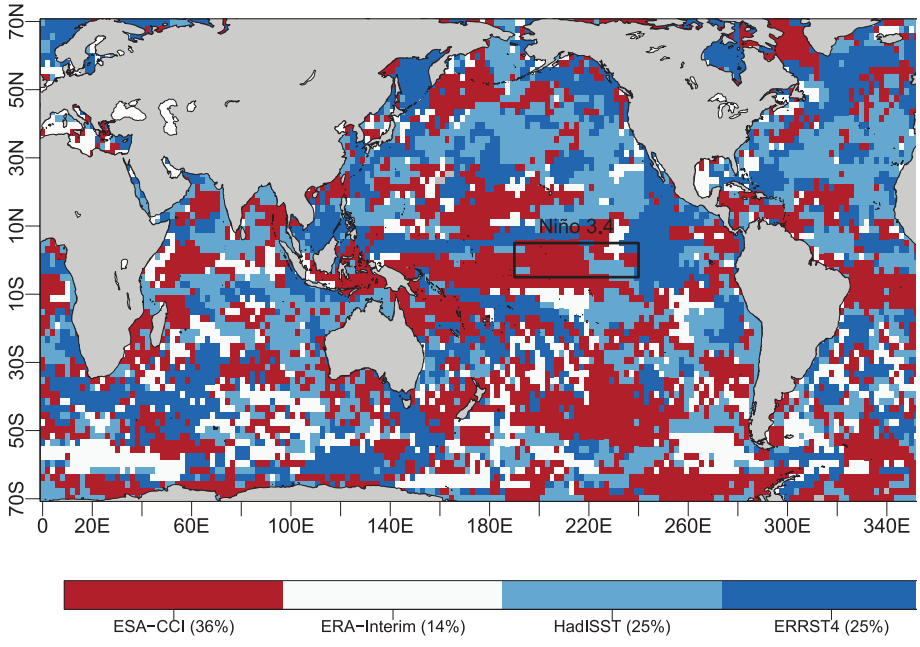

Fig. 4. Spatial distribution of observational reference quality. A total of 110 August SST forecasts were correlated (reference period: 1993 to 2009) to four observational references (ORs, legend). For each grid point, we display the OR that correlates best with most of the 110 forecasts. We show data only in grid points where at least one forecast achieves a significant correlation with one OR. The black box is the Niño3.4 region. Regions above 70°N or below 70°S are not considered, as these regions are usually ice-covered. The percentages below the color bar indicate the fraction of the oceans covered by each color. The corresponding figures for other months and alternative metrics can be found in the supplementary materials.

The differences in skill for different ORs, as depicted in Fig. 3, might be interpreted as an accidental result. Indeed, all forecasts are highly correlated to each other (fig. S2). If, by chance, the first forecast of the first model correlates better with the ESA-CCI OR, then it is likely that all subsequent forecasts would also tend to correlate better with that particular OR. We show, however, using bootstrapping and parametric tests, that a result as extreme as the one shown in Fig. 3 is very unlikely to have occurred by chance (*24*). In addition, the better performance of ESA-CCI in the Niño3.4 box is confirmed for another widely used metric of performance, the root mean squared error (RMSE) (*25*) (fig. S3). Finally, to push the analysis even further, this exercise is repeated on a different test case: summer Arctic sea ice extent prediction. In line with SST analyses, results show that sea ice concentration products relying on more recent algorithms tend to provide better estimates of model performance, or presented the other way around, that better observations are generally of higher skill when assessed against available forecasts (see supplementary materials for details).

The reasons why ESA-CCI outperforms other ORs in the Niño3.4 box are difficult to trace back formally. Indeed, the lack of information on SST uncertainty in all products, except ESA-CCI itself, precludes a clean comparison between the products' quality (*26*). It is therefore not possible to confirm whether the ESA-CCI error variance is lower than that of other products, as we would expect from lessons learned from the statistical toy model. However, we can gain further understanding of the role of observational quality if we extend the diagnostic of Fig. 3 to other regions of the world (Fig. 4). The map suggests that it is meaningless to designate any best OR in an absolute sense. Rather, it is clearly noticeable that where ORs are of a priori better quality, they score better: ORs that are partially or fully based on in situ data, shown in shades of blue, are more skillful in areas of intense shipping such as the North Atlantic (United States to Europe), the North Pacific (United States to Japan and China), or the Eastern Pacific (North America to South America).

The central idea behind our contribution relies on the symmetrical roles played by climate models and observational references as imperfect, but complementary, sources of information about reality. Symmetry enables one to revisit the concept of climate model evaluation and to expand it so as to simultaneously estimate the quality of observational references. A corollary is that ORs of higher quality will yield better skill scores to climate models, with systematic and non-negligible impacts on the estimated model performance. From the modeling side, considering multiple ORs in future model evaluation exercises such as CMIP6 (*27*, *28*) appears therefore as a priority. From the observational side, quantification of uncertainties will be vital to enable intercomparison of ORs and to account for observational uncertainty in model evaluation. In both cases, considering climate model evaluation as a bidirectional exercise (and not unidirectional as assumed by many up to now) is essential to remember that observations, no matter how good they appear, are also intrinsically uncertain.

REFERENCES AND NOTES

1. T. F. Stocker *et al.*, Eds, *Climate Change 2013: The Physical Science Basis. Contribution of Working Group I to the Fifth Assessment Report of the Intergovernmental Panel on Climate Change* (Cambridge Univ. Press, 2013).
2. World Meteorological Organization (WMO)'s Global Observing System for Climate (GCOS, www.wmo.int/pages/prog/gcos/) has defined a list of "essential climate variables" (ECVs) that are intended to best support the work of the United Nations Framework Convention on Climate Change (UNFCCC) and the Intergovernmental Panel on Climate Change (IPCC). Wind speed and direction, pressure, precipitation, and greenhouse gases, but also SST and sea ice, on which the present study is based, are primary ECVs.
3. G. Hegerl, *Environ. Res. Lett.* **10**, 071001 (2015).
4. M. Collins *et al.*, *Nat. Clim. Chang.* **2**, 403–409 (2012).
5. See, for instance, NASA's Earth Observing System (http://eospso.nasa.gov/), European Commission's Copernicus (www.copernicus.eu/), or China's Observation Satellite Programs (*29*).
6. There are protocols to assess the quality of ORs using independent in situ data; see, e.g., the GAIA-CLIM project www.gaia-clim.eu/. However, the data are by definition largely undersampled in space and time and cannot verify ORs exhaustively.
7. T. Reichler, J. Kim, *Bull. Am. Meteorol. Soc.* **89**, 303–311 (2008).
8. P. J. Gleckler, K. E. Taylor, C. Doutriaux, *J. Geophys. Res.* **113**, D06104 (2008).
9. A. P. Weigel, M. A. Liniger, C. Appenzeller, *Q. J. R. Meteorol. Soc.* **134**, 241–260 (2008).
10. B. Sanderson, R. Knutti, *Geophys. Res. Lett.* **39**, L1670 (2012).
11. S. Siegert *et al.*, *J. Clim.* **29**, 995–1012 (2016).
12. O. Bellprat, F. J. Doblas-Reyes, *Geophys. Res. Lett.* **43**, 2158–2164 (2016).
13. P. A. Janssen, S. Abdalla, H. Hersbach, J.-R. Bidlot, *J. Atmos. Ocean. Technol.* **24**, 1665–1677 (2007).
14. E. Kalnay, *Atmospheric Modeling, Data Assimilation and Predictability* (Cambridge Univ. Press, 2002).
15. Linear correlation of variables X and Y is defined as $\rho = \frac{C(X,Y)}{\sqrt{V(X)\cdot V(Y)}}$, where C and V denote covariance and variance, respectively. Sample correlation, denoted r throughout the text, is calculated using the same formula but with the covariance and variance replaced by sample covariance and sample variance, respectively. For application in climate sciences, see, for example, (*30*).
16. A. Scaife *et al.*, *Geophys. Res. Lett.* **41**, 2514–2519 (2014).
17. H. Bellenger, E. Guilyardi, J. Leloup, M. Lengaigne, J. Vialard, *Clim. Dyn.* **42**, 1999–2018 (2014).
18. F. Massonnet *et al.*, *Cryosphere* **5**, 687–699 (2011).
19. The toy model introduced here has the advantage of generalizing other simple models used in the literature to mimic large multimodel ensembles. See (*11*), section 2b, and the supplementary materials for a thorough discussion about hypotheses and interpretation of this toy model.
20. T. Palmer, R. Hagedorn, Eds, *Predictability of Weather and Climate* (Cambridge Univ. Press, New York, 2014).
21. C. J. Merchant *et al.*, *Geosci. Data J.* **1**, 179–191 (2014).
22. In fact, the ESA-CCI product was released after the simulations were conducted. See (*21*) for a description of the ESA-CCI product.
23. The spatial availability of SST in situ data (and its limited sampling of data in the equatorial Pacific compared to other regions) can be explored in the following reference: C. Deser and National Center for Atmospheric Research Staff, Eds, "The Climate Data Guide: ICOADS Surface Marine Weather Observations" (https://climatedataguide.ucar.edu/climate-data/icoads-surface-marine-weather-observations).
24. We challenge the null hypothesis that correlations are identical for all observational products using bootstrapping and parametric tests. (i) Bootstrapping: Synthetic 1993–2009 time series for the 110 August forecasts and the four ORs are generated 100,000 times from the known sample covariance matrix of the data, which we modify so that for each forecast, the correlation with all four ORs is forced to be identical (see supplementary materials for a detailed explanation). By doing so, we generate artificial data with exactly the same statistical properties as those of the original sample, except that no OR is chosen to be a priori better than any other one. A situation as extreme as the one witnessed—i.e., that one OR chosen a priori ranks first for at least 93 forecasts out of 110 (Fig. 3)—occurs 1.9% of the time. That is, the null hypothesis that all observations correlate equally to the 110 forecasts is very unlikely to be true, even if the strong correlation among forecasts is accounted for. (ii) Parametric test: The test for an increase in correlation in the presence of nonindependent samples (*31*) is performed for the pair of ERSST4/ESA-CCI for the August forecasts. For 101 of the 110 forecasts (92%), the P value returned by the test is lower than 10% (84% have a P value lower than 5%), i.e., far from the expected uniform distribution that would prevail if there were no true difference in the correlations.
25. $RMSE(X,Y) = \sqrt{\frac{1}{N}\sum_{i=1}^{N}(X_i - Y_i)^2}$ where N is the number of available samples. Note that, like the correlation (*15*), the RMSE is a symmetric operator. All results obtained with the RMSE instead of the correlation are available in the supplementary materials.
26. Even if the grid-point information on daily SST uncertainty is available (as is the case for the ESA-CCI product), propagating the statistics to climate scales (regional and monthly means) is far from trivial, as the spatial and temporal decorrelation time scales of errors are not properly characterized.
27. World Climate Research Programme (WCRP)'s Coupled Models Intercomparison Project, phase 6: www.wcrp-climate.org/wgcm-cmip/wgcm-cmip6.
28. V. Eyring *et al.*, *Geosci. Model Dev.* **9**, 1937–1958 (2016).
29. G. Xingfa, T. Xudong, *IEEE Trans. Geosci. Remote Sens.* **3**, 113–129 (2015).
30. K. E. Taylor, *J. Geophys. Res.* **106**, 7183–7192 (2001).
31. J. H. Steiger, J. M. Lind, "Statistically based tests for the number of common factors," paper presented at the annual meeting of the Psychometric Society, Iowa City, IA, 30 May 1980.
32. D. Wilks, *Statistical Methods in the Atmospheric Sciences* (Elsevier, Oxford, 2011), pp. 182–184.

ACKNOWLEDGMENTS

The research leading to these results has received funding from the Belgian Fonds National de la Recherche Scientifique (FNRS), the Ministerio de Economía y Competitividad (MINECO) Juan de la Cierva program, the Spanish national project PICA-ICE (GA CGL2012-31987), the European Union Seventh Framework Programme FP7 projects SPECS (GA 308378) and EUCLEIA (GA 607085), and the European Space Agency Living Planet Fellowship Programme under the project VERITAS, as well as the Climate Model User Group (CMUG) of the European Space Agency's Climate Change Initiative. We thank the National Oceanic and Atmospheric Administration, NSF, NASA, and U.S. Department of Energy for providing access to the North American Multi-Model Ensemble (NMME) database, and we acknowledge the help of the National Centers for Environmental Prediction, International Research Institute, and National Center for Atmospheric Research personnel in creating, updating, and maintaining the NMME archive. Acknowledgment is made for the use of the European Centre for Medium-Range Weather Forecasts computing and archive facilities in this research. We gratefully acknowledge the computer resources, technical expertise, and assistance provided by the Red Española de Supercomputación (RES). All data used for the analyses conducted in this study are available at https://doi.org/10.1594/PANGAEA.864680. We acknowledge managers of the PANGAEA project for hosting this content.

SUPPLEMENTARY MATERIALS

www.sciencemag.org/content/354/6311/452/suppl/DC1
Materials and Methods
Supplementary Text
Figs. S1 to S5
Source Code
References (*33*–*42*)

20 April 2016; accepted 20 September 2016
Published online 6 October 2016
10.1126/science.aaf6369

OCEAN CHEMISTRY

Dissolved organic sulfur in the ocean: Biogeochemistry of a petagram inventory

Kerstin B. Ksionzek,[1,2]* Oliver J. Lechtenfeld,[1,7] S. Leigh McCallister,[3] Philippe Schmitt-Kopplin,[4,5] Jana K. Geuer,[1] Walter Geibert,[1] Boris P. Koch[1,2,6]*

Although sulfur is an essential element for marine primary production and critical for climate processes, little is known about the oceanic pool of nonvolatile dissolved organic sulfur (DOS). We present a basin-scale distribution of solid-phase extractable DOS in the East Atlantic Ocean and the Atlantic sector of the Southern Ocean. Although molar DOS versus dissolved organic nitrogen (DON) ratios of 0.11 ± 0.024 in Atlantic surface water resembled phytoplankton stoichiometry (sulfur/nitrogen ~ 0.08), increasing dissolved organic carbon (DOC) versus DOS ratios and decreasing methionine-S yield demonstrated selective DOS removal and active involvement in marine biogeochemical cycles. Based on stoichiometric estimates, the minimum global inventory of marine DOS is 6.7 petagrams of sulfur, exceeding all other marine organic sulfur reservoirs by an order of magnitude.

In the early 1930s, Alfred Redfield noted that the ratio of carbon, nitrogen, and phosphorus in algal phyla remains surprisingly consistent across marine biomes. The canonical 106:16:1 Redfield ratio (*1*) originated from these observations and has since become a cornerstone of ocean biogeochemistry. Subsequent stoichiometric studies quantified the cellular quota of organic sulfur (OS) and found it to be similar to that of organic phosphorus ($C_{124}N_{16}P_1S_{1.3}$) (*2*). The magnitude of S acquisition, assimilation, and metabolism is not trivial given an average molar elemental ratio of $C_{124}N_{16}P_1S_{1.3}$ for marine algae (*2*). Based on this C/S ratio of ~*95*, the global phytoplankton biomass (~1 Pg C) (*3*) contains 0.028 Pg S, and the annual net marine primary production (48.5 Pg C $year^{-1}$) (*4*) requires a sulfur assimilation of 1.36 Pg S $year^{-1}$. Whereas regional marine dissolved organic sulfur (DOS) budgets have been constructed (*5*), quantification of the global inventory and its ties to other elemental biogeochemical cycles (C, N, P, and Fe) has been analytically hampered by the background concentration of sulfate (29 mmol S L^{-1}), which exceeds the concentration of DOS by five orders of magnitude.

The discovery of OS coupling to climate processes (*6*) generated a surge of interest in the OS cycle and dimethylsulfoniopropionate (DMSP) specifically. DMSP is the precursor of dimethylsulfide (DMS) (*7*), a gas that is assumed to contribute to aerosol formation and climate regulation (*6*). The estimated annual production of DMSP by phytoplankton of 3.8 Pg C $year^{-1}$ or 2.0 Pg S $year^{-1}$ (*8*) represents an important sulfur assimilation pathway with rapid turnover rates and provides a substantial source of reduced carbon and sulfur for heterotrophic bacteria (*9*, *10*). At the cellular level, the organic S and N cycles are intimately coupled through algal biosynthesis of the amino acids methionine and cysteine (*11*). Sulfur-rich peptides can also form metal-organic complexes and thus influence the speciation and mobility of trace metals in the ocean (*12*), with cascading effects on phytoplankton production, community composition, and carbon storage. Nonvolatile DOS is tightly linked to other major mineral assimilation pathways because it also comprises amino acids, vitamins, osmolytes, and primary metabolites (*13*, *14*). The major sinks for these marine biogenic sulfur compounds are (i) remineralization to sulfate, (ii) incorporation into microbial biomass, (iii) efflux to the atmosphere (*15*), and (iv) transformation into the sizeable pool of nonvolatile marine dissolved organic matter (DOM) (662 Pg C) (*16*). Despite the relevance of marine DOS for ocean biogeochemistry, its quantitative depiction and

[1]Alfred Wegener Institute, Helmholtz Center for Polar and Marine Research, Am Handelshafen 12, 27570 Bremerhaven, Germany. [2]MARUM Center for Marine Environmental Sciences, Leobener Straße, D-28359 Bremen, Germany. [3]Virginia Commonwealth University, Department of Biology, Center for Environmental Studies, 1000 West Cary Street, Richmond, VA 23284, USA. [4]Helmholtz Zentrum München (HMGU), German Research Centre for Environmental Health, Institute for Ecological Chemistry, Analytical BioGeoChemistry (BGC), Ingolstädter Landstraße 1, D-85764 Neuherberg, Germany. [5]Technische Universität München, Chair of Analytical Food Chemistry, Alte Akademie 10, 85354 Freising, Germany. [6]University of Applied Sciences, An der Karlstadt 8, 27568 Bremerhaven, Germany. [7]UFZ-Helmholtz Centre for Environmental Research, Department of Analytical Chemistry, Permoserstraße 15, D-04318 Leipzig, Germany. ***Corresponding author. Email: kerstin.ksionzek@awi.de (K.B.K); boris.koch@awi.de (B.P.K.)**

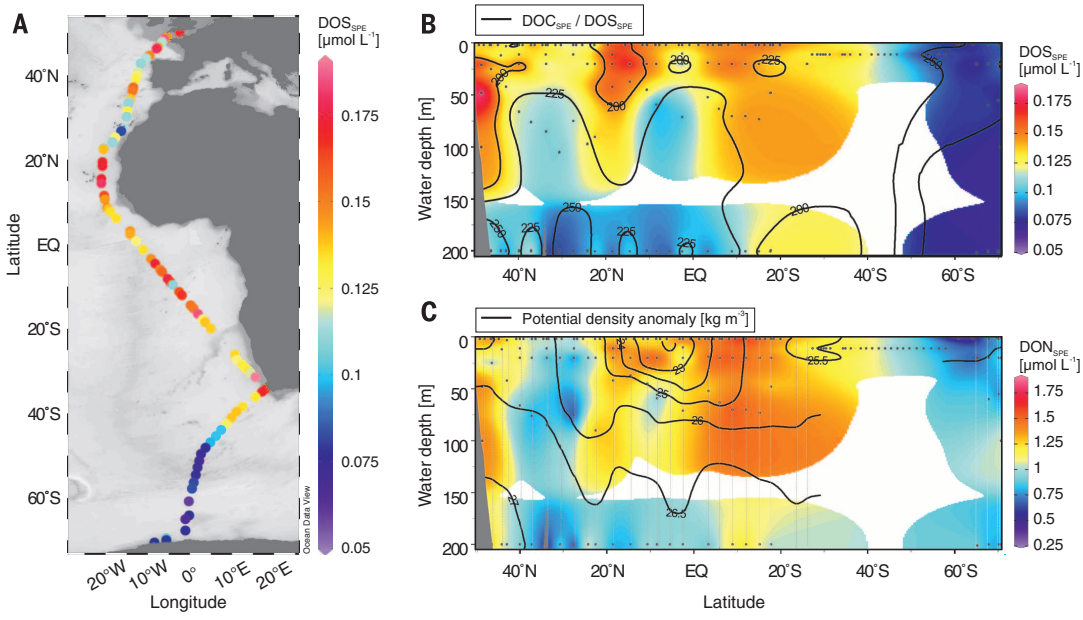

Fig. 1. Cruise track and distribution of DOS_{SPE} and DON_{SPE} and molar DOC_{SPE}/DOS_{SPE} ratios in the surface ocean. (**A**) Surface DOS_{SPE} concentrations (µmol L^{-1}) (colors) along the cruise track of research vessel *Polarstern* expeditions ANT XXV/1+2. (**B**) DOC_{SPE}/DOS_{SPE} ratios (contours) and DOS_{SPE} concentrations (µmol L^{-1}) (colors). (**C**) Potential density anomaly σ_0 (kg m^{-3}) (contours) and DON_{SPE} concentrations (µmol L^{-1}) (colors). For data below 200 m water depth, refer to Table 1.

connections and feedbacks to the C and N cycle remain elusive.

This study is based on water samples from the East Atlantic (EA) and the Southern Ocean (SO) collected in November and December 2008 between 50.2°N and 70.5°S (Fig. 1A) (*17*, *18*). The concentrations of solid-phase extractable DOS (DOS_{SPE} in μmol L^{-1} seawater) were analyzed by inductively coupled plasma sector field mass spectrometry (ICP-MS). Similar to the ambient dissolved organic carbon (DOC) concentration (*17*, *18*), DOS_{SPE} in the EA decreased significantly from 0.14 ± 0.02 μmol L^{-1} at surface depths of 0 to 105 m to ≤ 0.08 ± 0.01 μmol L^{-1} in deeper water ≥200 m ($P < 0.001$) (Fig. 1B and Table 1). DOS_{SPE} correlated linearly with both extractable dissolved organic nitrogen (DON_{SPE}) and DOC_{SPE} ($P < 0.001$, $R_{DOC} = 0.86$, $R_{DON} = 0.75$) (Fig. 1C and fig. S1A), whereas the slopes differed significantly ($P < 0.001$). The molar DOS_{SPE}/DON_{SPE} ratios of 0.11 ± 0.024 were almost constant (slope of 5.3) throughout the water column and comparable to phytoplankton stoichiometry (S/N ~ 0.08, C:N:S = 124:16:1.3) (*2*), suggesting a predominantly biogenic DOS imprint (*19*) rather than abiotic incorporation of S into DOM as found in oxygen-limiting conditions (*20*). In contrast, molar DOC_{SPE}/DOS_{SPE} ratios in the EA increased with depth from 213 ± 25 in the surface to 268 ± 39 in deeper water (slope of 99.7; $P < 0.001$), suggesting higher biological reactivity of DOS relative to DOC. This is supported by earlier studies showing that microbial growth can be limited by the availability of reduced sulfur sources such as DMSP (*9*, *10*).

DOS_{SPE} concentrations in the SO were pervasively low, whereas primary production was relatively high (see fig. S2 for chlorophyll concentrations). Depth-related changes in DOS_{SPE} concentrations of 0.08 ± 0.01 μmol L^{-1} in the surface and 0.07 ± 0.01 μmol L^{-1} at ≥200 m depth and changes in molar DOC_{SPE}/DOS_{SPE} ratios of 262 ± 28 in the surface and 254 ± 26 at ≥200 m were insignificant ($P > 0.05$) (Table 1). Molar DOS_{SPE}/DON_{SPE} ratios of 0.10 ± 0.027 were similar to those found in the EA. A correlation of chlorophyll *a* with DOC or DOS was not observed. We speculate that the biogenic signature of DOS production was not detected due to short residence times in the mixed surface water and upwelling of old (5226 ± 64 years), nonlabile DOS from the deep SO (*16*) with low DOS_{SPE} concentrations (0.07 ± 0.001 μmol S L^{-1}) (Table 1).

To provide an estimate of nonlabile DOS removal, we correlated measured and reconstructed DOC_{SPE} radiocarbon ages (*17*, *18*) with DOS_{SPE} concentrations (fig. S1B). Based on first-order kinetics, we found a strong correlation ($R = 0.75$, $P < 0.01$) of DOS_{SPE} concentration with age, similar to that previously determined for DOC_{SPE} (*17*, *18*) ($R = 0.61$, $P < 0.01$). The long-term degradation rate coefficients for DOS_{SPE} of $k_{DOS} = 2.54 \times 10^{-4}$ $year^{-1}$ and DOC_{SPE} of $k_{DOC} = 1.53 \times 10^{-4}$ $year^{-1}$ differed significantly ($P < 0.001$) and reflected a higher reactivity (lability) of DOS_{SPE} compared with DOC_{SPE}. The long-term net removal rate of 2.7×10^{-5} μmol S L^{-1} $year^{-1}$ for this nonlabile DOS_{SPE} pool (see the supplementary materials for definition) results in stoichiometric changes in DOM over time and depth, similar to the preferential remineralization of N (and P) relative to C (*21*). In contrast, degradation rate coefficients for DOS_{SPE} and DON_{SPE} were similar and, consequently, molar DOS_{SPE}/DON_{SPE} ratios did not change significantly with age. Differences between DOS_{SPE} and DOC_{SPE} degradation kinetics are also reflected in DOS_{SPE} and DOC_{SPE} lifetimes (time at which the DOM concentration decreases to 1/*e* of its initial value): We calculated the average lifetime of DOS_{SPE} of $\tau = 3937$ years, which is lower than the lifetime for DOC of $\tau = 4500$ years (*18*) and DOC_{SPE} of $\tau = 6536$ years (see the supplementary materials for details). As the molecular composition of the DOC and DOS pools differs, a direct comparison of DOS_{SPE} degradation kinetics with commonly applied DOC fractions (labile, semilabile, or refractory), which are based on the DOC removal rate and lifetime (*22*), cannot be applied. Our results also indicate that DOS degradation kinetics, similar to previous studies on DOC (*17*), are determined by a continuum of reactivities of the contributing sulfur compounds rather than discrete degradation stages.

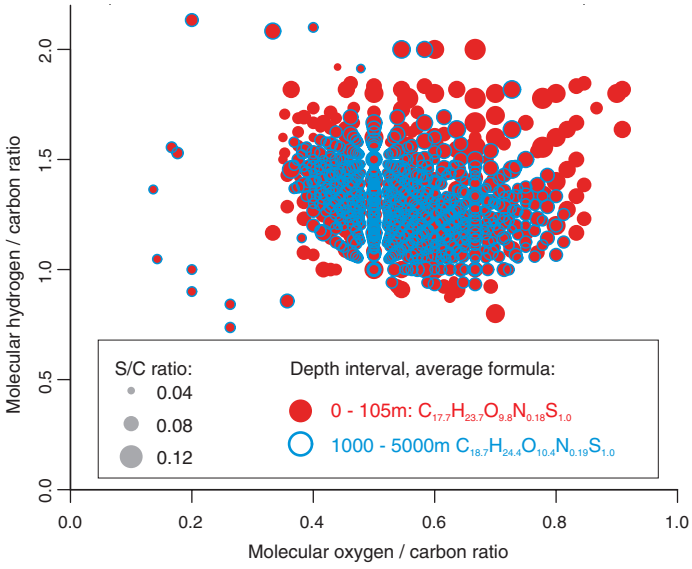

Fig. 2. Molecular changes of sulfur-containing compounds in the EA. Every dot represents a specific sulfur-containing molecular formula. Each formula is represented by its molecular H/C and O/C ratio (van Krevelen plot). The size of the data points represents the molecular S/C ratio. Higher S/C ratios indicate a higher amount of sulfur in the formula. Colors represent two depth intervals: 0 to 105 m (red dots) and >1000 m (blue circles). In the surface, the number of different formulas (chemical diversity) was higher. Most unique sulfur compounds in the surface showed a higher content of hydrogen (saturation) and oxygen (oxidation). The average molecular formula for each depth interval is displayed.

Relative changes in the contribution of labile DOS derived from biogenic production to the total DOS pool were assessed from two depth profiles analyzed for total hydrolysable methionine-sulfur yield [i.e., mole % of methionine-S versus total DOS_{SPE}]. In the EA, we found a higher molar methionine-sulfur yield of 1.02 ± 0.14% in the surface water compared with 0.21 ± 0.10% in deeper water (≥200 m). Accordingly, we observed a considerable decrease of the methionine-sulfur yield with age (fig. S3). In the SO, the methionine-sulfur yield of 0.18 ± 0.04% was consistently low throughout the water column. Assuming a methionine-S:cysteine-S ratio of 1.7 (*11*), less than 2 mol % of the DOS_{SPE} was protein-derived. This low value is consistent with previous data on amino acid carbon yield (*23*) suggesting that labile DOS in the form of sulfur-containing amino acids is efficiently remineralized or transformed, even in the surface ocean.

For the molecular characterization of DOS, we used Fourier transform ion cyclotron resonance mass spectrometry (FT-ICR-MS) and identified 803 unique molecular formulas containing predominantly one sulfur atom, 81 of which were exclusively identified in surface water ≤ 105 m (total number of S formulas in the data set, 81,037). None of the formulas we detected occurred uniquely at depth or matched the composition of a peptide. However, it is likely that other sulfur-containing compounds were also present and not covered by our analytical window. The diversity of sulfur-containing compounds identified by FT-ICR-MS and the average molecular S/C ratio in the EA decreased significantly from 0.06 ± 0.001 in surface water to 0.05 ± 0.001 in deeper water (≥200 m; $P < 0.001$) (Fig. 2), whereas comparable trends in the SO were not observed. Similar to previous molecular studies on DOC (*17*, *18*), the most persistent S formulas at depth showed higher unsaturation (lower molecular hydrogen/carbon ratio) (Fig. 2) and slightly larger molecular size (427 ± 5.6 Da in surface water and 441 ± 10.9 Da at ≥200 m).

The SPE method applied (*24*) yields lower extraction efficiencies for highly polar organic compounds (e.g., 22% for marine DON) as compared with DOC (42%) (*17*, *18*). Changes of the DOC and DON extraction efficiencies with depth, however, were insignificant ($P_{DOC} = 0.85$, $P_{DON} = 0.45$). Therefore, we can assume that the extraction yield for polar OS compounds is also lower than for DOC and independent of water depth. Using the average measured molar DOC_{SPE}/DOS_{SPE} ratio (Table 1) and the DOC concentrations in original seawater, we can reconstruct

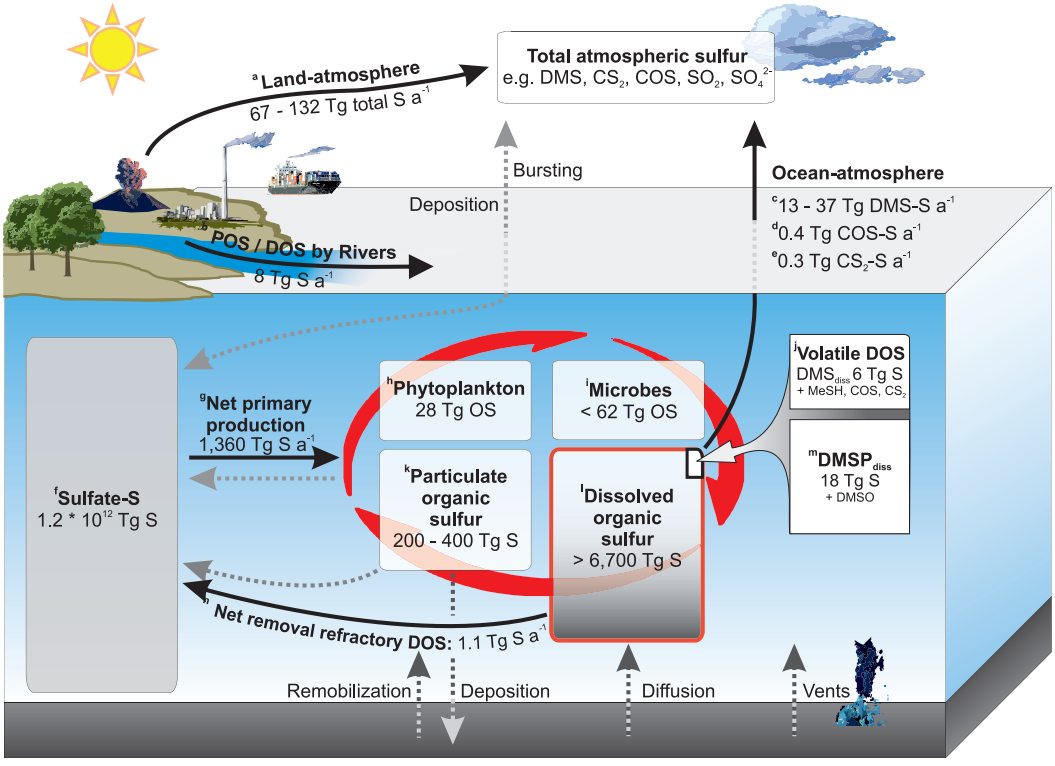

Fig. 3. Simplified marine organic sulfur cycle. Schematic overview of organic sulfur reservoirs and fluxes. All numbers refer to organic sulfur, except for the oceanic sulfate inventory and the land-atmosphere flux (total S). Known and calculated organic sulfur fluxes are shown as solid lines and unknown fluxes as dotted lines. The red circle indicates the rapid and important cycling of labile DOS compounds such as DMSP (depicted in the small white box). For corresponding data and references, see table S3.

Table 1. Average values and root mean square deviations of DOC and sulfur concentrations in the EA and SO and calculated global DOS_{MIN} inventory.

	Depth intervals				
	0–105 m	**200 m**	**201–1000 m**	**>1000 m**	**Total***
East Atlantic Ocean					
$n^{\dagger}$	106 (108)	21	5	11 (8)	143 (142)
DOC (μmol L^{-1})	71 ± 12	54 ± 4	49 ± 5	46 ± 2	47 ± 3
DOC_{SPE} (μmol L^{-1})	29 ± 5	23 ± 3	20 ± 1	20 ± 1	21 ± 1
DOS_{SPE} (μmol L^{-1})	0.14 ± 0.02	0.10 ± 0.02	0.09 ± 0.03	0.07 ± 0.01	0.08 ± 0.01
DOC_{SPE}/DOS_{SPE}	213 ± 25	235 ± 30	241 ± 47	276 ± 38	268 ± 39
$[DOS]_{MIN}$ (μmol L^{-1})	0.34 ± 0.08	0.23 ± 0.04	0.21 ± 0.05	0.16 ± 0.03	0.18 ± 0.03
Southern Ocean					
$n^{\dagger}$	22 (21)	3 (2)	3	3	31 (29)
DOC (μmol L^{-1})	50 ± 11	48	48 ± 6	49 ± 6	49 ± 7
DOC_{SPE} (μmol L^{-1})	21 ± 2	21 ± 1	21 ± 0.3	18 ± 4	19 ± 3
DOS_{SPE} (μmol L^{-1})	0.08 ± 0.01	0.07 ± 0.003	0.07 ± 0.005	0.07 ± 0.001	0.07 ± 0.01
DOC_{SPE}/DOS_{SPE}	262 ± 28	288 ± 17	294 ± 14	246 ± 29	255 ± 26
$[DOS]_{MIN}$ (μmol L^{-1})	0.19 ± 0.04	0.16	0.16 ± 0.02	0.20 ± 0.01	0.19 ± 0.01
Total average					
$n^{\dagger}$	128 (129)	24 (23)	8	14 (11)	174 (171)
DOC (μmol L^{-1})	68 ± 14	53 ± 4	49 ± 5	47 ± 4	48 ± 5
DOC_{SPE} (μmol L^{-1})	28 ± 5	23 ± 3	21 ± 1	20 ± 2	20 ± 2
DOS_{SPE} (μmol L^{-1})	0.13 ± 0.03	0.10 ± 0.02	0.08 ± 0.02	0.07 ± 0.01	0.08 ± 0.01
DOC_{SPE}/DOS_{SPE}	221 ± 31	241± 34	261 ± 46	270 ± 38	266 ± 39
$[DOS]_{MIN}$ (μmol L^{-1})	0.31 ± 0.09	0.23 ± 0.04	0.19 ± 0.05	0.17 ± 0.03	0.18 ± 0.03
Global					
DOC (Pg)[13]		47	138	477	662
DOS_{MIN} (Pg)		0.6	1.4	4.7	6.7

*Depth-integrated values. †Number of samples for the DOS_{SPE} analysis. Numbers in parentheses are the numbers of samples for DOC analysis.

a conservative minimum for the original DOS concentration in seawater ($[DOS]_{MIN}$) (Table 1 and Eq. 1).

$$[DOS]_{MIN} = [DOC]/(DOC_{SPE}/DOS_{SPE}) \quad (1)$$

where [DOC] is the molar DOC concentration in original seawater and DOC_{SPE}/DOS_{SPE} is the measured molar elemental ratio in the extracts. The calculated $[DOS]_{MIN}$ concentrations were 0.34 ± 0.08 and 0.19 ± 0.04 μmol L^{-1} in EA and SO surface waters, respectively (Table 1). This concentration range was consistent with previous data from the Sargasso Sea (0.04 to 0.4 μmol DOS L^{-1}) (*5*). For comparison, the mean concentrations of dissolved DMS and DMSP in the surface of the EA during our cruise were 0.0036 and 0.0032 μmol L^{-1}, respectively (*25*), representing ~2% of $[DOS]_{MIN}$ in the EA. The global average concentration for dissolved DMS and DMSP were previously estimated at 0.001 to 0.007 μmol L^{-1} (*26*) and 0.003 μmol L^{-1} (*27*), respectively, contributing only ~2.3% of the total $[DOS]_{MIN}$.

Based on the global oceanic DOC inventory of 662 Pg C (*16*) and depth-integrated molar DOC_{SPE}/DOS_{SPE} ratios, the minimum global oceanic DOS inventory (DOS_{MIN}) is 6.7 Pg S (6700 Tg), ~600 Tg of which are present in the upper 200 m of the water column (Table 1 and Fig. 3). If we assume that the molar C/S ratio of ~95 in phytoplankton is the lowest possible ratio for DOM, the maximum size of the global DOS inventory is 18.6 Pg S. Hence, DOS represents the major reservoir of organic S in the ocean, larger than OS in biomass, particles, or

volatile compounds combined (Fig. 3). More important, these numbers raise new questions on the marine sulfur budgets: Only 13 to 37 Tg S $year^{-1}$ of the total DOS pool (red frame in Fig. 3) are released to the atmosphere as DMS (*28*) and DOS degradation products such as carbonyl sulfide (COS) (0.4 Tg S $year^{-1}$) and carbon disulfide (CS_2) (0.3 Tg S $year^{-1}$) (Fig. 3) (*28*). In total, these fluxes represent less than 3% of the annual sulfur assimilation of 1.36 Pg S $year^{-1}$ by primary production, suggesting that rapid biogeochemical cycles of labile sulfur compounds (red cycle in Fig. 3) are superimposed on the large background of nonlabile DOS (red frame in Fig. 3), which we consider to be derived from the microbial carbon pump (*29*). Seasonal variation of C/S ratios by changes in production and microbial or photodegradation has an important effect on the DOS_{MIN} estimates in the surface (*5*). However, the value for our global DOS_{MIN} estimate is dominated by the relatively invariant C/S ratios of 266 ± 41 in the large water body below the photic zone (>200 m) and therefore only marginally affected by seasonal effects. Many previous studies focused on the labile (and partly volatile) proportion of the DOS cycle (Fig. 3). This study enables important insights into the biogeochemistry of the vast pool of nonlabile DOS. So far, the organic sulfur budgets cannot be closed, particularly because the connection between the rapid cycling of labile DOS and the nonlabile proportion of the organic sulfur cycle remain unquantified.

REFERENCES AND NOTES

1. A. C. Redfield, B. H. Ketchum, F. A. Richards, in *The Sea*, M. N. Hill, Ed. (Wiley, New York, 1963), vol. 2, chap. 2.
2. T. Y. Ho *et al.*, *J. Phycol.* **39**, 1145–1159 (2003).
3. P. G. Falkowski, R. T. Barber, V. Smetacek, *Science* **281**, 200–206 (1998).
4. C. B. Field, M. J. Behrenfeld, J. T. Randerson, P. Falkowski, *Science* **281**, 237–240 (1998).
5. G. A. Cutter, L. S. Cutter, K. C. Filippino, *Limnol. Oceanogr.* **49**, 555–565 (2004).
6. R. J. Charlson, J. E. Lovelock, M. O. Andreae, S. G. Warren, *Nature* **326**, 655–661 (1987).
7. M. O. Andreae, *Mar. Chem.* **30**, 1–29 (1990).
8. M. Galí, E. Devred, M. Levasseur, S.-J. Royer, M. Babin, *Remote Sens. Environ.* **171**, 171–184 (2015).
9. H. J. Tripp *et al.*, *Nature* **452**, 741–744 (2008).
10. R. P. Kiene, L. J. Linn, J. González, M. A. Moran, J. A. Bruton, *Appl. Environ. Microbiol.* **65**, 4549–4558 (1999).
11. J. Giovanelli, S. H. Mudd, A. H. Datko, *J. Biol. Chem.* **253**, 5665–5677 (1978).
12. D. S. Smith, R. A. Bell, J. R. Kramer, *Comp. Biochem. Physiol. C* **133**, 65–74 (2002).
13. M. A. Moran *et al.*, *Proc. Natl. Acad. Sci. U.S.A.* **113**, 3143–3151 (2016).
14. B. P. Durham *et al.*, *Proc. Natl. Acad. Sci. U.S.A.* **112**, 453–457 (2015).
15. P. Schmitt-Kopplin *et al.*, *Biogeosciences* **9**, 1571–1582 (2012).
16. D. A. Hansell, C. A. Carlson, D. J. Repeta, R. Schlitzer, *Oceanography* **22**, 202–211 (2009).
17. R. Flerus *et al.*, *Biogeosciences* **9**, 1935–1955 (2012).
18. O. J. Lechtenfeld *et al.*, *Geochim. Cosmochim. Acta* **126**, 321–337 (2014).
19. M. Gonsior *et al.*, *Mar. Chem.* **123**, 99–110 (2011).
20. R. L. Sleighter *et al.*, *Environ. Sci. Technol. Lett.* **1**, 345–350 (2014).
21. C. S. Hopkinson Jr., J. J. Vallino, A. Nolin, *Deep Sea Res. Part II Top. Stud. Oceanogr.* **49**, 4461–4478 (2002).
22. D. A. Hansell, *Ann. Rev. Mar. Sci.* **5**, 421–445 (2013).
23. J. Davis, R. Benner, *Limnol. Oceanogr.* **52**, 2434–2444 (2007).
24. T. Dittmar, B. P. Koch, N. Hertkorn, G. Kattner, *Limnol. Oceanogr. Methods* **6**, 230–235 (2008).
25. C. Zindler, C. A. Marandino, H. W. Bange, F. Schutte, E. S. Saltzman, *Geophys. Res. Lett.* **41**, 3181–3188 (2014).
26. A. Lana *et al.*, *Global Biogeochem. Cycles* **25**, 17 (2011).
27. R. P. Kiene, D. Slezak, *Limnol. Oceanogr. Methods* **4**, 80–95 (2006).
28. D. C. Yoch, *Appl. Environ. Microbiol.* **68**, 5804–5815 (2002).
29. N. Jiao *et al.*, *Nat. Rev. Microbiol.* **8**, 593–599 (2010).

ACKNOWLEDGMENTS

This work was supported by the DFG-Research Centre/Cluster of Excellence "The Ocean in the Earth System" and a Ph.D. grant by the Deutsche Forschungsgemeinschaft (DFG) in the framework of the priority program "Antarctic Research with comparative investigations in Arctic ice areas" (grant KO 2164/8-1+2). We are grateful to research vessel *Polarstern* captain, crew, and chief scientists G. Kattner (ANTXXV-1) and O. Böbel (ANTXXV-2); I. Stimac is acknowledged for technical support with ICP-MS analysis and K.-U. Ludwichowski for support with methionine analysis; we thank C. Marandino for DMS and DMSP data; S. Frickenhaus is acknowledged for support with statistical analysis, and B. Kanavati, M. Harir, and J. Uhl for support with FT-ICR-MS analyses. G. Kattner and R. Alheit are acknowledged for helpful discussions and proofreading. The data presented in this paper are available at the PANGEA data library (doi:10.1594/PANGAEA.858568). B.P.K. designed the research. O.J.L and B.P.K. collected and processed the samples. K.B.K. and W.G. performed ICP-MS analysis and data evaluation. J.G. carried out methionine analyses, S.L.M. performed ^{14}C analysis, and P.S.-K. performed FT-ICR-MS analysis. The paper was written by K.B.K. and B.P.K, with input from all coauthors.

SUPPLEMENTARY MATERIALS

www.sciencemag.org/content/354/6311/456/suppl/DC1
Materials and Methods
Figs. S1 to S3
Tables S1 to S3
References (*30*–*36*)

30 March 2016; accepted 15 September 2016
Published online 6 October 2016
10.1126/science.aaf7796

NEURONAL MATURATION

A disynaptic feedback network activated by experience promotes the integration of new granule cells

Diego D. Alvarez,* Damiana Giacomini,* Sung Min Yang, Mariela F. Trinchero, Silvio G. Temprana, Karina A. Büttner, Natalia Beltramone, Alejandro F. Schinder†

Experience shapes the development and connectivity of adult-born granule cells (GCs) through mechanisms that are poorly understood. We examined the remodeling of dentate gyrus microcircuits in mice in an enriched environment (EE). Short exposure to EE during early development of new GCs accelerated their functional integration. This effect was mimicked by in vivo chemogenetic activation of a limited population of mature GCs. Slice recordings showed that mature GCs recruit parvalbumin γ-aminobutyric acid–releasing interneurons (PV-INs) that feed back onto developing GCs. Accordingly, chemogenetic stimulation of PV-INs or direct depolarization of developing GCs accelerated GC integration, whereas inactivation of PV-INs prevented the effects of EE. Our results reveal a mechanism for dynamic remodeling in which experience activates dentate networks that "prime" young GCs through a disynaptic feedback loop mediated by PV-INs.

Neural stem cells (NSCs) of the adult hippocampus follow a multifaceted developmental program that culminates in the generation of dentate granule cells (GCs) capable of information processing (*1*–*4*). The pathway from NSC to GC offers multiple checkpoints that are controlled by physiological and pathological conditions, which ultimately modulate the efficacy and quality of the neurogenic process (*5*–*9*). Thus, simple experiences such as physical exercise or exploration of novel environments can influence the production, maturation, survival, and connectivity of adult-born GCs (*10*–*14*). Yet the early transition from NSC to neuron is much better understood than the processes that control the subsequent steps resulting in the functional integration of new neurons into the preexisting network. We investigated how experience is translated into local signals that can shape the developmental profile of new GCs.

Adult-born GCs were studied during their initial 3 weeks in the temporal hippocampus, where development occurs at a slow pace and is sensitive to behavior (*12*, *15*, *16*). We first asked whether an experience that activates the dentate gyrus might work as a signal to shape neuronal development. Because spatial exploration actively involves hippocampal processing (*17*–*19*), an enriched environment (EE) was selected as a stimulus to promote hippocampal activity. A brief exposure to EE reliably activated a substantial fraction of principal cells in the GC layer (fig. S1). We subsequently tested

Laboratorio de Plasticidad Neuronal, Fundación Instituto Leloir–Instituto de Investigaciones Bioquímicas de Buenos Aires–Consejo Nacional de Investigaciones Científicas y Técnicas (CONICET), Av. Patricias Argentinas 435, Buenos Aires C1405BWE, Argentina.
*These authors contributed equally to this work. **†Corresponding author. Email: aschinder@leloir.org.ar**

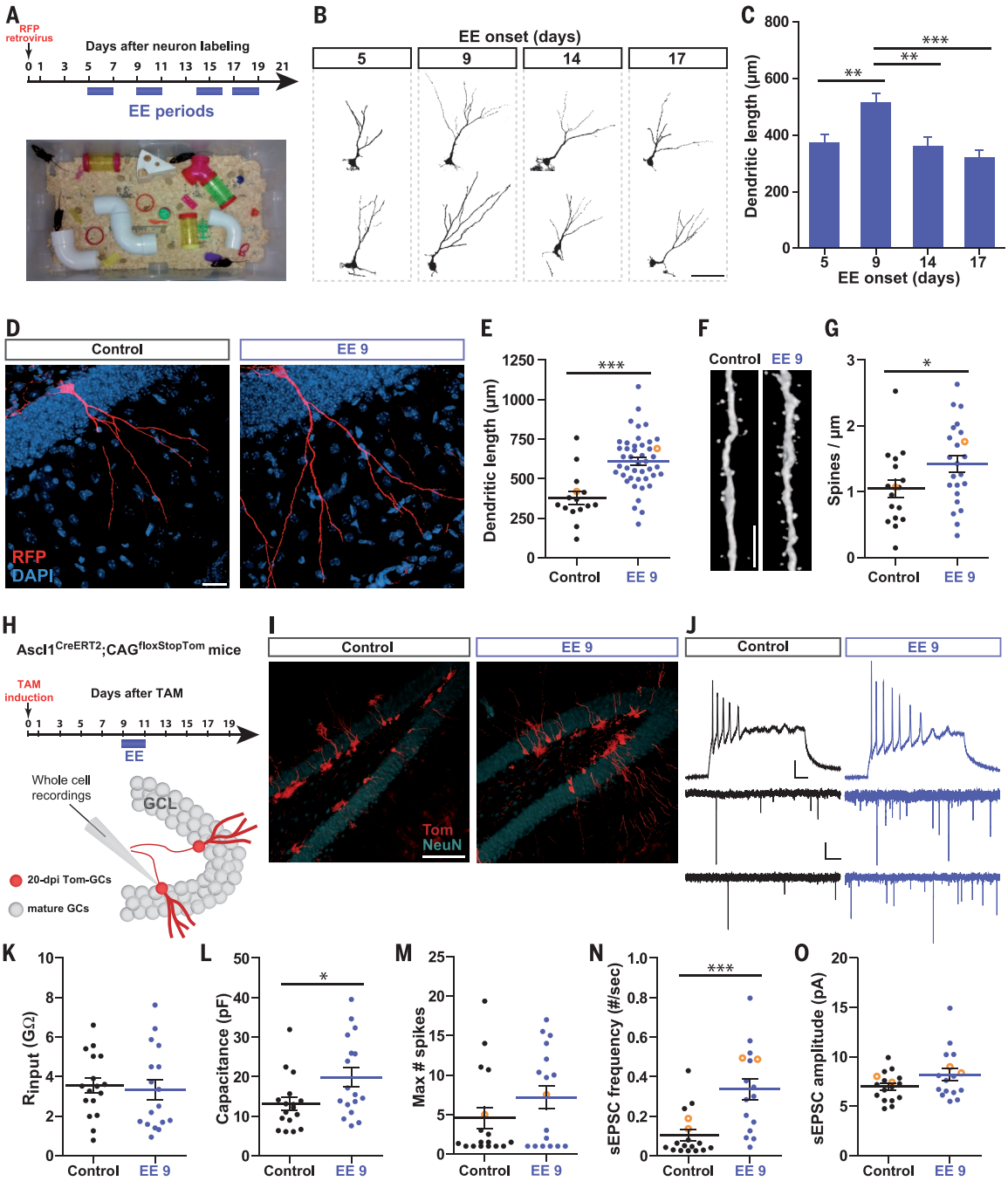

Fig. 1. EE accelerates growth and integration of new GCs during a critical period. (**A** to **G**) Brief experience in EE within a critical period accelerates morphological maturation. (A) Experimental design. RFP-expressing retrovirus was delivered to the temporal dentate gyrus to label adult-born GCs. Mice were allowed to freely explore in EE for 48 hours at different times after labeling (blue segments) or were left in a regular cage (control). Morphological parameters were analyzed in RFP-GCs at 21 dpi by immunofluorescence and confocal microscopy. (B) Representative confocal images of 21-dpi RFP-GCs for the different periods. Scale bar, 50 µm. (C) Dendritic lengths of neurons exposed to EE at different ages. $^{**}P < 0.01$, $^{***}P < 0.001$ for analysis of variance (ANOVA; $P < 0.0001$) followed by Bonferroni post hoc tests, with $n = 31$, 27, 24, and 27 neurons (from 3 or 4 mice) for EE onset at 5, 9, 14, and 17 days, respectively. Error bars denote SEM. [(D) to (G)] Separate set of experiments to compare GCs at 21 dpi from control versus EE 9 mice. (D) Representative confocal images, with 4′,6-diamidino-2-phenylindole (DAPI; blue) labeling the GC layer. Scale bar, 20 µm. (E) Dendritic lengths measured for the two conditions. $^{***}P < 0.0001$, *t* test with Welch's correction, with $n = 15$ and 44 neurons (from 3 to 5 mice) for control and EE 9 mice, respectively. Orange circles correspond to example neurons shown in (D). (F) Higher-resolution images to highlight dendritic spines at 21 dpi. Scale bar, 5 µm. (G) Spine densities for control and EE 9 mice. $^{*}P < 0.05$ after *t* test with Welch's correction with $n = 17$ and 23 segments (from 3 to 5 mice) for control and EE 9 mice, respectively. (**H** to **O**) Functional properties of new GCs from control and EE 9 mice. (H) Experimental design. Ascl1^{CreERT2};CAG^{floxStopTom} mice received TAM to label new GCs and were exposed to EE 9. Whole-cell recordings were carried out at 20 dpi in Tom-GCs. (I) Representative images of Tom-GCs obtained from control or EE 9 mice, with immunofluorescence for the neuronal marker NeuN (cyan) labeling the GC layer. Scale bar, 100 µm. (J) Top: Representative voltage traces depicting spiking in response to depolarizing current steps (60 pA, 500 ms) for control and EE 9 GCs. Scale bars, 20 mV, 50 ms. Bottom: Representative current traces (2 cells each) depicting sEPSCs obtained from control or EE 9 neurons held at −70 mV. Scale bars, 4 pA, 2 s. [(K) and (L)] Passive membrane properties. $^{*}P < 0.05$ after Mann-Whitney test with $n = 17$ neurons for each condition. (M) Maximum number of spikes elicited by depolarizing current steps. Orange circles correspond to traces shown in (J). [(N) and (O)] sEPSC frequency and amplitude. $^{***}P < 0.001$ after Mann-Whitney test with $n = 17$ and 16 neurons for control and EE 9 mice, respectively. In (E), (G), and (K) to (O), central horizontal bars denote means and error bars denote SEM.

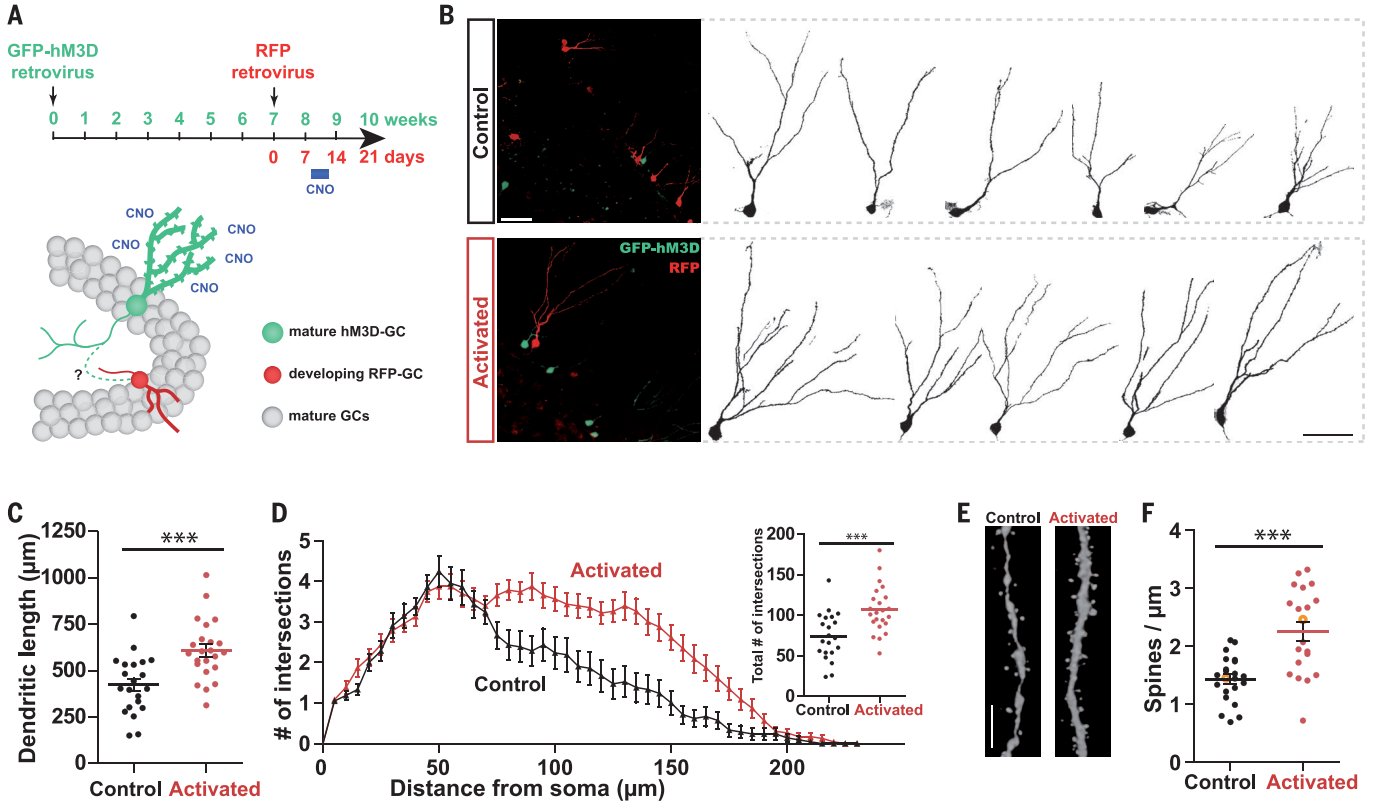

Fig. 2. Chemogenetic activation of mature GCs promotes the integration of new GCs undergoing the critical period. (**A**) Experimental design. A retrovirus expressing hM3D-EGFP was delivered to the dentate gyrus to transduce new GCs (hM3D-GCs). After 7 weeks, RFP-expressing retrovirus was injected to label a second cohort of new GCs (RFP-GCs). Nine days later, mice received CNO for 48 hours to stimulate mature hM3D-GCs neighboring 9-dpi RFP-GCs. Morphological analysis was done on RFP-GCs at 21 dpi. (**B**) Left: Representative dentate gyrus images depicting RFP-GCs at 21 dpi (red) and mature (70-dpi) hM3D-GCs from mice that received vehicle or CNO. Right: Representative examples of RFP-GCs. Scale bars, 50 μm. (**C** and **D**) Dendritic length (C) and Sholl analysis (D) demonstrate substantial dendritic growth in RFP-GCs from mice that received CNO. ***P < 0.001, t test with Welch's correction, with n = 21 and 23 neurons (from 5 mice) for control and activated circuits, respectively. (**E** and **F**) Neuronal segments shown to highlight dendritic spines. Scale bar, 5 μm. Spine density is higher after hM3D-GC activation. ***P < 0.001 after t test with Welch's correction, with n = 22 and 20 segments (from 5 mice) for control and activated circuits, respectively. In (D), triangles connected by straight lines denote means and error bars denote SEM. In (C), inset of (D), and (F), central horizontal bars denote means and error bars denote SEM.

whether exposure to EE during a restricted period modulates GC development and whether such modulation is dependent on the developmental stage of new GCs. Mice received a retroviral injection in the temporal dentate gyrus to express red fluorescent protein (RFP) in a restricted cohort of new GCs (RFP-GCs) and were exposed for 48 hours to EE at different days postinjection (dpi). The morphology of RFP-GCs was examined at 21 dpi (Fig. 1A). RFP-GCs displayed longer dendrites when exposure to EE occurred within a restricted time window beginning at 9 days of age (EE 9), but not before or after that period (Fig. 1, B and C). A more detailed analysis revealed morphological features of enhanced connectivity, such as higher dendritic complexity and spine density, in GCs exposed to EE at 9 days versus nonexposed controls (Fig. 1, D to G, and fig. S2, A to C). We also noted more RFP-GCs in sections obtained from EE mice, which suggested increased survival (fig. S2D) (*8*).

To determine whether the morphological changes observed in stimulated mice are linked to functional integration, we made electrophysiological recordings in 3-week-old GCs after EE 9. Adult-born GCs were labeled using $Ascl1^{CreERT2}$; $CAG^{floxStoptdTomato}$ mice and tested 3 weeks after activation of the recombinase by tamoxifen (TAM; Fig. 1, H and I) (*20*–*22*). In general, GCs expressing tdTomato (Tom-GCs) showed electrical properties typical of immature neurons, such as high input resistance, low membrane capacitance, and limited capacity to spike repetitively (Fig. 1, J to M). Tom-GCs recorded from mice exposed to EE 9 showed membrane resistance and firing properties similar to those from control mice, indicating similar degrees of functional maturation. Their slightly higher values of membrane capacitance were consistent with the more elaborated dendrites. However, Tom-GCs from stimulated mice displayed a factor of >3 increase in the frequency (but not the amplitude) of spontaneous excitatory postsynaptic currents (sEPSCs), reflecting enhanced integration into excitatory networks through an increased number of input connections (Fig. 1, N and O).

We next investigated how exploratory experience may be transduced into local signals that act on functional integration of new individual cells. Because exploration strongly activates the GC layer (fig. S1), we asked whether activation of the local network would be sufficient to influence developing GCs. In recent work, we used the synthetic receptor hM3D to activate adult-born GCs upon binding of the synthetic ligand clozapine-*N*-oxide (CNO) (*23*, *24*). Here, the hM3D-expressing retrovirus was injected in the dentate gyrus to transduce a cohort of new GCs (hM3D-GCs) and, 7 weeks later, a RFP-expressing retrovirus was used to label a new cohort of developing GCs in the same region (Fig. 2A). This resulted in simultaneous expression of hM3D in fully mature GCs (hM3D-GCs) and RFP in developing GCs (RFP-GCs). Mice received CNO for 2 days to stimulate hM3D-GCs at 8 weeks, at which time neighboring RFP-GCs were undergoing the critical period of high sensitivity to experience that was expressed at about 9 days of age. Dendritic growth was then assessed in RFP-GCs at 21 days. Activation of a limited group of mature adult-born GCs for 2 days increased the complexity of the dendritic tree and the density of dendritic

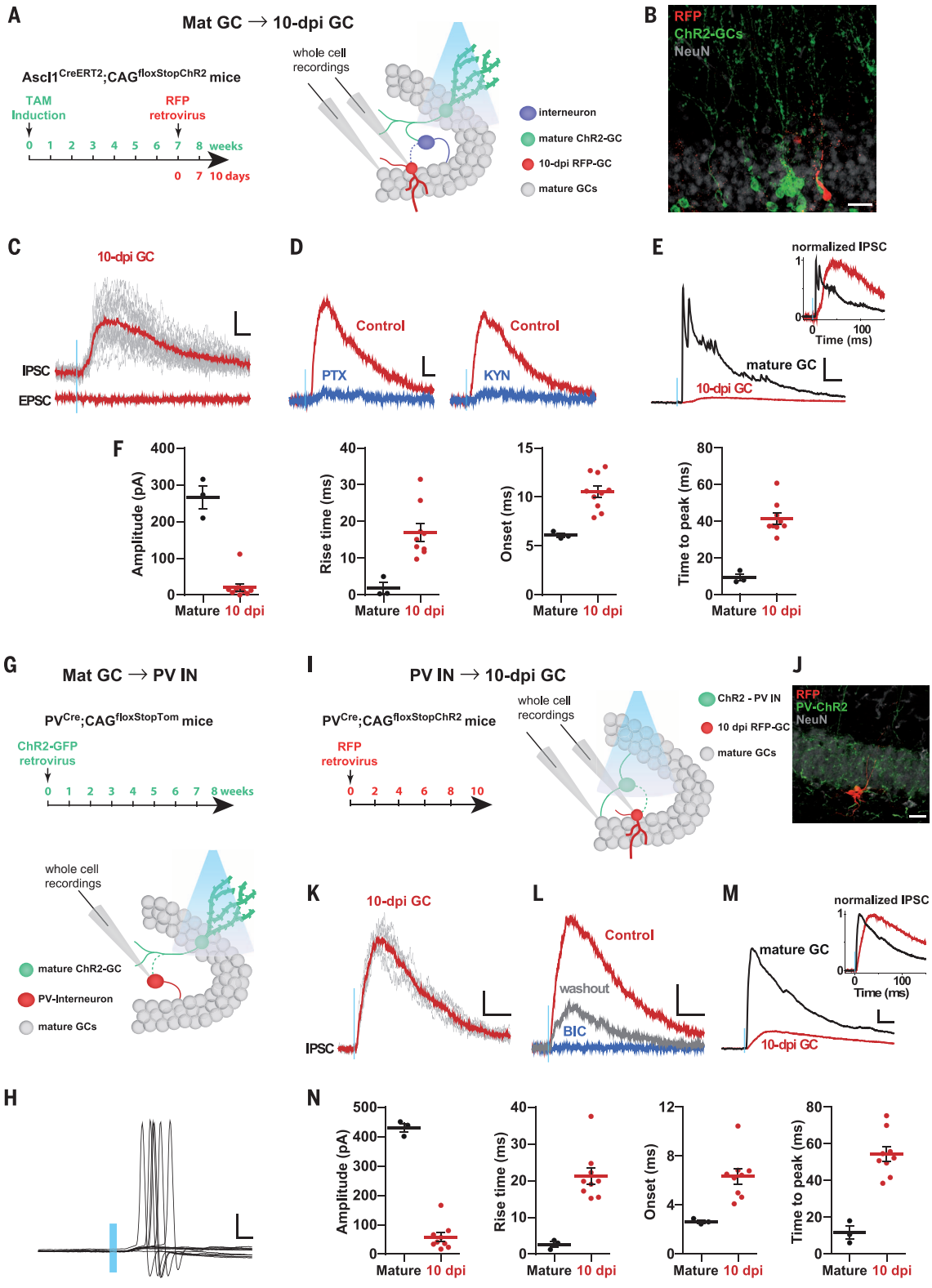

Fig. 3. Mature GCs signal onto developing GCs through PV interneurons. (**A** to **F**) Mature GCs connect to developing GCs. (A) Experimental design. Ascl1^{CreERT2};CAG^{floxStopChR2EYFP} mice received TAM to label a pool of adult-born GCs (mature ChR2-GCs). After 7 weeks, an RFP-expressing retrovirus was injected to label a different cohort of new GCs (RFP-GCs). Whole-cell recordings were carried out 10 days later in RFP-GCs. (B) Confocal image showing TAM-induced mature ChR2-GCs and a 10-dpi RFP-GC. Scale bar, 20 μm. (C) Representative current traces depicting IPSCs and EPSCs obtained from 10-dpi RFP-GCs in response to laser-evoked activation of mature ChR2-GCs (1 ms; blue line). Average (red) and individual traces (gray) are shown. Scale bars, 5 pA, 20 ms. (D) IPSC currents were abolished (>90% block) by 100 μM picrotoxin (PTX; n = 3) and 4 mM kynurenic acid (KYN; n = 2). Scale bars, 5 pA, 20 ms. (E) Comparison of light-evoked IPSCs from unlabeled mature GCs and 10-dpi GCs. Scale bars, 50 pA, 20 ms. Inset shows normalized traces. (F) Characterization of disynaptic IPSCs from 10-dpi RFP-GCs (n = 9 cells, 4 mice) and mature GCs (n = 3 cells, 2 mice). (**G** and **H**) Mature GCs activate PV-interneurons. (G) PV^{Cre};CAG^{floxStopTom} mice received ChR2-expressing retrovirus to transduce adult-born GCs (mature ChR2-GCs). Whole-cell recordings were carried out 8 weeks later in Tom-PV-INs. (H) Example voltage traces depicting spiking of a PV-IN upon light-activation of mature ChR2-GCs (1 ms; blue line). Scale bars, 20 mV, 2 ms. (**I** to **N**) PV-INs synapse onto developing GCs. (I) PV^{Cre};CAG^{floxStopChR2EYFP} mice received RFP-expressing retrovirus to label new GCs. Whole-cell recordings were carried out in 10-dpi RFP-GCs. (J) Confocal image of a 10-dpi RFP-GC and mature GCs surrounded by axons from ChR2-PV-INs. Scale bar, 20 μm. (K) Representative laser-evoked (200 μs; blue line) IPSC obtained from a 10-dpi RFP-GC. Scale bars, 10 pA, 50 ms. (L) IPSCs were blocked >99% by 20 μM bicuculline (BIC; n = 5). Scale bars, 10 pA, 50 ms. (M) Light-evoked IPSCs from unlabeled mature GCs and 10-dpi GCs. Scale bars, 50 pA, 20 ms. Inset shows normalized traces. (N) Monosynaptic IPSC parameters from 10-dpi RFP-GCs (n = 9 cells, 3 mice) and mature GCs (n = 3 cells, 2 mice). In (F) and (N), central horizontal bars denote mean and error bars denote SEM.

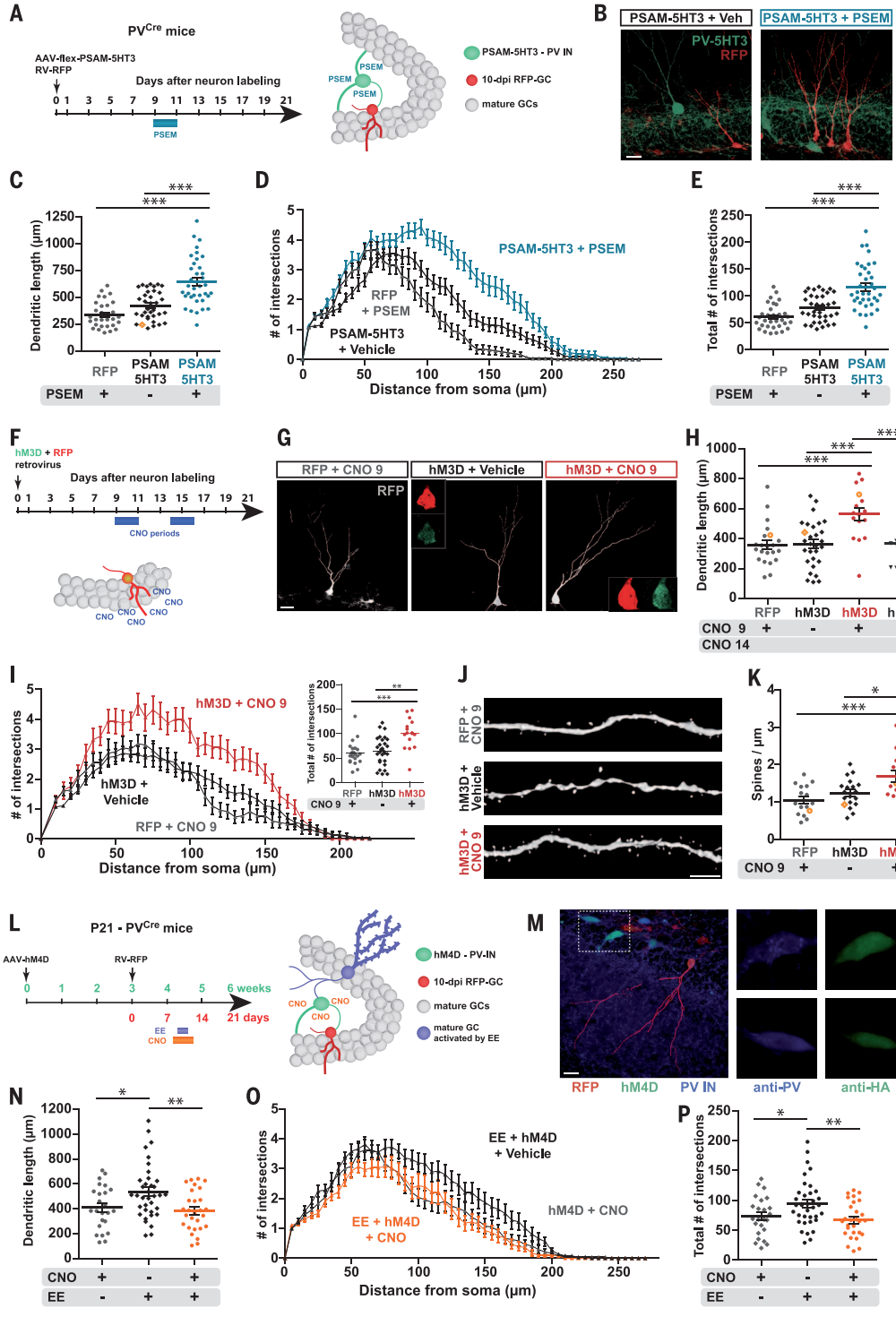

Fig. 4. PV interneurons and intrinsic activity during the critical period promote integration of new GCs. (**A** to **E**) PV-INs accelerate GC integration. (A) Experimental design. PV^{Cre} mice received AAV-PSAM-5HT3 and RFP retrovirus to transduce PV-INs and new GCs. $PSEM^{308}$ (10 mg/kg) or vehicle were delivered at 9 dpi (8 intraperitoneal injections in 48 hours) to stimulate PSAM-5HT3-PV-INs. Morphological analysis was done on RFP-GCs at 21 dpi. (B) Representative confocal images of RFP-GCs surrounded by labeled PV-INs and their axons, obtained from mice treated with vehicle (left) or $PSEM^{308}$ (right). Scale bar, 20 μm. (C) Dendritic lengths measured for the different treatments. The orange symbol corresponds to the example neuron shown in (B). [(D) and (E)] Sholl analysis for dendrites of new GCs under different treatments. ***P < 0.001 after Kruskal-Wallis ANOVA followed by Dunn post hoc test, with n = 35, 37, and 32 GCs (from 3 or 4 mice) for RFP + PSEM, PSAM-5HT3 + vehicle, and PSAM-5HT3 + PSEM, respectively [(C) and (E)]. (**F** to **K**) Intrinsic depolarization accelerates GC integration. (F) Retroviruses expressing hM3D-EGFP or RFP were delivered to the dentate gyrus to transduce new GCs. Mice received CNO for 48 hours to stimulate hM3D-GCs at 9 or 14 dpi, and morphological analysis was done on RFP-GCs and hM3D-GCs at 21 dpi. (G) Representative confocal images of 21-dpi neurons in the temporal dentate gyrus obtained from mice that received RFP + CNO (left), hM3D-EGFP and RFP + vehicle (center), or hM3D-EGFP and RFP + CNO (right). Insets show colocalization of RFP and EGFP in the soma of co-infected neurons. Scale bar, 20 μm. (H) Dendritic lengths measured for the different conditions. ***P < 0.001 after ANOVA followed by Bonferroni post hoc test, with n = 22, 29, 16, and 28 GCs (from 4 or 5 mice) for RFP, hM3D + vehicle, hM3D + CNO 9, and hM3D + CNO 14, respectively. Orange symbols correspond to example neurons shown in (G). (I) Sholl analysis demonstrates substantial dendritic growth induced by CNO 9 treatment in hM3D-GCs. **P < 0.01, ***P < 0.001 after Kruskal-Wallis ANOVA followed by Dunn post hoc test. (J) Neuronal segments shown to highlight dendritic spines. Scale bar, 5 μm. (K) Spine density is higher after hM3D-GC activation. *P < 0.05, ***P < 0.001 after ANOVA followed by Bonferroni post hoc test, with n = 16, 19, and 13 GCs (from 4 or 5 mice) for RFP, hM3D + vehicle, and hM3D + CNO 9, respectively. (**L** to **P**) PV interneurons mediate the effects of EE. (L) PV^{Cre} mice received AAV-hM4Di and RFP-expressing retrovirus at the indicated times and were exposed to EE 9. CNO was delivered from day 8 to day 12 to block GABA release from hM4Di-PV-INs. Morphology of RFP-GCs was analyzed at 21 dpi. (M) Representative confocal image of RFP-GCs surrounded by labeled PV-INs expressing HA-HM4Di. Scale bar, 20 μm. Right panels show colocalization of anti-PV and anti-HA-hM4Di immunofluorescence from neurons in the dashed area. [(N) to (P)] Dendritic lengths and Sholl analysis for dendrites of new GCs after different treatments. *P < 0.05, **P < 0.01 after ANOVA followed by Bonferroni post hoc test, with n = 24, 36, and 28 GCs (from 4 or 5 mice) for CNO, EE, and CNO + EE, respectively. All error bars denote SEM.

spines of RFP-GCs to an extent similar to that elicited by EE (Fig. 2, B to F).

One possible pathway to convey activity-mediated signaling would be direct or indirect synaptic transmission from mature GCs onto developing GCs undergoing the critical period. At this early developmental stage, new GCs receive depolarizing γ-aminobutyric acid–releasing (GABAergic) inputs but lack glutamatergic afferents (*25*–*28*). A transient direct connection between mature and immature GCs was recently proposed (*29*). We therefore selectively expressed the light-activated channel Channelrhodopsin-2 (ChR2) in mature GCs by means of $Ascl1^{CreERT2}$; $CAG^{floxStopChR2EYFP}$ mice induced with TAM at a young adult stage (*30*). Seven weeks after TAM administration, a cohort of new GCs was labeled by retroviral transduction of RFP (Fig. 3, A and B). Acute slices were obtained 10 days later to monitor responses in 10-day-old RFP-GCs (fig. S3) elicited by light-mediated stimulation of mature ChR2-GCs. No glutamatergic responses were evoked from mature to immature GCs (0 of 9 cells; Fig. 3C). However, mature ChR2-GCs reliably recruited inhibitory postsynaptic currents (IPSCs) onto RFP-GCs (9 of 10 cells) that were blocked by the $GABA_A$ receptor antagonist picrotoxin or the ionotropic glutamate receptor blocker kynurenic acid, indicating a polysynaptic GABAergic feedback connection (Fig. 3D). IPSCs recorded from RFP-GCs displayed small amplitude and slow kinetics, in contrast to those recorded from mature GCs, consistent with a period of incipient GABAergic synaptogenesis (Fig. 3, E and F).

We next investigated the nature of the feedback pathway. Parvalbumin-expressing GABAergic interneurons (PV-INs) are main targets of GCs and also contact developing GCs at early stages of development (*8*, *31*). Activation of mature GCs can reliably recruit spiking of PV-INs (*24*) (Fig. 3, G and H). To determine whether PV-INs can signal onto GCs at early developmental stages relevant to the critical period observed here, we delivered RFP-expressing retrovirus to PV^{Cre}; $CAG^{floxStopChR2EYFP}$ young adult mice to monitor connectivity from ChR2-expressing PV-INs to 10-day-old RFP-GCs (Fig. 3, I and J). Laser-evoked stimulation of ChR2-PV-INs reliably elicited GABAergic IPSCs in RFP-GCs (9 of 9 cells) that were blocked by bicuculline (Fig. 3, K and L). In contrast to IPSCs recorded from mature GCs, RFP-GCs displayed IPSCs with small amplitude and slow kinetics, indicative of immature monosynaptic contacts (Fig. 3, M and N). GABAergic synaptic responses in 10-dpi RFP-GCs displayed similar properties when evoked by direct stimulation of ChR2-PV-INs and indirectly by stimulation of mature ChR2-GCs (fig. S4). Because of the high intracellular chloride concentration, GABAergic transmission is depolarizing in immature GCs and it becomes inhibitory at 3 to 4 weeks of age (*26*–*28*). Current-clamp recordings were performed to determine whether 10-dpi GCs undergo noticeable depolarization despite their weak GABAergic postsynaptic currents. RFP-GCs were depolarized (~20 mV) by laser-mediated stimulation of ChR2-PV-INs in brief trains that mimic PV-IN activity, but not by single pulses (fig. S5). Therefore, mature GCs recruit a disynaptic GABAergic feedback mediated by PV-INs that depolarizes developing GCs.

To determine whether this feedback circuit may link EE exploration to local dentate signaling, we investigated the possibility that activation of dentate PV-INs in vivo modulates the integration of GCs. We used an adeno-associated virus (AAV) to express the synthetic ligand-gated cationic channel PSAM-5HT3-GFP under control of a flex switch in PV^{Cre} mice to allow specific expression in PV interneurons and, consequently, restricted activation of PV-INs upon delivery of the synthetic agonist $PSEM^{308}$ (*32*). Mice received both AAV-PSAM-5HT3 and RFP retrovirus; $PSEM^{308}$ or vehicle were administered from 9 to 11 dpi, and morphology of RFP-GCs was analyzed at 21 dpi (Fig. 4, A and B). Stimulation of PV-INs produced robust dendritic growth in new GCs, mimicking the effects of EE (Fig. 4, C to E). We then investigated the consequence of simply depolarizing young GCs. A retrovirus expressing hM3D-EGFP (hM3D fused to enhanced green fluorescent protein) was used to transduce a cohort of new GCs in young adult mice, which received CNO for 48 hours starting at 9 or 14 days of age. Morphology of hM3D-EGFP–expressing GCs analyzed at 21 days showed that brief intrinsic stimulation within the critical period (9 dpi), but not outside (14 dpi), was sufficient to accelerate dendritic growth (Fig. 4, F to K). These findings suggest that the signal conveyed by intrinsic depolarization is sufficient to promote the integration of GCs by 9 dpi, but not later. Accordingly, chronic CNO stimulation beyond this time rendered effects on hM3D-GCs similar to the effects of a 2-day CNO stimulus during the critical period (fig. S6). Enhanced growth was detected rapidly upon stimulation at early stages of GC development, suggesting a process that triggers the initial preparation for input integration (fig. S7).

To determine whether PV-INs mediate the signaling from EE to new GCs, we used an AAV to express the synthetic ligand-gated G protein–coupled receptor hM4Di with a hemagglutinin tag (AAV-flex-HA-hM4Di) in PV^{Cre} mice to block GABA release from PV-INs of the dentate gyrus upon delivery of the synthetic agonist CNO (*33*). Mice received AAV at postnatal day 21 and RFP retrovirus at 6 to 7 weeks, and were then exposed to EE 9 in the presence or absence of CNO (Fig. 4, L to P). Silencing dentate gyrus PV-INs during exposure to EE abolished the accelerated integration of developing GCs triggered by experience.

Our results reveal a positive feedback loop of circuit remodeling in the GC layer with direct influence from behavior, whereby mature GCs activate PV-INs that accelerate the functional integration of incoming cohorts of very immature neurons—a process that we call "priming." Under basal conditions, new GCs become potentially relevant for information processing after about 4 weeks of age. At this time, they receive sufficient cortical excitation to become activated by experience and acquire the capacity to refine their cortical inputs in an activity-dependent manner, a process that might be relevant for learning (*4*, *34*, *35*). Our results show that a brief experience in EE acts upon developing GCs long before they acquire cortical excitatory inputs, and accelerates glutamatergic synaptogenesis, which might shorten the interval required for achieving functional significance in a behaving animal.

In our concept, "primed" GCs rapidly increase their excitatory drive while maintaining the enhanced excitability (high input resistance), resulting in immature neurons with expanded connectivity. This may favor their recruitment by incoming cortical signals and enhance their capacity for activity-dependent synaptic remodeling in response to novel challenges (*4*, *35*–*37*). Because priming is mediated by GABAergic interneurons and occurs in immature GCs lacking excitation, it may serve as a generalized mechanism that prepares new neurons to become recruited in a manner that is not restricted to the triggering experience, maximizing available resources. This cohort of highly excitable and highly connected GCs may be particularly prone to be recruited by incoming information, which would strengthen their connections and promote their permanence in the network to encode relevant features of the novel experience.

REFERENCES AND NOTES

1. F. H. Gage, S. Temple, *Neuron* **80**, 588–601 (2013).
2. G. Lepousez, A. Nissant, P. M. Lledo, *Neuron* **86**, 387–401 (2015).
3. D. N. Abrous, J. M. Wojtowicz, *Cold Spring Harb. Perspect. Biol.* **7**, a018952 (2015).
4. E. Kropff, S. M. Yang, A. F. Schinder, *Curr. Opin. Neurobiol.* **35**, 21–26 (2015).
5. J. Song *et al*., *Nature* **489**, 150–154 (2012).
6. J. Andersen *et al*., *Neuron* **83**, 1085–1097 (2014).
7. N. Urbán, F. Guillemot, *Front. Cell. Neurosci.* **8**, 396 (2014).
8. J. Song *et al*., *Nat. Neurosci.* **16**, 1728–1730 (2013).
9. E. G. Waterhouse *et al*., *J. Neurosci.* **32**, 14318–14330 (2012).
10. G. Kempermann, H. G. Kuhn, F. H. Gage, *Nature* **386**, 493–495 (1997).
11. H. van Praag, G. Kempermann, F. H. Gage, *Nat. Neurosci.* **2**, 266–270 (1999).
12. V. C. Piatti *et al*., *J. Neurosci.* **31**, 7715–7728 (2011).
13. J. H. Chancey *et al*., *J. Neurosci.* **33**, 6614–6622 (2013).
14. M. Bergami *et al*., *Neuron* **85**, 710–717 (2015).
15. J. S. Snyder, S. C. Ferrante, H. A. Cameron, *PLOS ONE* **7**, e48757 (2012).
16. M. V. Wu, A. Sahay, R. S. Duman, R. Hen, *Cold Spring Harb. Perspect. Biol.* **7**, a018978 (2015).
17. S. Leutgeb, J. K. Leutgeb, M. B. Moser, E. I. Moser, *Curr. Opin. Neurobiol.* **15**, 738–746 (2005).
18. M. K. Chawla *et al*., *Hippocampus* **15**, 579–586 (2005).
19. B. L. McNaughton, F. P. Battaglia, O. Jensen, E. I. Moser, M. B. Moser, *Nat. Rev. Neurosci.* **7**, 663–678 (2006).
20. L. Madisen *et al*., *Nat. Neurosci.* **13**, 133–140 (2010).
21. E. J. Kim, J. L. Ables, L. K. Dickel, A. J. Eisch, J. E. Johnson, *PLOS ONE* **6**, e18472 (2011).
22. S. M. Yang, D. D. Alvarez, A. F. Schinder, *J. Neurosci.* **35**, 15379–15390 (2015).
23. G. M. Alexander *et al*., *Neuron* **63**, 27–39 (2009).
24. S. G. Temprana *et al*., *Neuron* **85**, 116–130 (2015).
25. M. S. Espósito *et al*., *J. Neurosci.* **25**, 10074–10086 (2005).

26. L. Overstreet Wadiche, D. A. Bromberg, A. L. Bensen, G. L. Westbrook, *J. Neurophysiol.* **94**, 4528–4532 (2005).
27. S. Ge *et al.*, *Nature* **439**, 589–593 (2006).
28. S. Heigele, S. Sultan, N. Toni, J. Bischofberger, *Nat. Neurosci.* **19**, 263–270 (2016).
29. C. Vivar *et al.*, *Nat. Commun.* **3**, 1107 (2012).
30. L. Madisen *et al.*, *Nat. Neurosci.* **15**, 793–802 (2012).
31. L. Acsády, A. Kamondi, A. Sík, T. Freund, G. Buzsáki, *J. Neurosci.* **18**, 3386–3403 (1998).
32. C. J. Magnus *et al.*, *Science* **333**, 1292–1296 (2011).
33. T. J. Stachniak, A. Ghosh, S. M. Sternson, *Neuron* **82**, 797–808 (2014).
34. S. Ge, C. H. Yang, K. S. Hsu, G. L. Ming, H. Song, *Neuron* **54**, 559–566 (2007).
35. A. Marín-Burgin, L. A. Mongiat, M. B. Pardi, A. F. Schinder, *Science* **335**, 1238–1242 (2012).
36. A. Tashiro, V. M. Sandler, N. Toni, C. Zhao, F. H. Gage, *Nature* **442**, 929–933 (2006).
37. D. Dupret *et al.*, *PLOS Biol.* **5**, e214 (2007).

ACKNOWLEDGMENTS

We thank S. Arber and M. Soledad Espósito for providing AAV-hM4Di and AAV-PSAM-5HT3 particles and for invaluable advice on their use, M. C. Monzón Salinas for technical help, S. Sternson for PSEM^{308}, B. Roth for the hM3Dq and hM4Di constructs, G. Davies Sala for preliminary experiments using retroviral expression of hM3Dq, J. Johnson for Ascl1^{CreERT2} mice, S. Arber for PV^{Cre} mice, members of the A.F.S. and G. Lanuza labs for insightful discussions, and V. Piatti for critical comments on the manuscript. D.G. and A.F.S. are investigators of the Consejo Nacional de Investigaciones Científicas y Técnicas (CONICET). Supported CONICET fellowships (D.D.A., S.M.Y., M.F.T., and S.G.T.), Howard Hughes Medical Institute SIRS grant 55007652 (A.F.S.), Argentine Agency for the Promotion of Science and Technology grant PICT2013-1685, and NIH grant FIRCA R03TW008607-01. The data reported in this manuscript are tabulated in the main paper and the supplementary materials. Author contributions: D.D.A. and D.G. contributed to the concept, designed and performed the experiments, analyzed the data, and wrote the manuscript; S.M.Y. and S.G.T. performed electrophysiological recordings and analyzed the data; M.F.T. and K.A.B. contributed to experiments involving enriched environment and analyzed the data; N.B. prepared retroviruses; and A.F.S. contributed to the concept, designed the experiments, analyzed the data, wrote the manuscript, and provided financial support.

SUPPLEMENTARY MATERIALS

www.sciencemag.org/content/354/6311/459/suppl/DC1
Materials and Methods
Figs. S1 to S7
References (*38*–*41*)

14 January 2016; accepted 16 September 2016
10.1126/science.aaf2156

CLIMATE CHANGE

Climate change: The 2015 Paris Agreement thresholds and Mediterranean basin ecosystems

Joel Guiot[1]* and Wolfgang Cramer[2]

The United Nations Framework Convention on Climate Change Paris Agreement of December 2015 aims to maintain the global average warming well below 2°C above the preindustrial level. In the Mediterranean basin, recent pollen-based reconstructions of climate and ecosystem variability over the past 10,000 years provide insights regarding the implications of warming thresholds for biodiversity and land-use potential. We compare scenarios of climate-driven future change in land ecosystems with reconstructed ecosystem dynamics during the past 10,000 years. Only a 1.5°C warming scenario permits ecosystems to remain within the Holocene variability. At or above 2°C of warming, climatic change will generate Mediterranean land ecosystem changes that are unmatched in the Holocene, a period characterized by recurring precipitation deficits rather than temperature anomalies.

The United Nations Framework Convention on Climate Change (UNFCCC) Paris Agreement of December 2015 aims "to hold the increase in the global average temperature to below 2°C above preindustrial levels and to pursue efforts to limit the temperature increase to 1.5°C...." For many regions of the world, achieving the global 2°C target would still imply substantially higher average temperatures, with daily maxima reaching extreme values (*1*). Recent ~1°C warming has caused damage in many systems already today (*2*). The degree to which future damage could be avoided by ambitious warming thresholds is uncertain. Regional temperatures in the Mediterranean basin are now ~1.3°C higher than during 1880–1920, compared with an increase of ~0.85°C worldwide (Fig. 1). The difference between (global) warming of 1.5° and >2°C above preindustrial levels is critically important for adaptation policies in the Mediterranean region, notably with respect to land-use systems and the conservation of biodiversity. Simulations with impact models have shed some light on the risks and sensitivities to climate change, but they face limitations when applied at the regional scale and for low levels of warming (*3*).

To assess the regional effects of different Paris Agreement thresholds for the Mediterranean basin, the Holocene reconstruction of spatiotemporal ecosystem dynamics from pollen allows the development of reliable scenarios of climate-driven change in land ecosystems (*4*). Despite the effects of human land use, broader-scale past ecosystem dynamics have been mostly driven by regional climate change.

Mediterranean basin ecosystems are a hot spot of the world's biodiversity (*5*) and supply numerous services to people, including clean water, flood protection, carbon storage, and recreation. Thus, the broad-scale vulnerability of ecosystems to climate change can be used as an indicator of the importance of the warming thresholds identified by the Paris Agreement for the environment and human well-being. Given the confidence with which past ecosystems and climate change can be reconstructed from numerous pollen profiles, the development and validation of more reliable numerical models for the ecosystem-climate relationship have become possible. We apply such an approach to future climate conditions, using simulations from the Coupled Model Intercomparison Project phase 5 (CMIP5) for three different greenhouse gas (GHG) forcings [see table S2 and (*6*) for details]. An analysis of the annual mean temperatures for these three scenarios for all climate models at the global and Mediterranean scale, an observational time series, and a spatiotemporal historical reconstruction at the Mediterranean scale (Fig. 1) indicate that (i) the projected warming in the Mediterranean basin exceeds the global trend for most simulations; (ii) the first decade of the 21st century has already surpassed the Holocene temperature variability; (iii) the global warming, but also the regional warming, is approximately a linear function of the CO_2 concentration; and (iv) only a few simulations provide global warming lower than 2°C at the end of the 21st century.

Mediterranean land ecosystems are sensitive not only to warming but also to changes in water availability. Even if past variations in precipitation and their projections for the future are spatially more heterogeneous than temperature fields (*7*), for most scenarios, the changes in both fields will combine to reduce water availability and trigger losses of Mediterranean ecosystems and their biodiversity during the coming decades (*8*–*10*). During the Holocene (especially in the second half of this epoch), periods of precipitation deficits have occurred, but in contrast to the 21st-century situation, temperatures did not rise above the present average (Fig. 1) (*4*). These periods of precipitation deficits [~6 to ~5.2, ~4.2 to ~4, and ~3.1 to ~2.9 thousand years before the present (yr B.P.)] have been identified as possible

[1]Aix-Marseille Université, CNRS, Institut de Recherche pour le Développement (IRD), Collège de France, Centre Européen de Recherche et d'Enseignement de Géosciences de l'Environnement (CEREGE), Ecosystèmes Continentaux et Risques Environnementaux (ECCOREV), Aix-en-Provence, France. [2]Mediterranean Institute for Biodiversity and Ecology (IMBE), Aix-Marseille Université, CNRS, IRD, Avignon University, 13545 Aix-en-Provence, France.
*Corresponding author. Email: guiot@cerege.fr

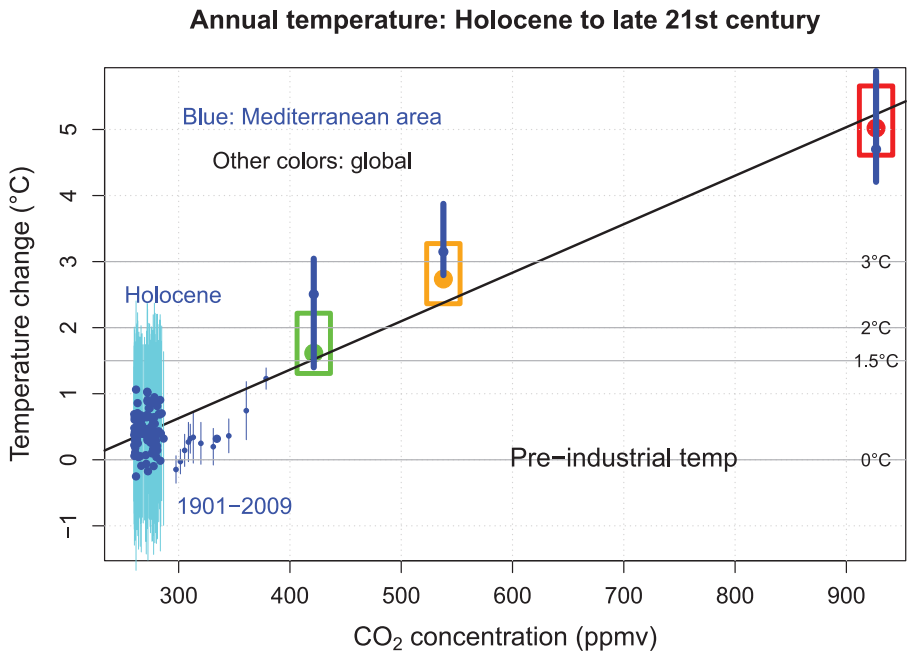

Fig. 1. Annual temperature change (from the preindustrial mean) versus CO_2 atmospheric concentrations. Colored boxes represent the Intergovernmental Panel on Climate Change RCP scenarios for 2010–2100 (25th, 50th, and 75th percentiles): RCP2.5 (green), RCP4.5 (orange), and RCP8.5 (red). Solid blue circles with vertical bars concern the same three scenarios for the Mediterranean region (10°W to 45°E, 28°N to 48°N). For the Holocene, the blue circles with cyan error bars (1σ) are derived from climate reconstructions from pollen for each century from 10,000 to 100 yr B.P. by steps of 100 years (*4*) (the variability is multiplied by a factor of 3 to account for the fact that the time resolution is 100 years instead of 10-year averages for the scenarios). The vertical bars represent the ±1 SDs provided by the reconstruction method. The medium-sized 1901–2009 circles are the Climatic Research Unit TS3.1 gridded observations (*20*) averaged in the same area and smoothed with a time step of 10 years. The vertical bars represent the corresponding SDs. The horizontal lines indicate the preindustrial mean temperature and the three thresholds referred to in the Paris Agreement (1.5°, 2°, and 3°C). The black regression line is based on the three global scenarios. ppmv, parts per million by volume.

causes of declines or collapses in civilization in the eastern Mediterranean region (*11*–*13*). A recent study (*14*) has attributed important crop failures in Syria to two strong drought episodes—characterized by a lack of precipitation (reduced by up to 30% in the 6-month winter season) and high temperatures (warming of 0.5° to 1.0°C in the annual mean relative to the 20th-century average)—in the eastern Mediterranean between 1998 and 2010. The 1998–2012 period was the driest of the last 500 years (*15*). Even if societal factors have likely been the primary causes of these crises (*16*, *17*), Holocene droughts and the associated variability in land productivity may have also played a role, indicating the potential effect of climate change on agriculture-based economies.

To relate the past variability of climate and ecosystems with possible future conditions, we use the process-based ecosystem model BIOME4 (*6*), which, when compared with correlation techniques, allows a more reliable reconstruction of past climate-vegetation equilibria. Direct human impacts, such as the cultivation of crops or degradation processes, are not taken into account. For the Holocene, BIOME4 was inverted to generate gridded climate patterns by time steps of 100 years and associated ecosystems ("biomes") from pollen records (*4*). For the future, the forward application of the same model yields ecosystem distributions from climate projections (*6*). The limitations of a relatively simple ecosystem model are largely offset by two factors. First, this method directly relates the physical environment, including its seasonal variability, and atmospheric CO_2 to plant processes and thereby avoids the strong assumptions made by niche models (*18*). Second, past observations are analyzed with the same process-based model that is used for the future projections, thus providing a more coherent framework for the assessment.

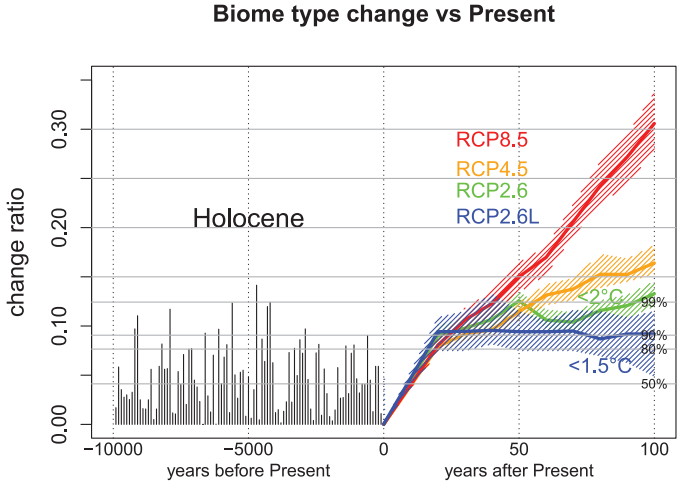

Fig. 2. Proportion of grid cells with a biome change relative to the preindustrial period for the Mediterranean area (10°W to 45°E, 28°N to 48°N). The horizontal axis represents the time scale, in years before the present (20th century) for the past (negative numbers) and in years after the present (CE 2000–2010) for the future (positive numbers). Holocene biomes (in black) are based on reconstructions from pollen data (*4*). Colored lines are given by the BIOME4 model as applied to the RCP projections (see text). Horizontal lines represent the 50th, 80th, 90th, and 99th percentiles of the Holocene values. The colored areas illustrate the interquartile interval provided by the intermodel variability.

Figure 2 indicates reconstructed and estimated shifts in the distribution of major Mediterranean biomes (temperate conifer forest, deciduous forest, warm mixed forest, xerophytic shrubland, and steppe) over time for the past and future, relative to their current distribution. During the Holocene, only up to 15% of the land has had different ecosystems from those existing today at any moment. The 10% level was exceeded only during eight 100-year time slices, and all of these periods occurred before 4200 yr B.P. All of these were relatively humid periods, which became less frequent after this date (*4*). The past four millennia, and notably the past century, were generally dry compared with the first half of the Holocene.

The future is represented by the following three classes of simulated time-space fields

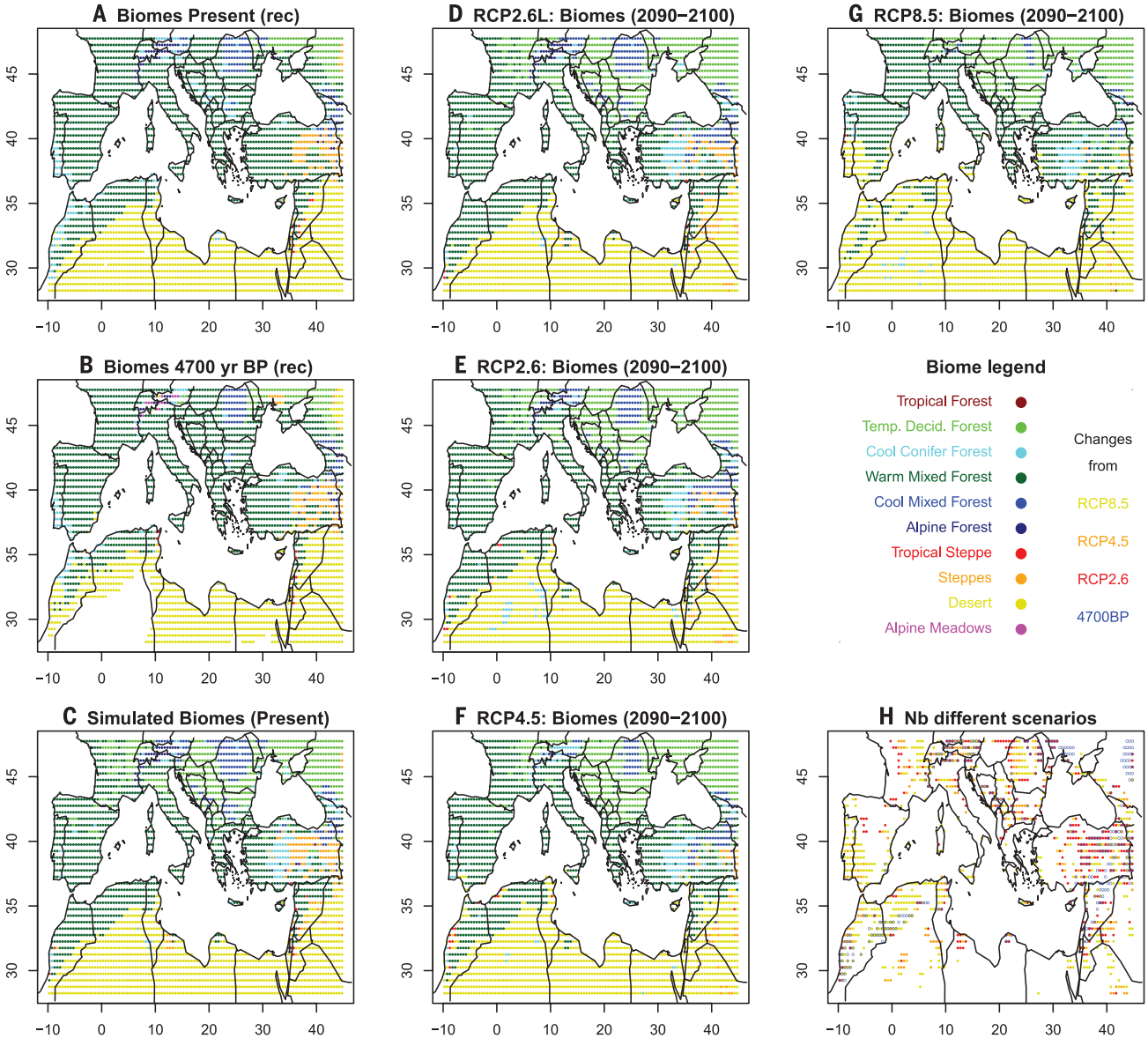

Fig. 3. Mediterranean biome maps. Distribution of Mediterranean biomes (**A**) reconstructed (rec) from pollen for the present; (**B**) reconstructed from pollen for 4700 yr B.P.; (**C**) simulated by the BIOME4 model for the present; and (**D** to **G**) for scenarios RCP2.6L, RCP2.6, RCP4.5, and RCP8.5, respectively, at the end of the 21st century. For the simulations, each point indicates the most frequent biome in the ensemble of CMIP5 climate simulations. Map (**H**) indicates, for each point, the number of scenarios different from the simulated present. Yellow areas indicate when only RCP8.5 is different; orange areas denote when RCP4.5 and RCP8.5 are different; red areas indicate when RCP2.6, RCP4.5, and RCP8.5 are different; and blue circles mark areas in which the biome type at 4700 yr B.P. is different from the present biome type.

of temperature and rainfall, which are derived from the CMIP5 project (table S2): Representative Concentration Pathway 8.5 (RCP8.5) (22 simulations), RCP4.5 (23 simulations), and RCP2.6 (16 simulations). RCP2.6 approximates the 2°C target. To assess the 1.5°C target, we created a fourth class (denoted RCP2.6L) from selected CMIP5 scenarios [see (*6*) for details]. Up to 2030, all four classes generate similar ecosystem distributions and generally remain within the bounds of Holocene fluctuations. By the end of the 21st century, RCP2.6L remains in the range of the 80th and 99th percentiles of the Holocene, whereas RCP2.6 simulates Mediterranean ecosystems as they were during the most extreme period of the Holocene (at 4700 yr B.P.), with a change of 12 to 15%.

The limits of the Mediterranean vegetation types defined by biogeographers (*19*) broadly coincide with our simulated warm mixed forest biome (Fig. 3A), with the following two exceptions: (i) Simulated warm mixed forests also extend to the Atlantic Ocean in the west of France, indicating the inability of BIOME4 to distinguish Atlantic pine forests, and (ii) the narrow strip of Mediterranean vegetation on the Libyan and Egyptian coast, which is below the spatial resolution of our climatic data. The reconstruction for the period of the Holocene (4700 yr B.P.) (Fig. 3B) with the greatest difference from today (Fig. 3A) shows that the main differences are related to the further regression of forested areas in the southern Mediterranean associated with expanding desert areas.

Simulations for the RCP2.6L and RCP2.6 scenarios do not change biome distributions much at the end of the 21st century (Fig. 3, D to E). However, for the same period, the RCP4.5 scenario induces desert extension toward North Africa, the regression of alpine forests, and the extension of Mediterranean sclerophyllous vegetation. Under the RCP8.5 scenario, all of

southern Spain turns into desert, deciduous forests invade most of the mountains, and Mediterranean vegetation replaces most of the deciduous forests in a large part of the Mediterranean basin. Figure 3H illustrates the variation from areas without any changes, regardless of scenario (stable white areas), to areas in which changes from scenario RCP2.6 already appear (red areas). As expected, the most-sensitive areas are those located at the limit between two biomes—for example, in the mountains at the transition between temperate and montane forest or in the southern Mediterranean at the transition between forest and desert biomes. The map for 4700 yr B.P., in which the past changes were among the highest (Fig. 3B), has the largest changes in the southwest, eastern steppe areas, and the mountains, but these changes are relatively sparse.

Our analysis shows that, in approximately one century, anthropogenic climate change without ambitious mitigation policies will likely alter ecosystems in the Mediterranean in a way that is without precedent during the past 10 millennia. Despite known uncertainties in climate models, GHG emission scenarios at the level of country commitments before the UNFCCC Paris Agreement will likely lead to the substantial expansion of deserts in much of southern Europe and northern Africa. The highly ambitious RCP2.6 scenario seems to be the only possible pathway toward more limited impacts. Only the coldest RCP2.6L simulations, which correspond broadly to the 1.5°C target of the Paris Agreement, allow ecosystem shifts to remain inside the limits experienced during the Holocene.

This analysis does not account for other human impacts on ecosystems, in addition to climate change (i.e., land-use change, urbanization, soil degradation, etc.), which have grown in importance after the mid-Holocene and have become dominant during the past centuries. Many of these effects are likely to become even stronger in the future because of the expanding human population and economic activity. Most land change processes reduce natural vegetation or they seal or degrade the soils, representing additional effects on ecosystems, which will enhance, rather than dampen, the biome shifts toward a drier state than estimated by this analysis. This assessment shows that, without ambitious climate targets, the potential for future managed or unmanaged ecosystems to host biodiversity or deliver services to society is likely to be greatly reduced by climate change and direct local effects.

REFERENCES AND NOTES

1. S. I. Seneviratne, M. G. Donat, A. J. Pitman, R. Knutti, R. L. Wilby, *Nature* **529**, 477–483 (2016).
2. W. Cramer *et al.*, in *Climate Change 2014: Impacts, Adaptation, and Vulnerability. Part A: Global and Sectoral Aspects. Contribution of Working Group II to the Fifth Assessment Report of the Intergovernmental Panel on Climate Change*, C. B. Field *et al.*, Eds. (Cambridge Univ. Press, 2014), pp. 979–1037.
3. C.-F. Schleussner *et al.*, *Earth Syst. Dyn. Discuss.* **6**, 2447–2505 (2015).
4. J. Guiot, D. Kaniewski, *Front. Earth Sci.* **3**, 28 (2015).
5. F. Médail, N. Myers, in *Hotspots Revisited: Earth's Biologically Richest and Most Endangered Terrestrial Ecoregions*, R. A. Mittermeier *et al.*, Eds. (Conservation International, 2004), pp. 144–147.
6. Materials and methods are available as supplementary materials on *Science* Online.
7. E. Xoplaki, J. F. González-Rouco, J. Luterbacher, H. Wanner, *Clim. Dyn.* **23**, 63–78 (2004).
8. L. Maiorano *et al.*, *Philos. Trans. R. Soc. London Ser. B* **366**, 2681–2692 (2011).
9. T. Keenan, J. Maria Serra, F. Lloret, M. Ninyerola, S. Sabate, *Glob. Change Biol.* **17**, 565–579 (2011).
10. W. Thuiller, S. Lavorel, M. B. Araújo, *Glob. Ecol. Biogeogr.* **14**, 347–357 (2005).
11. B. Weninger *et al.*, *Doc. Praehist.* **36**, 7–59 (2009).
12. D. Kaniewski, E. Van Campo, H. Weiss, *Proc. Natl. Acad. Sci. U.S.A.* **109**, 3862–3867 (2012).
13. N. Roberts, D. Brayshaw, C. Kuzucuoglu, R. Perez, L. Sadori, *Holocene* **21**, 3–13 (2011).
14. C. P. Kelley, S. Mohtadi, M. A. Cane, R. Seager, Y. Kushnir, *Proc. Natl. Acad. Sci. U.S.A.* **112**, 3241–3246 (2015).
15. B. I. Cook, K. J. Anchukaitis, R. Touchan, D. M. Meko, E. R. Cook, *J. Geophys. Res.* **121**, 2060–2074 (2016).
16. G. Middleton, *J. Archaeol. Res.* **20**, 257–307 (2012).
17. A. B. Knapp, S. W. Manning, *Am. J. Archaeol.* **120**, 99–149 (2016).
18. C. B. Yackulc, J. D. Nichols, J. Reid, R. Der, *Ecology* **96**, 16–23 (2015).
19. C. Roumieux *et al.*, *Ecol. Mediterr.* **36**, 17–24 (2010).
20. I. Harris, P. D. Jones, T. J. Osborn, D. H. Lister, *Int. J. Climatol.* **34**, 623–642 (2014).

ACKNOWLEDGMENTS

The authors are members of the Observatoire des Sciences de l'Univers Pytheas Institute and the ECCOREV network. This research has been funded by Labex OT-Med (project ANR-11-LABEX-0061), the "Investissements d'Avenir" French government project of the French National Research Agency (ANR), AMidex (project 11-IDEX-0001-02), and the European Union FP7-ENVIRONMENT project OPERAs (grant 308393). We acknowledge the World Climate Research Programme's Working Group on Coupled Modelling, which is responsible for CMIP, and we thank the climate modeling groups (table S2) for producing and making their model outputs available. For CMIP, the U.S. Department of Energy's Program for Climate Model Diagnosis and Intercomparison provides coordinating support and led the development of software infrastructure, in partnership with the Global Organization for Earth System Science Portals. R. Suarez and S. Shi have extracted and preprocessed the model simulations. Holocene climate reconstructions are available at http://database.otmed.fr/geonetworkotmed/srv/eng/search - |54b9bf34-57ae-45ea-b455-9f90351e538f. Future climate projections are available at http://cmip-pcmdi.llnl.gov/cmip5/.

SUPPLEMENTARY MATERIALS

www.sciencemag.org/content/354/6311/465/suppl/DC1
Materials and Methods
Table S1 and S2
References (*21*–*28*)

6 July 2016; accepted 21 September 2016
10.1126/science.aah5015

GENE EXPRESSION

Xist recruits the X chromosome to the nuclear lamina to enable chromosome-wide silencing

Chun-Kan Chen,[1] Mario Blanco,[1] Constanza Jackson,[1] Erik Aznauryan,[1] Noah Ollikainen,[1] Christine Surka,[1] Amy Chow,[1] Andrea Cerase,[2] Patrick McDonel,[3] Mitchell Guttman[1]*

The Xist long noncoding RNA orchestrates X chromosome inactivation, a process that entails chromosome-wide silencing and remodeling of the three-dimensional (3D) structure of the X chromosome. Yet, it remains unclear whether these changes in nuclear structure are mediated by Xist and whether they are required for silencing. Here, we show that Xist directly interacts with the Lamin B receptor, an integral component of the nuclear lamina, and that this interaction is required for Xist-mediated silencing by recruiting the inactive X to the nuclear lamina and by doing so enables Xist to spread to actively transcribed genes across the X. Our results demonstrate that lamina recruitment changes the 3D structure of DNA, enabling Xist and its silencing proteins to spread across the X to silence transcription.

The Xist long noncoding RNA (lncRNA) initiates X chromosome inactivation (XCI), a process that entails chromosome-wide transcriptional silencing (*1*) and large-scale remodeling of the three-dimensional (3D) structure of the X chromosome (*2*–*4*), by spreading across the future inactive X chromosome and excluding RNA polymerase II (PolII) (*1*, *5*). Xist initially localizes to genomic DNA regions on the X chromosome that are not actively transcribed (*6*–*8*), before spreading to actively transcribed genes (*7*–*9*). Deletion of a highly conserved region of Xist that is required for transcriptional silencing, called the A-repeat (*10*), leads to a defect in Xist spreading (*7*) and spatial exclusion of active genes from the Xist-coated nuclear compartment (*9*). Whether these structural changes are required for, or merely a consequence of, transcriptional silencing mediated by the A-repeat of Xist remains unclear (*7*, *9*). Recently, we and others identified by means of mass spectrometry the proteins that interact with Xist (*11*–*13*). One of these proteins is the Lamin B receptor (LBR) (*11*, *13*), a transmembrane protein that is anchored in the inner nuclear membrane, binds to Lamin B,

and is required for anchoring chromatin to the nuclear lamina (*14*)—a nuclear compartment that helps shape the 3D structure of DNA (*15*) and is enriched for silencing proteins (*14*, *16*). Because induction of XCI leads to recruitment of the inactive X-chromosome to the nuclear lamina (*4*), we hypothesized that the Xist-LBR interaction might be required to shape nuclear structure and regulate gene expression during XCI.

To test this, we knocked down LBR and measured the expression of five X chromosome genes and two autosomal genes before and after Xist induction (supplementary materials, materials and methods, note 1). Knockdown of LBR led to a defect in Xist-mediated silencing of these X chromosome genes but showed no effect on autosomal genes (Fig. 1A and figs. S1 and S2). We observed a similar silencing defect upon knockdown or knockout of LBR in differentiating female embryonic stem cells (fig. S3 and note 2). This silencing defect is not merely caused by disruption of the nuclear lamina because knockdown of Lamin B1 or Emerin, additional components of the nuclear lamina (*14*), had no effect on Xist-mediated silencing (Fig. 1A and fig. S4).

We hypothesized that the arginine-serine (RS) motif of LBR might be required for interacting with Xist (fig. S4A and note 3). A truncated LBR protein containing a deletion of the RS motif (ΔRS-LBR) (fig. S5 and materials and methods) did not interact with Xist (~97% reduced binding) (Fig. 1B and materials and methods) and failed to rescue the silencing defect upon knockdown of LBR (Fig. 1C and figs. S1B and S6). In contrast, deletion of seven of the eight transmembrane domains (ΔTM-LBR) (fig. S5) did not affect Xist binding (Fig. 1B) and was able to rescue the silencing defect upon knockdown of LBR (Fig. 1C, figs. S1B and S6, and note 4). To ensure that ΔRS-LBR fails to silence X chromosome genes because of its RNA binding ability, we fused three copies of the viral BoxB RNA aptamer, which binds tightly to the viral λN coat protein (*17*), to the 3′ end of the endogenous Xist RNA (Xist-BoxB) (fig. S7). Expression of ΔRS-LBR-λN in Xist-BoxB cells rescued the silencing defect observed upon LBR knockdown (Fig. 1D). Together, these results demonstrate that the Xist-LBR interaction is required for Xist-mediated transcriptional silencing.

We identified three discrete LBR binding sites (LBSs) that are spread across >10,000 nucleotides of the Xist RNA (Fig. 2A and materials and methods, note 5). One LBR binding site (LBS-1) overlaps the ~900 nucleotide region of Xist required for silencing (ΔA-repeat region) (Fig. 2A) (*10*). We tested LBR binding within a ΔA-repeat cell line (*10*) and found that LBR binding is disrupted across the entire Xist RNA (Fig. 2B), including the LBR binding sites that do not overlap the ΔA-repeat region (fig. S8). Because the Xist-binding protein SMRT/HDAC1–associated repressor protein (SHARP, also called Spen) also binds within the ΔA-repeat region (Fig. 2A) (*12*, *18*) and its binding is also disrupted in ΔA-Xist (Fig. 2B) (*12*), we generated a mutant Xist that precisely deletes a region within the LBR binding site that is not within the SHARP binding site (ΔLBS-Xist) (Fig. 2A). In ΔLBS-Xist, LBR binding was lost across the entire Xist RNA without affecting SHARP binding (Fig. 2B and fig. S8). ΔLBS-Xist fails to silence X chromosome transcription to a similar level, as observed in the ΔA-Xist (Fig. 2C, figs. S1 and S9, and notes 6 and 7).

To ensure that the observed silencing defect in ΔLBS-Xist cells is due to LBR-binding alone and not disruption of another unknown protein interaction, we tested whether we could rescue the observed silencing defect by reestablishing the ΔLBS-LBR interaction. To do this, we generated an endogenous ΔLBS-BoxB Xist RNA (materials and methods) and confirmed that expression of LBR-λN, but not LBR fused to a different RNA-binding domain (MS2-coat protein) (*19*), was able to rescue the silencing defect observed in ΔLBS-BoxB cells (Fig. 2D, fig. S10, and materials and methods). In contrast, expression of other silencing proteins fused to λN, such as SHARP and embryonic ectoderm development (EED), did not rescue the observed silencing defect (Fig. 2D and fig. S11), demonstrating that the LBR-binding site that overlaps the ΔA-repeat region of Xist is required for silencing.

We hypothesized that the Xist-LBR interaction might be required for recruiting the inactive X chromosome to the nuclear lamina (*4*). To test this, we measured the distance between the Xist-coated nuclear compartment and Lamin B1 in the nucleus using RNA fluorescence in situ hybridization (FISH), X chromosome paint, and immunofluorescence (fig. S12A and materials and methods). Upon Xist induction in wild-type cells, we found that the Xist compartment overlaps Lamin B1 signal (~90% of cells) (Fig. 3A, figs. S12 and S13, and note 8). In contrast, upon LBR knockdown or knockout, ΔLBS-Xist, or ΔA-Xist cells, there was a clear separation between the Xist-coated compartment and Lamin B1, demonstrating a >20-fold increase in distance relative to wild-type Xist (Fig. 3 and figs. S12 and S13). Thus, recruitment of the inactive X chromosome to the nuclear lamina is directly mediated by the Xist RNA through its interaction with LBR.

To determine whether LBR-mediated recruitment of the X chromosome to the nuclear lamina leads to Xist-mediated transcriptional silencing, we replaced the Xist-LBR interaction with another protein that interacts with the nuclear lamina; specifically, we used our endogenous ΔLBS-BoxB Xist, which fails to interact with LBR,

[1]Division of Biology and Biological Engineering, California Institute of Technology, Pasadena, CA 91125, USA. [2]European Molecular Biology Laboratory–Monterotondo, Via Ramarini 32, 00015 Monterotondo (RM), Italy. [3]Program in Molecular Medicine, University of Massachusetts Medical School, Worcester, MA 01655, USA.
*Corresponding author. Email: mguttman@caltech.edu

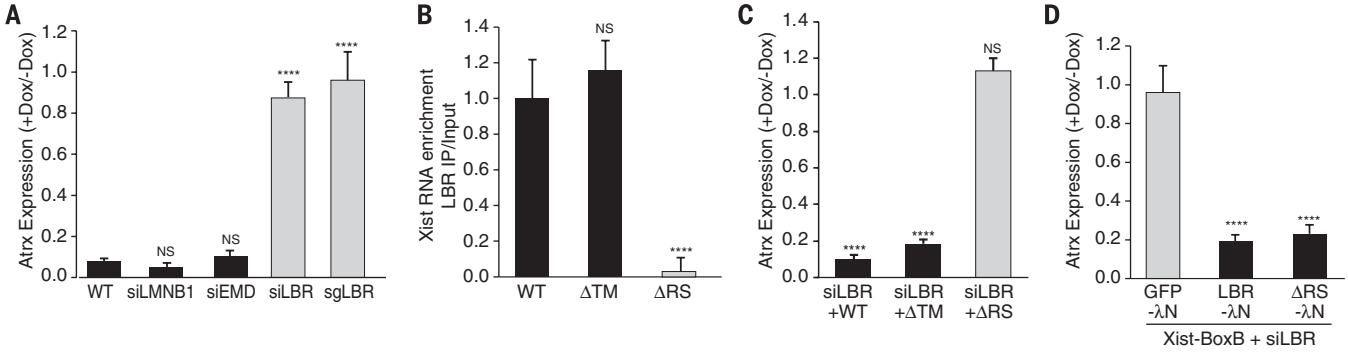

Fig. 1. LBR requires its RS motif to interact with Xist and silence transcription. (**A**) Atrx mRNA levels after Xist induction (+dox) relative to pre-Xist (−dox) levels upon knockdown of various nuclear lamina proteins. WT, scrambled small interfering RNA (siRNA) control; siEMD, Emerin knockdown; siLMNB1, Lamin B1 knockdown; sgLBR, knockdown of LBR by using dCas9-KRAB (materials and methods). (**B**) Xist enrichment after immunoprecipitation of a 3x-FLAG–tagged full-length LBR (WT), ΔRS-LBR, or ΔTM-LBR (materials and methods). Error bars indicate SEM from three independent IP experiments. (**C**) Relative Atrx mRNA expression upon knockdown of the endogenous LBR and expression of full length LBR (WT), ΔTM-LBR, or ΔRS-LBR. (**D**) Relative Atrx mRNA expression in Xist-BoxB cells after knockdown of the endogenous LBR and expression of green fluorescent protein (GFP)–λN (control), LBR-λN, or ΔRS-LBR-λN. NS, not significant. ****$P < 0.001$ relative to [(A) and (B)] wild-type cells, (C) cells transfected with siRNAs alone [shown in (A)], or (D) cells transfected with GFP-λN by means of an unpaired two-sample *t* test. Error bars indicate SEM across 50 individual cells.

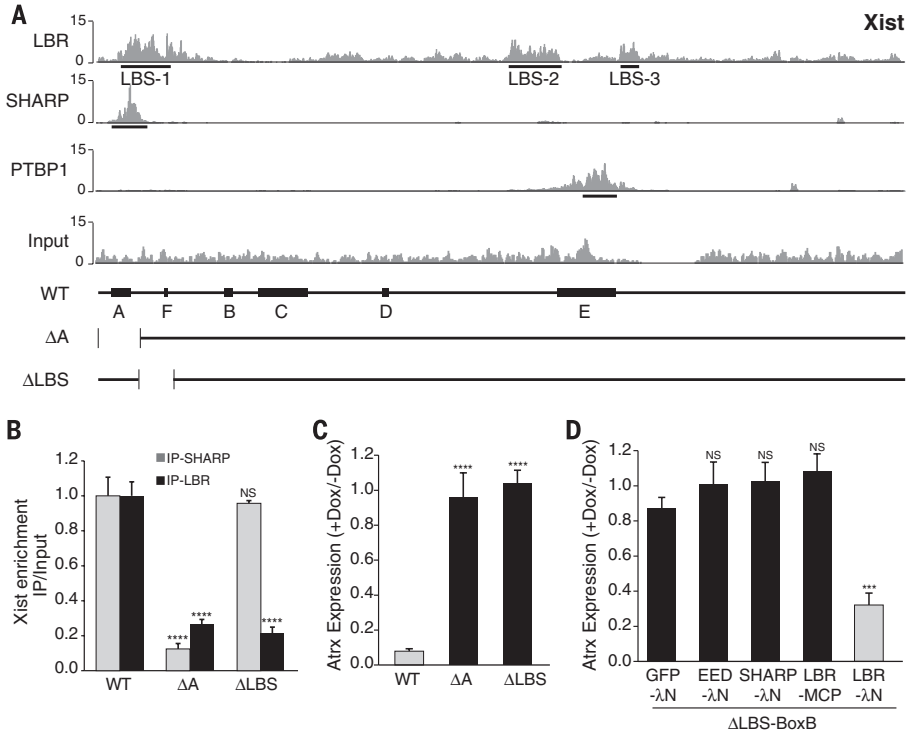

Fig. 2. LBR binds to precise regions of the Xist RNA that are required for silencing. (**A**) Cross-linking immunoprecipitation (CLIP) data plotted across the Xist RNA for LBR, SHARP, and PTBP1 proteins. The values represent fold-enrichment at each position on Xist normalized to a size-matched input RNA control. Input represents the total RNA control for the LBR sample. (Bottom) A schematic of the annotated repeat regions on the Xist RNA (WT) and the locations of the deleted regions in ΔA (nucleotides 1–937) and ΔLBS (nucleotides 898–1682). (**B**) Xist RNA enrichment level measured with quantitative reverse transcription polymerase chain reaction after immunoprecipitation of endogenous LBR or SHARP in wild-type, ΔA, or ΔLBS cells. Error bars indicate SEM from four independent immunoprecipitation experiments. (**C**) Relative Atrx mRNA expression in wild-type, ΔA, or ΔLBS-Xist cells. (**D**) Expression of ΔLBS-Xist with a 3x-BoxB fusion (ΔLBS-BoxB) along with expression of GFP-λN (control), EED-λN, SHARP-λN, or LBR-λN. As an additional control, we expressed LBR fused with the bacteriophage MS2 coat protein (LBR-MCP). Error bars indicate SEM across 50 individual cells. NS, not significant. ***$P < 0.005$, ****$P < 0.001$ relative to wild-type cells [(B) and (C)], or cells transfected with GFP-λN (D) by means of an unpaired two-sample *t* test.

to create an interaction between Xist and Lamin B1 (fig. S14A). We expressed a Lamin B1-λN fusion protein and confirmed that in cells expressing ΔLBS-BoxB Xist, the Xist-compartment was recruited to the nuclear lamina to a similar extent as that observed in wild-type conditions (Fig. 3, A and B, and fig. S12). Tethering Xist to the nuclear lamina rescues the Xist-silencing defect observed in ΔLBS cells to the same extent as that observed after rescuing directly with LBR-λN (Fig. 3C and fig. S14). Thus, Xist-mediated recruitment of the X chromosome to the nuclear lamina is required for Xist-mediated transcriptional silencing, and the function of LBR in Xist-mediated silencing is to recruit the X chromosome to the nuclear lamina.

We considered the possibility that recruitment to the nuclear lamina, a nuclear territory enriched for silenced DNA and repressive chromatin regulators (*14*, *16*), may act to directly silence transcription on the X chromosome (*20*, *21*). To test this, we knocked down SHARP, which fails to silence transcription on the X chromosome (*11*, *12*, *18*, *22*), and observed that the Xist-coated compartment was still localized at the nuclear lamina, demonstrating a comparable distance distribution between Xist and Lamin B1 to that observed for wild-type Xist (Fig. 3, A and B, and fig. S12). Therefore, Xist-mediated recruitment of the X chromosome to the nuclear lamina does not directly lead to transcriptional silencing because the X chromosome can still be transcribed even when localized at the nuclear lamina.

Instead, we considered the possibility that LBR-mediated recruitment of the X chromosome to the nuclear lamina could reposition active genes into the Xist-coated nuclear compartment, allowing Xist to spread across the X chromosome. Indeed, the Xist RNA gradually localizes to genes that are actively transcribed before initiation of XCI (*7*), but deletion of the A-repeat leads to a

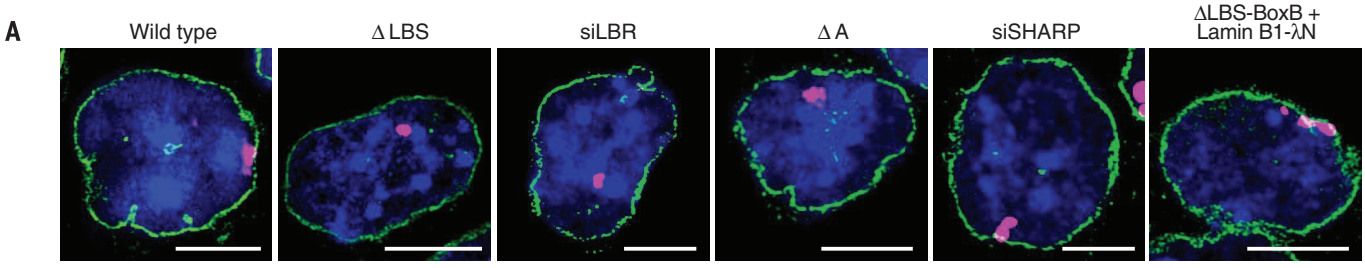

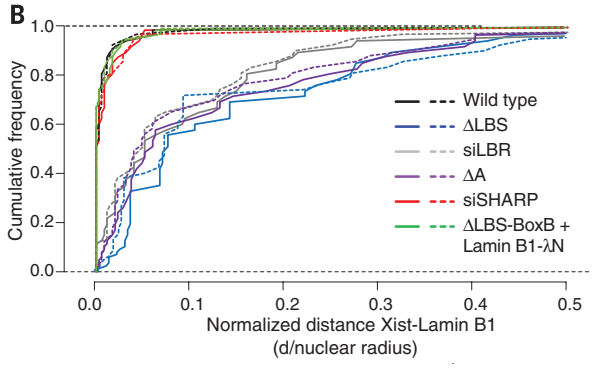

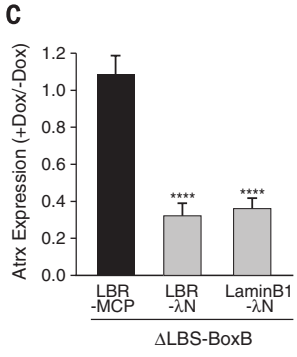

Fig. 3. Xist-mediated recruitment of DNA to the nuclear lamina is required for transcriptional silencing. (**A**) Images of Xist (red), Lamin B1 (green), and 4′,6-diamidino-2-phenylindole (DAPI) (blue) across different conditions. Scale bars, 5 μm. (**B**) The cumulative frequency distribution of normalized distances between Xist and Lamin B1 across 40 individual cells across different conditions. Dashed lines represents a second independent experiment. (**C**) Relative Atrx mRNA expression in ΔLBS-BoxB cells along with expression of LBR-MCP (control), LBR-λN, or LaminB1-λN. Error bars indicate SEM across 50 individual cells. NS, not significant. ****$P < 0.001$ relative to cells transfected with LBR-MCP by means of an unpaired two-sample *t* test.

defect in Xist spreading to these actively transcribed regions (*7*, *9*). In ΔLBS-Xist cells or upon knockdown of LBR, we observed a strong depletion of Xist RNA localization across regions of actively transcribed genes, comparable with the defect observed in ΔA-Xist cells (Fig. 4, A and B, and figs. S15 and S16) (*7*). We found that Xist RNA localization is even more strongly depleted over more highly transcribed genes (Fig. 4B). Knockdown of SHARP, which also binds the A-repeat, did not affect Xist localization (Fig. 4B and fig. S15). Synthetically tethering ΔLBS-BoxB to the nuclear lamina by using a Lamin B1-λN fusion enables Xist to spread to active genes to a similar level as that observed in wild-type conditions (Fig. 4B and figs. S15 and S16).

To determine whether this spreading defect is due to a failure to reposition actively transcribed genes into the Xist-coated compartment, we measured the position of the genomic loci of three actively transcribed genes relative to the Xist-coated compartment (Fig. 4C and materials and methods, note 9). In ΔLBS cells or upon knockdown or knockout of LBR, the distance between the Xist compartment and the loci of these actively transcribed X chromosome genes (Gpc4, Mecp2, and Pgk1 loci) were comparable with the distance between Xist and an autosomal gene (Notch2 locus) (Fig. 4, D and E, and figs. S17 and S18). Upon knockdown of SHARP, we found that these actively transcribed loci overlapped the Xist compartment (~80% of cells) (fig. S17), comparable with the Xist genomic locus itself (~90% of cells) (fig. S17). Because Xist can still spread to active genes upon knockdown of SHARP, which is known to be required for the exclusion of RNA PolII (*11*), our results demonstrate that spreading to active genes and exclusion of RNA PolII are independent functions that are both required for chromosome-wide transcriptional silencing.

Our results suggest a model for how Xist shapes the 3D nuclear structure of the inactive X chromosome to spread to active genes and silence chromosome-wide transcription (Fig. 4F and fig. S19). Xist initially localizes to the core of the X chromosome territory by localizing at DNA sites that are in close 3D proximity to its transcriptional locus (*7*). These initial Xist localization sites are generally inactive before Xist induction (*6*, *7*, *9*). The Xist-coated DNA, like other chromosomal DNA regions, will dynamically sample different nuclear locations (*23*) and, because Xist binds LBR, will become tethered at the nuclear lamina when it comes into spatial proximity. This lamina association is known to constrain chromosomal mobility

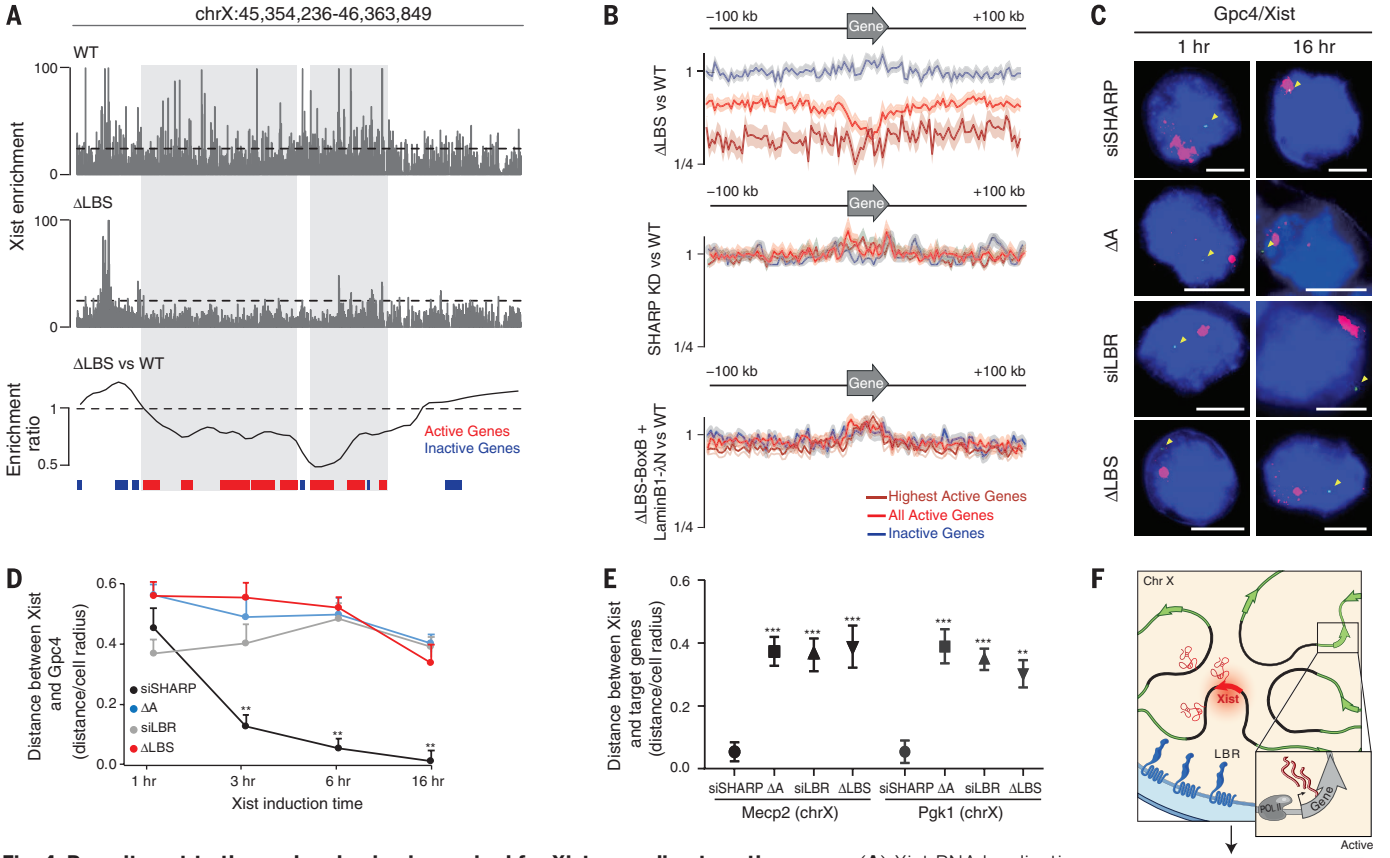

Fig. 4. Recruitment to the nuclear lamina is required for Xist spreading to active genes. (**A**) Xist RNA localization as measured with RNA antisense purification (RAP)–DNA for wild type (top), ΔLBS-Xist (middle), and the smoothed fold change (bottom) across a region of the X chromosome containing active (red) and inactive (blue) genes. The dashed line indicates average Xist enrichment in wild-type cells. (**B**) Aggregate Xist enrichment relative to the genomic locations of highly active genes [dark red, reads per kilobase per million (RPKM) > 5], all active genes (red, RPKM > 1), and inactive genes (blue) on the X-chromosome for ΔLBS, SHARP knockdown, and ΔLBS-BoxB + LMNB1-λN cells compared with wild-type cells. Shaded areas represent 95% confidence interval. (**C**) Images of Xist (red), Gpc4 locus (green), and DAPI (blue) across different cell lines (rows) after Xist induction for 1 or 16 hours. Yellow arrowheads indicate the genomic DNA location of Gpc4. Scale bars, 5 μm. (**D**) The median distance from Gpc4 locus to the Xist-compartment after Xist induction for 1, 3, 6, and 16 hours. Error bars represent the standard error of the median across 50 individual cells. $^{**}P < 0.01$ relative to 1-hour induction by means of an unpaired two-sample *t* test. (**E**) The median distance from the Mecp2 and Pgk1 locus to the Xist compartment after Xist induction for 16 hours across different conditions. Error bars represent the standard error of the median across 50 individual cells. $^{**}P < 0.01$, $^{***}P < 0.005$ relative to siRNAs targeting SHARP (siSHARP) by means of an unpaired two-sample *t* test. (**F**) A model for how Xist-mediated recruitment to the nuclear lamina enables spreading to active genes and transcriptional silencing on the X chromosome.

(*24*) and by doing so would position the Xist-coated DNA away from the actively transcribed Xist transcription locus. This would enable other DNA regions on the X chromosome, which are physically linked to these tethered regions, to be brought into closer spatial proximity of the Xist transcription locus. In this way, Xist and its silencing factors can spread to these newly accessible DNA regions on the X chromosome.

REFERENCES AND NOTES

1. R. Galupa, E. Heard, *Curr. Opin. Genet. Dev.* **31**, 57–66 (2015).
2. E. Splinter *et al.*, *Genes Dev.* **25**, 1371–1383 (2011).
3. S. S. Rao *et al.*, *Cell* **159**, 1665–1680 (2014).
4. A. Rego, P. B. Sinclair, W. Tao, I. Kireev, A. S. Belmont, *J. Cell Sci.* **121**, 1119–1127 (2008).
5. A. Wutz, *Nat. Rev. Genet.* **12**, 542–553 (2011).
6. C. M. Clemson, L. L. Hall, M. Byron, J. McNeil, J. B. Lawrence, *Proc. Natl. Acad. Sci. U.S.A.* **103**, 7688–7693 (2006).
7. J. M. Engreitz *et al.*, *Science* **341**, 1237973 (2013).
8. M. D. Simon *et al.*, *Nature* **504**, 465–469 (2013).
9. J. Chaumeil, P. Le Baccon, A. Wutz, E. Heard, *Genes Dev.* **20**, 2223–2237 (2006).
10. A. Wutz, T. P. Rasmussen, R. Jaenisch, *Nat. Genet.* **30**, 167–174 (2002).
11. C. A. McHugh *et al.*, *Nature* **521**, 232–236 (2015).
12. C. Chu *et al.*, *Cell* **161**, 404–416 (2015).
13. A. Minajigi *et al.*, *Science* **349**, aab2276 (2015).
14. Y. Gruenbaum, A. Margalit, R. D. Goldman, D. K. Shumaker, K. L. Wilson, *Nat. Rev. Mol. Cell Biol.* **6**, 21–31 (2005).
15. A. Pombo, N. Dillon, *Nat. Rev. Mol. Cell Biol.* **16**, 245–257 (2015).
16. J. Kind, B. van Steensel, *Curr. Opin. Cell Biol.* **22**, 320–325 (2010).
17. J. Baron-Benhamou, N. H. Gehring, A. E. Kulozik, M. W. Hentze, *Methods Mol. Biol.* **257**, 135–154 (2004).
18. A. Monfort *et al.*, *Cell Reports* **12**, 554–561 (2015).
19. A. R. Buxbaum, G. Haimovich, R. H. Singer, *Nat. Rev. Mol. Cell Biol.* **16**, 95–109 (2015).
20. L. E. Finlan *et al.*, *PLOS Genet.* **4**, e1000039 (2008).
21. K. L. Reddy, J. M. Zullo, E. Bertolino, H. Singh, *Nature* **452**, 243–247 (2008).
22. B. Moindrot *et al.*, *Cell Rep.* 10.1016/j.celrep.2015.06.053 (2015).
23. W. F. Marshall *et al.*, *Curr. Biol.* **7**, 930–939 (1997).
24. J. R. Chubb, S. Boyle, P. Perry, W. A. Bickmore, *Curr. Biol.* **12**, 439–445 (2002).

ACKNOWLEDGMENTS

We thank K. Plath for extensive discussions; A. Collazo for microscopy help; A. Shur, P. Quintero, and V. Grishkevich for technical help; M. Lai for analytical help; J. Engreitz, S. Quinodoz, M. Garber, I. Amit, and J. Rinn for comments on the manuscript; and S. Knemeyer for illustrations. Imaging was performed in the Biological Imaging Facility, and sequencing was performed in the Millard and Muriel Jacobs Genetics and Genomics Laboratory at the California Institute of Technology. C.-K.C. is supported by a NIH National Research Service Award training grant (T32GM07616). This research was funded by the New York Stem Cell Foundation, a NIH Director's Early Independence Award (DP5OD012190), the Edward Mallinckrodt Foundation, Sontag Foundation, Searle Scholars Program, Pew-Steward Scholars program, and funds from the California Institute of Technology. M.G. is a New York Stem Cell Foundation–Robertson Investigator. Sequencing data are available online from the National Center for Biotechnology Information Gene Expression Omnibus (www.ncbi.nlm.nih.gov/geo) accession no. GSE80510 (RAP data) and GSE86250 (CLIP data), and additional data and information are available at www.lncRNA.caltech.edu/data.php.

SUPPLEMENTARY MATERIALS

www.sciencemag.org/content/354/6311/468/suppl/DC1
Materials and Methods
Supplementary Text
Figs. S1 to S19
References (*25*–*49*)

5 December 2015; accepted 25 July 2016
Published online 4 August 2016
10.1126/science.aae0047

VASCULAR DISEASE

Senescent intimal foam cells are deleterious at all stages of atherosclerosis

Bennett G. Childs,[1] Darren J. Baker,[2] Tobias Wijshake,[2,3] Cheryl A. Conover,[4] Judith Campisi,[5,6] Jan M. van Deursen[1,2]*

Advanced atherosclerotic lesions contain senescent cells, but the role of these cells in atherogenesis remains unclear. Using transgenic and pharmacological approaches to eliminate senescent cells in atherosclerosis-prone low-density lipoprotein receptor–deficient (*Ldlr*$^{-/-}$) mice, we show that these cells are detrimental throughout disease pathogenesis. We find that foamy macrophages with senescence markers accumulate in the subendothelial space at the onset of atherosclerosis, where they drive pathology by increasing expression of key atherogenic and inflammatory cytokines and chemokines. In advanced lesions, senescent cells promote features of plaque instability, including elastic fiber degradation and fibrous cap thinning, by heightening metalloprotease production. Together, these results demonstrate that senescent cells are key drivers of atheroma formation and maturation and suggest that selective clearance of these cells by senolytic agents holds promise for the treatment of atherosclerosis.

Atherosclerosis initiates when oxidized lipoprotein infiltrates the subendothelial space of arteries, often due to aberrantly elevated levels of apolipoprotein B–containing lipoproteins in the blood (*1*). Chemotactic signals arising from activated endothelium and vascular smooth muscle attract circulating monocytes that develop into lipid-loaded foamy macrophages, a subset of which adopt a proinflammatory phenotype through a mechanism that is not fully understood. The proinflammatory signals lead to additional rounds of monocyte recruitment and accumulation of other inflammatory cells (including T and B cells, dendritic cells, and mast cells), allowing initial lesions, often termed "fatty streaks," to increase in size and develop into plaques (*2*). Plaque stability, rather than absolute size, determines whether atherosclerosis is clinically silent or pathogenic because unstable plaques can rupture and produce vessel-occluding thrombosis and end-organ damage. Stable plaques have a relatively thick fibrous cap, which largely consists of vascular smooth muscle cells (VSMCs) and extracellular matrix components, partitioning soluble clotting factors in the blood from thrombogenic molecules in the plaque (*3*). In advanced disease, plaques destabilize when elevated local matrix metalloprotease production degrades the fibrous cap, increasing the risk of lesion rupture and subsequent thrombosis.

Advanced plaques contain cells with markers of senescence, a stress response that entails a permanent growth arrest coupled to the robust secretion of numerous biologically active molecules and is referred to as the senescence-associated secretory phenotype (SASP). The senescence markers include elevated senescence-associated β-galactosidase (SA β-Gal) activity and $p16^{Ink4a}$, p53, and p21 expression (*4*, *5*). However, whether and how senescent cells contribute to atherogenesis remains unclear (*6*, *7*). Human plaques contain cells with shortened telomeres, which predispose cells to undergo senescence (*8*). Consistent with a proatherogenic role of senescence is the observation that expression of a loss-of-function telomere-binding protein (Trf2) in VSMCs accelerates plaque growth in the *ApoE*$^{-/-}$ mouse model of atherosclerosis, although in vivo evidence for increased senescence in plaques was not provided. On the other hand, mice lacking core components of senescence pathways, such as p53, p21, or $p19^{Arf}$ (*7*, *9*–*11*), show accelerated atherosclerosis, implying a protective role for senescence. Studies showing that human and mouse polymorphisms that reduce expression of $p16^{Ink4a}$ and $p14^{Arf}$ ($p19^{Arf}$ in mice) correlate with increased atheroma risk support this conclusion (*7*, *12*, *13*). Thus, whether senescent cells accelerate or retard atherogenesis is unclear.

We used genetic and pharmacological methods of eliminating senescent cells to examine the role of naturally occurring senescent cells at different stages of atherogenesis. First, we verified that senescent cells accumulate in low-density lipoprotein receptor–deficient (*Ldlr*$^{-/-}$) mice, a model of atherogenesis. We fed 10-week-old *Ldlr*$^{-/-}$ mice a high-fat diet (HFD) for 88 days. We then performed SA β-Gal staining, which

[1]Department of Biochemistry and Molecular Biology, Mayo Clinic, Rochester, MN 55905, USA. [2]Department of Pediatric and Adolescent Medicine, Mayo Clinic, Rochester, MN 55905, USA. [3]Department of Pediatrics, University of Groningen, University Medical Center Groningen, 9713 AV Groningen, Netherlands. [4]Division of Endocrinology, Metabolism, and Nutrition, Mayo Clinic, Rochester, MN 55905, USA. [5]Buck Institute for Research on Aging, Novato, CA 94945, USA. [6]Life Sciences Division, Lawrence Berkeley National Laboratory, Berkeley, CA 94720, USA.
*Corresponding author. Email: vandeursen.jan@mayo.edu

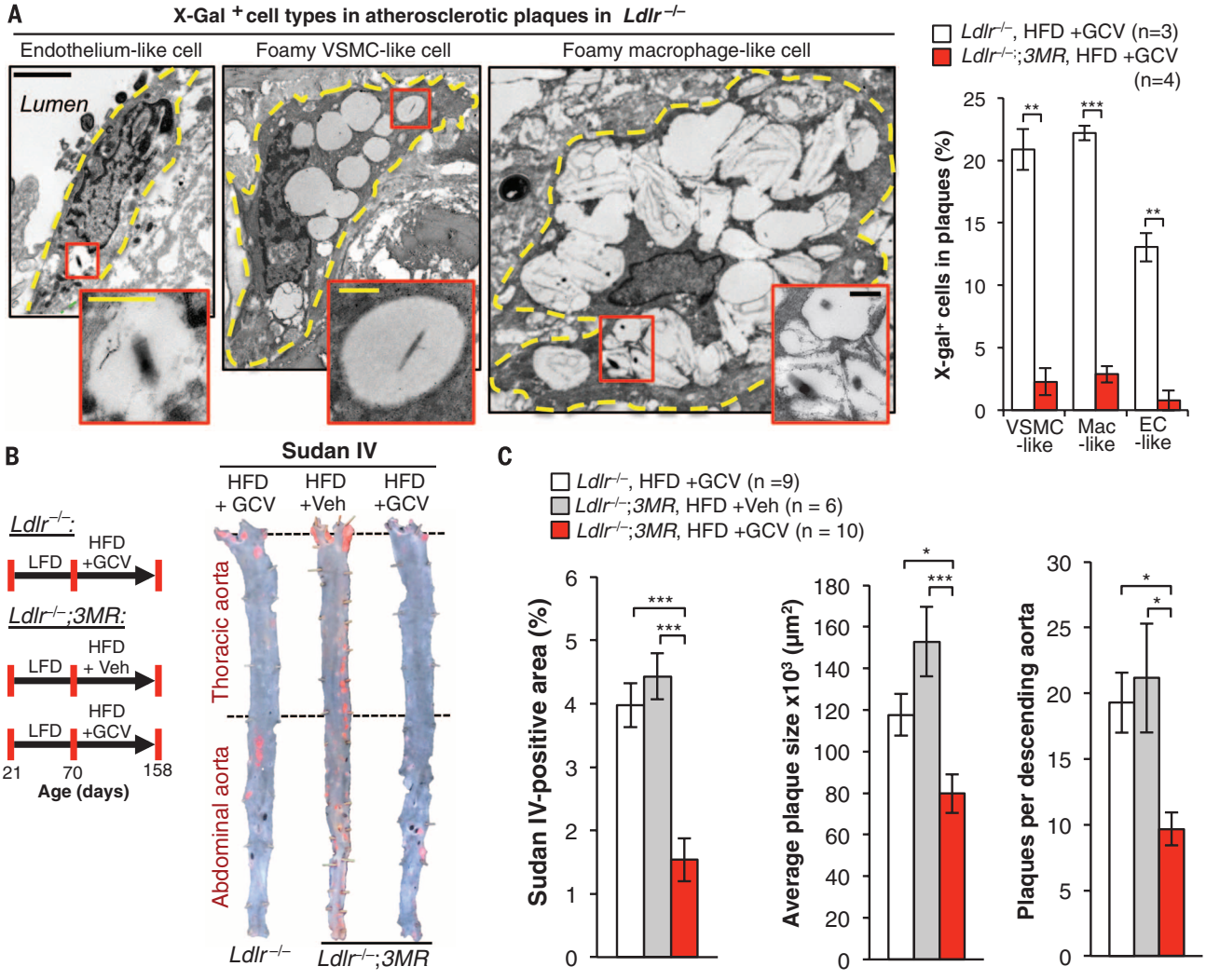

Fig. 1. $p16^{Ink4a+}$ senescent cells drive formation of atherosclerotic plaques. (**A**) (Left) X-Gal electron microscopy images showing three types of senescent cells in plaques of $Ldlr^{-/-}$ mice on a HFD for 88 days. Cell outlines are traced by dashed yellow lines. Endothelial-like cells are elongated and adjacent to the lumen. VSMC-like cells are elongated spindle-shaped cells or irregularly shaped ramified cells. Macrophage-like cells are highly vacuolated circular cells. (Right) Senescent cell quantification in plaques. Mac, macrophage; EC, endothelial cell. (**B**) (Left) Experimental design for testing the effect of senescent cell clearance on atherogenesis. Veh, Vehicle. (Right) Sudan IV–stained descending aortas (not including the aortic arch). (**C**) Quantification of total descending aorta plaque burden, number, and lesion size. Scale bars: 2 µm (A); 500 nm [(A), insets]. Data represent mean ± SEM (error bars) [biological *n* is indicated on graphs and refers to individual plaques in (A) (one per mouse) and aortas in (C)]. $*P < 0.05$; $**P < 0.01$; $***P < 0.001$ (unpaired two-tailed *t* tests with Welch's correction).

revealed that senescent cells are present in atherosclerotic lesions but not in the normal adjacent vasculature or aortas of $Ldlr^{-/-}$ mice fed a low-fat diet (LFD) (fig. S1A). In addition, plaque-rich aortic arches had elevated transcript levels of $p16^{Ink4a}$, $p19^{Arf}$, and various canonical SASP components, including the matrix metalloproteases *Mmp3* and *Mmp13* and the inflammatory cytokines *Il1α* and *Tnfα* (fig. S1B). To eliminate senescent cells from plaques, we used *p16-3MR* (*3MR*) mice (*14*), a transgenic model that expresses the herpes simplex virus thymidine kinase under the control of the $p16^{Ink4a}$ gene promoter and kills $p16^{Ink4a+}$ senescent cells upon administration of ganciclovir (GCV). Plaques of $Ldlr^{-/-}$;*3MR* mice fed a HFD for 88 days and then treated short term with GCV had low levels of SA β-Gal activity compared with $Ldlr^{-/-}$ mice (fig. S1C), indicating efficient clearance of senescent cells. Examination of the plaques by transmission electron microscopy (TEM) revealed that three morphologically distinct cell types—elongated, vacuolated cells located in the endothelial layer; spindly foam cells with histological properties of VSMCs; and large foamy cells resembling lipid-loaded macrophages—produced X-galactosidase (X-Gal) crystals (Fig. 1A). We refer to these cells as endothelial-like, foamy VSMC–like, and foamy macrophage–like cells, respectively, because cells within plaques change shape and lineage markers, precluding accurate assessment of cell origin (*15*, *16*). All three senescent cell types were efficiently eliminated by treatment with GCV (Fig. 1A).

To assess the impact senescent cells have on plaque development, we placed 10-week-old $Ldlr^{-/-}$;*3MR* mice on a HFD for 88 days and simultaneously treated them with GCV or vehicle during this period (Fig. 1B) to intermittently remove $p16^{Ink4a+}$ cells. To control for potential effects of GCV, independent of 3MR expression, we also examined GCV-treated $Ldlr^{-/-}$ mice on a HFD. En face staining of descending aortas with Sudan IV revealed that plaque burden was ~60% lower in GCV-treated $Ldlr^{-/-}$;*3MR* mice than in vehicle-treated $Ldlr^{-/-}$;*3MR* or GCV-treated $Ldlr^{-/-}$ mice, owing to decreases in both plaque number and size (Fig. 1C). Similarly, GCV-treated $Ldlr^{-/-}$;*3MR* mice showed reduced plaque burden and destruction of aortic elastic fibers beneath the neointima in the brachiocephalic artery (fig. S2, A to C), a site that rapidly develops advanced atherosclerotic plaques (*17*). Compared with vehicle-treated $Ldlr^{-/-}$;*3MR* mice,

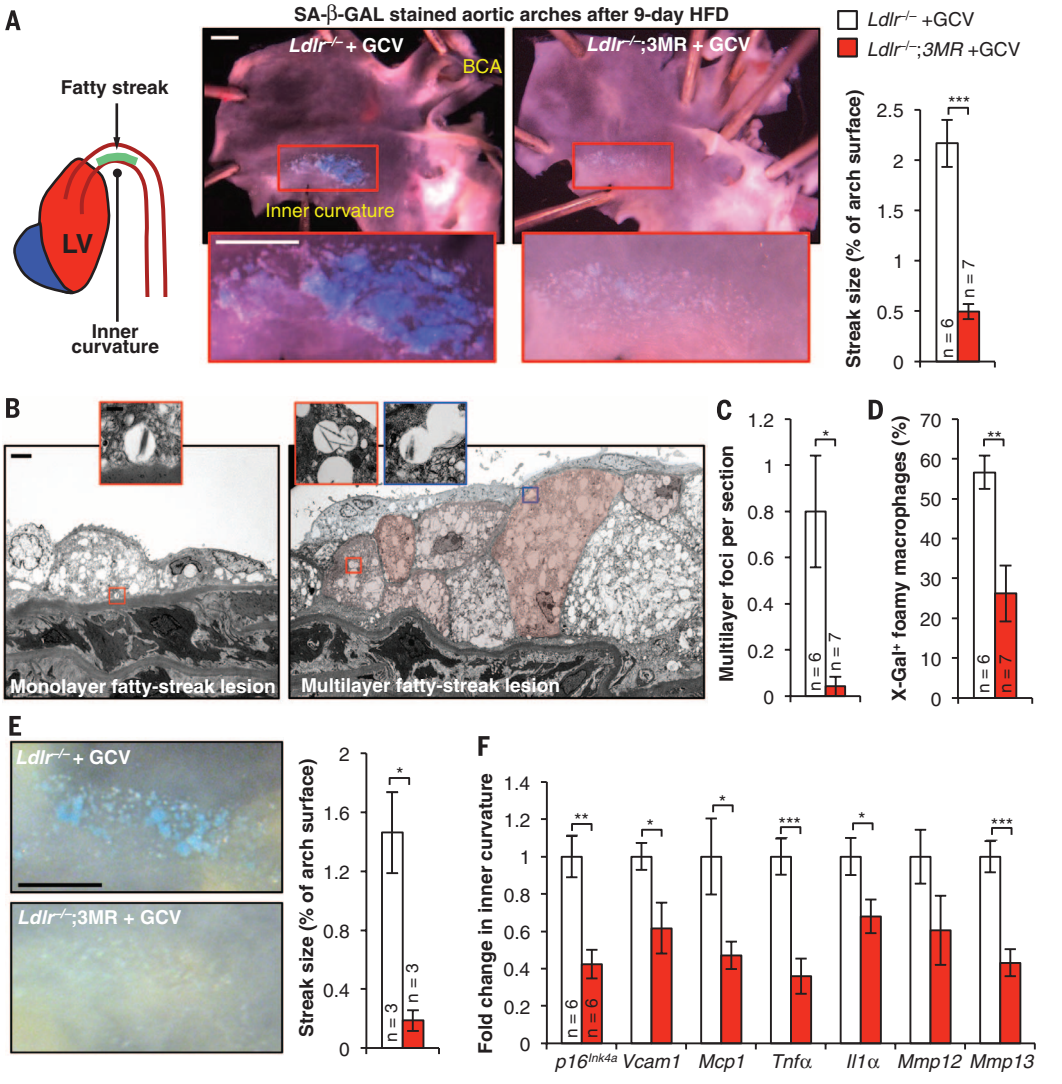

Fig. 2. Intimal senescent foamy macrophages form during early atherogenesis and foster production of proatherogenic factors. (**A**) (Left) Schematic of the inner curvature of the aortic arch. LV, left ventricle. (Middle) Examples of SA β-Gal–stained 9-day fatty streaks with and without senescent cell clearance and quantification. (Right) Measurements of streak size. Treatment involved the administration of 25 mg/kg of GCV once daily. BCA, brachiocephalic artery. (**B**) TEM images of $Ldlr^{-/-}$ mice after 9-day HFD feeding, showing fatty-streak foci with X-Gal–positive foam cell macrophages (artificial coloring articulates cell boundaries in the multilayer). (**C**) Quantification of multilayer foci in day-9 fatty streaks with and without senescent cells. (**D**) Quantification of foam cell macrophages with X-Gal crystal–containing vesicles without and with clearance. (**E**) (Left) Representative SA β-Gal–stained 12-day fatty streaks without and with GCV treatment (25 mg/kg of GCV three times daily) for the last 3 days. (Right) Quantification of lesion burden. (**F**) RT-qPCR analysis of senescence marker expression in fatty streaks collected from $Ldlr^{-/-}$ and $Ldlr^{-/-}$;*3MR* mice on a 12-day HFD and treated with GCV for the last 3 days. Scale bars: 1 mm (A) and (E); 2 μm (B); and 500 nm [(B), insets]. Bar graphs represent mean ± SEM (error bars) [biological *n* is indicated directly on all graphs and refers to individual aortic arches in (A) and (C) to (E) or dissected aortic arch inner curvatures in (F)]. **P* < 0.05; ***P* < 0.01; ****P* < 0.001 (unpaired two-tailed *t* tests with Welch's correction).

GCV-treated $Ldlr^{-/-}$;*3MR* mice expressed lower amounts of $p16^{Ink4a}$ mRNA and other senescence-marker mRNAs in aortic arches, confirming that $p16^{Ink4a+}$ senescent cells were efficiently cleared by GCV (fig. S3A). Expression of *3MR*, as measured by reverse transcription quantitative polymerase chain reaction (RT-qPCR) analysis of monomeric red fluorescent protein transcripts, increased in HFD-fed mice but remained at baseline levels with GCV treatment. Complementary en face SA β-Gal staining of aortas confirmed that $p16^{Ink4a+}$ senescent cells were effectively cleared (fig. S3B). GCV-treatment of $Ldlr^{-/-}$ mice did not alter SA β-Gal staining or other senescence markers (fig. S3, B and C). GCV-treated $Ldlr^{-/-}$ and $Ldlr^{-/-}$;*3MR* mice did not differ in body weight, fat mass, and fat deposit weight (fig. S4, A to D). Circulating monocytes, lymphocytes, platelets, and neutrophils, all of which are involved in atherogenesis, were unaffected (fig. S4, E to H). Levels of atherogenic lipids in the blood of GCV-treated $Ldlr^{-/-}$ and $Ldlr^{-/-}$;*3MR* mice and vehicle-treated $Ldlr^{-/-}$;*3MR* mice were highly elevated compared with levels in LFD-fed controls, with no differences between the distinct HFD-fed cohorts (fig. S4I). Thus, the atheroprotective effect in GCV-treated $Ldlr^{-/-}$;*3MR* mice is due to the killing of $p16^{Ink4a+}$ senescent cells rather than changes in feeding habits, blood lipids, or circulating immunocytes. Reductions in plaque burden, number, and size observed with *p16-3MR* were reproducible with two independent transgenic systems [*INK-ATTAC* (fig. S5) (*18*, *19*) and *INK-Nitroreductase* (*NTR*) (fig. S6)] designed to kill $p16^{Ink4a+}$ senescent cells through distinct mechanisms, as well as with the senolytic drug ABT263, which inhibits the anti-apoptotic proteins Bcl-2 and Bcl-xL and selectively kills senescent cells (fig. S7) (*20*).

To investigate how senescent cells drive plaque initiation and growth, we focused on atherogenesis onset at lesion-prone sites of the vasculature (*21*). After just 9 days on an atherogenic diet, $Ldlr^{-/-}$ mice had overtly detectable fatty-streak lesions solely in the inner curvature of the aortic arch (Fig. 2A and fig. S8A). Surprisingly, these early lesions were highly positive for SA β-Gal activity (Fig. 2A). By contrast, $Ldlr^{-/-}$ mice containing *3MR* and treated daily with GCV during the 9-day HFD-feeding period had low levels of SA β-Gal activity and much smaller fatty streaks (Fig. 2A). Histological examination by TEM of the SA β-Gal–stained samples revealed that fatty streaks of HFD-fed $Ldlr^{-/-}$ mice consisted of foci of foam cell macrophages arranged in mono- or multilayers (Fig. 2, B and C). The lesions had intact elastic fibers and no fibrous cap. X-Gal crystals were detectable exclusively in foam cell macrophages, irrespective of lesion size (Fig. 2, B and D). Foam cell macrophages in foci of 9-day lesions of $Ldlr^{-/-}$;*3MR* mice receiving daily, high-dose GCV were rarely arranged in multilayers and had a much lower incidence of crystals (Fig. 2, C

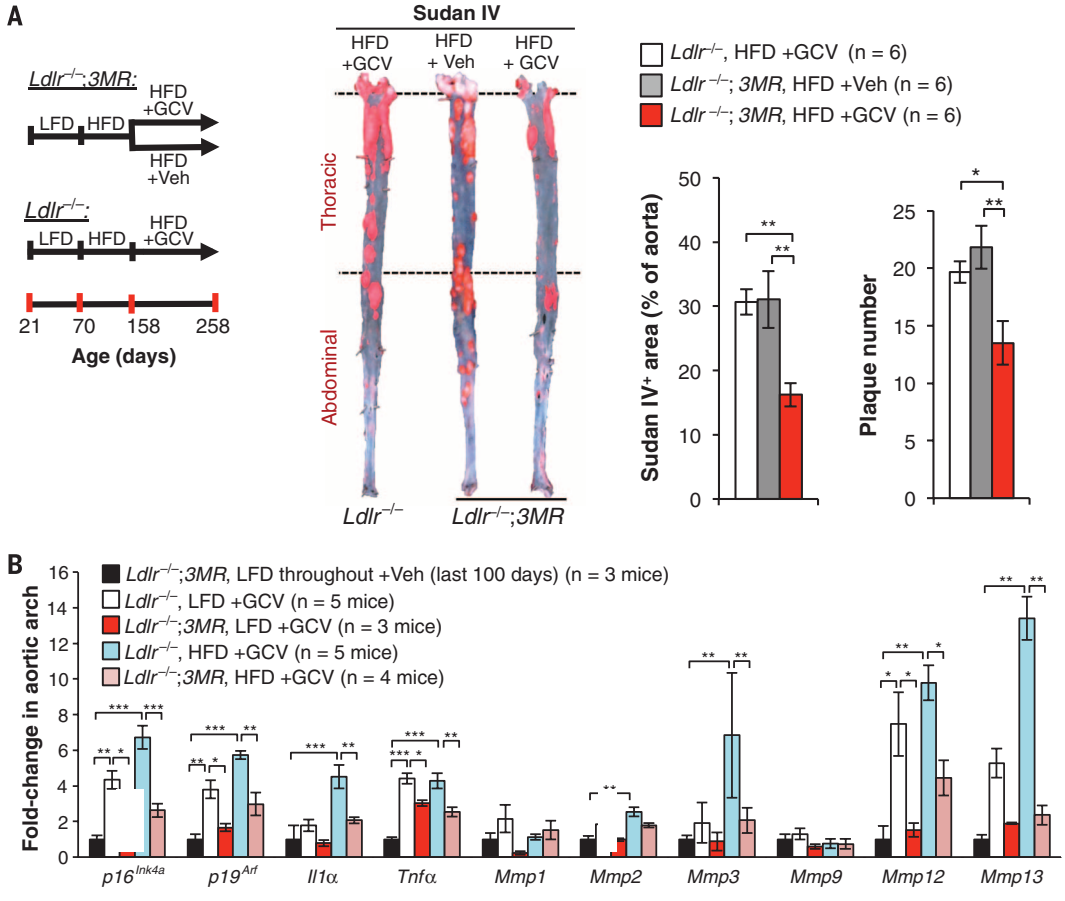

Fig. 3. Removal of p16^{Ink4a+} cells in established plaques perturbs the proatherogenic microenvironment. (**A**) (Left) Experimental design. (Middle) Sudan IV–stained descending aortas (not including the arch). (Right) Quantification of Sudan IV^{+} areas and plaque number. (**B**) RT-qPCR for senescence markers in aortic arches from indicated cohorts. Aortic arches from *Ldlr*$^{-/-}$;*3MR* females fed a LFD until 258 days of age and treated with Veh for the last 100 days were used to assess baseline expression levels. Treatments in (A) and (B) involved daily injections of 5 mg/kg of GCV (or Veh) for 5 days, followed by 14 days off; this cycle was repeated for 100 days. Bar graphs represent mean ± SEM (error bars) [biological *n* is indicated directly on all graphs and refers to individual aortas in (A) or aortic arches in (B)]. *$P < 0.05$; **$P < 0.01$; ***$P < 0.001$ [analysis of variance (ANOVA) with Sidak's post-hoc correction for family-wise error in (A) and unpaired two-tailed *t* test with Welch's correction in (B)].

and D). Elevated SA β-Gal activity in fatty streaks correlated with increased levels of *p16*^{Ink4a} and various other senescence markers, including *Mmp3, Mmp13*, *Il1α*, and *Tnfα* (fig. S8B). Nine-day treatment of HFD-fed *Ldlr*$^{-/-}$ mice with ABT263 confirmed that senolysis reduces atherogenesis onset (fig. S8C).

To determine how senescent foamy macrophages contribute to early atherogenesis, we established 9-day fatty streaks in *Ldlr*$^{-/-}$ and *Ldlr*$^{-/-}$;*3MR* mice and then administered high-dose GCV for 3 days while continuing to feed the mice a HFD. Short-term clearance of senescent cells markedly reduced streak size and SA β-Gal positivity (Fig. 2E). TEM images showed that cleared foci were drastically remodeled, with acellular debris retained in the subendothelium and few foamy macrophages containing X-Gal crystals (fig. S8, D and E). RT-qPCR revealed a stark reduction in p16^{Ink4a} and SASP components (including *Mmp3*, *Mmp13*, *Il1α*, and *Tnfα*), as well as two key molecular drivers of monocyte recruitment (the chemokine *Mcp1* and the leukocyte receptor *Vcam1*), whose expression is partly driven by *Tnfα* (Fig. 2F). These data suggest that subendothelial senescent foamy macrophages arising in early lesions enhance *Tnfα*-mediated *Vcam1* expression, as well as the *Mcp1* gradient, to perpetuate monocyte recruitment from the blood.

Next, we examined the role of senescent cells in the maturation of benign plaques to complex advanced lesions. Although mouse models for atherosclerosis do not develop clinical symptoms associated with plaque ruptures, plaque maturation in these mice can be studied using surrogate markers of plaque instability, including fibrous cap thinning (*22*, *23*), decreased collagen deposition, elastic fiber degradation, and plaque calcification (*24*). To assess the effect of senescent cell clearance on the maturation of existing plaques, we employed late-disease senescent cell clearance protocols in which we placed *Ldlr*$^{-/-}$ and *Ldlr*$^{-/-}$;*3MR* mice on a HFD for 88 days to create plaques, followed by 100 days of GCV treatment. During GCV treatment, mice were fed a HFD or LFD to promote continued plaque advancement or stasis, respectively (Fig. 3A and fig. S9). *Ldlr*$^{-/-}$;*3MR* mice maintained on the HFD and receiving GCV showed attenuated disease progression, as evidenced by a lower plaque number and size compared with GCV-treated *Ldlr*$^{-/-}$ or vehicle-treated *Ldlr*$^{-/-}$;*3MR* controls (Fig. 3A). Whereas plaques of GCV-treated *Ldlr*$^{-/-}$;*3MR* mice on a LFD had markedly reduced Sudan IV staining compared with plaques of control mice, the lesion-covered aortic area did not change (fig. S10A), even though *3MR*-mediated senescent cell killing was confirmed by SA β-Gal staining (fig. S10B) and RT-qPCR for senescence markers (Fig. 3B). Regardless of diet, senescent cell clearance reduced expression of inflammatory cytokines (Fig. 3B) and monocyte recruitment factors (fig. S10C). GCV treatment decreased expression of matrix metalloproteases linked to plaque destabilization, including *Mmp3, Mmp12*, and *Mmp13* (*25*, *26*) (Fig. 3B), which suggests that senescent cell elimination stabilizes the fibrous cap.

To investigate this and other features of plaque maturation, we conducted histopathology on plaques collected from the above cohorts. When *Ldlr*$^{-/-}$ mice originally fed a HFD for 88 days were left on the diet for an additional 100 days, their descending aorta plaques showed reduced cap thickness, diminished collagen content (by Masson's trichrome staining), and more disrupted aortic elastic fibers (by Voerhoff von Gieson staining) in comparison with those of LFD-fed mice (Fig. 4, A and B, and fig. S11). In contrast, all of these markers of plaque instability were decreased with clearance of p16^{Ink4a+} cells, regardless of diet, during the 100-day GCV treatment period. Similarly, clearance of p16^{Ink4a+} cells increased cap thickness and collagen content in brachiocephalic arteries from mice reverted to LFD (fig. S12). We extended these studies by switching *Ldlr*$^{-/-}$;*3MR* and *Ldlr*$^{-/-}$ mice after 88 days of HFD feeding to a LFD with GCV injections for 35 days (fig. S13A). In this experiment, senescent cell elimination preserved fibrous cap

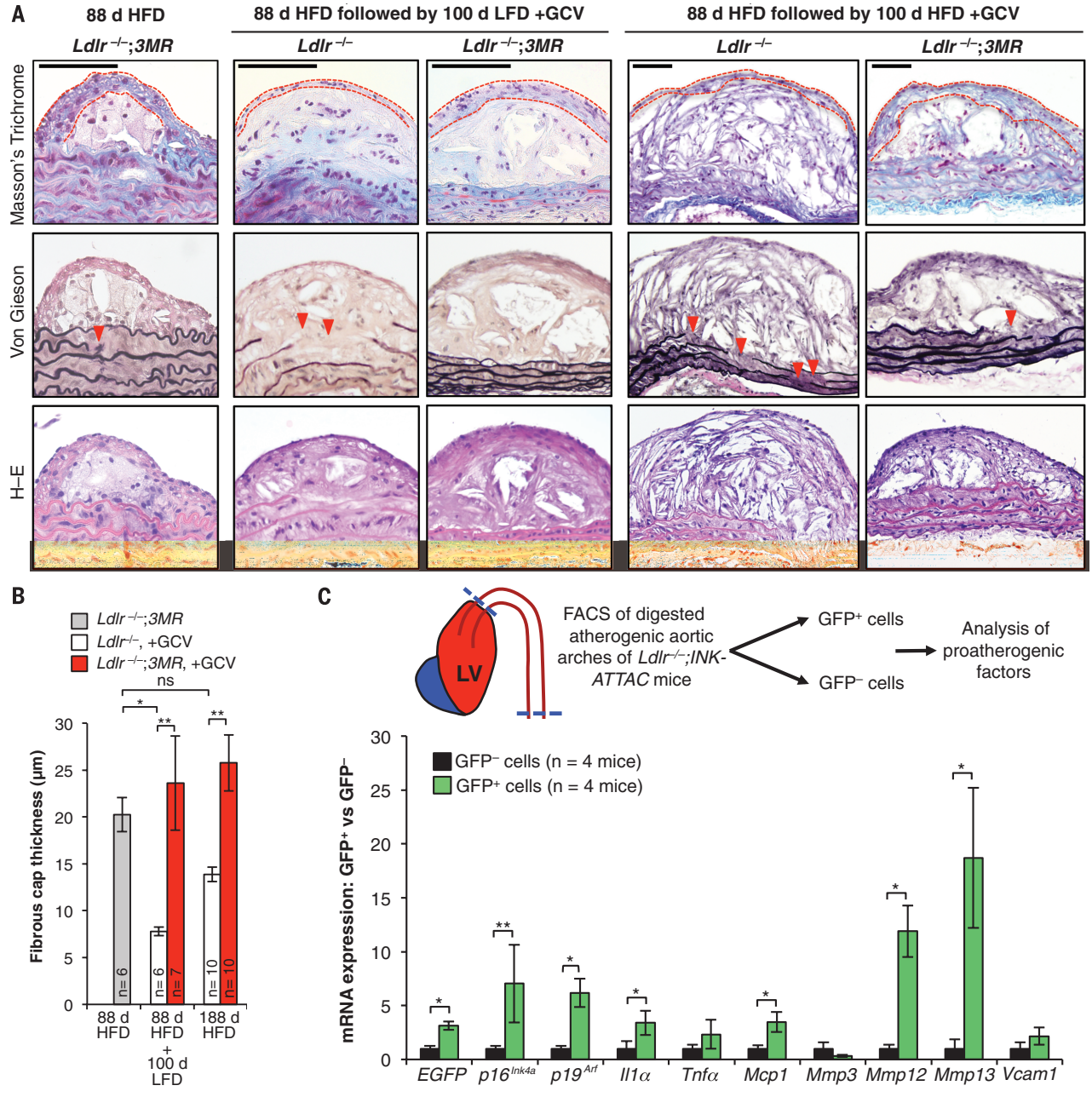

Fig. 4. Senescent cells promote plaque instability by elevating metalloprotease production. (**A**) Representative sections from descending aorta plaques of mice with the indicated genotypes, treatments, diets, and histological stainings. Red dashed lines trace the fibrous cap; red arrowheads indicate ruptured aortic elastic fibers. H–E, hematoxylin and eosin. (**B**) Quantification of fibrous cap thickness in plaques from (A). (**C**) (Top) Experimental overview. (Bottom) RT-qPCR analysis of senescence markers in GFP$^+$ and GFP$^-$ cells. *EGFP*, enhanced green fluorescent protein. Bar graphs represent mean ± SEM (error bars) [biological *n* is indicated directly on all graphs and refers to individual descending aorta mouse plaques in (B) and flow-sorted cell fractions isolated from individual mice in (C)]. *P < 0.05; **P < 0.01; ns, not significant [ANOVA with Sidak's post-hoc correction for familywise error in (B) and ratio paired t test in (C)].

thickness (fig. S13, B and C). Furthermore, lesional foamy macrophage–like cell content was reduced, whereas VSMC-like cell content increased (fig. S13, D and E), resulting in plaques with a higher VSMC-like/macrophage-like cell ratio, a marker for greater stability (fig. S13F) (*27*). Clearance markedly reduced monocyte attachment to plaque-adjacent endothelium (fig. S13G), thus supporting our conclusion from early fatty-streak experiments that enhanced monocyte chemotaxis may partially explain the proatherogenic nature of senescent cells. These results strongly suggest that eliminating p16^{Ink4a+} cells promotes plaque stability.

To further investigate the mechanism by which senescent cells drive atherogenesis, we tested the possibility that senescent cells in plaques express proatherogenic factors. We dissected lesion-bearing tissue from HFD-fed *Ldlr*$^{-/-}$*;ATTAC* mice, prepared single-cell suspensions, and exploited *p16*^{Ink4a}-dependent expression of green fluorescent protein (GFP) by *ATTAC* to collect GFP$^+$ senescent and GFP$^-$ nonsenescent cell populations for analysis by RT-qPCR (Fig. 4C). Senescent cells expressed a broad spectrum of proatherogenic factors, including *Il1α*, *Tnfα*, *Mmp3*, *Mmp12*, *Mmp13*, *Mcp1*, and *Vcam1* (Fig. 4C). A subset of these factors (including *Il1α*, *Mmp12*, *Mmp13*, and *Mcp1*) was expressed at markedly elevated levels compared with expression in nonsenescent cells.

Using both transgenic and pharmacological approaches to clear p16^{Ink4a+} cells without interfering with the senescence program, we showed

that senescent cells are uniformly deleterious throughout atherogenesis. Very early fatty streaks contain abundant senescent foam cell macrophages, which create an environment conducive to further lesion growth by up-regulating inflammatory cytokines and monocyte chemotactic factors. Removal of $p16^{Ink4a+}$ foamy macrophages from fatty streaks led to marked lesion regression. In contrast, advanced plaques contain three morphologically distinct senescent cell types that not only drive lesion maturation through inflammation and monocyte chemotaxis but also promote extracellular matrix degradation. Clearing senescent cells from advanced lesions inhibits both plaque growth and maladaptive plaque remodeling processes associated with plaque rupture, including fibrous cap thinning and elastic fiber degeneration. Furthermore, senescent cells in lesions show heightened expression of key SASP factors and effectors of inflammation, monocyte chemotaxis, and proteolysis, including *Il1α*, *Mcp1*, *Mmp12*, and *Mmp13*. These data suggest that senescent cells can directly influence core proatherogenic processes through specific secreted factors. By comparison, the expression of other factors such as *Mmp3*, *Tnfα*, and *Vcam1* is reduced with senolysis, but these factors are not enriched in $p16^{Ink4a+}$ cells, which implies that senescent cells also can influence the proatherogenic milieu indirectly. Collectively, our results show that senescent cells drive atherosclerosis at all stages through paracrine activity and raise the possibility that druglike molecules that remove senescent cells from patients without toxic side effects could contribute to therapeutic management of the disease.

REFERENCES AND NOTES

1. I. Tabas, G. García-Cardeña, G. K. Owens, *J. Cell Biol.* **209**, 13–22 (2015).
2. C. Weber, H. Noels, *Nat. Med.* **17**, 1410–1422 (2011).
3. K. Sakakura *et al.*, *Heart Lung Circ.* **22**, 399–411 (2013).
4. I. Gorenne, M. Kavurma, S. Scott, M. Bennett, *Cardiovasc. Res.* **72**, 9–17 (2006).
5. T. Minamino *et al.*, *Circulation* **105**, 1541–1544 (2002).
6. J. C. Wang, M. Bennett, *Circ. Res.* **111**, 245–259 (2012).
7. D. Muñoz-Espín, M. Serrano, *Nat. Rev. Mol. Cell Biol.* **15**, 482–496 (2014).
8. J. Wang *et al.*, *Circulation* **132**, 1909–1919 (2015).
9. A. K. Khanna, *J. Biomed. Sci.* **16**, 66 (2009).
10. J. Mercer, N. Figg, V. Stoneman, D. Braganza, M. R. Bennett, *Circ. Res.* **96**, 667–674 (2005).
11. H. González-Navarro *et al.*, *J. Am. Coll. Cardiol.* **55**, 2258–2268 (2010).
12. K. Wouters *et al.*, *PLOS ONE* **7**, e32440 (2012).
13. C. L. Kuo *et al.*, *Arterioscler. Thromb. Vasc. Biol.* **31**, 2483–2492 (2011).
14. M. Demaria *et al.*, *Dev. Cell* **31**, 722–733 (2014).
15. S. Feil *et al.*, *Circ. Res.* **115**, 662–667 (2014).
16. L. S. Shankman *et al.*, *Nat. Med.* **21**, 628–637 (2015).
17. H. Williams, J. L. Johnson, K. G. Carson, C. L. Jackson, *Arterioscler. Thromb. Vasc. Biol.* **22**, 788–792 (2002).
18. D. J. Baker *et al.*, *Nature* **479**, 232–236 (2011).
19. D. J. Baker *et al.*, *Nature* **530**, 184–189 (2016).
20. J. Chang *et al.*, *Nat. Med.* **22**, 78–83 (2016).
21. Y. Nakashima, E. W. Raines, A. S. Plump, J. L. Breslow, R. Ross, *Arterioscler. Thromb. Vasc. Biol.* **18**, 842–851 (1998).
22. J. L. Johnson, C. L. Jackson, *Atherosclerosis* **154**, 399–406 (2001).
23. M. C. Clarke *et al.*, *Nat. Med.* **12**, 1075–1080 (2006).
24. N. Maldonado *et al.*, *Am. J. Physiol. Heart Circ. Physiol.* **303**, H619–H628 (2012).
25. C. Silvestre-Roig *et al.*, *Circ. Res.* **114**, 214–226 (2014).
26. S. M. Ghaderian, R. Akbarzadeh Najar, A. S. Tabatabaei Panah, *Coron. Artery Dis.* **21**, 330–335 (2010).
27. A. V. Finn, M. Nakano, J. Narula, F. D. Kolodgie, R. Virmani, *Arterioscler. Thromb. Vasc. Biol.* **30**, 1282–1292 (2010).

ACKNOWLEDGMENTS

We thank R.-M. Laberge and M. Demaria for sharing data on the senolytic properties of ABT263, as well as N. David, Y. Poon, M. Hofker, B. van de Sluis, and the van Deursen lab for helpful discussions. This work was supported by a grant from the Paul F. Glenn Foundation (to J.M.v.D. and D.J.B.) and NIH grants R01CA96985 and CA168709 (to J.M.v.D.). J.M.v.D. and J.C. are cofounders of Unity Biotechnology, a company developing senolytic medicines including small molecules that selectively eliminate senescent cells. J.M.v.D., D.J.B., B.G.C., and J.C. are co-inventors on patent applications licensed to or filed by Unity Biotechnology. The p16-3MR mice are available from J.C. under a material transfer agreement. *INK-ATTAC* and *INK-NTR* mice are available from J.M.v.D. under a material transfer agreement.

SUPPLEMENTARY MATERIALS

www.sciencemag.org/content/354/6311/472/suppl/DC1
Materials and Methods
Figs. S1 to S13
References (*28*, *29*)

11 March 2016; resubmitted 6 September 2016
Accepted 29 September 2016
10.1126/science.aaf6659

APE GENETICS

Chimpanzee genomic diversity reveals ancient admixture with bonobos

Marc de Manuel,[1]* Martin Kuhlwilm,[1]* Peter Frandsen,[2,3]* Vitor C. Sousa,[4,5] Tariq Desai,[6] Javier Prado-Martinez,[1,7] Jessica Hernandez-Rodriguez,[1] Isabelle Dupanloup,[4,5] Oscar Lao,[8,9] Pille Hallast,[7,10] Joshua M. Schmidt,[11] José María Heredia-Genestar,[1] Andrea Benazzo,[12] Guido Barbujani,[12] Benjamin M. Peter,[13] Lukas F. K. Kuderna,[1] Ferran Casals,[1] Samuel Angedakin,[14] Mimi Arandjelovic,[14] Christophe Boesch,[14] Hjalmar Kühl,[14] Linda Vigilant,[14] Kevin Langergraber,[15] John Novembre,[13] Marta Gut,[8] Ivo Gut,[8] Arcadi Navarro,[1,8,16] Frands Carlsen,[3] Aida M. Andrés,[11] Hans. R. Siegismund,[2] Aylwyn Scally,[6] Laurent Excoffier,[4,5] Chris Tyler-Smith,[9] Sergi Castellano,[11] Yali Xue,[9] Christina Hvilsom,[3]† Tomas Marques-Bonet[1,8,16]†

Our closest living relatives, chimpanzees and bonobos, have a complex demographic history. We analyzed the high-coverage whole genomes of 75 wild-born chimpanzees and bonobos from 10 countries in Africa. We found that chimpanzee population substructure makes genetic information a good predictor of geographic origin at country and regional scales. Multiple lines of evidence suggest that gene flow occurred from bonobos into the ancestors of central and eastern chimpanzees between 200,000 and 550,000 years ago, probably with subsequent spread into Nigeria-Cameroon chimpanzees. Together with another, possibly more recent contact (after 200,000 years ago), bonobos contributed less than 1% to the central chimpanzee genomes. Admixture thus appears to have been widespread during hominid evolution.

Compared with our knowledge of the origins and population history of humans, much less is known about the extant species closest to humans, chimpanzees (*Pan troglodytes*) and bonobos (*Pan paniscus*). Unraveling the demographic histories of our closest living relatives provides an opportunity for comparisons with our own history and thus for studying processes that might have played a recurring role in hominid evolution. Because of a paucity of fossil records (*1*), our understanding of the demographic history of the *Pan* genus has primarily relied on population genetic data from mitochondrial genomes (*2*, *3*), nuclear fragments (*4*, *5*), and microsatellites (*6*, *7*). More recently, the analysis of whole-genome sequences from chimpanzees and bonobos has hinted at a complex evolutionary history for the four taxonomically recognized chimpanzee subspecies (*8*). However, although chimpanzees and bonobos hybridize in captivity (*9*), the extent of interbreeding among chimpanzee subspecies and between chimpanzees and bonobos in the wild remains unclear.

We analyzed 75 complete genomes from the *Pan* genus, of which 40 were sequenced for this project to a mean sequence coverage of 25-fold. Our samples span 10 African countries, from the westernmost to the easternmost regions of the chimpanzee range (Fig. 1A). We discovered 32% more variable sites than previously identified (*8*, *10*), highlighting the value of our sampling scheme. Different lines of evidence suggest larger historical effective population sizes in central chimpanzees, including haplotype diversity in each subspecies (fig. S5), Y chromosome diversity (fig. S3), fixation index (F_{ST})–based phylogenies (fig. S16), and genome-wide linkage disequilibrium (fig S6). An analysis of the long-term demographic

history with the Pairwise Sequentially Markovian Coalescent model (*11*) (fig. S17) and a composite-likelihood modeling approach performed to fit the observed joint site frequency spectrum (SFS) (*12*) indicate a high long-term population size in central chimpanzees (*10*). The apportionment of genetic diversity among *Pan* populations reveals that central chimpanzees retain the highest diversity in the chimpanzee lineage, whereas the western, Nigeria-Cameroon, and eastern subspecies harbor signals of population bottlenecks.

We explored chimpanzee population structure to determine the extent to which genetic information can predict geographic origin. This is important because determining the geographical origin of confiscated individuals can help to localize hotspots of illegal trafficking (*13*). Principal component analysis (PCA) and population clustering analyses both reveal local stratification in central and eastern chimpanzees (Fig. 1, B and C) (*10*). Although we could not include enough geolocalized samples to assess fine-scale population structure in Nigeria-Cameroon and western chimpanzees, we expect that similar stratification would be found with broader sampling. To test the accuracy of our predictions, we produced low-coverage whole-genome sequences for six additional individuals whose geographical origins were known (table S1) and sequenced chromosome 21 from four Global Positioning System (GPS)–labeled fecal samples, all from central and eastern chimpanzees (*10*). The genetic predictions are accurate to the levels of country and region within a country (Fig. 1, B and C). In the future, the origins of confiscated chimpanzees will probably be discernible with sufficient data from reference populations, with implications for the in situ and ex situ management of this species.

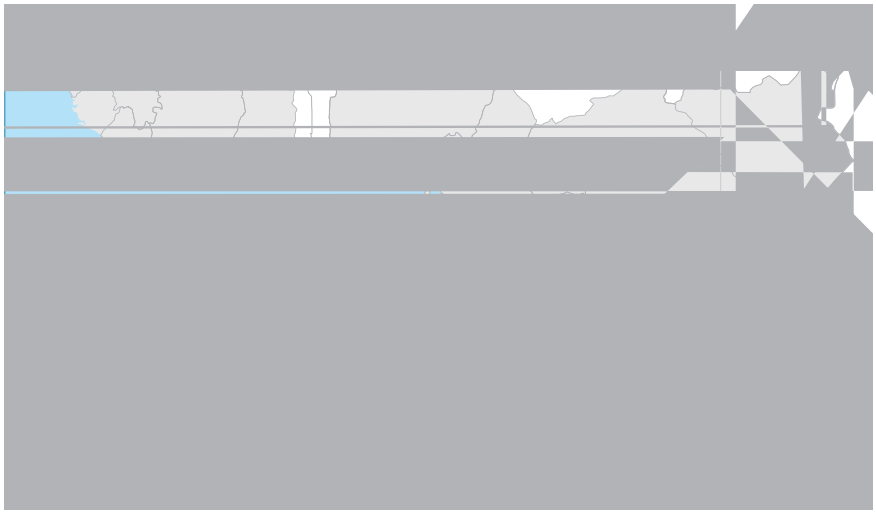

Given that multiple events of gene flow between modern and archaic humans have been described (*14*–*17*), we explored similar evidence of admixture within the *Pan* genus. In our SFS-based demographic model, we found support for gene flow among chimpanzee subspecies embedded in an improved picture of the complex population history (*10*, *12*). Previously, gene flow between chimpanzees and bonobos was not supported in analyses of low-coverage genomes (*18*). However, we found that central, eastern, and Nigeria-Cameroon chimpanzees share significantly more derived alleles with bonobos than western chimpanzees do (Fig. 2A and fig. S26). Although an excess of derived allele sharing has been reported previously, it was attributed to greater genetic drift in the western subspecies (*6*, *19*) or described as inconclusive owing to insufficient sampling (*20*), but using high-coverage data from more individuals allows us to investigate the possibility of migration. Because the chance of derived alleles being introduced through gene flow from bonobos into chimpanzees increases with the frequency in the donor population, alleles that occur at high frequencies are expected to exhibit greater sharing (*15*, *17*). Indeed, derived alleles that occur at high frequencies in bonobos are disproportionally shared with central chimpanzees relative to western chimpanzees (Fig. 2B and fig. S28). Because we used sites with high sequence coverage, we can exclude contamination as a potential source of unequal allele sharing. Furthermore, gene flow should introduce bonobo alleles into chimpanzee populations at low frequencies. We found that these shared derived alleles do segregate at low and moderate frequencies in the nonwestern chimpanzee populations (Fig. 2C and fig. S30). This observation suggests ancient low-level gene flow from bonobos, with a minority of introgressed alleles drifting to moderate frequencies after segregating in the chimpanzee populations—a scenario that is supported by the demographic model, particularly with respect to gene flow into the ancestor of central and eastern chimpanzees

[1]Institut de Biologia Evolutiva (Consejo Superior de Investigaciones Científicas–Universitat Pompeu Fabra), Barcelona Biomedical Research Park, Doctor Aiguader 88, Barcelona, Catalonia 08003, Spain. [2]Section for Computational and RNA Biology, Department of Biology, University of Copenhagen, 2200 Copenhagen, Denmark. [3]Center for Zoo and Wild Animal Health, Copenhagen Zoo, 2000 Frederiksberg, Denmark. [4]Computational and Molecular Population Genetics, Institute of Ecology and Evolution, University of Berne, 3012 Berne, Switzerland. [5]Swiss Institute of Bioinformatics, 1015 Lausanne, Switzerland. [6]Department of Genetics, University of Cambridge, Cambridge CB2 3EH, UK. [7]Wellcome Trust Sanger Institute, Wellcome Genome Campus, Hinxton CB10 1SA, UK. [8]National Centre for Genomic Analysis–Centre for Genomic Regulation, Barcelona Institute of Science and Technology, 08028 Barcelona, Spain. [9]Universitat Pompeu Fabra, 08003 Barcelona, Spain. [10]Institute of Molecular and Cell Biology, University of Tartu, Tartu 51010, Estonia. [11]Department of Evolutionary Genetics, Max Planck Institute for Evolutionary Anthropology, 04103 Leipzig, Germany. [12]Department of Life Sciences and Biotechnology, University of Ferrara, 44121 Ferrara, Italy. [13]Department of Human Genetics, University of Chicago, Chicago, IL 60637, USA. [14]Department of Primatology, Max Planck Institute for Evolutionary Anthropology, 04103 Leipzig, Germany. [15]School of Human Evolution and Social Change and Institute of Human Origins, Arizona State University, Tempe, AZ 85287, USA. [16]Institucio Catalana de Recerca i Estudis Avançats (ICREA), Barcelona, Catalonia 08010, Spain.
*These authors contributed equally to this work. **†Corresponding author. Email: ch@zoo.dk (C.H.); tomas.marques@upf.edu (T.M.-B.)**

Corrected 26 October 2016. See full text.

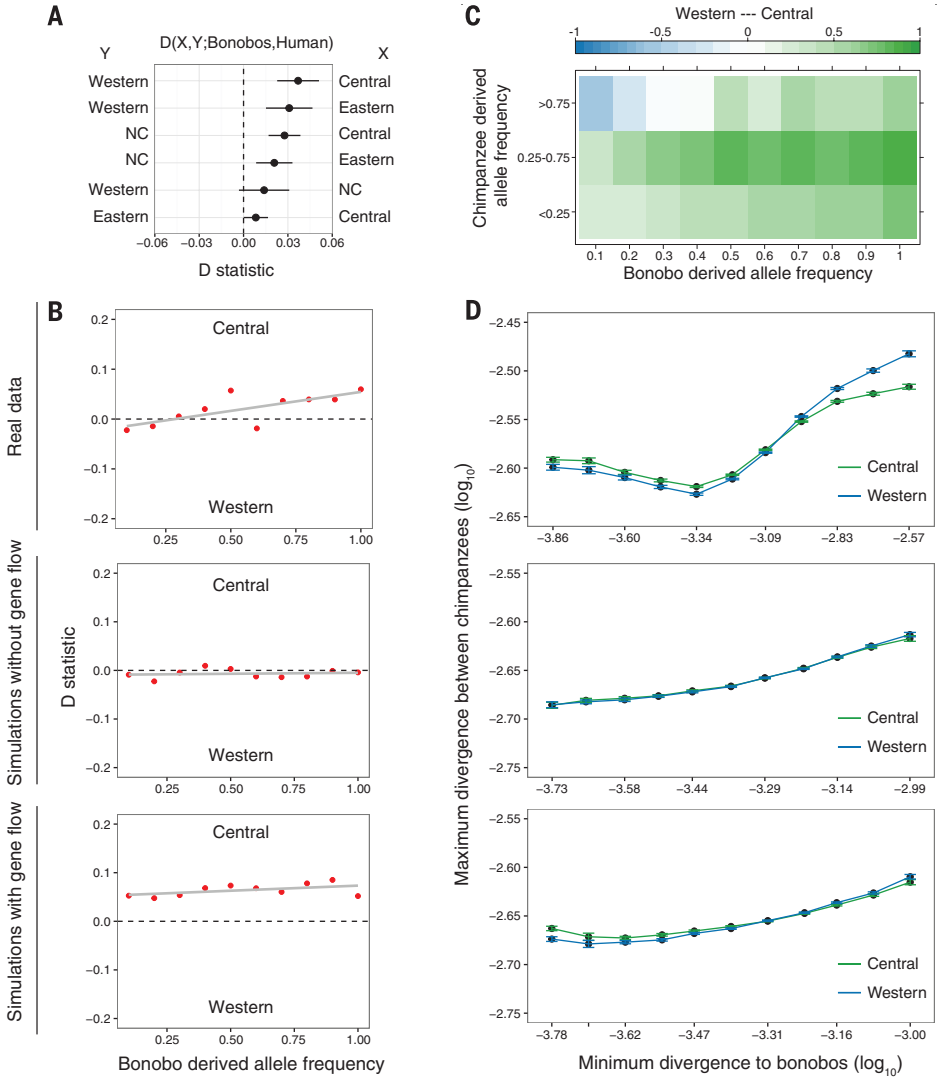

Fig. 2. Genome-wide statistics support gene flow between chimpanzees and bonobos. (**A**) Population-wise *D* statistic of the form *D*(X,Y; bonobos, human). Error bars correspond to two standard errors. Nonwestern chimpanzees share more derived alleles with bonobos than western chimpanzees do. (**B**) Western and central chimpanzee allele sharing with bonobos, binned by derived allele frequency in bonobos (D_j); bonobo alleles are more often shared with central chimpanzees across bonobo allele frequencies. Top, real data; middle, simulations without gene flow; bottom, simulations of a model with gene flow into nonwestern chimpanzees. Lines of best fit are in gray. (**C**) Western and central chimpanzee allele sharing with bonobos, stratified by both bonobo and chimpanzee derived allele frequency, calculated at a given frequency in bonobos and at least one of the chimpanzee subspecies (the color gradient represents the extent of sharing). (**D**) Divergence between chimpanzee subspecies versus minimum divergence to bonobos at sites with bonobo derived allele frequencies of ≥90% in windows of 50 kbp. Error bars represent 95% confidence intervals from 500 bootstrap replicates. Segments in the genomes of central chimpanzees with low divergence to bonobos show high divergence to western chimpanzees. Top, real data; middle, simulated data without gene flow; bottom, simulated data with gene flow.

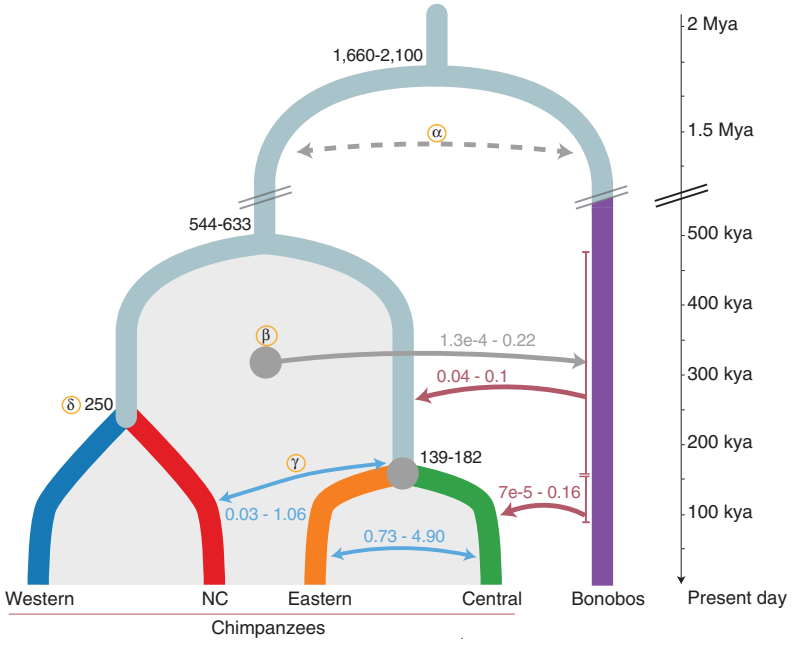

Fig. 3. Conceptual model of a complex population history. SFS-based modeling indicates several contacts between chimpanzees and bonobos after their divergence. Split times (thousands of years ago, kya) and migration rates correspond to 95% confidence intervals obtained with the demographic model with western, central, and eastern chimpanzees (*10*). Gene flow is quantified as the scaled migration rate (2*Nm*). Red arrows, gene flow from bonobos into chimpanzees. The ancestral population of central and eastern chimpanzees received the highest amount of bonobo alleles, whereas central chimpanzees received additional, more recent gene flow (<200,000 years ago). Blue arrows, highest inferred migrations within chimpanzee subspecies (intense gene flow between central and eastern chimpanzees). α (dotted line), putative ancient gene flow between the ancestors of all chimpanzees and bonobos. β, more recent gene flow from chimpanzees into bonobos. Shaded area, range of estimates across all chimpanzee populations. γ, admixture between Nigeria-Cameroon and central and eastern chimpanzees; indirect gene flow from bonobos into Nigeria-Cameroon chimpanzees might have occurred through these contacts. δ, divergence time between western and Nigeria-Cameroon chimpanzees, estimated by using MSMC2 (*10*).

Corrected 26 October 2016. See full text.

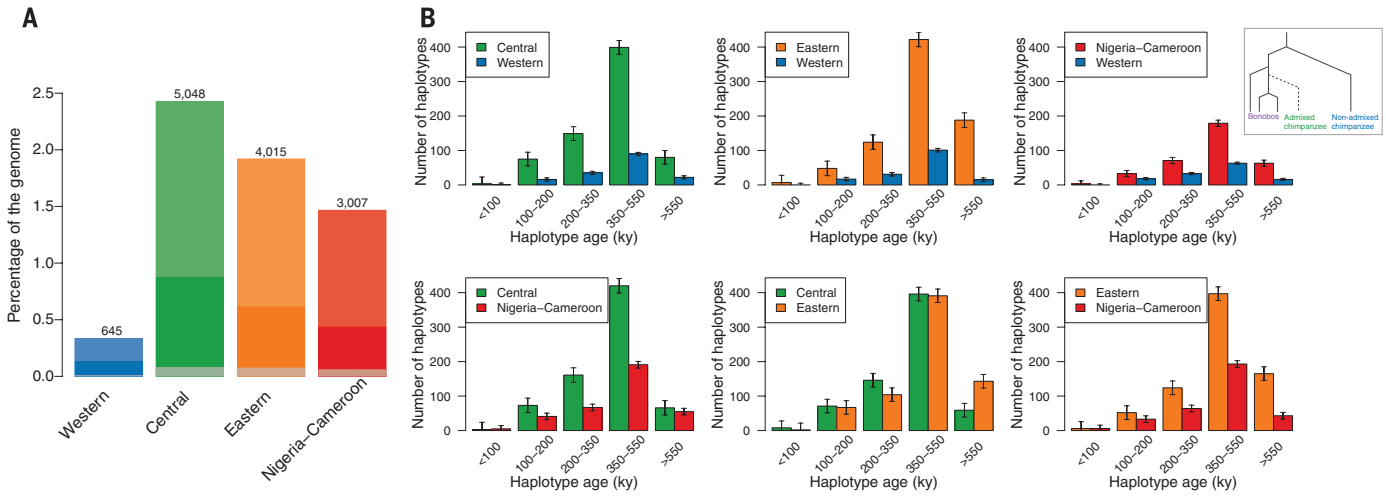

Fig. 4. Introgressed segments and inferred age of introgressed haplotypes. (**A**) Numbers of putatively introgressed heterozygous segments per population (top of each bar) and percentage of the chimpanzee genome that they constitute (bars). Dark bars represent segments uniquely found in each population; gray bars represent simulated data without gene flow. (**B**) Age distribution of bonobo-like haplotypes in chimpanzee populations, as estimated by ARGweaver. Chimpanzee subspecies are compared pairwise, and bonobo-like haplotypes are defined as regions of at least 50 kbp that coalesce within the bonobo subtree before coalescing with the other chimpanzee population (inset). Error bars represent 95% confidence intervals across Markov chain Monte Carlo replicates (*10*).

(Fig. 3). An alternative explanation for such shared ancestry through incomplete lineage sorting would predict such alleles to drift toward fixation after their separation (*10*).

If bonobos contributed alleles to chimpanzees, these should be recognizable as introgressed segments in chimpanzees (i.e., regions with unusually low divergence to bonobos and unusually high heterozygosity). Following an approach used to identify gene flow from modern humans into Neandertals (*17*), we calculated the divergence from bonobos to the chimpanzee alleles that result in the minimum divergence to derived alleles occurring at high frequencies (≥90%) in sequence windows of 50 kilo–base pairs (kbp) (*10*), and we compared it with the maximum divergence between chimpanzee subspecies. Genomic regions in the nonwestern chimpanzees that are least divergent to bonobos are more divergent to western chimpanzees than vice versa (Fig. 2D and fig. S36). These windows also show an increase in heterozygosity (fig. S37).

We identified discrete putatively introgressed regions in the individual genomes harboring heterozygous bonobo-like and chimpanzee haplotypes (*17*). We detected almost an order of magnitude more of such haplotypes in central chimpanzees than in western chimpanzees, making up a total of ~2.4% across the genomes of 10 individuals, whereas the amount is smaller in eastern and Nigeria-Cameroon chimpanzees (Fig. 4A and table S6). Furthermore, central chimpanzees carry an excess of haplotypes that do not overlap with any of the other subspecies ($P < 0.01$, G-test). These regions also show a significant depletion in background selection (*21*) ($P < 0.01$, Wilcoxon rank test), suggesting that bonobo alleles might have been disadvantageous in a chimpanzee genetic background (*10*). This observation, together with the X chromosome not carrying more derived alleles shared between bonobos and nonwestern chimpanzees (fig. S31), resembles patterns in modern and archaic human genomes (*16*, *22*, *23*).

Further support for a scenario of gene flow between chimpanzees and bonobos is provided by a model-based inference from TreeMix (*24*) (fig. S24) and the SFS-based demographic models described above (*10*), which have significantly higher likelihoods when they include multiple gene flow events between species (figs. S50 and S52). The best-fitting models indicate a complex admixture history, including low-level gene flow from bonobos to central chimpanzees and the ancestors of central and eastern chimpanzees, as well as from chimpanzees into bonobos (Fig. 3 and figs. S51 and S54).

We used simulations to test whether these differential allele-sharing patterns would be expected in the absence or presence of gene flow under the demographic history inferred from our models (*10*). Only a scenario including gene flow reproduced stratified *D* statistics that were different from zero (fig. S33), and even substantial genetic drift in the western subspecies could not explain the asymmetries in derived alleles shared with bonobos (figs. S34 and S35). Additionally, only models with gene flow from bonobos into the ancestors of central and eastern chimpanzees, and to a lesser extent into Nigeria-Cameroon chimpanzees, reproduced the observed patterns in sequence windows (Fig. 2D and figs. S38 to S43) and heterozygous regions (fig. S45). In sum, the unequal allele and haplotype sharing is unlikely to result from alternative demographic models without gene flow from bonobos into chimpanzee populations. Although alternative models—e.g., with different gene flow events or differences in population size—may explain some features of the data, none of those tested in this study could reproduce all features of the data (*10*).

Lastly, if gene flow occurred between the *Pan* species after their separation 1.5 to 2.1 million years ago (Fig. 3), haplotypes younger than this should be shared among them. Using ARGweaver (*25*), we estimated the age of haplotypes for which one chimpanzee subspecies coalesces within the subtree of bonobos more recently than with another chimpanzee subspecies (*10*). A fraction of these haplotypes may result from incomplete lineage sorting, but it has been shown that gene flow introduces an excess of young haplotypes into the receiving population (*17*). We found that central chimpanzees carry 4.4-fold more bonobo-like haplotypes than western chimpanzees do and that these are longer ($P < 0.01$, Wilcoxon rank test), whereas eastern and Nigeria-Cameroon chimpanzees carry smaller amounts (table S10). These haplotypes are inferred to coalesce 200,000 to 550,000 years ago, consistent with gene flow from bonobos into the ancestors of central and eastern chimpanzees less than 650,000 years ago (Figs. 3 and 4B). The smaller amount of such haplotypes in Nigeria-Cameroon and western chimpanzees might result from subsequent gene flow between chimpanzee populations. Additionally, central chimpanzees carry a slightly larger proportion of younger haplotypes (from 100,000 to 200,000 years ago), supporting another, more recent phase of secondary contact between chimpanzees and bonobos. These estimates agree with the phases of gene flow before and after the split of central and eastern chimpanzees (<180,000 years ago) inferred from our demographic model (Fig. 3) and with the excess of bonobo-like alleles and haplotypes in central chimpanzees. We estimate the overall contribution to individual genomes at less than 1% (*10*).

Through the analysis of multiple high-coverage genomes, we were able to reconstruct a complex history of admixture within the *Pan* genus. It appears that there was gene flow from an ancestral

bonobo population mostly into nonwestern chimpanzees several hundred thousand years ago. Although we cannot distinguish whether the gene flow occurred at low levels over a long time or in discrete pulses, it seems likely that at least two phases of secondary contact between the two species took place. This study reveals that our closest living relatives experienced a history of admixture similar to that within the *Homo* clade. Thus, gene flow might have been widespread during the evolution of the great apes and hominins.

REFERENCES AND NOTES

1. S. McBrearty, N. G. Jablonski, *Nature* **437**, 105–108 (2005).
2. C. Hvilsom, F. Carlsen, R. Heller, N. Jaffré, H. R. Siegismund, *Primates* **55**, 101–112 (2014).
3. I. Lobon *et al.*, *Genome Biol. Evol.* **8**, 2020–2030 (2016).
4. J. L. Caswell *et al.*, *PLOS Genet.* **4**, e1000057 (2008).
5. A. Fischer *et al.*, *PLOS ONE* **6**, e21605 (2011).
6. C. Becquet, N. Patterson, A. C. Stone, M. Przeworski, D. Reich, *PLOS Genet.* **3**, e66 (2007).
7. T. Fünfstück *et al.*, *Am. J. Phys. Anthropol.* **156**, 181–191 (2015).
8. J. Prado-Martinez *et al.*, *Nature* **499**, 471–475 (2013).
9. H. Vervaecke, L. Van Elsacker, *Mammalia* **56**, 667–669 (1992).
10. Materials and methods are available as supplementary materials on *Science* Online.
11. H. Li, R. Durbin, *Nature* **475**, 493–496 (2011).
12. L. Excoffier, I. Dupanloup, E. Huerta-Sánchez, V. C. Sousa, M. Foll, *PLOS Genet.* **9**, e1003905 (2013).
13. S. K. Wasser *et al.*, *Science* **349**, 84–87 (2015).
14. R. E. Green *et al.*, *Science* **328**, 710–722 (2010).
15. K. Prüfer *et al.*, *Nature* **505**, 43–49 (2014).
16. Q. Fu *et al.*, *Nature* **524**, 216–219 (2015).
17. M. Kuhlwilm *et al.*, *Nature* **530**, 429–433 (2016).
18. K. Prüfer *et al.*, *Nature* **486**, 527–531 (2012).
19. Y.-J. Won, J. Hey, *Mol. Biol. Evol.* **22**, 297–307 (2005).
20. C. Becquet, M. Przeworski, *Genome Res.* **17**, 1505–1519 (2007).
21. G. McVicker, D. Gordon, C. Davis, P. Green, *PLOS Genet.* **5**, e1000471 (2009).
22. S. Sankararaman *et al.*, *Nature* **507**, 354–357 (2014).
23. B. Vernot *et al.*, *Science* **352**, 235–239 (2016).
24. J. K. Pickrell, J. K. Pritchard, *PLOS Genet.* **8**, e1002967 (2012).
25. M. D. Rasmussen, M. J. Hubisz, I. Gronau, A. Siepel, *PLOS Genet.* **10**, e1004342 (2014).

ACKNOWLEDGMENTS

All sequence data have been submitted to the European Nucleotide Archive and are available under accession code PRJEB15086. We greatly appreciate all the sample providers: Centre de Conservation pour Chimpanzés, Chimfunshi Wildlife Orphanage Trust, Centre de Primatologie, Centre International de Recherches Médicales de Franceville, Jeunes Animaux Confisqués Au Katanga, Ngamba Island Chimpanzee Sanctuary, Sweetwaters Chimpanzee Sanctuary, Stichting AAP, Bioparc Valencia, Edinburgh Zoo, Furuviksparken, Kolmårdens Djurpark, Zoo de Barcelona, Parc le Pal, Zoo Aquarium de Madrid, Zoo Parc de Beauval, and Zoo Zürich. We respectfully thank the Agence Nationale des Parcs Nationaux (Gabon), Centre National de la Recherche Scientifique (Gabon), Uganda National Council for Science and Technology, and the Ugandan Wildlife Authority for permission to collect fecal samples in Gabon and Uganda. We particularly thank K. Prüfer for advice on technical aspects; M. Meyer and A. Weihmann for helping with the capture of fecal samples; M. J. Hubisz for advice on ARGweaver; and J. Bertranpetit, C. Lalueza-Fox, M. Mondal, and S. Han for reading the manuscript and providing valuable comments. M.d.M. is supported by a Formació de personal Investigador fellowship from Generalitat de Catalunya (FI_B01111). M.K. is supported by a Deutsche Forschungsgemeinschaft fellowship (KU 3467/1-1). V.C.S., I.D., and L.E. are supported by Swiss National Science Foundation grants 31003A-143393 and 310030B-16660. T.D. is funded by the Gates Cambridge Trust. O.L. is supported by a Ramón y Cajal grant from Ministerio de Economía y Competitividad (MINECO) (RYC-2013-14797) and MINECO grant BFU2015-68759-P [Fondo Europeo de Desarrollo Region (FEDER)]. P.H. is supported by Estonian Research Council grant PUT1036. J.M.S., A.M.A., and S.C. are funded by the Max Planck Society. J.P.-M., C.T.-S., and Y.X. were supported by The Wellcome Trust (098051). J.M.H.-G. is supported by the María de Maeztu Programme (MDM-2014-0370). A.S. is supported by an Isaac Newton Trust/Wellcome Trust Institutional Strategic Support Fund Joint Research Grant. J.N. had support from a U.S. NIH U01CA198933 grant, and B.M.P. is supported by a Swiss National Science Foundation postdoctoral fellowship. A.N. is supported by MINECO grant BFU2015-68649-P. The collection of fecal samples was supported by the Max Planck Society and Krekeler Foundation's generous funding for the Pan African Programme. T.M.-B. thanks ICREA; the European Molecular Biology Organization Young Investigator Programme 2013; MINECO grants BFU2014-55090-P (FEDER), BFU2015-7116-ERC, and BFU2015-6215-ERCU01; U.S. NIH grant MH106874; Fundacio Zoo Barcelona; and Secretaria d'Universitats i Recerca del Departament d'Economia i Coneixement de la Generalitat de Catalunya for the support to his laboratory.

SUPPLEMENTARY MATERIALS

www.sciencemag.org/content/354/6311/477/suppl/DC1
Materials and Methods
Figs. S1 to S58
Tables S1 to S19
References (*26*–*90*)
Data S1

2 June 2016; accepted 9 September 2016
10.1126/science.aag2602

IMMUNOMETABOLISM

Aerobic glycolysis promotes T helper 1 cell differentiation through an epigenetic mechanism

Min Peng,[1]* Na Yin,[1]* Sagar Chhangawala,[2,3] Ke Xu,[1,4] Christina S. Leslie,[2] Ming O. Li[1]†

Aerobic glycolysis (the Warburg effect) is a metabolic hallmark of activated T cells and has been implicated in augmenting effector T cell responses, including expression of the proinflammatory cytokine interferon-γ (IFN-γ), via 3′ untranslated region (3′UTR)–mediated mechanisms. Here, we show that lactate dehydrogenase A (LDHA) is induced in activated T cells to support aerobic glycolysis but promotes IFN-γ expression independently of its 3′UTR. Instead, LDHA maintains high concentrations of acetyl–coenzyme A to enhance histone acetylation and transcription of *Ifng*. Ablation of LDHA in T cells protects mice from immunopathology triggered by excessive IFN-γ expression or deficiency of regulatory T cells. These findings reveal an epigenetic mechanism by which aerobic glycolysis promotes effector T cell differentiation and suggest that LDHA may be targeted therapeutically in autoinflammatory diseases.

T cell activation and differentiation are associated with metabolic rewiring (*1*–*4*). A metabolic hallmark of activated T cells is aerobic glycolysis (*5*), the conversion of glucose to lactate in the presence of oxygen, but its physiopathological functions remain incompletely understood (*6*–*8*). As the major carbon source, glucose plays important roles in T cell development, proliferation, and function (*9*–*15*). However, the specific contribution of aerobic glycolysis to T cell responses has not been well defined. Using galactose as a sugar source, aerobic glycolysis was proposed to support interferon-γ (IFN-γ) expression through 3′UTR-mediated mechanisms (*12*). Although galactose is metabolized at a slower rate than glucose via the Leloir pathway, both sugars are converted to lactate (*16*), rendering the galactose system unable to model aerobic glycolysis deficiency in a definitive manner.

By converting pyruvate to lactate with regeneration of nicotinamide adenine dinucleotide (NAD^+) (*17*), lactate dehydrogenase (LDH) defines the biochemical reaction of aerobic glycolysis. LDHA and LDHB form five tetrameric LDH isoenzymes (A_4B_0, A_3B_1, A_2B_2, A_1B_3, and A_0B_4) with distinct kinetic properties (*17*). In a zymography assay, activated $CD4^+$ T cells manifested LDH activity predominantly in the form of A_4B_0, similar to that of muscle tissues (fig. S1A). Consistently, LDHA, but not LDHB, was induced upon T cell activation (fig. S1B), likely due to hypoxia-inducible factor 1α (HIF-1α)– and c-Myc–induced transcription of *Ldha* (*10*, *11*).

To study the definitive function of aerobic glycolysis, we deleted LDHA specifically in T cells ($CD4^{Cre}Ldha^{fl/fl}$, designated as knockout, KO) (fig. S1B) (*18*). Compared to activated wild-type (WT) $CD4^+$ T cells, KO T cells barely produced lactate (Fig. 1A). Furthermore, glucose consumption in KO T cells was reduced to ~30% of WT amounts (Fig. 1B), in line with a critical role for LDHA in sustaining aerobic glycolysis through regeneration of NAD^+ consumed at the glyceraldehyde-3-phosphate dehydrogenase (GAPDH) step of glycolysis (*17*).

[1]Immunology Program, Memorial Sloan Kettering Cancer Center (MSKCC), New York, NY 10065, USA. [2]Computational Biology Program, Memorial Sloan Kettering Cancer Center, New York, NY 10065, USA. [3]Physiology Biophysics and Systems Biology Graduate Program, Weill Cornell Graduate School of Medical Sciences, Cornell University, New York, NY 10065, USA. [4]Immunology and Microbial Pathogenesis Graduate Program, Weill Cornell Graduate School of Medical Sciences, Cornell University, New York, NY 10065, USA.
*These authors contributed equally to this work. †**Corresponding author. Email: lim@mskcc.org**

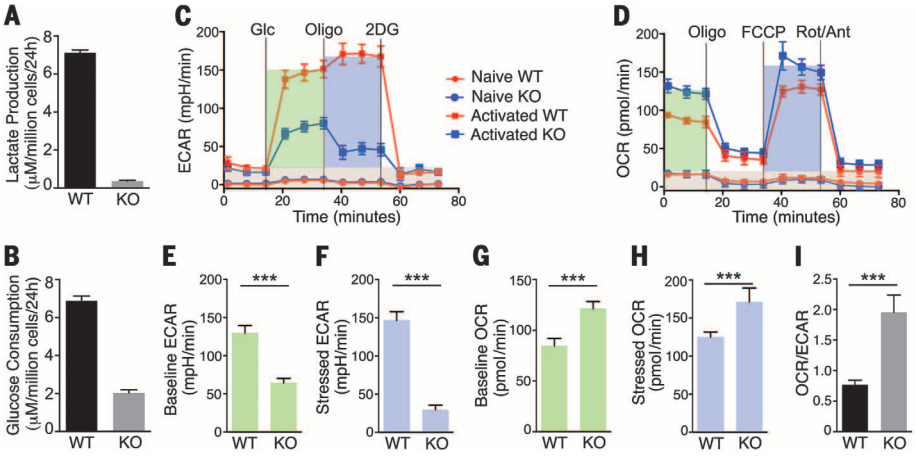

Fig. 1. LDHA dictates aerobic glycolysis in activated CD4$^+$ T cells. (**A** and **B**) Naïve CD4$^+$ T cells isolated from wild-type (WT) or CD4^{Cre}*Ldha*$^{fl/fl}$ (KO) mice were stimulated with anti-CD3 and anti-CD28 in the presence of IL-2 for 2 days. Cells were replenished with fresh medium, which was harvested 24 hours later. Lactate production (A) and glucose consumption (B) were determined with triplicates. (**C** to **I**) Naïve WT or KO CD4$^+$ T cells were stimulated as in (A). Extracellular acidification rate (ECAR) and oxygen consumption rate (OCR) were measured with a glycolysis stress test kit [(C), (E), and (F)] or a Mito stress test kit [(D) and (G) to (I)]. Baseline ECAR (E) and stressed ECAR (F) of activated CD4$^+$ T cells were calculated according to (C). Baseline OCR (G), stressed OCR (H) and baseline OCR/ECAR (I) were calculated according to (D). Statistics (E) to (I) were from one of two independent experiments each with eight biological replicates (n = 8); data represent mean ± SD, two-tailed unpaired t test, ***$P \le 0.001$.

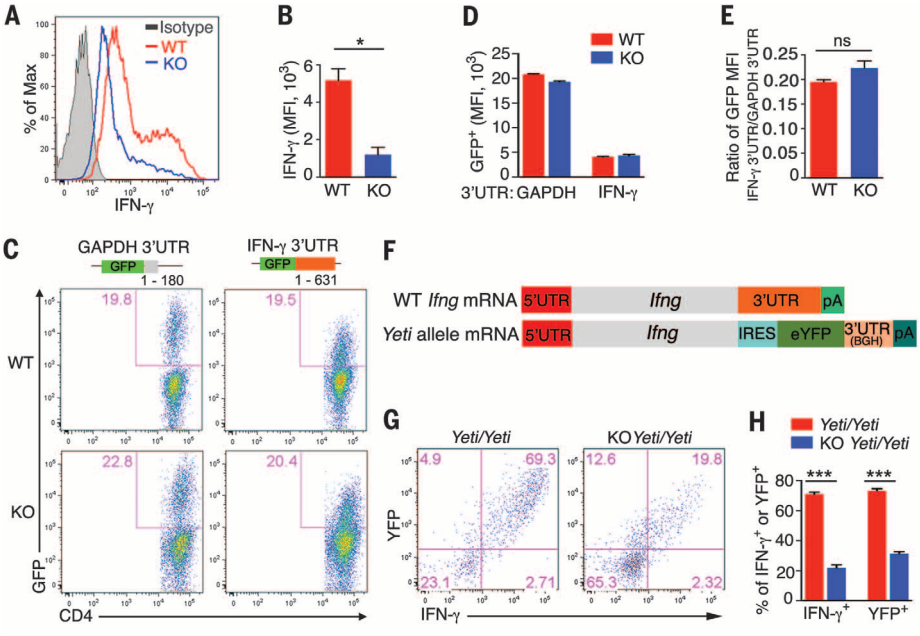

Fig. 2. LDHA regulates IFN-γ expression independent of its 3′UTR. (**A** and **B**) Naïve wild-type (WT) or CD4^{Cre}*Ldha*$^{fl/fl}$ (KO) CD4$^+$ T cells were differentiated under T$_H$1 conditions for 3 days, and restimulated with phorbol myristate acetate (PMA) and ionomycin for 4 hours. IFN-γ expression was determined by intracellular staining. Representative plots (A) and mean fluorescence intensity (MFI) (B) are shown. (**C** to **E**) Naïve WT or KO CD4$^+$ T cells were activated for 2 days and transduced with green fluorescent protein (GFP) constructs fused with the 3′ untranslated region (3′UTR) of the *Ifng* or *Gapdh* gene. GFP expression was measured 48 hours after transduction. Representative plots (C) and MFI of GFP in GFP$^+$ cells are shown (D). (E) MFI of GFP from IFN-γ 3′UTR was normalized to that of GAPDH 3′UTR control. (**F**) A diagram of IFN-γ mRNA expressed from the WT *Ifng* or *Yeti* allele. (**G** and **H**) Naïve CD4$^+$ T cells from *Yeti/Yeti* or KO*Yeti/Yeti* mice were differentiated as in (A). The expression of IFN-γ and eYFP were determined by flow cytometry. Representative plots and respective statistical analysis are shown in (G) and (H). Statistics (B), (E), and (H) were from one of two independent experiments each with three biological replicates (n = 3); data represent mean ± SD, two-tailed unpaired t test, *$P \le 0.05$; ***$P \le 0.001$; ns, not significant.

Consistent with low Glut1 (*13*) and LDHA expression (fig. S1B), naïve CD4$^+$ T cells showed little activity of glucose metabolism, with negligible glucose-induced extracellular acidification rate (ECAR) or oxygen consumption rate (OCR) (Fig. 1, C and D). Upon activation, ECAR was increased in WT CD4$^+$ T cells, which was largely diminished in KO T cells (Fig. 1, C, E, and F). In contrast, both basal and maximal OCR were elevated in KO T cells (Fig. 1, D, G, and H).

^{13}C-isotope–labeled glucose ($^{13}C_6$-glucose) tracing experiments showed that glycolysis was slowed down at the GAPDH step in KO T cells (fig. S2). However, ^{13}C-labeled citrate was increased in the absence of LDHA (fig. S2). In particular, doubly (m+2) and quadruply (m+4) ^{13}C-labeled citrate, readouts of tricarboxylic acid (TCA) cycle activity through the first and second turns, respectively, were much increased in KO T cells (fig. S2), in line with enhanced OCR (Fig. 1, D, G, and H). Together, these findings reveal that glucose metabolism in activated CD4$^+$ T cells is shifted from aerobic glycolysis toward oxidative phosphorylation in the absence of LDHA (Fig. 1I).

LDHA deficiency did not affect thymic development of conventional or regulatory T (T$_{reg}$) cells (fig. S3), or T cell homeostasis in peripheral (fig. S4). LDHA deficiency also did not alter expression of activation markers, size, or survival of activated CD4$^+$ T cells (fig. S5, A to D), whereas proliferation was slightly delayed (fig. S5E). These phenotypes were distinct from those of Glut1-deficient T cells (*13*), suggesting that general glucose metabolism, but not aerobic glycolysis, is required for T cell development and homeostasis.

Glycolysis promotes expression of effector molecules including the type 1 cytokine IFN-γ (*9*, *12*–*15*). Indeed, LDHA deficiency led to diminished IFN-γ expression in T cells differentiated under T helper 1 (T$_H$1) conditions (Fig. 2, A and B). A recent study proposed that aerobic glycolysis enhanced IFN-γ production by sequestering GAPDH away from binding to the *Ifng* 3′UTR, thereby enhancing IFN-γ translation (*12*). To determine whether such regulation accounted for reduced IFN-γ expression in KO T cells, we used a green florescent protein (GFP) reporter in which the GFP open reading frame was fused to the 3′UTR of *Ifng* or *Gapdh*, with the latter not known to repress mRNA translation (*19*). As previously reported (*19*), GFP expression controlled by the *Ifng* 3′UTR showed decreased mean fluorescence intensity compared to that regulated by the *Gapdh* 3′UTR in WT T cells (Fig. 2, C to E). GFP expression under the control of *Ifng* 3′UTR was diminished to a similar extent in KO T cells (Fig. 2, C to E), suggesting that *Ifng* 3′UTR is insufficient to mediate aerobic glycolysis regulation of IFN-γ expression.

To explore the definitive function of 3′UTR in LDHA control of IFN-γ expression, we used an *Ifng* reporter allele *Yeti* (yellow-enhanced transcript for IFN-γ) (*20*), in which the *Ifng* 3′UTR was replaced by 3′UTR of the bovine growth hormone (*BGH*) gene (Fig. 2F). We found that expression of both IFN-γ and yellow fluorescent protein (YFP) driven by the internal ribosome entry site (IRES) element

in the reporter allele were proportionally reduced in the absence of LDHA (Fig. 2, G and H), demonstrating that *Ifng* 3′UTR is not required for LDHA control of IFN-γ expression.

To determine whether reduced IFN-γ production in KO T cells was caused by diminished transcription, we performed RNA sequencing experiments. A total of 363 transcripts were differentially expressed between WT and KO T_H1 cells, among which 220 transcripts, including *Ifng*, were down-regulated in KO T cells (figs. S6A and S7A and table S1). IFN-γ transcription in T_H1 cells is induced by T-bet (*21*). However, T-bet expression was not affected in KO T cells (fig. S7, B and C), suggesting that LDHA promotes IFN-γ expression via T-bet–independent mechanisms.

Glucose metabolism is implicated in the control of gene expression through epigenetic mechanisms that include histone acetylation (*7*, *22*). Chromatin immunoprecipitation–sequencing (ChIP-seq) analysis of histone H3 acetylation at the lysine 9 residue (H3K9Ac), a histone mark associated with active transcription, showed that the differentially expressed genes between WT and KO T_H1 cells had varying amounts of H3K9Ac (fig. S6B and tables S2 and S3), which encoded proteins involved in signal transduction, transcription, metabolism, and effector functions (fig. S6C). Notably, 86% of down-regulated transcripts that included *Ifng* had decreased H3K9Ac in KO T cells (fig. S6B and table S3), suggesting that LDHA may promote IFN-γ expression by modulating histone acetylation.

Compared to the constitutively active *Cd3e* locus, diminished H3K9Ac was observed in *Ifng* promoter, gene body, and the conserved noncoding sequence 22 kilobase pairs upstream of *Ifng* (CNS-22) in KO T cells (Fig. 3, A and B). Acetylation of histone H3 at lysine 27 (H3K27Ac) was also reduced, whereas total histone H3 was comparable (fig. S8, A and B). Notably, diminished histone acetylation was associated with reduced RNA polymerase II (Pol II) recruitment to the *Ifng* locus in KO T cells (fig. S8C). Histone acetylation requires acetyl–coenzyme A (acetyl-CoA) as a substrate, with glucose being a critical source. Considering enhanced TCA cycle activity in KO T cells (Fig. 1 and fig. S2), we hypothesized that in the absence of LDHA, less citrate would be exported from the mitochondria for acetyl-CoA regeneration. Indeed, cytosolic acetyl-CoA was decreased in LDHA-deficient T_H1 cells (Fig. 3C).

To determine whether reduced cytosolic acetyl-CoA was sufficient to repress IFN-γ expression, we inhibited adenosine 5′-triphosphate (ATP)–citrate lyase (ACL), the enzyme converting citrate to acetyl-CoA, and found that IFN-γ expression was diminished in WT T cells (fig. S9, A to D). Acetyl-CoA can be generated from acetate by acetyl-CoA synthetase independent of citrate (*23*). Acetate supplementation augmented acetyl-CoA production (fig. S9E) and corrected IFN-γ expression in KO T cells (Fig. 3, D and E) without affecting T-bet expression (fig. S9F). Instead, enhanced IFN-γ production was associated with normalization of H3K9Ac in *Ifng* promoter and enhancer regions (Fig. 3F). Histone acetylation is a dynamic

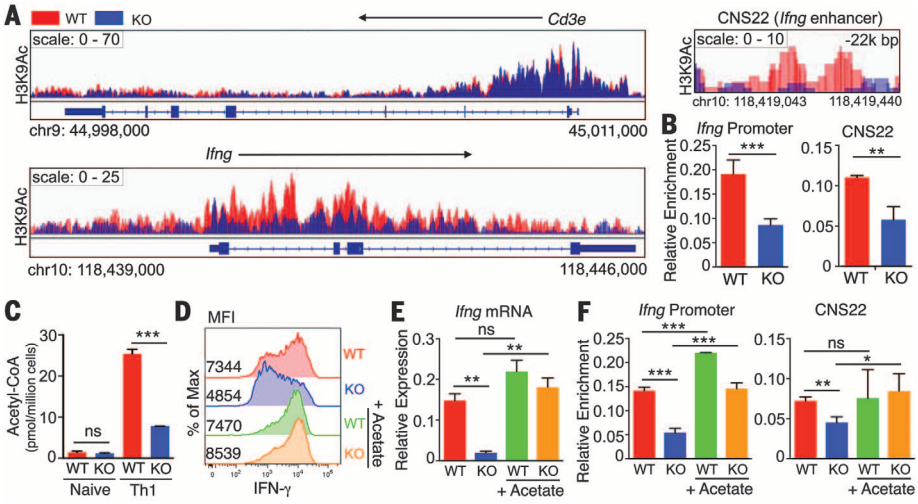

Fig. 3. LDHA promotes IFN-γ expression through an epigenetic mechanism. (**A**) Representative H3K9 acetylation (H3K9Ac) peaks at the *Cd3e* or *Ifng* promoter and enhancer (CNS22) regions from one of two ChIP-Seq experiments are shown. (**B**) H3K9Ac at the *Ifng* promoter and CNS22 enhancer regions in WT or KO T_H1 cells were assessed by ChIP-qPCR (quantitative polymerase chain reaction). Enrichment was normalized to H3K9Ac at the *Cd3e* promoter region. (**C**) Naïve WT or KO $CD4^+$ T cells were differentiated under T_H1 conditions, and acetyl-CoA concentrations were measured by an acetyl-CoA assay kit. (**D** and **E**) Naïve WT or KO $CD4^+$ T cells were differentiated under T_H1 conditions for 3 days and either left untreated or supplemented with 20 mM sodium acetate for another 24 hours. Cells were subsequently restimulated with PMA and ionomycin for 4 hours. The expression of IFN-γ protein (D) and mRNA (E) was determined by flow cytometry and qPCR, respectively. mRNA level of IFN-γ was normalized to that of β-actin. MFIs of IFN-γ are shown in (D). (**F**) T cells were cultured as in (D), and H3K9Ac at the *Ifng* promoter and CNS22 enhancer regions were assessed by ChIP-qPCR. Enrichment was normalized to that of H3K9Ac at the *Cd3e* promoter region. Statistics (B), (C), (E), and (F) were from one of three independent experiments each with three biological replicates ($n = 3$); data represent mean ± SD, two-tailed unpaired *t* test, $^*P \le 0.05$; $^{**}P \le 0.01$; $^{***}P \le 0.001$; ns, not significant.

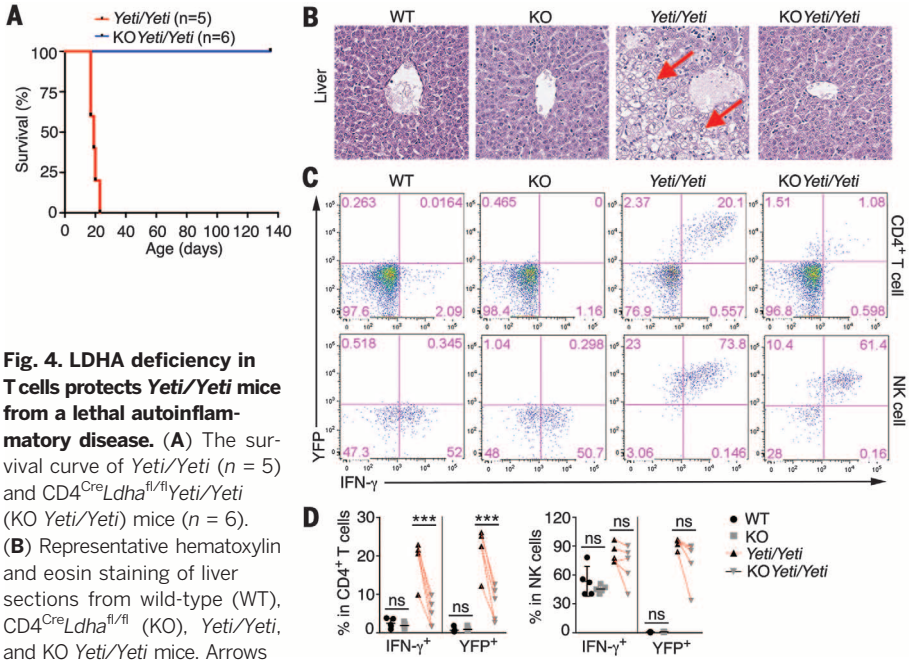

Fig. 4. LDHA deficiency in T cells protects *Yeti/Yeti* mice from a lethal autoinflammatory disease. (**A**) The survival curve of *Yeti/Yeti* ($n = 5$) and $CD4^{Cre}Ldha^{fl/fl}Yeti/Yeti$ (KO *Yeti/Yeti*) mice ($n = 6$). (**B**) Representative hematoxylin and eosin staining of liver sections from wild-type (WT), $CD4^{Cre}Ldha^{fl/fl}$ (KO), *Yeti/Yeti*, and KO *Yeti/Yeti* mice. Arrows indicate the necrotic regions. (**C** and **D**) Splenocytes from mice of the indicated genotypes were stimulated with PMA and ionomycin for 4 hours. IFN-γ and YFP expression in $CD4^+$ T cells and $NK1.1^+TCR^-$ NK cells was determined by flow cytometry. Representative plots (C) and statistics (D) are shown; data represent mean ± SD, $n = 4$ to 5 mice per genotype, two-tailed paired *t* test, $^{***}P \le 0.001$; ns, not significant.

process controlled by competing activities of histone acetyltransferases (HATs) and histone deacetylases (HDACs) (*24*). TSA, a HDAC inhibitor, rectified IFN-γ expression in KO T cells without affecting T-bet expression (fig. S9, G and H), which was associated with increased H3K9Ac in the *Ifng* locus (fig. S9I). Collectively, these findings demonstrate that LDHA promotes IFN-γ expression through an epigenetic mechanism of histone acetylation.

In the absence of endogenous 3′UTR, the *Ifng* transcript in *Yeti/Yeti* mice is stable, resulting in sustained IFN-γ production and a lethal autoinflammatory phenotype (*25*). Indeed, all *Yeti/Yeti* mice succumbed to death by 3 weeks of age (Fig. 4A), which was associated with severe liver damage (Fig. 4B and fig. S10A). Deletion of *Ldha* in T cells corrected the liver immunopathology and conferred long-term survival of *Yeti/Yeti* mice (Fig. 4, A and B, and fig. S10A). LDHA deficiency did not substantially affect the cellularity or activation of *Yeti/Yeti* $CD4^+$ T cells (fig. S10, B to E). However, IFN-γ expression in *Yeti/Yeti* $CD4^+$ T cells was diminished in the absence of LDHA, whereas its expression in LDHA-sufficient *Yeti/Yeti* natural killer (NK) cells was not affected (Fig. 4, C and D). The correction of a lethal autoinflammatory disease in *Yeti/Yeti* mice by T cell–specific deletion of *Ldha* supports the notion that aerobic glycolysis promotes IFN-γ expression in T cells through an epigenetic mechanism of *Ifng* transcription but not via a 3′UTR-dependent mechanism of translation in vivo.

To further explore aerobic glycolysis in control of effector T cell responses, we used Scurfy mice with a mutation in the T_{reg} cell lineage *Foxp3* gene (*Foxp3*^{sf}) (*26*). LDHA deficiency in T cells corrected the Scurfy phenotype and extended life span of *Foxp3*^{sf} mice (fig. S11, A and B), which was associated with reduced inflammation in multiple organs without affecting lymphadenopathy or splenomegaly (fig. S11, C to F). T cell activation and expansion were comparable between *Foxp3*^{sf} and KO *Foxp3*^{sf} mice (fig. S11, G and H), which was in line with our in vitro findings (fig. S5, A to E). Nevertheless, $CD4^+$ T cells produced less IFN-γ in the absence of LDHA (fig. S11, I and J), demonstrating a critical role for LDHA-mediated aerobic glycolysis in promoting autoreactive T_H1 cell responses.

Our findings do not support a translational mechanism of aerobic glycolysis in IFN-γ production (*12*), as LDHA promotes IFN-γ expression independent of its 3′UTR. Previous studies have shown that utilization of glycolytic intermediates for biosynthesis accounts for a small fraction (~7%) of the glucose consumed in activated T cells (*27*), whereas aerobic glycolysis produces the majority (~60%) of ATP (*28*). Hence, LDHA-mediated aerobic glycolysis may primarily relieve the burden of mitochondria as an energy house to "burn" carbons to generate ATP. As a result, more citrate can be exported out of mitochondria to generate acetyl-CoA and promote histone acetylation in selected gene loci (fig. S12). LDHA inhibitors are being developed to target tumor cell metabolism (*29*). Our data suggest that LDHA inhibitors could be immunosuppressive, and thus may complicate their applications in cancer. Instead, LDHA inhibitors, as well as inhibitors targeting other enzymes involved in acetyl-CoA metabolism, such as ACL, may be useful in treatment of autoimmune diseases and transplant rejection.

REFERENCES AND NOTES

1. R. Wang, D. R. Green, *Nat. Immunol.* **13**, 907–915 (2012).
2. E. L. Pearce, M. C. Poffenberger, C. H. Chang, R. G. Jones, *Science* **342**, 1242454 (2013).
3. N. J. MacIver, R. D. Michalek, J. C. Rathmell, *Annu. Rev. Immunol.* **31**, 259–283 (2013).
4. K. Ganeshan, A. Chawla, *Annu. Rev. Immunol.* **32**, 609–634 (2014).
5. K. A. Frauwirth *et al.*, *Immunity* **16**, 769–777 (2002).
6. M. G. Vander Heiden, L. C. Cantley, C. B. Thompson, *Science* **324**, 1029–1033 (2009).
7. C. Lu, C. B. Thompson, *Cell Metab.* **16**, 9–17 (2012).
8. M. V. Liberti, J. W. Locasale, *Trends Biochem. Sci.* **41**, 211–218 (2016).
9. C. M. Cham, T. F. Gajewski, *J. Immunol.* **174**, 4670–4677 (2005).
10. R. Wang *et al.*, *Immunity* **35**, 871–882 (2011).
11. L. Z. Shi *et al.*, *J. Exp. Med.* **208**, 1367–1376 (2011).
12. C. H. Chang *et al.*, *Cell* **153**, 1239–1251 (2013).
13. A. N. Macintyre *et al.*, *Cell Metab.* **20**, 61–72 (2014).
14. J. Blagih *et al.*, *Immunity* **42**, 41–54 (2015).
15. P. C. Ho *et al.*, *Cell* **162**, 1217–1228 (2015).
16. E. Bustamante, P. L. Pedersen, *Proc. Natl. Acad. Sci. U.S.A.* **74**, 3735–3739 (1977).
17. J. J. L. Holbrook, A. Liljas, S. J. Steindel, M. G. Rossmann, in *The Enzymes*, P. D. Boyer, Ed. (Academic Press, New York, ed. 3, 1975), vol. 11, pp. 191–292.
18. See materials and methods in supplementary materials on *Science* Online.
19. A. V. Villarino *et al.*, *Immunity* **34**, 50–60 (2011).
20. D. B. Stetson *et al.*, *J. Exp. Med.* **198**, 1069–1076 (2003).
21. S. J. Szabo *et al.*, *Cell* **100**, 655–669 (2000).
22. K. E. Wellen *et al.*, *Science* **324**, 1076–1080 (2009).
23. A. Luong, V. C. Hannah, M. S. Brown, J. L. Goldstein, *J. Biol. Chem.* **275**, 26458–26466 (2000).
24. E. Verdin, M. Ott, *Nat. Rev. Mol. Cell Biol.* **16**, 258–264 (2015).
25. R. L. Reinhardt *et al.*, *J. Immunol.* **194**, 2358–2368 (2015).
26. M. E. Brunkow *et al.*, *Nat. Genet.* **27**, 68–73 (2001).
27. D. A. Hume, J. L. Radik, E. Ferber, M. J. Weidemann, *Biochem. J.* **174**, 703–709 (1978).
28. M. Guppy, E. Greiner, K. Brand, *Eur. J. Biochem.* **212**, 95–99 (1993).
29. K. Augoff, A. Hryniewicz-Jankowska, R. Tabola, *Cancer Lett.* **358**, 1–7 (2015).

ACKNOWLEDGMENTS

We thank R. Locksley for the *Yeti* mice, A. Abbas and A. Villarino for the 3′UTR GFP constructs, and J. Cross and J. Ye for help with Seahorse experiments. We also thank the Li laboratory for discussions. The data presented in this manuscript are tabulated in the main paper and in the supplementary materials. MSKCC has filed a provisional patent application with the U.S. Patent and Trademark Office (application no. 62/394,859). The application is directed toward inhibition of acetyl-CoA metabolism for treatment and prevention of immune disease and disorders. M.P., N.Y., and M.O.L. are listed as inventors on this patent application. This work was supported by the Ludwig Center for Cancer Immunology (M.O.L.), the Functional Genomics Initiative (M.O.L.), a Faculty Scholar grant from the Howard Hughes Medical Institute (M.O.L.), and the Memorial Sloan Kettering Cancer Center Support Grant/Core Grant (P30 CA008748). RNA-seq and ChIP-Seq data are deposited in the Genome Expression Omnibus under accession number GSE86188.

SUPPLEMENTARY MATERIALS

www.sciencemag.org/content/354/6311/481/suppl/DC1
Materials and Methods
Figs. S1 to S12
Tables S1 to S3
References (*30*–*37*)

4 March 2016; accepted 1 September 2016
Published online 29 September 2016
10.1126/science.aaf6284

Cas 9 Nuclease

XactEdit Cas9 Nuclease with Nuclear Localization Signal is a highly active, purified recombinant *Streptococcus pyogenes* Cas9 protein that mediates site-specific double-stranded DNA cleavage when complexed with a guide RNA (gRNA). The introduction of Cas9/gRNA ribonucleoprotein (RNP) complexes into cells creates double-stranded DNA breaks, which have been used for a variety of targeted genome-editing studies, such as homologous knockin and gene knockout. Available as a kit or a standalone enzyme (1 mg/mL or 10 mg/mL), XactEdit Cas9 delivers consistent and robust performance. With no detectable nonspecific nuclease activity and low endotoxin levels, this nuclease is ideal for in vitro assays or for introduction into cells by electroporation or transfection. Unlike vector or messenger RNA-based Cas9 systems, the XactEdit Cas9 RNP complex does not require transcription or translation and can act immediately after entering a cell.

SGI DNA
For info: 855-474-4362
https://sgidna.com

Organoid Culture Reagents

A new R-Spondin1 cell line provides labs a cost-effective solution for obtaining a long-term supply of R-Spondin1 (RSPO1)—a critical ingredient used in the maintenance and proliferation of mouse and human organoid progenitor stem cells. R-Spondins positively regulate Wnt/beta-catenin signaling, most probably by acting as a ligand for LGR4-6 receptors and an inhibitor for ZNRF3. AMS Biotechnology's (AMSBIO's) 293T cell line is stably transfected to express murine RSPO1 with an N-terminal hemagglutinin epitope tag and fused to a C-terminal murine IgG2a Fc fragment. This cell line can be used to produce either purified RSPO1- or RSPO1-conditioned media. The murine RSPO1 protein from this cell line has been demonstrated to lower the cost of organoid culture and to maintain Lgr5+ stem cells. AMSBIO has also introduced a new organoid harvesting solution that separates intact organoids from extracellular proteins in the hydrogel for passaging, cryopreservation, biochemical analysis, and the facilitation of patient-derived xenograft models.

AMS Biotechnology
For info: +44-(0)-1235-828200
www.amsbio.com

Multi-Imaging System

The ChemoLum multi-imaging system has been upgraded to include a new high-quality f0.95 lens, enabling the system's size to be reduced. This improved lens specification makes the ChemoLum much easier to fit on any bench space and further guarantees superb image quality. The ChemoLum C1R features a 16-bit CCD camera with 8.3 megapixels; the large pixel size of 5.4 µm × 5.4 µm ensures high sensitivity. Several binning levels are possible, which further increase the C1R's sensitivity and allow it to quickly capture images of any faint blot. The extended cooling to ΔT= –40°C ensures noise-free images at all exposure settings. There are four presets for different sample sizes. In addition, the system software controls a five-position motorized filter wheel to ensure the correct selection for each application.

HeroLab
For info: +44-(0)-1223-515440
www.herolab.de

Vitrification Media

Irvine Scientific, a world leader in the development and manufacture of assisted reproductive technologies, is the first company to receive FDA 510(k) clearance for expanded use of Vit Kit vitrification media to include human oocytes. Vit Kit-Freeze and Vit Kit-Thaw are now intended for worldwide use with oocytes (metaphase II), pronuclear zygotes through day 3 cleavage-stage embryos, and blastocyst-stage embryos. Vitrification is a cryopreservation technique that provides excellent survivability of embryos and oocytes through dehydration and ultrarapid cooling. This process eliminates the concerns of damaging ice crystal formation associated with traditional slow freezing. Egg freezing offers women the choice to preserve healthy eggs before undergoing cancer treatment, chemotherapy, or radiation therapy, all of which compromise ovarian function and egg viability. Age negatively impacts a woman's egg supply in both quality and quantity, so freezing eggs while young is also an option for those who wish to delay starting a family.

Irvine Scientific
For info: 800-577-6097
www.irvinesci.com

Gel Imaging Systems

The Omega Fluor is an entry-level gel imaging system that comes standard with the basic components and exceptional safety features for DNA- and protein-gel imaging. With the introduction of a single-wavelength UV transilluminator that is fully integrated into a light-tight cabinet, gone are the days of modular hoods sitting awkwardly on top of light boxes. A UV-safety switch, auto UV shutoff, and a UV-blocking viewport are standard features, while a high-resolution camera and focus-free lens with SmartCapture Technology maintain sample integrity with exceptional imaging performance. Omega Fluor comes with a 5-megapixel camera and a 24 cm x 20 cm imaging area. It is capable of working with UV- and white-light illumination across an extensive list of dyes, including the SYBR family, ethidium bromide, Coomassie Blue, silver stain, AdvanStain Scarlet, SYPRO Ruby, Oriole, and more. The small footprint is matched with a small price.

Gel Company/Aplegen
For info: 415-247-8760
www.gelcompany.com

Electronically submit your new product description or product literature information! Go to www.sciencemag.org/about/new-products-section for more information.

Newly offered instrumentation, apparatus, and laboratory materials of interest to researchers in all disciplines in academic, industrial, and governmental organizations are featured in this space. Emphasis is given to purpose, chief characteristics, and availability of products and materials. Endorsement by *Science* or AAAS of any products or materials mentioned is not implied. Additional information may be obtained from the manufacturer or supplier.

eppendorf & Science

PRIZE FOR NEURO BIOLOGY

Dr. Peter Stern, Science Editor & Prize Jury Chair

Dr. Shigeki Watanabe, 2015 Prize Winner

Neuroscience 2016, San Diego
Sunday, November 13, 2016
2:00 – 3:00 pm, Booth #901

Meet & Greet

Neuroscience 2016
The Eppendorf & Science Prize for Neurobiology is an international research prize. It is awarded annually to one young scientist not older than 35 years for the most outstanding neurobiological research based on methods of molecular and cell biology.

You could be next to win this prize.
Stop by the Eppendorf Booth #901 and meet the 2015 Winner, Dr. Shigeki Watanabe. Learn more about his research on synaptic vesicle endocytosis. Ask the Prize Jury Chair, Dr. Peter Stern, about the prize application process and what makes a winning paper.

Register for prize updates to receive an Eppendorf & Science Prize for Neurobiology t-shirt*!

*Subject to prize eligibility while supplies last.

Learn more about the prize at:
www.eppendorf.com/prize

eppendorf Science AAAS

life science EXPERT and e-commerce leader

The life science leaders of
EMD Millipore + Sigma-Aldrich
have joined together and, with our agile e-commerce and global distribution, we can help to simplify your world.
So you can focus with confidence on tackling life science's biggest challenges.

MilliporeSigma now offers:

- **An extended global network** across more than 66 countries
- **A world-class e-commerce platform** to simplify transactions
- **A vast portfolio** that has grown to over 300,000 products

Our combined strengths will deliver the **knowledge, know-how, and best-in-class resources.**

Learn more at **milliporesigma.com**

The life science business of Merck KGaA, Darmstadt, Germany operates as MilliporeSigma in the U.S. and Canada.

MilliporeSigma

Science & Diplomacy

Science & Diplomacy provides an open access forum for rigorous thought, analysis, and insight to serve stakeholders who develop, implement, or teach all aspects of science and diplomacy. Learn more about the latest ideas in science diplomacy and receive regular updates by following @SciDip on Twitter, liking the quarterly's page on Facebook (www.facebook.com/sciencediplomacy), and registering for free at **www.sciencediplomacy.org/user/register**.

WWW.SCIENCEDIPLOMACY.ORG

Science & Diplomacy is published by the Center for Science Diplomacy of the American Association for the Advancement of Science (AAAS), the world's largest general scientific society.

Science & Diplomacy

AAAS
ADVANCING SCIENCE SERVING SOCIETY

eppendorf

New: 4 liter capacity!

More Capacity

Centrifuge 5920 R

The new Centrifuge 5920 R delivers extraordinary high capacity in a very compact and ergonomic product design. Its state-of-the-art refrigeration system provides excellent cooling performance and keeps your temperature sensitive samples safe.

> Max. capacity: 4 × 1000 mL or 52 × 50 mL conical
> Outstanding rotor versatility
> Space-saving design
> Advanced temperature management
> NEW: Eppendorf Conical Tubes, 15 mL and 50 mL

www.eppendorf.com/centrifugation

Watch video!

MY WORK IS A STORY OF INTENSITY.

When you're fighting the Zika virus, how fast is fast enough? My team develops tests that help our customers diagnose and combat infectious diseases. At Thermo Fisher Scientific, we responded to the outbreak by creating a mobile diagnostic kit that could serve hundreds of thousands of people in the hardest-hit areas—in only three weeks. Even in a place as innovative as the Bay Area, our work stands out. I'm passionate about the discoveries we're making and excited about where our innovation and imagination will take us next.

If you're ready to take on some of the biggest challenges in the world, you'll discover that, at Thermo Fisher Scientific, each one of our 50,000 extraordinary minds has a unique story to tell. And we all contribute to a singular mission — enabling our customers to make the world healthier, cleaner and safer.

Jonathan

R&D Leader

What story will you tell?

Explore our opportunities at
jobs.thermofisher.com and join our team.

ThermoFisher SCIENTIFIC

CELL SIGNALING TECHNOLOGY

EPIGENETICS:
DISCOVERY THROUGH VALIDATION

692 CST antibodies for epigenetic-related targets, including histone modifications, epigenetic regulators, and general transcription factors.

226 CST antibodies validated for ChIP according to ENCODE* Consortium guidelines.

Validated Tools for Discovery:

» SimpleChIP® Kits to facilitate Chromatin IP from cells and tissue.

» PTMScan® Kits and Services to enable MS-based discovery of methylated and acetylated proteins.

» Most ChIP-validated antibodies approved for additional applications like IHC, Flow, IF and WB.

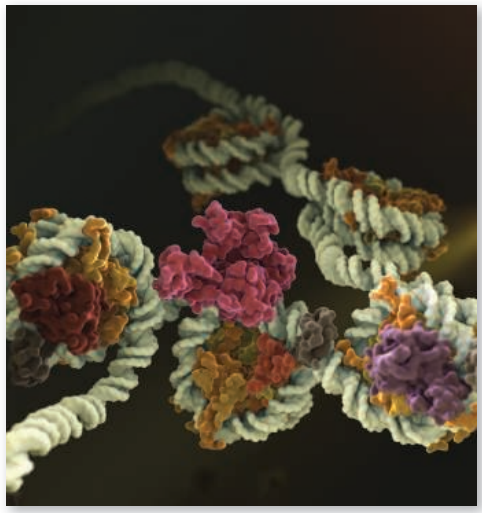

Molecular model of chromatin.

Learn more at: www.cellsignal.com/epigeneticdiscovery

*Landt S.G. et al. (2012) *Genome Res.* 22, 1813–1831.

15PADEPIGNONE0079ENG_00

Cell Signaling TECHNOLOGY®

By **Rochelle Poole**

Bullied out of research

We were 4 days into the field expedition when I overheard my Ph.D. supervisor making disparaging remarks about someone. He was speaking in Dutch, probably assuming that I wouldn't understand because I'm American, saying that "she"—or "*zij*"—was simple, physically weak, and loud. He compared *zij* to his "other stupid students." I listened carefully to the crimes *zij* had committed, gradually becoming more and more certain that I—the only woman at the research station—was *zij*. This was the bully who pushed me out of research.

My experience was all the more disappointing because I had been very deliberate about my decision to pursue a Ph.D. It had to focus on predator-prey ecology, contribute to conservation, and offer adventure. Unlikely as it seemed, I came across a Ph.D. opportunity that ticked all of my boxes. I applied immediately and was thrilled to be selected by my future supervisor and an independent scientific board. My adviser-to-be seemed friendly and ambitious. It seemed too good to be true—and, indeed, it was.

On the first day of my first field expedition, my adviser abruptly shifted all the field resources to a different topic that didn't match my experience or career ambitions, ignoring our rigorous research plans—and my growing objections. Such a capricious change was unacceptable, I said, but my adviser countered my resistance. "I have the power to do this," he said. "This is how science works; you are just naïve." To some extent he was right: Ph.D. advisers wield the power to create or destroy research careers, and students typically have few—if any—ways to protect themselves from advisers who misuse this responsibility, especially during remote fieldwork. I was upset, but he was the field manager, so I put my head down, carried on with the work, and kept a log of his behavior. I assumed that we would talk sensibly and find a solution once we had returned home and enjoyed the Christmas break.

Instead, while I was away visiting family for the holiday, my adviser began sending me emails about my contract, copying heads of the department. He organized a disciplinary meeting with human resources (HR) for the morning of the day I returned to work, where he recommended that my contract be terminated. He said that I was too stupid to be one of *his* students and made bizarre false claims about my personal habits. The meeting ended when the HR manager cut him off and suggested that we meet another time.

"Students typically have few—if any—ways to protect themselves from advisers."

Bewildered by his behavior, I asked the HR manager why she thought he was acting this way. "I do not think he likes strong women," she replied. He was a known bully of both male and female students, but I was the first student he had tried to intimidate by staging such an aggressive HR hearing. Perhaps he reacted that way because I was the first woman to challenge him. The realization that simply being a woman who stands up for myself could derail my career was devastating.

After lengthy further discussions, my funding body instructed the institution to appoint a new supervisor for me, which it did—at its satellite site at the other end of the country, where I would be doing work that didn't meet the requirements I had initially set for myself. I felt I was being punished for my supervisor's behavior, but I was optimistic that I would be able to persevere despite the disruption of moving my family, the 4-month lapse in research, and my general emotional exhaustion. After a few months, though, my need for self-care overpowered my guilt about leaving and I resigned.

I have struggled with how to think about this experience. I've found a fulfilling life in science communication and education, but I sometimes feel disappointed that I had to abandon my doctoral studies. I remind myself, though, that resigning doesn't mean that I "lost." I would have lost if I had accepted bullying as a rite in academe and sacrificed my mental health and quality of life. I know that taking on this bully was right for me, and I hope that speaking about my experience will encourage others to stand up for themselves, too. Doing so may put their career plans on hold or even at risk, but it's the only way to make academic life more egalitarian. ■

Rochelle Poole is a pseudonym. Send your career story to SciCareerEditor@aaas.org.

ILLUSTRATION: ROBERT NEUBECKER